

Institute of Experimental and Clinical Pharmacology and Toxicology

Faculty of Medicine

Saarland University

**Electrophysiological characterization and interplay of
TRPC1 channels and voltage-gated Ca²⁺ channels**

Dissertation submitted for obtaining the university degree of

Doctor rerum naturalium

Barbara Wardas

Born on 20th August 1988

Bielsko-Biała, Poland

November 2020

Dean: Prof. Dr. Michael Menger

Day of defence: 15.10.2021

First referee and "Doktorvater": Prof. Dr. Veit Flockerzi, MD

Second referee: Prof. Dr. Xing-Zhen Chen (University of Alberta, Canada)

Homburg, November 2020

Scientific supervisor: Dr. rer. nat. Andreas Beck

To my father

Acknowledgements

I would like to thank my supervisors Dr. Andreas Beck and Prof. Veit Flockerzi for the extremely interesting topic and for providing the required materials and equipment. Furthermore, I would like to thank both for the constructive assistance and discussions of the experiments and results.

Moreover, I would like to thank Dr. Petra Weißgerber and all members of the animal facility, Dr. Anouar Belkacemi and Dr. Ahsan Raza for providing cells, Western Blots, PCRs and constructive discussions, PD. Dr. Stephan Philipp and Alexander Becker for generating and providing $CaV\beta3^{-/-}$ Ins-1 cells and PD. Dr. Ulrich Wissenbach for generating and providing different cDNAs.

I would also like to thank Stefanie Buchholz, Heidi Löhr, Ute Soltek, Martin Simon-Thomas and Christine Wesely for their technical assistance.

I would like to thank Sandra Plant and Dr. Thabet Belkacemi for the pleasant working atmosphere and help with experimental/technical questions.

Many thanks to the entire Pharmacology and Toxicology department for the good working atmosphere, the helpfulness and willingness to discuss, as well as for the warm welcome in the working group.

Special thanks to my family and friends for their support.

Contributions

Hereby I would like to acknowledge the contributions of the following colleagues:

Dr. Andreas Beck for the measurements of TRPC5 currents and help with designing experiments (Figure 13).

PD. Dr. Ulrich Wissenbach and Dr. Laura Hofmann for generating and providing cDNAs of TRPC1 VL, TMEM 201, STAC1, Latrophilin 2 and eGFP-TRPC4-C1_{S5-S6 linker} chimera.

PD. Dr. Stephan Philipp and Alexander Becker for generating and providing CaV β 3^{-/-} Ins-1 cells.

Dr. Anouar Belkacemi for providing MEF cells, all CaV β 3 Western Blots (Figure 37, Figure 38, Figure 39; Figure 41) and the help with the dot blot binding assay.

Dr. Ahsan Raza for preparing the osteoclasts, for providing the PCR of the osteoclasts (Figure 30) and generating the TRPC1 IRES Cre mouse line.

Dr. Hongmei Wang for staining the pituitary gland, the transcript expression of all TRPCs in the pituitary, teaching me the preparation and dissociation of the pituitary cells and for providing the TRPC1 protein structure (Figure 27).

Stefanie Buchholz for cloning all cDNAs.

Heidi Löhrr for generating the CaV3.2 wt; CaV3.2 G1064R and TRPC1 VL cell lines.

Christine Wesely for performing Western Blots of HEK-cells (Figure 31; Figure 43).

Table of content

Acknowledgements	V
Contributions	VI
List of Abbreviations	XI
List of Figures.....	XIV
List of Tables.....	XVII
Summary.....	XXII
Zusammenfassung.....	XXIV
Introduction	1
1.1 Calcium signaling	1
1.2 Transient Receptor Potential (TRP) channels	2
1.2.1 The canonical TRP subfamily	4
1.2.1.1 TRPC1.....	6
1.2.1.2 TRPC4 and TRPC5	8
1.3 Voltage-gated calcium channels (CaVs)	9
1.3.1 L-type CaV channels	11
1.3.1.1 CaV1.2 channel.....	12
1.3.2 T-type channels.....	13
1.3.2.1 CaV3.2 channel.....	14
1.4 Aims	15
Material and Methods.....	16
2.1 Cell culture	16
2.1.1 Stable immortal cell lines	16
2.1.2 Transfection of cDNA.....	16
2.1.3 Dissociation of the murine pituitary	17
2.1.4 Preparation of murine embryonic fibroblasts (MEFs)	18
2.1.5 Culturing of osteoclasts	18
2.2 Polymerase chain reaction (PCR) of dissociated pituitary cells.....	19
2.3 cRNA-synthesis.....	19
2.3.1 Subcloning of cDNA into vectors for <i>in vitro</i> transcription.....	19

2.3.2 Transformation and plating of competent <i>E. coli</i>	20
2.3.3 Plasmid preparation	20
2.3.4 Linearization and Purification of the plasmid DNA	20
2.3.5 <i>in vitro</i> transcription	21
2.3.6 cRNA injection into <i>Xenopus laevis</i> oocytes	21
2.4 Protein detection by Western Blots	21
2.5 Protein surface localization (Biotinylation).....	23
2.6 Dot blot.....	25
2.6.1 <i>in vitro</i> transcription	25
2.6.2 Gel filtration and radioactivity detection	25
2.7 Electrophysiology	26
2.7.1 Patch clamp technique	26
2.7.1.1 Patch clamp set-up.....	28
2.7.1.2 Experimental procedure and protocols for patch clamp	29
2.7.1.2.1 Transient receptor potential channel recordings	31
2.7.1.2.2 Voltage-gated calcium channel recordings	32
2.7.2 Two-electrode voltage clamp technique.....	34
2.7.2.1 TEVC set-up.....	34
2.7.2.2 Experimental procedure and protocols for TEVC	34
2.8 Analysis, graphing and statistics.....	35
Results.....	37
3.1 Electrophysiological characterization of canonical Transient Receptor Potential (TRPC) channels.....	37
3.1.1 Electrophysiological properties of TRPC1.....	37
3.1.2 Effect of Englerin A on the heteromeric TRPC4 α /TRPC1 channel	38
3.1.3 Mutations of the putative lower gate of TRPC1	39
3.1.4 Characterization of TRPC4-TRPC1 _{S5-S6 linker} chimera	45
3.1.5 TRPC1 function <i>in vivo</i>	51
3.1.6 TRPC channels in murine osteoclasts	55
3.2 Electrophysiological characterization of voltage-gated calcium channels.....	56

3.2.1 Characterization of L-type CaV currents	56
3.2.1.1 Interaction of CaV1.2 with different CaV β subunits	56
3.2.1.1.1 Impact of different CaV β 2 splice variants on CaV1.2	56
3.2.1.1.2 Effect of Englerin A on CaV1.2 currents.....	60
3.2.1.1.3 Impact of the CaV β 3 subunit on CaV1.2	61
3.2.2 Characterization of the CaV current in rat Ins-1 cells	62
3.2.3 CaV channels in murine embryonic fibroblasts	64
3.2.4 CaV channels in osteoclasts.....	66
3.2.5 Characterization of hCaV3.2 wt and hCaV3.2 G1064R.....	67
3.2.6 Effect of Englerin A on CaV3.2 currents.....	70
3.2.7 Impact of different CaV β subunits on the CaV3.2 current	71
Discussion.....	75
4.1 Electrophysiological characterization of TRP channels.....	75
4.1.1 Does TRPC1 function as an ion channel?	75
4.1.2 TRPC1 function in osteoclasts and in pituitary cells.....	77
4.2 Electrophysiological characterization of voltage-gated calcium channels.....	79
4.2.1 Impact of CaV β subunits on L-type and T-type CaV channels	79
4.2.2 The CaV channel independent function of CaV β 3	81
4.2.3 hCaV3.2 G1064R mutation and hypertension in a Spanish family	82
4.3 Effect of Englerin A on TRPC channels and CaVs.....	84
References.....	86
Appendix	100
5.1 Cell lines and plasmids.....	101
5.2 TRPC4 β /TRPC1 cRNA expression in <i>Xenopus laevis</i> oocytes.....	105
5.2.1 Mutations of the lower gate of TRPC1	105
5.2.2 Characterization of the TRPC4 β -C1 _{S5-S6 linker} chimera in <i>Xenopus laevis</i> oocytes	106
5.3 Additional characterization of the TRPC4 α -C1 _{S5-S6 linker} chimeras in HEK-cells.....	108
5.3.1 Coexpression of TRPC4 α -C1 _{S5-S6 linker} with TRPC4 α and stimulation with hormones (CCh plus DAMGO) and with Englerin A (EA).....	108

5.3.2 Coexpression of TRPC4 β -C1 _{S5-S6 linker} chimera 1 or 2 with TRPC4 β and stimulation with hormone (CCh)	110
5.3.3 Coexpression of TRPC4 α -C1 _{S5-S6 linker} with TRPC1 and stimulation with hormones (CCh plus DAMGO) and with Engerlin A (EA).....	111
5.4 Funtional interaction of TRPC4 non-TRPC proteins.....	113
5.4.1 Summary: Funtional interaction of TRPC4 non-TRPC proteins.....	125
Curriculum vitae	127
Publications.....	128

List of Abbreviations

°C	degree Celsius
aa	amino acid
ad.	adjust
AID	α-interaction domain
Ba ²⁺	bariumion
BSA	bovine-serum-albumin
Ca ²⁺	calcium ion
CaM	calmodulin
CaV	voltage-gated calcium channel
CCh	carbachol
CIRB	calmodulin/ Inositol-1,4,5-trisphosphate Receptor-binding
cryo-EM	cryo electron microscopy
Csrp1	cysteine and glycine-rich protein 1
DAG	diacylglycerol
DAMGO	D-Ala, N-MePhe, Gly-ol-enkephalin
DMEM	Dulbecco's modified Eagle's medium
DNA	deoxyribonucleic acid
DVF	divalent-free
EA	Englerin A
EBSS	Earle's Balanced Salt Solution
<i>E. coli</i>	<i>Escherichia coli</i>
EDTA	ethylenediaminetetraacetic acid
eg.	<i>exempli gratia</i>
ER	endoplasmic reticulum
<i>et al.</i>	<i>et alii</i>
FBS	fetal bovine serum
GΩ	gigaohm
GDP/GTP	guanosine diphosphate/ guanosine trisphosphate
GFP	green fluorescent protein
GPCR	G-protein-coupled receptor
Gramd	GRAM domain-containing protein
h	hour
hEEA1	human early endosome antigen 1

HEK	human embryonic kidney
HVA	high voltage activated
i. e.	<i>id est</i>
IP ₃	inositol-1,4,5-trisphosphate
IP ₃ R	inositol-1,4,5-trisphosphate receptor
kDa	kilodalton
Lasp1	LIM and SH3 domain protein 1
LVA	low voltage activated
MEF	mouse embryonic fibroblast
min	minutes
ml	milliliter
mM	millimolar
ms	milliseconds
M2R/M3R	muscarinic m2 receptors/ muscarinic m3 receptors
mV	millivolt
MVF	monovalent-free
Na ⁺	sodium ion
nM	nanomolar
NMDG	N-methyl-D-glucamine
NDPK-B	nucleoside-diphosphate kinase-B
OAG	1-oleoyl-2-acetyl-sn-glycerol
pA/pF	picoampere per picofarad
PBS	phosphate-buffered saline
PCR	polymerase chain reaction
PIP ₂	phosphatidylinositol-4,5-bisphosphate
PLC	phospholipase C
PLL	Poly-L-Lysine
P/S	penicillin/streptomycin
RNA	ribonucleic acid
rpm	revolutions per minute
s	seconds
Stac2	SH3 and cysteine-rich domain-containing protein 2
TMEM 201	transmembrane protein 201
TRP	transient receptor potential

U	unit of enzyme catalytic activity
V _h	holding potential
VOC	voltage-operated channel
wt	wild-type
μg	microgram
μl	microliter
μOR	μ-opioid receptor

List of Figures

Figure 1 TRPC channels couple extracellular signals to membrane depolarization and activation of voltage-gated channels.	1
Figure 2 Phylogenetic tree and topology of the TRP channel family.	2
Figure 3 Protein domains of a TRPC channel protein.	4
Figure 4 TRPC channel activation.	5
Figure 5 Voltage-gated calcium channels.	9
Figure 6 Domain structure of the different CaV β subunits.	10
Figure 7 Patch clamp configurations.	27
Figure 8 Schematic setting of a patch clamp set-up.	28
Figure 9 Ramp protocol and application protocol for the TRP current recordings.	32
Figure 10 Patch clamp protocols for recording currents from L-type voltage-gated calcium channels.	32
Figure 11 Protocols for current recordings of T-type voltage-gated calcium channels.	33
Figure 12 TEVC protocol.	35
Figure 13 Electrophysiological properties of TRPC1.	37
Figure 14 EA-induced currents in TRPC4 α /TRPC1 expressing HEK-cells.	38
Figure 15 Alignment of TRPC channels.	39
Figure 16 Mutations within the LIAM motif of TRPC1.	40
Figure 17 Mutation within the S4-S5 linker and the S5 of TRPC1.	41
Figure 18 Mutation in the TRPC1 TRP helix.	43
Figure 19 Summary of all TRPC1 mutations and their impact on TRPC4 α /TRPC1 currents.	44
Figure 20 DAMGO/CCh-induced currents in the presence of TRPC1 V741A.	45
Figure 21 The TRPC4 α -TRPC1 _{S5-S6 linker} chimera.	46
Figure 22 Effect of DAMGO/CCh on the TRPC4 α -C1 _{S5-S6 linker} currents.	47
Figure 23 Impact of EA on TRPC4 α -C1 _{S5-S6 linker} chimera.	47
Figure 24 Effect of NMDG on the TRPC4 α -C1 _{S5-S6 linker} chimera current.	48
Figure 25 Effect of the non-specific TRP-blocker SKF on homomeric TRPC4 α and homomeric TRPC4 α -C1 _{S5-S6 linker} chimera.	49
Figure 26 CCh-induced currents through TRPC4- β C1 _{S5-S6 linker} chimera.	50
Figure 27 Visualizing TRPC1-expressing cells.	52
Figure 28 Impact of different intracellular Ca ²⁺ concentrations on current in TRPC1- τ GFP and TRPC1-deficient pituitary cells.	53
Figure 29 Ion permeability in TRPC1- τ GFP and TRPC1-deficient pituitary cells.	54
Figure 30 TRPC channels in osteoclasts.	55

Figure 31 Protein domain and exon structure of CaV β subunits.	56
Figure 32 Impact of different CaV β 2 splice variants on CaV1.2.	57
Figure 33 Ba ²⁺ currents of CaV1.2 coexpressed with CaV β 2N3a or CaV β 2N3b.	59
Figure 34 Currents of CaV1.2 with a long N-terminus.	59
Figure 35 Effect of EA on the current of CaV1.2 with the long N-terminus.	60
Figure 36 Ba ²⁺ and Ca ²⁺ currents via CaV1.2 channels coexpressed with CaV β 3 or CaV β 2N4a.	61
Figure 37 CaV currents in Ins-1 wt and Ins1 CaV β 3 ^{-/-} cells.	62
Figure 38 Pharmacological characterization of the CaV current in Ins-1 cells.	64
Figure 39 CaV currents in wt and CaV β 3 ^{-/-} murine embryonic fibroblasts.	65
Figure 40 CaV currents in wt and CaV β 2 ^{-/-} murine embryonic fibroblasts.	65
Figure 41 CaV currents in pre-osteoclasts and multinucleated osteoclasts.	66
Figure 42 Pedigree of the Spanish family carrying the CaV3.2 G1064R mutation.	67
Figure 43 Comparison of hCaV3.2 and hCaV3.2 G1064R currents.	68
Figure 44 Impact of exon 26 deletion on CaV3.2 wt and CaV3.2 G1064R currents. ...	69
Figure 45 Steady-state activation and inactivation of hCaV3.2 Δ Ex26 and hCaV3.2 G1064R Δ Ex26 currents.	70
Figure 46 Inhibitory effect of EA on the CaV3.2 wt and CaV3.2 G1064R currents.	71
Figure 47 Impact of CaV β 1 splice variants on the CaV3.2 current.	72
Figure 48 CaV β 2 subunit splice variants and their impact on the CaV3.2 current.	73
Figure 49 CaV3.2 coexpression with CaV β 2N4b or CaV β 3.	74
Figure A1 TRPC1ss V611A heterologous protein expression in <i>Xenopus laevis</i> oocytes.	105
Figure A2 TRPC4 β -C1 _{S5-S6 linker} chimera currents in <i>Xenopus laevis</i> oocytes.	107
Figure A3 TRPC4 α -C1 _{S5-S6 linker} chimera in stable expressing TRPC4 α cells.	108
Figure A4 Impact of DAMGO/CCh pre-application on EA-induced currents of TRPC4 α coexpressed with TRPC1 or TRPC4 α -C1 _{S5-S6 linker} chimera	109
Figure A5 Currents through TRPC4- β C1 _{S5-S6 linker} chimera in TRPC4 β expressing M2R cells.	111
Figure A6 TRPC4 α -C1 _{S5-S6 linker} chimera in stable expressing TRPC1 cells.	112
Figure A7 Impact of Gramd1a and Gramd3 on TRPC4	115
Figure A8 Impact of Stac2 on homomeric TRPC4 and heteromeric TRPC4/TRPC1 currents.	116
Figure A9 Impact of hEEA1 on homomeric TRPC4 and heteromeric TRPC4/TRPC1 currents.	118
Figure A10 Impact of Latrophilin 2 on homomeric TRPC4 channels.	119
Figure A11 Impact of Latrophilin 2 on heteromeric TRPC4/TRPC1 channels.	120

Figure A12 Impact of TMEM 201 on heteromeric TRPC4/TRPC1-currents.....121
Figure A13 Impact of Csrp1 and Lasp1 on TRPC4 and TRPC5 currents.....122
Figure A14 Impact of NDPK-B wt and NDPK-B H118N on TRPC4 currents.....124
Figure A15 Impact of NDPK-B wt or NDPK-B H118N on TRPC5 currents.....125

List of Tables

Table 1 Transfection protocol with Lipofectamine 3000.....	17
Table 2 Transfection protocol with Biotool transfection reagent.....	17
Table 3 Oligodeoxynucleotide primers for real-time PCR.....	19
Table 4 Antibodies used for Western Blot	23
Table 5 Buffers for Biotinylation.	24
Table 6 External and internal solutions for TRPC measurements.	30
Table 7 External and internal solution for CaV measurements.....	30
Table 8 List of TRP and CaV agonists and antagonists.	30
Table A1 Immortal Cell lines.....	101
Table A2 List of transfected plasmids.	102
Table A3 List of plasmids used for cRNA synthesis.....	104
Table A3 Summary of the effects of different proteins on TRPC4 and TRPC4/TRPC1 currents.....	113

Summary

In many non-excitabile cells, which do not generate action potentials by themselves, extracellular chemical signals, like hormones and neurotransmitters, are transduced into membrane depolarizations, which in turn activate voltage-gated Ca^{2+} (CaV) channels. Hormones and their GPCRs activate transient receptor potential TRPC channels, which allow Na^+ and Ca^{2+} influx, initiating Ca^{2+} -dependent signalling pathways and, in addition, depolarize the plasma membrane and thereby activate CaV channels. To be able to investigate the interplay of TRPC and CaV channels the present study focused on the electrophysiological characterization of L- and T-type CaVs, their β subunits and TRPC ion channels, especially TRPC1, TRPC4, TRPC5, TRPC4/TRPC1 and TRPC5/TRPC1.

Expression of TRPC1 wild-type or TRPC1 with mutations at the putative lower gate in HEK-cells did not reveal any detectable current. However, TRPC1 coexpressed with TRPC4 reveals functional heteromeric TRPC4/TRPC1 channels with altered biophysical properties as compared to monomeric TRPC4. While most of the TRPC1 mutations had no effect, TRPC1 V741A significantly increased TRPC4/TRPC1 currents. In addition, chimeras of TRPC4 backbone with TRPC1 pore revealed constitutive activity, sensitive to the TRPC blocker SKF 96365. The results suggest that TRPC1 contributes to the pore in TRPC4/TRPC1 heteromers and can form a permeable constitutive active channel pore itself.

A subset of pituitary cells functionally expresses heteromeric TRPC5/TRPC1 channels. Pituitary cells isolated from TRPC1-deficient mice revealed homomeric TRPC5 currents with altered current-voltage relationship, lower amplitudes and higher Ca^{2+} permeability as compared to TRPC5/TRPC1 heteromeric channels in wild-type. Thus, TRPC1 modulates activity and Ca^{2+} permeability of TRPC5 *in vivo* and thereby the Ca^{2+} influx in pituitary cells.

Auxiliary subunits, the CaV β proteins, are required for the function of CaV channels. To study the impact of CaV β subunits on the function of L- and T-type CaV channels, different β subunits were coexpressed with the CaVs in HEK-cells. CaV β 2 splice variants increased the L-type CaV1.2 current, but did not significantly affect T-type CaV3.2 currents, whereas CaV β 3 significantly inhibit CaV3.2 currents. In addition, CaV β 3 serves Ca^{2+} channel independent functions in fibroblasts, where I could not detect CaV currents and where CaV β 3 changes the sensitivity of the inositol trisphosphate (IP_3) receptor for low concentrations of IP_3 .

CaV3.2 currents are also inhibited by Englerin A (EA; EC_{50} 222 nM), which had so far assumed to be a specific agonist of TRPC4, TRPC5, TRPC4/TRPC1 and TRPC5/TRPC1 channels. An electrophysiological characterization of a CaV3.2 mutant,

identified in a Spanish family and linked to hyper-aldosteronism and hypertension is ongoing.

The Appendix contains additional experiments supplying the data described in the Results section.

Zusammenfassung

In vielen nicht erregbaren Zellen, die selbst keine Aktionspotentiale erzeugen, werden extrazelluläre chemische Signale wie beispielsweise Hormone und Neurotransmitter in Membrandepolarisationen umgewandelt, die wiederum spannungsabhängige Calcium Kanäle aktivieren. Die Hormone beziehungsweise die durch sie stimulierten GPCRs können transiente Rezeptorpotential TRPC Kanäle aktivieren, was einen Na^+ - und Ca^{2+} -Einstrom ermöglicht. Der Ca^{2+} -Einstrom initiiert Ca^{2+} -abhängige Signalwege, und der Na^+ -Einstrom führt zur Depolarisation der Plasmamembran wodurch spannungsgesteuerte Ca^{2+} (CaV) Kanäle aktiviert werden. Um das Zusammenspiel von TRPC und CaV Kanälen untersuchen zu können, konzentrierte sich die vorliegende Studie auf die elektrophysiologische Charakterisierung von CaVs vom L- und T-Typ, ihren β -Untereinheiten und von TRPC Ionenkanälen, insbesondere TRPC1, TRPC4, TRPC5, TRPC4/TRPC1 und TRPC5/TRPC1.

Die Expression von TRPC1 Wildtyp oder TRPC1 mit Mutationen am mutmaßlichen unteren Gate ergab in HEK-Zellen keinen nachweisbaren Strom. Mit TRPC4 coexprimiert führt TRPC1 jedoch zu funktionellen heteromeren TRPC4/TRPC1 Kanälen, die veränderte biophysikalische Eigenschaften im Vergleich zu monomerem TRPC4 aufweisen. Während die meisten TRPC1 Mutationen keine Wirkung auf TRPC4/TRPC1 Ströme hatten, erhöhte TRPC1 V741A die TRPC4/TRPC1 Ströme signifikant. Zusätzlich zeigten Chimären des TRPC4-Rückgrats mit TRPC1-Poren eine konstitutive Aktivität, die mit dem TRPC-Blocker SKF 96365 inhibiert werden konnte. Die Ergebnisse legen nahe, dass TRPC1 zur Pore in TRPC4/TRPC1-heteromeren Kanälen beiträgt und selbst eine Ionenpermeable konstitutiv aktive Kanalpore bilden kann.

Ein Teil von Hypophysenzellen exprimiert funktionell heteromere TRPC5/TRPC1 Kanäle. Aus TRPC1-defizienten Mäusen isolierte Hypophysenzellen zeigten homomere TRPC5 Ströme mit veränderter Strom-Spannungs-Beziehung, niedrigeren Amplituden und höherer Ca^{2+} -Permeabilität im Vergleich zu heteromeren TRPC5/TRPC1 Kanälen in Wildtyp Hypophysenzellen. Somit moduliert TRPC1 die Aktivität und Ca^{2+} -Permeabilität von TRPC5 *in vivo* und damit den Ca^{2+} -Einstrom in die Hypophysenzellen.

Die $\text{CaV}\beta$ -Proteine werden für die Funktion von CaV Kanälen benötigt. Um den Einfluss von $\text{CaV}\beta$ -Untereinheiten auf die Funktion von CaV Kanälen vom L- und T-Typ zu untersuchen, wurden verschiedene β -Untereinheiten mit den CaVs in HEK-Zellen coexprimiert. $\text{CaV}\beta 2$ -Spleißvarianten erhöhten den $\text{CaV}1.2$ Strom vom L-Typ, beeinflussten jedoch die $\text{CaV}3.2$ Ströme vom T-Typ nicht signifikant, während $\text{CaV}\beta 3$ die $\text{CaV}3.2$ Ströme signifikant inhibierte. Darüber hinaus erfüllt $\text{CaV}\beta 3$ CaV -unabhängige Funktionen in Fibroblasten, bei denen ich keinen CaV Strom nachweisen

konnte und bei denen CaV β 3 die Empfindlichkeit des Inositoltrisphosphat (IP₃) Rezeptors für niedrige IP₃-Konzentrationen verändert. CaV3.2 Ströme werden auch durch Englerin A (EA, EC₅₀ 222 nM) gehemmt. Für EA wurde bisher angenommen, dass es ein spezifischer Agonist von TRPC4, TRPC5, TRPC4/TRPC1 und TRPC5/TRPC1 Kanälen ist.

Die elektrophysiologische Charakterisierung einer CaV3.2 Mutante, die in einer spanischen Familie identifiziert und mit Hyperaldosteronismus und Hypertonie in Verbindung gebracht wurde, ist noch nicht abgeschlossen.

Der Anhang enthält zusätzliche Experimente zu den im Ergebnis teil beschriebenen Daten.

Introduction

1.1 Calcium signaling

Calcium ions (Ca^{2+}) play a key role in different cellular processes like exocytosis, contraction, regulation of enzymes and gene expression, cell proliferation, apoptosis, and protein function [reviewed by Clapham, 2007; Parekh and Penner, 1997; Westheimer, 1987]. The intracellular and extracellular Ca^{2+} concentrations are in the range of 100 nM and 1 mM, respectively, and thus can differ by a factor of $\geq 10\,000$.

The cytoplasmic Ca^{2+} concentration is controlled by different ion channels and transporters within the plasma membrane and within the membranes of intracellular organelles. In most excitable cells, action potentials activate voltage-gated calcium channels (CaVs). In non-excitable cells, which do not generate action potentials by themselves, extracellular chemical signals are transduced into membrane depolarization, which in turn activates CaV channels. For example, in smooth muscle of the intestine acetylcholine is released from parasympathetic nerve terminals. This acetylcholine is the extracellular chemical signal, which stimulates muscarinic G-protein-coupled receptors (GPCRs) in the plasma membrane of smooth muscle cells. The stimulated GPCRs activate phospholipase C (PLC) dependent intracellular pathways, which in turn activate transient receptor potential (TRP) channels (Figure 1) [Tsvilovskyy

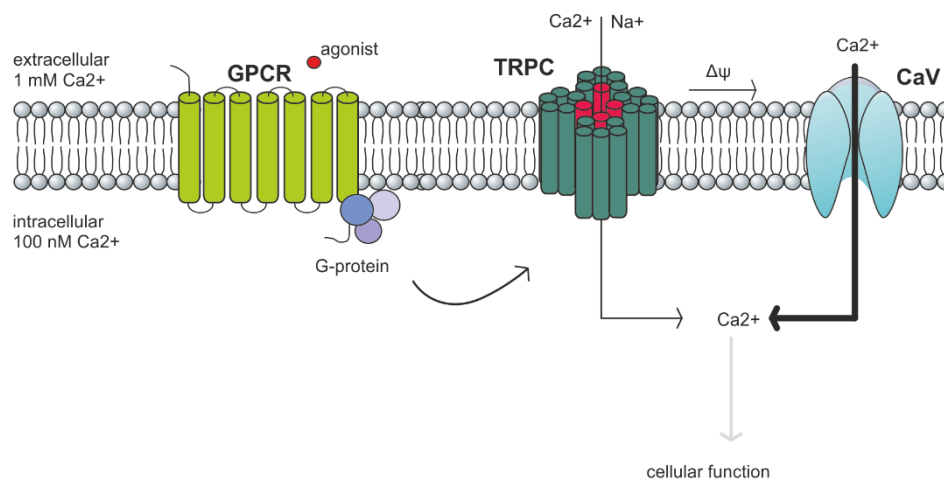


Figure 1 TRPC channels couple extracellular signals to membrane depolarization and activation of voltage-gated channels. Cells are expressing a variety of ion channels and transporters to control the cytosolic Ca^{2+} concentration. G-protein-coupled receptors (GPCRs) are activated by extracellular compounds or agonists leading to an activation of G-proteins followed by the opening of transient receptor potential canonical (TRPC) channels. The Ca^{2+} and Na^{+} influx into the cell via TRPC channels by itself initiates intracellular Ca^{2+} -dependent pathways but also depolarizes the plasma membrane leading to the activation of voltage-gated calcium channels (CaV) resulting in additional Ca^{2+} influx. The extracellular Ca^{2+} concentration is much higher (~ 1 mM) as compared to the intracellular Ca^{2+} concentration (~ 100 nM). This concentration gradient drives Ca^{2+} influx [Tsvilovskyy *et al.*, 2009].

et al., 2009]. The activated TRP channels allow Na⁺ and Ca²⁺ influx, which initiates Ca²⁺-dependent signaling pathways but also depolarizes the plasma membrane and thereby activates CaV channels, which allow the bulk of Ca²⁺ to enter the cell and the smooth muscle cell contracts. In the following, three major TRP channels, TRPC1, TRPC4 and TRPC5, are briefly described after a short introduction to TRP channels.

1.2 Transient Receptor Potential (TRP) channels

The transient receptor potential (TRP) channel family is a cation channel family, which plays a role in Ca²⁺ homeostasis especially in coupling extracellular chemical signals to membrane depolarization. Initially, the first TRP channel was identified in *Drosophila melanogaster*. After stimulation with bright light mutant fly photoreceptors showed only a transient photoreceptor potential, whereas photoreceptors from wild-type flies responded to the stimulation with bright light with a sustained receptor potential [Cosens and Manning, 1969]. According to this phenotype the mutant was called *transient receptor potential* or *TRP*. It took another 20 years to identify the mutant gene, the *trp* gene, by Montell and Rubin. The authors predicted that the TRP protein comprise eight transmembrane segments and intracellular N- and C-termini and suggested that this protein forms an ion channel [Montell and Rubin, 1989]. By hybridizing mammalian cDNA libraries with low stringency with the *Drosophila* TRP cDNA, 28 homologous cDNAs were identified in cDNA libraries from mammalian tissues. Today, the TRP channel family includes 30 members in seven subfamilies: TRPC (classic or canonical), TRPM

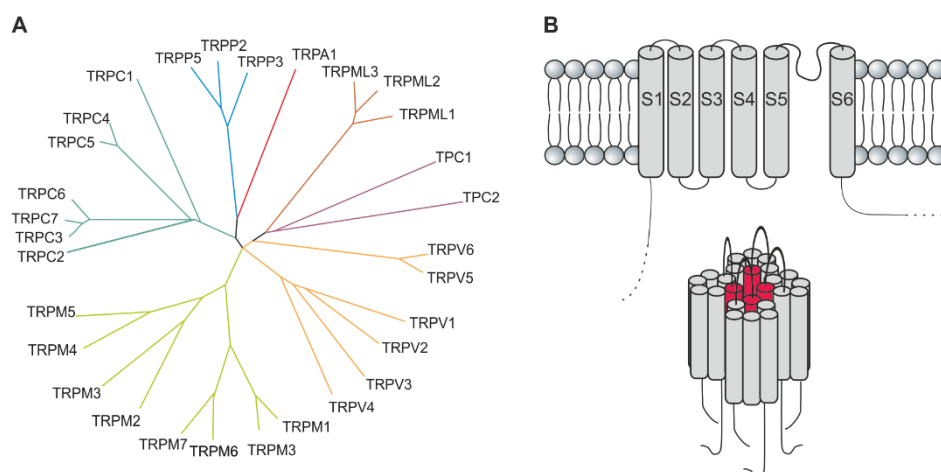


Figure 2 Phylogenetic tree and topology of the TRP channel family. **A** The TRP channel family has 30 members classified into seven subfamilies: TRPC, TRPM, TRPV, TRPML, TRPA, TPC and TRPP. **B** Shared topology of TRP channel family members. All TRP channels have six transmembrane segments (S1-S6) with cytosolic N- and C-termini (upper panel). A functional TRP channel has four of these domains and the linker between S5 and S6 of each domain forms the channel pore (lower panel). One TPC channel protein contains two six transmembrane units and the functional TPC channels comprise two subunits.

(melastatin), TRPV (vanilloid), TRPA (ankyrin), TRPP (polycystin), TRPML (mucolipin) and TPC (two pore segment channel) (Figure 2 A). In 2013, Cao and colleagues [Cao *et al.*, 2013] showed the first cryo electron microscopy (cryo-EM) structures of a TRP channel (TRPV1) and until today the cryo-EM structure of almost all TRP channels have been described except the structures of the founding TRP and TRP-like from *Drosophila*: From the TRP channel proteins structures are available for TRPC3 [Tang *et al.*, 2018], TRPC4, TRPC5 [Duan *et al.*, 2018; Duan *et al.*, 2019] and TRPC6 [Azumaya *et al.*, 2018], all TRPVs [Cao *et al.*, 2013; Hughes *et al.*, 2018; Shigematsu *et al.*, 2010; Singh *et al.*, 2018; Singh *et al.*, 2018; Zubcevic *et al.*, 2016], TRPM2 [Wang *et al.*, 2018], TRPM4 [Autzen *et al.*, 2018], TRPM7 [Duan *et al.*, 2018] and TRPM8 [Yin *et al.*, 2018], TRPA1 [Paulsen *et al.*, 2015], TRPP2 [Shen *et al.*, 2016] and TRPP3 [Su *et al.*, 2018], TRPML1 [Zhang *et al.*, 2017] and TRPML3 [Hirschi *et al.*, 2017]. All the structures confirm the proposed TRP channel structure of homotetrameric channel complexes, where each domain contains six transmembrane segments (S1–S6) with N- and C-termini located on the cytosolic side and a pore forming loop between S5 and S6 (Figure 2 B) [Hofmann *et al.*, 2017]. These proteins show an amino acid (aa) sequence homology of around 30 % to 47 % between subfamilies and within one subfamily even of up to 90 %. Moreover, the proteins exhibit repetitive motifs of up to 33 aa at their N-terminus, the so called ankyrin repeats. TRPCs have 3 to 4, TRPVs have 6 and TRPA1 has 14 to 15 ankyrin repeats. All TRP proteins have a highly conserved 25 amino acid long motif at the C-terminus, the TRP domain. In addition, TRPM2, TRPM6 and TRPM7 contain enzymatic domains at their C-terminus [Montell *et al.*, 2002; Nilius and Owsianik, 2011]. They are therefore called chanzymes, which emphasizes their ion conducting channel and enzymatic domain.

TRP channels are expressed in the nervous system as well as in non-excitabile cells and are linked to several human diseases. Mutations of TRPC6 are linked to focal and segmental glomerulosclerosis (FSGS), where the patients suffer from progressive kidney dysfunction. TRPV4 mutations are found in patients with disorders of bone and skeletal muscle growth like scapuloperoneal spinal muscular atrophy (SPSMA). Patients with this disorder suffer from abnormal bone growth and muscle weakness. The autosomal-recessive congenital stationary night blindness (CSNB) is linked to TRPM1 mutations. Mutations in TRPM4 or TRPM6 are linked to autosomal-dominant progressive familial heart block type 1 (PFHB1) and to hypomagnesemia with secondary hypocalcemia (HSH/HOMG), respectively. TRPA1 is involved in autosomal-dominant familial episodic pain syndrome (FEPS) and some TRPML1 mutations result in muscolipidosis type IV. Moreover, mutations in the TRPP2 are causing the polycystic kidney disease (PKD) [Montell *et al.*, 2002; Nilius and Owsianik, 2011; Flockerzi and Wardas, in print].

1.2.1 The canonical TRP subfamily

The canonical or classical TRP subfamily (TRPC) are nonselective cation channels with seven family members (TRPC1-TRPC7). They have unique structure features among the TRP channel family. The N-terminus of TRPC channels contains four ankyrin repeat domains and seven (TRPC4 and TRPC5) to nine (TRPC3 and TRPC6) linker helix followed by a Pre-S1 helix and the homologous six transmembrane helices (Figure 3). The so called TRP box is a conserved domain forming a hub for intramolecular contacts of the four subunits of the tetrameric channels. At the C-terminus of the TRPC channels, a calmodulin- and IP₃R-binding site (CIRB) is conserved. *In vitro*, the affinities of the binding sites for calmodulin differ between the TRPC channels from 10 nM to 290 nM [Trost *et al.*, 1999; Trost *et al.*, 2001; Zhu, 2005]. TRPC1 has a unique structural feature among the TRPC family. A new start codon was found, which extends the N-terminus by 91 amino acids (Figure 3), so that the protein starts with a more upstream located CUG (encodes a leucine) instead with an AUG (encodes a methionine) codon [Ong *et al.*, 2013 and own results].

The seven members of the TRPC subfamily can be divided into two subgroups due to their sequence homology and activation: TRPC1/4/5 and TRPC2/3/6/7. The TRPC channels are indirectly activated by GPCRs. The stimulation of muscarinic m2 receptors (M2R) by carbachol activates the G_{i/o}-protein. Carbachol is an external chemical signal not only for M2R but also of muscarinic m3 receptors (M3R) leading to the activation of the G_{q/11}-protein, which in turn stimulates the PLC. The PLC hydrolyzes PIP₂ to inositoltrisphosphat (IP₃) and diacylglycerol (DAG). There is consensus that both receptor types have to be stimulated to activate TRPCs (Figure 4). After stimulation of the G_{i/o}-coupled receptor, α_i might directly bind to the TRPC channel or its βγ-subunits. At the same time the hydrolysis of PIP₂ after stimulation of G_{q/11}-coupled receptor takes away the inhibition of TRPC by PIP₂ [Otsuguro *et al.*, 2008]. In addition, DAG obtained from the breakdown of PIP₂ is required for activation of TRPC2, TRPC3, TRPC6 and TRPC7 [Hofmann *et al.*, 1999] and under certain conditions for activation of TRPC4 and TRPC5 [Storch *et al.*, 2016]. Finally, IP₃, also generated by breakdown of PIP₂ releases

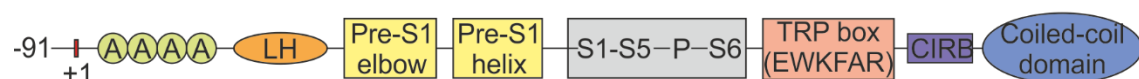


Figure 3 Protein domains of a TRPC channel protein. The N-terminus of TRPC channels has four ankyrin repeats (A) followed by seven to nine a linker helix (LH), a Pre-S1 elbow and a Pre-S1 helix. TRPCs, like all TRP channels, reveal six transmembrane segments (S1 to S6) with a pore forming loop (P) between S5 and S6. The sequence EWKFAR, the so called TRP box, is located after S6 followed by a calmodulin- and IP₃R-binding side (CIRB) and a coiled-coil domain at the C-terminus. TRPC1 starts instead of the usually AUG codon (indicated with +1, red bar) at a CUG codon (-91) (modified from Dietrich *et al.*, 2014).

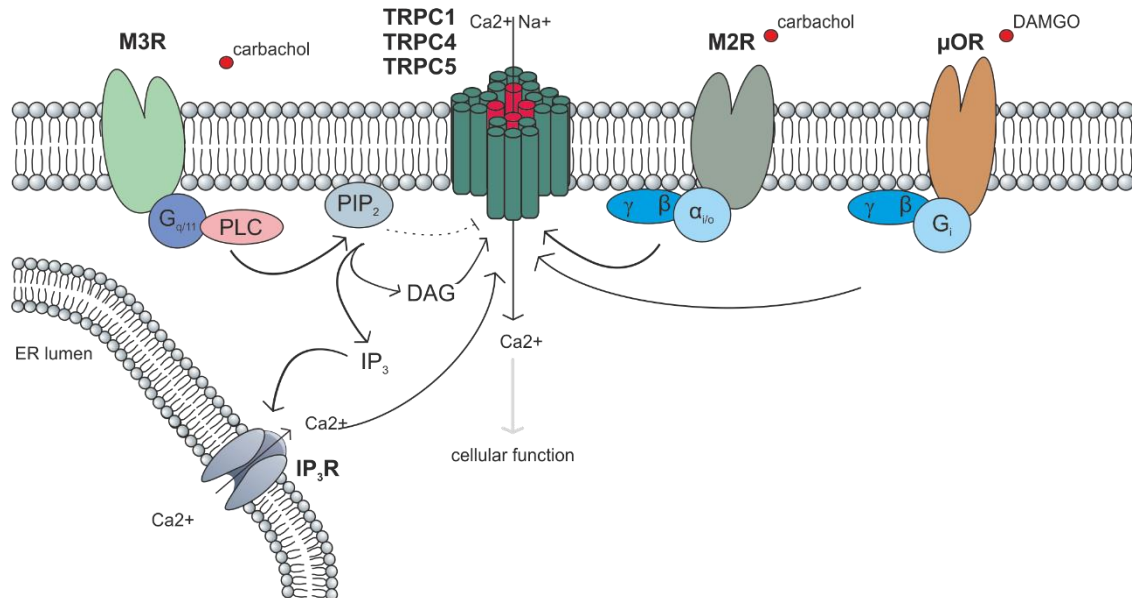


Figure 4 TRPC channel activation. TRPC channels are activated by muscarinic m2 receptor (M2R) and muscarinic m3 receptor (M3R) in smooth muscle or by μ -opioid receptor (μ OR). Carbachol is an external chemical signal for M2R and M3R, while μ OR is activated by DAMGO. The activation of M3R leads to an activation of the G_{q/11}-protein, which activates the PLC leading to the hydrolysis of PIP₂ into IP₃ and DAG. DAG can activate TRPC channels, while IP₃ activates the inositol trisphosphate receptor (IP₃R) in the ER membrane resulting in a Ca²⁺ release from the ER. This Ca²⁺ co-activates the TRPC channels. Stimulation of M2R or μ OR activates the G_{i/o}-protein, which activates TRPC1, TRPC4 and TRPC5 channels.

Ca²⁺ from the endoplasmic reticulum. Part of this Ca²⁺ is also required as co-activator of TRPC channels [Tsvilovskyy *et al.*, 2009].

HEK293-cells, used in my study, do endogenously express M3 receptors, which are coupled to G_{q/11}-protein. To be able to stimulate G_{i/o}-coupled GPCRs I used HEK-cells stably expressing the M2 receptor (also activated by carbachol) or the μ -opioid receptor (μ OR), which can be activated by DAMGO ([D-Ala², N-MePhe⁴, Gly-ol]-enkephalin; Figure 4). Both cell lines were kindly provided by Professor Michael X. Zhu (Houston, USA).

TRPC1 is found at high expression levels in mouse fetal brain and at low expression levels in mouse fetal liver and kidney, while in adult mice TRPC1 expression levels are high in heart, testis, ovary, in brain gland [Feng, 2017; Riccio *et al.*, 2002] and in the pituitary [own results]. TRPC2 is a pseudogene in human [Wes *et al.*, 1995]; however, this channel is required for pheromone detection in rodents, where it is expressed in the vomeronasal sensory neurons (VSN) [Li, 2017; Zufall, 2005]. The TRPC3 channel, which can be stimulated by DAG, is expressed in heart, lung and brain [Lemonnier *et al.*, 2009; Riccio *et al.*, 2002; Li, 2017] and astrocytes [Belkacemi *et al.*, 2017]. TRPC4 is expressed in the brain [Philipp *et al.*, 1996] as well as in bone, kidney, adrenal glands, intestinal

pacemaker cells, endothelium [Freichel *et al.*, 2001] and smooth muscle cells [Tsvilovskyy *et al.*, 2009]. TRPC5 is expressed in the brain [Philipp *et al.*, 1998] and in the pituitary gland [Beck *et al.*, 2017 and own results]. TRPC6 mRNA was found in special brain regions like the substantia nigra, cortex, cerebellum and hippocampus, cardiac neurons, olfactory epithelium neurons, placenta, erythrocytes and thrombocytes. TRPC7 is mainly expressed in the pituitary gland, in kidney and at a lower level in some parts of the brain [Li, 2017; Riccio *et al.*, 2002].

1.2.1.1 TRPC1

The TRPC1 cDNA was the first mammalian TRP protein cloned in 1995 [Wes *et al.*, 1995; Zhu *et al.*, 1995; Zitt *et al.*, 1996]. Nevertheless, there are only a few publications to this day showing that TRPC1 is a functional ion channel at all. The group of Schultz [Zitt *et al.*, 1996] concluded from their TRPC1 expression studies, that TRPC1 contributes to the store-operated Ca^{2+} entry in three different expression systems. Moreover, they show that TRPC1 can be activated by intracellular infusion of either IP_3 or thapsigargin both causing Ca^{2+} release from the endoplasmic reticulum. Noise analysis revealed a single channel conductance of 16 pS for TRPC1 [Zitt *et al.*, 1996]. In other studies, no TRPC1 current could be detected, neither after cDNA expression, nor in cultured or acutely isolated cells endogenously expressing the TRPC1 mRNA. The so far detected currents reveal a linear current-voltage relationship and a very small amplitude even after overexpression of the cDNA [Ong *et al.*, 2013]. In many cases the TRPC1 protein does not seem to be translocated to the plasma membrane, it localizes in membrane compartments of the ER or cytosolic vesicles [Alfonso *et al.*, 2008; Hofmann *et al.*, 2002].

Although the function of TRPC1 is still not solved, the protein has to have an important physiological role, since it is widely but not ubiquitously expressed [Riccio *et al.*, 2002 and own results]. In 2007, Dietrich and colleagues introduced TRPC1-deficient mice, which were viable and fertile. However, these mice have an increased body length and body weight (own results) compared to their wild-type littermates. TRPC1 is expressed in bone and the lack of TRPC1 in TRPC1-deficient mice could cause slightly larger tibiae and skulls in the TRPC1-deficient mice compared to their wild-type littermates [Dietrich *et al.*, 2007; Dietrich *et al.*, 2014]. Ong *et al.* described in 2013 that single TRPC1-deficient mice showed some slight but not significant increase in body mass and decrease in osteoclast numbers [Ong *et al.*, 2013]. Since TRPC1 is not only expressed in bone, [Riccio *et al.*, 2002 and own results, Figure 30 A], the absence of TRPC1 may have pathologic effects in other tissues as well. In TRPC1-deficient mice the fluid

secretion from the salivary gland is reduced. In addition, these mice have less myofibrillar protein, an increased muscle fatigue, smaller fiber-cross sectional areas, slower muscle regeneration after muscle injury and express less myogenic transcription factors [Liu *et al.*, 2007; Zanou *et al.*, 2010; Zanou *et al.*, 2012]. So far, it is not clear, whether TRPC1 is present in platelets. Platelet aggregation and thrombus formation is not affected in TRPC1-deficient mice [Varga-Szabo *et al.*, 2008]. TRPC1 may also be involved in neuronal functions, especially in neurons of dorsal root ganglia. The down-regulation of TRPC1 in these neurons results in a reduced mechanosensitivity [StAAF *et al.*, 2009]. Furthermore, it is shown, that patients suffering from Parkinson disease have reduced TRPC1 expression levels in dopaminergic neurons of the substantia nigra and more unfolded proteins are found in brain lysates [Selvaraj *et al.*, 2012].

While it is still discussed if TRPC1 forms functional homotetrameric channels, it definitely forms heterotetrameric channels *in vitro* with other TRP proteins especially TRPC4 and TRPC5 [Hofmann *et al.*, 2002; Kepura *et al.*, 2020; Lepannetier *et al.*, 2018], but eventually with TRPC3 [Lintschinger *et al.*, 2000], TRPC6, TRPC7 [Storch *et al.*, 2012], TRPP2 [Tsiokas *et al.*, 1999], TRPV6 [Courjaret *et al.*, 2013; Schindl *et al.*, 2012] and TRPV4 [Ma *et al.*, 2011]. The presence of TRPC1 in these heterotetrameric channels changes the channel properties significantly. In combination with TRPC1 the current-voltage relationship of TRPC4 and TRPC5 is changed as well as their Ca²⁺ permeability, which is significantly reduced in the heterotetrameric channels [Kepura *et al.*, 2020; Lepannetier *et al.*, 2018; Storch *et al.*, 2012 and own results]. Homomeric TRPC4 and TRPC5 channels generate in- and outward rectifying currents with a conductance of about 38 pS. The corresponding heteromeric TRPC4/TRPC1 or TRPC5/TRPC1 channels are only outwardly rectifying with a reduced conductance. The change of the current-voltage relationship is most probably due to a loss of the Mg²⁺ block, which is observed in homomeric TRPC4 as well as TRPC5 channels. However, like the homomeric TRPC4 and TRPC5 channels, TRPC4/TRPC1 and TRPC5/TRPC1 channels are activated by G-protein-coupled receptors and are sensitive to the same agonists and antagonists [Strübing *et al.*, 2001 and own results].

In vitro, the TRPV6 current is inhibited by the presence of TRPC1 and the amount of TRPV6 is reduced in the plasma membrane of TRPC1 coexpressing cells [Courjaret *et al.*, 2013; Schindl *et al.*, 2012]. Therefore, TRPC1 may operate as a negative regulator of Ca²⁺ signaling mediated by TRPV6. However, it has not been shown, whether *in vivo*, the TRPC1 and the TRPV6 proteins are present in the same cell. Furthermore, the single channel conductance of TRPP2/TRPC1 heterotetrameric channels was reduced as compared to the single channel conductance of TRPP2 alone [Zhang *et al.*, 2009].

TRPC1 has a binding site for the Homer protein at the N- and at the C-terminus. This protein Homer promotes the physical interaction of TRPC1 with the IP₃ receptor via the CIRB, which leads to a regulation of the TRPC1 function [Stiber *et al.*, 2008; Yuan *et al.*, 2003].

1.2.1.2 TRPC4 and TRPC5

The cDNA of TRPC4 was cloned in 1996 [Philipp *et al.*, 1996] and two splice variants exist, TRPC4 α and TRPC4 β . The TRPC4 α splice variant has an 84 amino acid insertion within the C-terminus [Plant and Schaefer, 2003]. Independent of the splice variant, currents through TRPC4 channels have a double rectifying current-voltage relationship. The cytosolic aspartic acid residue D633 is responsible for the inward rectification of the inward TRPC5 current [Schaefer *et al.*, 2000; Obukhov and Nowycky, 2005]. Furthermore, TRPC4 can form heteromeric channels with TRPC1 and TRPC5 with changed channel properties [Hofmann *et al.*, 2002; Strübing *et al.*, 2001]. The activation of TRPC4 depends on the pathways shown in Figure 4. The main products of the enzymatic hydrolysis of PIP₂, IP₃ and DAG, are not activating the channel [Clapham, 2001], but activated PLC rather relieves the tonic inhibition by PIP₂ [Otsuguro *et al.*, 2008; Tsvilovskyy *et al.*, 2009]. Infusion of the non-hydrolyzable guanosine 5'-O-[gamma-thio] triphosphate (GTP γ S) a G-protein-activating analog of guanosine triphosphate (GTP) in the cells activates TRPC4 [Plant and Schaefer, 2003 and own results]. Moreover, TRPC4 requires stimulation by a G_{i/o}-coupled GPCR, for example the μ OR by DAMGO or M2R by carbachol (CCh) [Griffin *et al.*, 2016; Thakur *et al.*, 2016; Tsvilovskyy *et al.*, 2009]. In 2015, a direct TRPC4 and TRPC5 agonist was extracted from the tree *Phyllanthus engleri* named Englerin A (EA) [Akbulut *et al.*, 2015]. EA is a potent agonist [see results 3.1.1] and amino acid residues K554, H594 and E598 of the TRPC5 pore may be part of the TRPC5 binding pocket for EA [Jeong *et al.*, 2019]. In 2018, the cryo-EM structure of TRPC4 was solved and revealed a unique feature of the TRPC4 pore, which is stabilized by a disulfide bond (C553, C558) [Duan *et al.*, 2018]. In 2019, the cryo-EM structure of TRPC5 was solved indicating some unique features of TRPC5, too. The transmembrane segment S3 is shorter compared to the S3 of TRPC3 and TRPC6 and TRPC5 has a small loop (aa 544 to 552) in the linker of S5 and the pore helix right before the disulfide bond (C553, C558) [Duan *et al.*, 2019]. A special property of TRPC5 channels is their sensitivity to intracellular Ca²⁺, which potentiates agonist-activated TRPC5 currents [Blair *et al.*, 2009; Gross *et al.*, 2009].

As shown in Figure 1, TRPC-activation initiates intracellular Ca²⁺ signaling pathways but also couples extracellular signals acting on GPCRs to membrane depolarization. This

membrane depolarization can activate voltage-dependent Ca^{2+} entry, which by itself reinforces intracellular Ca^{2+} signaling but also induces additional intracellular Ca^{2+} -dependent pathways. In the following paragraph I summarize properties of these voltage-gated calcium channels, especially of $\text{CaV}1.2$ and its auxiliary subunits $\text{CaV}\beta 2$ and $\text{CaV}\beta 3$ and of $\text{CaV}3.2$.

1.3 Voltage-gated calcium channels (CaVs)

The voltage-gated calcium channels are major plasma membrane Ca^{2+} -entry pathways. They are present in muscle cells, neurons, but also in endocrine cells [Catterall, 2011]. The voltage-gated calcium (CaVs) channel family comprises 10 members (Figure 5 A) [Hofmann *et al.*, 2014]. The ion conducting pores of these channels have a pseudotetrameric structure with four domains (I-IV) present in one molecule. Each domain contains six transmembrane segments (S1-S6). The transmembrane segments S4 in each domain functions as a voltage sensor, while the sequence between S5 and S6 of each domain forms the pore-loop of the channel (Figure 5 B, C). Recent cryo-EM structures of two members of the CaV family $\text{CaV}1.1$ and $\text{CaV}3.1$ confirm this overall

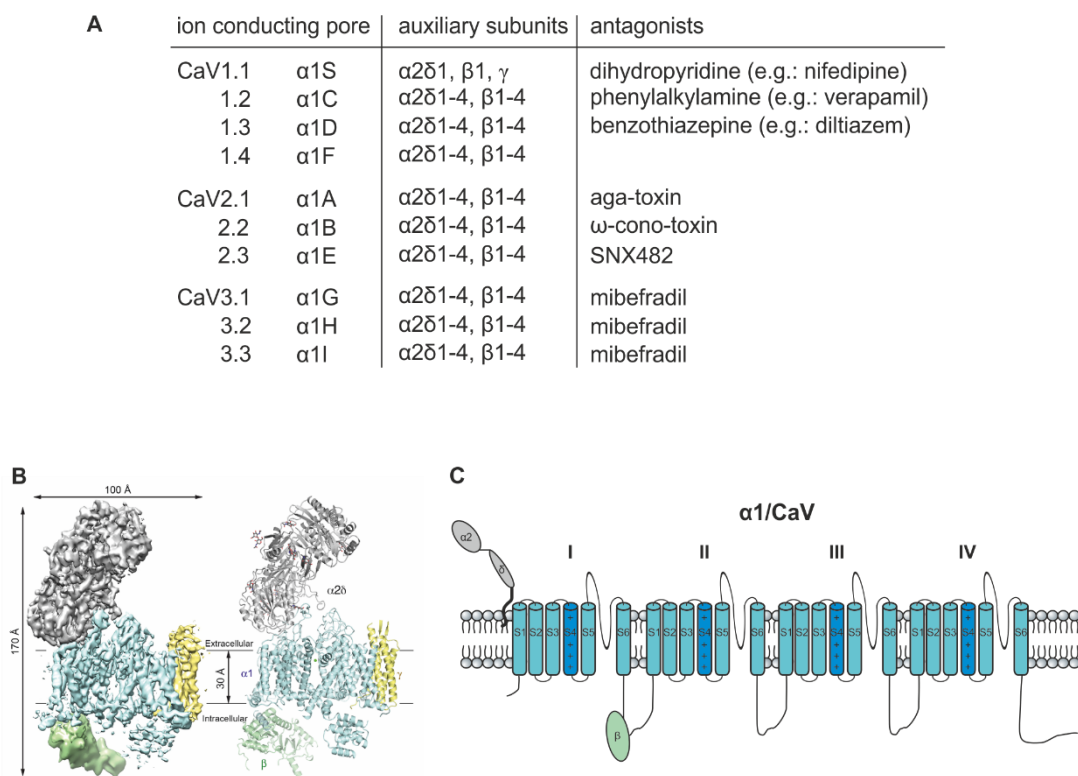


Figure 5 Voltage-gated calcium channels. **A** Summary of conducting $\alpha 1$ subunits of CaV channels with their auxiliary subunits and antagonists. **B** Cryo electron microscopy density map (left) and structure (right) of $\text{CaV}1.1$ with the $\alpha 1$ subunits in blue, the $\text{CaV}\beta 1$ subunit in green, the $\alpha 2\delta 1$ subunits in gray and the γ subunit in yellow [with permission, from Wu *et al.*, 2015]. **C** Scheme of the $\alpha 1$ subunits (blue) with the auxiliary $\text{CaV}\beta$ subunit (green) and $\alpha 2\delta$ subunit (gray). Transmembrane segment S4 functions as a voltage sensor (dark blue).

architecture (Figure 5) [Wu *et al.*, 2015; Zhao *et al.*, 2019]. According to their voltage-dependence the CaVs are subdivided into two groups: the low voltage activated (LVA) CaV channels are the T-Type channels CaV3.1 (*CACNA1G*), CaV3.2 (*CACNA1H*) and CaV3.3 (*CACNA1I*). The high voltage activated (HVA) CaV channels are the L-type channels CaV1.1 (*CACNA1S*), CaV1.2 (*CACNA1C*), CaV1.3 (*CACNA1D*), CaV1.4 (*CACNA1F*), the P/Q-type CaV2.1 (*CACNA1A*), the N-type CaV2.2 (*CACNA1B*) and the R-type CaV2.3 (*CACNA1E*) (Figure 5 A) [Catterall, 2000; Hofmann *et al.*, 2014].

The auxiliary subunits associated with the ion conducting pores or $\alpha 1$ subunits of the LVA channels determine translocation of $\alpha 1$ to the plasma membrane and regulate current kinetics. These auxiliary proteins are the CaV β , CaV $\alpha 2\delta$ and CaV γ subunits [Cain *et al.*, 2011; Catterall, 2000; Flockerzi *et al.*, 1986; Hofmann *et al.*, 2014; Takahashi *et al.*, 1987]. The CaV β s exist in four isoforms (CaV $\beta 1$, CaV $\beta 2$, CaV $\beta 3$, CaV $\beta 4$) and interact with the intracellular loop between domain I and II of the CaV $\alpha 1$ subunit (Figure 5 C). All CaV β proteins share the same domain structure (Figure 6) with a Src homology 3 module (SH3) and a guanylate kinase module linked by a HOOK domain [Chen *et al.*, 2004; Link *et al.*, 2009; Pragnell *et al.*, 1994; Van Petegem *et al.*, 2004]. The highly conserved SH3 region plays a role in the interaction of the CaV β proteins with other proteins, while the HOOK region differs in amino acid sequence and the length among the CaV β proteins and may be involved in the inactivation of the CaV channels and PIP₂ sensing [Park *et al.*, 2017; Richards *et al.*, 2007]. The amino acid sequences of the N-termini and the C-termini differ between CaV $\beta 1$, CaV $\beta 2$, CaV $\beta 3$ and CaV $\beta 4$, and in addition within one CaV β subunit there is alternative splicing of the N-terminus (Figure 6). CaV $\beta 1$ and CaV $\beta 2$ subunits are expressed mainly in heart, skeletal muscle and also in brain, while CaV $\beta 4$ is mainly expressed in different parts of the brain like cortex, hippocampus, olfactory bulb or the cerebellum [Ludwig *et al.*, 1997]. CaV $\beta 3$ is expressed in many

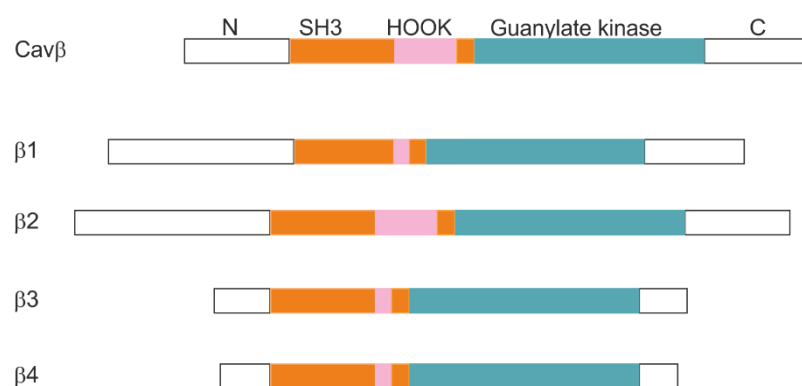


Figure 6 Domain structure of the different CaV β subunits. The CaV β subunits consist of the highly conserved Src homology 3 module (SH3, orange) and a guanylate kinase module (blue), which are linked by a HOOK domain (pink) and differ between the CaV β subunits. The N- and C-termini of the CaV β subunits differ in their amino acid sequence.

tissues and cells including brain, endocrine pancreas and vascular smooth muscle. In addition, CaV β 3 appears to be expressed independently of the ion conducting α 1 subunit serving calcium channel independent functions [Belkacemi *et al.*, 2018].

1.3.1 L-type CaV channels

Four genes encode high voltage activated (HVA) L-type calcium channel α 1 subunits: *CACNA1S* (CaV1.1), *CACNA1C* (CaV1.2), *CACNA1D* (CaV1.3) and *CACNA1F* (CaV1.4). They are expressed in many cell types and tissues like neuronal and endocrine cells, smooth, skeletal and cardiac muscle. In the 1960's the L-type CaVs were described for the first time due to their electrophysiological properties [Reuter, 1967]. Compared to the T-type CaVs, the L-type CaVs are activated at more positive membrane potentials (-30 mV) and inactivate in a Ca²⁺-dependent manner [Hofmann *et al.*, 1994]. The L-type CaV channels are associated with the subunits CaV β , CaV α 2 δ and, in skeletal muscle, CaV γ . These auxiliary proteins determine plasma membrane trafficking of the ion conducting α 1 subunit as well as channel gating and current kinetics. Since the presence of CaV β subunits enhance the amount of L-type CaV channels in the plasma membrane, they also enhance the peak amplitude of the voltage-gated Ca²⁺ currents [Singer *et al.*, 1991].

Because of the essential role of L-type CaV channels as well as of the CaV β subunits for the mammalian physiology, mutations within the genes of some of these proteins cause several diseases. The L-type CaV1.1 is expressed in skeletal muscle and mutations of this gene cause the autosomal dominant hypokalemic periodic paralysis (HypoPP) or malignant hyperthermia susceptibility (MHS) disease. In patients suffering from the HypoPP with muscle weakness, several mutations of the *CACNA1S* gene (CaV1.1) located in the voltage-sensor of the protein had been identified [Cain *et al.*, 2011; Cannon, 2010; Monnier *et al.*, 1997]. Mutations of the *CACNA1C* gene (CaV1.2) cause Timothy Syndrome (TS) and Brugada Syndrome [Antzelevitch *et al.*, 2007; Cain *et al.*, 2011] including cardiac arrhythmias with prolonged QT syndrome, fusion of fingers, facial abnormalities and physical malformations in heart. Mutations of the *CACNA1D* gene (CaV1.3) are causing a bradycardia and congenital deafness [Baig *et al.*, 2011; Cain *et al.*, 2011], whereas mutations of the *CACNA1F* gene (CaV1.4) cause cone-rod dystrophy (CORDX). Furthermore, mutations of the *CACNA1F* gene are found in patients suffering from incomplete X-linked congenital stationary night blindness (IXLCSNB) causing different degrees of night blindness [Cain *et al.*, 2011; Hope *et al.*, 2005; Jalkanen *et al.*, 2006].

Deletion of CaV1.1 [Chaudhari, 1992] and CaV1.2 [Seisenberger *et al.*, 2000] genes in mice are lethal during embryonic development. Because CaV1.1 and CaV1.2 are associated with CaV β 1 (CaV1.1) and CaV β 2 (CaV1.2); deletion of the genes of both CaV β subunits are lethal as well. In the CaV β 2-deficient mice [Weissgerber *et al.*, 2006], L-type Ca²⁺ currents are essentially reduced in cardiac myocytes and the animals die before embryonic day 11 because of heart failure. The CaV β 1-deficient mice die perinatally because of respiratory insufficiency: The skeletal muscle required for breathing do not contract [Gregg *et al.*, 1996].

Mice lacking CaV β 2 in all tissues besides the heart, are viable but deaf and have visual defects, which are similar symptoms of stationary night blindness patients [Katiyar *et al.*, 2015]. Furthermore, mutations in the N-terminus as well as in the C-terminus of CaV β 2 have been linked to Brugada syndrome in human patients [Antzelevitch *et al.*, 2007; Cordeiro *et al.*, 2009].

In contrast, CaV β 3 and CaV β 4 gene deficient mice are viable. The CaV β 3-deficient mice reveal lower blood glucose levels after being challenged by glucose [Berggren *et al.*, 2004], an enhanced insulin secretion from pancreatic β -cells and, under a high-salt diet, the mice suffer from high blood pressure and hypertrophy of heart and aortic smooth muscle [Berggren *et al.*, 2004; Murakami *et al.*, 2003]. Moreover, the CaV β 3-deficient mice are more aggressive and have an increased nighttime activity compared to wild-type mice [Murakami *et al.*, 2007].

A naturally occurring mutation with an insertion of four nucleotides in the CaV β 4 gene causing a frame shift resulting in a shorter nonfunctional protein was identified as the underlying mutation of *lethargic* mice. These mice are suffering from paroxysmal dyskinesia, absence epilepsy, seizures as well as from ataxia [Burgess *et al.*, 1997]. In wild-type mice, at postnatal day 15 (P15), the expression of CaV β 4 increases in the brain, therefore, the phenotype of CaV β 4-deficient mice appears at P15 [McEnery *et al.*, 1998]. Mutations of CaV β 4 are not only described in mice, but also in human patients suffering from ataxia and epilepsy patients have mutations in this gene [Escayg *et al.*, 2000; Ohmori *et al.*, 2008].

1.3.1.1 CaV1.2 channel

The L-type CaV1.2 is widely expressed in the heart, in endocrine pancreas, in smooth muscle, neurons and the adrenal gland. Ca²⁺ influx through this channel regulates hormone secretion, muscle contraction, transmitter release and gene transcription [Berger and Bartsch, 2014; Catterall, 2000; Hofmann *et al.*, 2014]. There are several isoforms of CaV1.2, which differ in their N- and C-termini, in the transmembrane segment

S5 and S6 of domain I, S2 of domain II, S2-S3 and S3-S4 of domain IV and in the linkers of domain I and domain II, as well as of domain II and domain III. CaV1.2 is associated with different auxiliary proteins, in the cardiac tissue for example with the CaV β 2 subunit [Link *et al.*, 2009]. The LVA channels including CaV1 and CaV2 channels exist in different states characterized as I) null mode (channels do not open), II) mode 1 (low probability and brief opening), III) mode 2 (higher probability and longer opening) and IV) closed state [Hess *et al.*, 1984]. Transitions between these states depend on the membrane potential. The CaV1.2 channel has two inactivation phases: a fast voltage-dependent inactivation (10 ms) and a slow Ca²⁺-dependent inactivation (90 ms). The Ca²⁺-dependent inactivation is regulated by the binding of calmodulin to the IQ domain at the C-terminus of CaV1.2 [Van Petegem *et al.*, 2005].

1.3.2 T-type channels

The low voltage activated CaV channels are expressed in many tissues including brain or skeletal muscle. Carbone and Lux described in 1984 and Fedulova *et al.* in 1985 for the first time very fast or “tiny” Ca²⁺ currents, which were activated at low voltages in a voltage-dependent manner. Because of the transient kinetics and the tiny current, the channels were named T-type channels. The T-type or LVA channels have major electrophysiological properties, which distinguish them from the HVA channels including voltage-dependent activation of the channel at low voltages (at -75 mV to -60 mV) (I), the Ca²⁺-independent inactivation of the channels within milliseconds (II) and the deactivation of the T-type channels is very slow near the resting potential of the plasma membrane (III) [Carbone *et al.*, 2014; Talavera and Nilius, 2006; Carbone and Lux, 1984, 1987].

Three variants of T-type channels do exist, CaV3.1, CaV3.2 and CaV3.3. In contrast to HVA channels the three LVA or T-type channels comprise only the ion conducting pores α 1G (CaV3.1), α 1H (CaV3.2) and α 1I (CaV3.3), but no auxiliary subunits. Coexpression of T-type CaV channels and potential auxiliary proteins did not change channel properties [Perez-Reyes, 2006]. There are some splice variants known for all three T-type CaV genes, which contain between 35 to 38 exons. *CACNA1G* (encoding CaV3.1) and *CACNA1H* (encoding CaV3.2) share some splice events in the linkers of domain III and domain IV, where exon 25 is either completely or partially missing so that shorter proteins are synthesized. Another common splice variant is a combination of partially missing exons 25 and 26, which also results in a shorter T-type CaV protein. When expressed these splice variants reveal changed current kinetics and voltage dependences [Chemin *et al.*, 2001; Lee *et al.*, 1999; Monteil *et al.*, 2000; Perez-Reyes,

2006; Wu and Krainer, 1999]. Since T-type CaV channels are activated near the resting membrane potential they are involved in low-threshold spikes and oscillatory cell activity. They initiate hormone and neurotransmitter release, muscle contraction, cell growth, differentiation as well as proliferation [reviewed by Carbone *et al.*, 2014]. Furthermore, new T-type-selective blockers (e.g.: TTA-P2 or efonidipine) were used to characterize the functions of these channels in the uterus, urinary tract as well as in the bladder, and in their contribution to pacemaker activity in the heart [Senatore and Spafford, 2015].

T-type CaVs are also involved in many diseases like absence epilepsy, autism spectrum disorders or Alzheimer's disease. The Genetic Absence Epilepsy Rat from Strasbourg (GAERS) carries a gain-of-function mutation in the CaV3.2 gene and is a model for absence epilepsy. In human gain-of function mutations of CaV3.1 and CaV3.2 were linked to the absence epilepsy and some antiepileptic drugs, like phenytoin, zonisamide or valproate, target and inhibit the T-type Ca²⁺ channels [Broicher *et al.*, 2008; Cain *et al.*, 2011; Tsakiridou *et al.*, 1995]. Missense mutations in the *CACNA1H* gene in humans are associated with autism. These mutations result in a reduced activity of CaV3.2, which can lead to neuronal dysfunction, affect the brain development and causes the autism spectrum disorders phenotype [Cain *et al.*, 2011; Splawski *et al.*, 2006]. In 2010, Strom and colleagues also identified *CACNA1G* as a potential gene involved in autism spectrum disorders [Cain *et al.*, 2011; Strom *et al.*, 2010]. In the Alzheimer's disease, T-type CaV channel expression is downregulated in an age-dependent manner. This results in a higher amyloid beta (A β) production followed by an enhanced neuronal cell death. The enhancement of T-type CaV activation by new compounds like ST101 and SAK3 improved the cognitive function and inhibit A β production in Alzheimer's disease mice [Fukunaga *et al.*, 2019; Rice *et al.*, 2014].

1.3.2.1 CaV3.2 channel

The T-type CaV3.2 is expressed in renal smooth muscle, skeletal muscle, heart, testis, adrenal gland, pancreas, pituitary gland and in many brain areas. The channel is located in presynaptic terminals, where it is involved in the neurotransmitter release by increasing the presynaptic Ca²⁺ concentration [Carbone *et al.*, 2014; Perez-Reyes, 2003; Perez-Reyes, 2006]. The surface expression and channel gating of CaV3.2 is regulated by its intracellular loop between domain I and domain II [Dubel *et al.*, 2004; Monteil *et al.*, 2015]. The voltage-dependent kinetics of CaV3.2 are similar to the kinetics of CaV3.1 but differ from CaV3.3. The channel is activated fast (1–2 ms) and inactivates slower (11–16 ms) with a slow recovery after inactivation. However, the inactivation is much faster with Ba²⁺ as compared to Ca²⁺. Therefore, CaV3.2 and CaV3.1 are mainly involved

in short burst firing, while CaV3.3 is involved in sustained burst firing [Perez-Reyes, 2003]. Furthermore, the channel activity is regulated by G-protein-coupled receptors and their downstream effectors. CaV3.2 is directly inhibited by the G-protein $\beta_2\gamma_2$ subunits [Perez-Reyes, 2010].

Since CaV3.2 is expressed in adrenal glomerulosa cells and in nociceptors, it mediates Ca^{2+} influx in aldosterone producing cells and is involved in pain. CaV3.2 was identified to play a role in early onset hypertension. Patients suffering at the age of 10 years from this disease revealed the heterozygous mutation CACNA1H M1549V in CaV3.2 [Scholl *et al.*, 2015]. Due to this mutation the activation and inactivation of CaV3.2 was changed resulting in more hyperpolarized potentials causing an increased cytoplasmic Ca^{2+} concentration. This increased intracellular Ca^{2+} concentration augments for aldosterone production leading to higher blood aldosterone levels causing high blood pressure [Reimer *et al.*, 2016; Scholl *et al.*, 2015; Spät and Hunyady, 2004]. In 2018, four more germline CaV3.2 mutations (M1549I, S196L, P2083L, V1951E) were found in aldosterone producing adenoma of patients suffering from primary aldosteronism. Like CaV3.2 M1549V, all these mutations are gain-of-function mutations [Daniil *et al.*, 2016]. Moreover, mutations of CaV3.2 are associated with idiopathic generalized epilepsies and neuropathic pain due to an increased and a decreased channel activity, respectively. This makes CaV3.2 an interesting therapeutic target to treat these diseases [Perez-Reyes, 2010].

1.4 Aims

The aim of this work was a further functional characterization of TRPC1 and CaV channels using the patch clamp technique. Of particular interest had been the following questions:

1. What is the functional impact of different ancillary CaV β subunits and their splice variants on the L- and T-type CaV channels?
2. How does the point mutation G1064R in the T-type CaV3.2 gene, identified in a Spanish family suffering from high blood pressure, effect CaV3.2 channel properties?
3. Does TRPC1 form functional ion channels and how can it be brought to life?

For the later question, in addition to cellular and acutely isolated cultured cells from diverse TRPC1-expressing tissues, various mutations and chimeras of TRPC4 and TRPC1 expressed in HEK-cells and *Xenopus laevis* oocytes had to be functionally characterized.

Material and Methods

2.1 Cell culture

2.1.1 Stable immortal cell lines

Immortal cell lines (Appendix Table A1) were cultured in 75 cm² culture flasks (TC-Flasche T75, Sarstedt AG & Co. KG, Nümbrecht, Germany) containing 13 ml of Dulbecco's Modified Eagle Medium (DMEM; Gibco, Thermo Fisher Scientific, Waltham, USA; Appendix Table A1), 10 % fetal bovine serum (FBS, Gibco, Thermo Fisher Scientific, USA) and antibiotics at 37 °C and 5 % CO₂ until they were confluent. After the cells reached a confluence of ~80 %, they were detached from the bottom of the culture flasks and from each other by trypsin (Sigma-Aldrich, Merck KGaA, Darmstadt, Germany) and transferred to a new culture flask containing fresh DMEM. For patch clamp experiments, the cells were plated on small glass coverslips (12 cm ø, Thermo Fisher Scientific, USA), which were placed in petri dishes (35 x 10 mm, Falcon, Thermo Fisher Scientific, USA) filled with 2 ml DMEM.

2.1.2 Transfection of cDNA

Transfection is introducing DNA or RNA into eukaryotic cells by increasing the permeability of the plasma membrane with transfection reagents.

Cells (Appendix, Table A1) were plated in petri dishes (35 x 10 mm) until a confluent layer was reached and transfected either with Lipofectamine 3000 (Invitrogen, Thermo Fisher Scientific, Waltham, USA; Table 1), Biotool (DNA Transfection Reagent, Biotool, Munich, Germany; Table 2) or FuGene HD (Promega GmbH, Walldorf, Germany). For experiments these cells were transferred to petri dishes (35 x 10 mm), which contained glass coverslips (12 cm ø) and were used 24 to 48 h after transfection. For the FuGene transfection 100 µl Optimem, 2 µg cDNA and 5 µl FuGene HD (Promega) were mixed and incubated for 15 min at room temperature, afterwards the content was added dropwise to the cells.

The plasmids (Appendix, Table A2) used for transfection were cloned and provided by Stefanie Buchholz and Ulrich Wissenbach.

Table 1 Transfection protocol with Lipofectamine 3000. This transfection reagent was used to transfect plasmids for TRPC expression in HEK-cells.

Reaction tube 1	Reaction tube 2
125 µl Optimem + 3.75 µl Lipofectamine 3000	125 µl Optimem + 2.5 µg DNA + 5 µl P3000 reagent
mix	mix
content of reaction tube 2 was added to reaction tube 1 and mixed	
incubation for 5 min at room temperature	
content was added to the cells in 2 ml DMEM	

Table 2 Transfection protocol with Biotool transfection reagent.

Reaction tube 1	Reaction tube 2
250 µl Optimem	250 µl Optimem
4 µg DNA	10 µl Biotool transfection reagent
each reaction tube was mixed and incubated for 5 min at room temperature	
content of reaction tube 1 was added to reaction tube 2 and mixed	
incubation for 20 min at room temperature	
content was added to the cells in 2 ml DMEM	

2.1.3 Dissociation of the murine pituitary

For dissociation of the murine pituitary, four or eight weeks old male mice were anesthetized by isoflurane (Baxter Deutschland GmbH, Unterschleißheim, Germany), decapitated and the whole brain was removed to reach the pituitary. Before the pituitary was extracted, a thin membrane surrounding the pituitary had to be removed to reduce the contamination of the cell culture with other cell types. Fine forceps were placed underneath the pituitary to remove the tissue and to transfer it to 1.5 ml reaction tubes containing Earle's Balanced Salt Solution (EBBS-buffer; Papain Dissociation System, Worthington Biochemical Corporation, Lakewood, USA).

The pituitary was dissociated by incubating the whole tissue in 600 µl of a papain (130 U) and DNase (1230 U) mixture (Papain Dissociation System, Worthington Biochemical Corporation) for 45 min at 37 °C and 5 % CO₂. After the incubation, a 1 ml pipette was used to separate the cells by pipetting ~30 times up and down. The suspension was transferred to 15 ml tubes, centrifuged at 1000 rpm and 4 °C for 4 min, afterwards the supernatant was discarded, and the pellet resuspended in 1 ml FACS-buffer (0.1 % BSA, 1 % EDTA in PBS). By using the FACS-buffer, the enzymatic activity of the papain was stopped. The resuspended cells were centrifuged at 1000 rpm and 4 °C for 4 min, the supernatant was discarded, and the pellet resuspended at 1 ml DMDM. Afterwards the

cells were plated on glass coverslips (12 cm \varnothing) in a 24-well-plate (Falcon, Thermo Fisher Scientific) in 500 μ l DMEM, penicillin/streptomycin (P/S; Sigma-Aldrich, Merck KGaA, Darmstadt, Germany) and incubated at 37 °C and 5 % CO₂. The glass coverslips had been pretreated with Poly-L-Lysine (PLL; Sigma-Aldrich) for at least 30 min and washed two times with PBS (137 mM NaCl, 2.7 mM KCl, 4.3 mM Na₂HPO₄, 1.47 mM KH₂PO₄).

2.1.4 Preparation of murine embryonic fibroblasts (MEFs)

Murine embryos at embryonic stage 14.5 were used to prepare the murine embryonic fibroblast (MEF) cells. Therefore, the embryos were removed, organs and limbs of these embryos were taken out and the remaining tissue was minced with dissecting scissors. The tissue was transferred to a 50 ml tube and incubated with 1 ml trypsin per embryo for 10 min at 37 °C. Cells were separated by pipetting up and down with a 25 ml, 10 ml and 5 ml pipette (30 times each) and incubated for 5 min at 37 °C. The 50 ml tube containing the embryos was filled with 25 ml DMEM medium, mixed by using a 10 ml pipette and incubated for 5 min at 37 °C. Cells were transferred to a cell culture flask and used up to passage 5.

2.1.5 Culturing of osteoclasts

Osteoclasts were prepared from the femurs of adult mice, which were sacrificed by cervical dislocation. The skin was cleaned with 70 % ethanol and the femurs were removed by using scissors and forceps. Femurs were carefully removed from the limbs, cleaned from the surrounding tissue and placed into a small petri dish containing 3 ml mouse osteoclast (MOC) medium (α -MEM (Minimal Essential Medium from Gibco), 10 % FBS, 170 IE/mL heparin, 100 U/mL penicillin, 100 μ g/mL streptomycin, 250 ng/mL amphotericin B). The distal part of the bone was removed and the remaining bone was placed into a 1.5 ml reaction tube containing an inserted sieve and 250 μ l of MOC medium. After centrifugation at 4500 rpm for 3 min, the inserted sieve was removed together with the bone from the reaction tube and the remaining pellet was resuspended in 750 μ l MOC medium. The cell suspension was transferred to a 15 ml tube containing 10 ml MOC medium and centrifuged at 1500 rpm and 4 °C for 5 min. The supernatant was discarded and 1 ml of MOC medium together with 9 ml of erylisis buffer (155 mM NH₄Cl, 10 ml KHCO₃, 0.1 mM EDTA) were added to the pellet and incubated for 5 min at room temperature. After a centrifugation at 1500 rpm and 4 °C for 5 min, the pellet was washed twice with 5 ml MOC medium by centrifugation at 1100 rpm for 5 min each time. The cells were counted with a Neubauer counting chamber (Blaubrand®, BRAND GMBH + CO KG, Wertheim, Germany), diluted to a density of 1x10⁵ cells were plated in

ibidi treat μ -Dish (35 mm, low; ibidi GmbH; Gräfelfing, Germany). To each petri dish 1.5 ml of MOC medium containing 30 ng/ml M-CSF (R&D Systems, Inc., Minneapolis, USA) and 20 ng/ml RANKL (R&D Systems, Inc.) was added. During the culturing two-third of the medium was replaced every 2 to 3 days until the experiments were performed 7 to 9 days after preparation.

2.2 Polymerase chain reaction (PCR) of dissociated pituitary cells

Dissociated green fluorescent TRPC1 τ GFP pituitary cells were sorted by using BD Biosciences FACS Aria II with the excitation at 488 nm and emission detected at 508 nm for RNA purification according to the manufacturer's protocol of the RNeasy Plus Micro kit (Quiagen). The RNA concentration was measured with a NanoDrop 1000 Spectrophotometer (Fisher Scientific) and stored at -80 °C until use.

The SensiFAST SYBR No-ROX one-step kit (Bioline) was used for complementary DNA synthesis and real-time PCR according to the manufacturer's protocol in a CFX-96 real-time PCR detection system (BioRad) using oligodeoxynucleotide primers (Quiagen; Table 3). Following cycling conditions were used: 10 min at 45 °C, followed by 2 min at 95 °C and 40 cycles (5 s at 95 °C and 20 s at 58 °C). The housekeeping genes *hprt* and *actb* were used as controls. Obtained results represent the abundance of the target gene expression relative to *hprt* by using 2-fold induction of target gene expression using the $2^{-\Delta\Delta CT}$ method.

Table 3 Oligodeoxynucleotide primers for real-time PCR.

gene	NCBI accession number	Cat. No.	PCR product size (bp)
Mm_trpc1	NM_011643	QT00134988	92
Mm_trpc3	NM_019510	QT00124194	98
Mm_trpc4	NM_001253682	QT00115444	113
Mm_trpc5	NM_009428	QT00169757	100
Mm_trpc6	NM_013838	QT00170905	114
Mm_trpc7	NM_012035	QT00124145	98
Mm_hprt	NM_013556	QT00166768	168
Mm_actb	NM_007393	QT00095242	149

2.3 cRNA-synthesis

2.3.1 Subcloning of cDNA into vectors for *in vitro* transcription

The cDNA of TRPC1 and TRPC4 were subcloned into the multiple cloning site of the pMXT vector [Zhen *et al.*, 2018] under the control of the T3 polymerase (TRPC1 constructs) and of the pSGEM vector [Zhen *et al.*, 2018a] under the control of the T7

(TRPC4 constructs) polymerase, respectively. After subcloning, the cDNA and their subcloning sites were sequenced on both strands.

2.3.2 Transformation and plating of competent *E. coli*

Plasmids containing the target DNA sequence were transformed into chemically competent *DH5 α -E. coli* (Life Technologies GmbH). For this purpose, the bacteria were thawed on ice, then 1 μ l of the plasmid was added followed by a 30 min incubation on ice. After the attachment of the plasmids on the bacterial membrane, a 35 s long heat shock at 42 °C was performed. This step was followed by mixing the bacterial suspension with 0.5 ml LB medium containing ampicillin and incubated for 30 min at 37 °C. The bacteria were plated on ampicillin containing LB-agar plates and incubated over night at 37 °C. On the next day, single colonies were picked into tubes containing 2 ml LB medium (100 μ g/ml ampicillin) and incubated over night at 37 °C.

2.3.3 Plasmid preparation

Plasmid preparation was carried out to extract the plasmid from the *E. coli*. Before the purification of the plasmid DNA, the bacterial suspension was transferred into 2 ml reaction tubes and centrifuged at 13200 rpm for 1 min. The plasmid DNA was obtained from the pellet using the GeneJET Miniprep Kit (Thermo Fisher Scientific Inc.) for isolation and purification. The plasmid DNA concentration was then determined by using a NanoDrop (Thermo Scientific™ NanoDrop 2000).

2.3.4 Linearization and Purification of the plasmid DNA

The following restriction digest reaction was used to linearize the plasmid DNA before *in vitro* transcription:

DNA-template	10 μ g
enzyme	4 μ l
10x Digest Buffer	5 μ l
water	ad. to 50 μ l

Incubation for 3 h at 37 °C

The SbfI restriction enzyme (New England Biolabs) was used to digest the pSGEM plasmids and the SacI restriction enzyme (New England Biolabs) was used to digest the pMXT-MCS plasmids.

Purification of the plasmid DNA was performed according to the protocol of the GeneJET PCR Purification Kit (Thermo Fisher Scientific Inc.). Deviating from the manufacturer's protocol, for elution 25 µl water was used instead of 50 µl elution buffer. The DNA concentration was then determined using a NanoDrop apparatus.

2.3.5 *in vitro* transcription

The *in vitro* transcription was performed according to the *in vitro* protocol transcription kit mMESSAGE mMACHINE T7 (for TRPC4 constructs) or mMESSAGE mMACHINE T3 (for TRPC1 constructs) (Life Technologies GmbH). After an incubation of 3 h at 37 °C, lithium chloride precipitation of the cRNA was done as described in the manufacturer's protocol and the cRNA concentration was determined using a NanoDrop apparatus.

2.3.6 cRNA injection into *Xenopus laevis* oocytes

Oocytes from developmental stages V and VI were used for cRNA injection. Since the individual stages of development are metabolically different, using different stages might influence the heterologous expression and thus the results. Injection needles were pulled with a horizontal puller (P-1000, Sutter Instruments) using heat-sterilized glass capillaries (7" Drummond #3-000-203-G/XL, Drummond Scientific Company) filled with 2 µl cRNA, fixed onto a holder and the tip was cut until a drop size of approximately 0.5 mm. This drop size had a volume of 8 nl. The oocytes were lined up in a petri dish and injected with cRNA, the injection needle was withdrawn from the oocyte after 5-6 s. Each oocyte was injected with a cRNA concentration of 1 ng/nl in a volume of 25 nl. Injection pressure had to be increased three times the starting pressure to reach the injected volume of 25 nl. After the injection, the oocytes were incubated for two days at 16 °C in a barth solution (88 mM NaCl, 2.4 mM NaHCO₃, 1 mM KCl, 0.33 mM Ca(NO₃)₂, 0.41 mM CaCl₂, 0.82 mM MgSO₄, 5 mM HEPES, Sodium Pyruvate (100x; Gibco), penicillin/streptomycin (Gibco; 5000 Units/ml penicillin, 5000 µg/ml streptomycin; pH 7.5) before used for experiments.

2.4 Protein detection by Western Blots

The protein expression in HEK-cells, primary cells as well as in oocytes was checked with Western Blots, to determine possible differences in the amount of protein. (Western Blots of HEK-cells and primary cells were performed by Christine Wesely, of oocytes by

myself). This method consists of three steps: gel electrophoresis, transfer to the membrane (blotting) and immunodetection.

Preparation of HEK- and primary cell lysates for Western Blot:

Transfected HEK-cells or primary cells were plated in petri dishes (35 x 10 mm) cultured for two days until a density of approximately 90 % was reached. The cells were mixed with 150 μ l Laemmli buffer and a cell scraper (Falcon, Thermo Fisher Scientific, USA) was used to detach the cells from the petri dish. Afterwards the cells were sheared with a 1 ml syringe (B. Braun Melsungen AG, Melsungen, Germany) using a 0.55 x 25 mm cannula (Gr. 17, B. Braun Melsungen AG, Germany) and incubated for 20 min at 60 °C for denaturation. After an incubation on ice for 5 min the samples were loaded onto a SDS-gel and the Western Blot was performed.

Preparation of oocyte lysates for Western Blot:

The injected oocytes (minimum five oocytes per group) were lysed by using CellLytic™ MT Cell Lysis Reagent (Sigma) containing protease inhibitor (40 μ L per oocyte), followed by up and down pipetting until becoming a homogenous solution. This solution was centrifugated at 4 °C and 13.2 rpm for 15 min and afterwards, the supernatant was carefully removed from the tube and transferred into a new 1.5 ml tube. This step was repeated until the supernatant was clear, 5x loading buffer was added and the suspension was incubated for 5 min in a 65 °C water bath. Either the Western Blot was immediately performed or the suspension was frozen at -20 °C until it was used.

The Western Blot for HEK-cells, primary cells as well as for oocytes was performed as follows. The SDS-gel (8 % separating gel: 21.4 ml water, 10 ml 1.5 M TRIS-HCl pH 8.8, 400 μ l 10 % SDS, 8 ml 40 % acrylamide/Bis, 200 μ l 10 % ammonium persulfate, 20 μ l TEMED; Stacking gel: 8.6 ml water, 3.4 ml 0.5 M TRIS-HCl pH 6.8, 140 μ l 10 % SDS, 1.4 ml 40 % acrylamide/Bis, 70 μ l 10 % ammonium persulfate, 14 μ l TEMED) was placed into the chamber (Life Technologies GmbH) filled with the running buffer (25 mM Tris, 190 mM glycine, 0.1 % SDS, pH 8.3) and loaded with the sample (20 μ l in sample buffer) and 5 μ l of protein standard (Precision Plus Protein™ All Blue Standard; BioRad). The protein separation was done in two steps with the following protocol: 80 mV until the sample reaches the separating gel, then the voltage was increased to 120 mV until the loading dye runs out. Afterwards the electrophoretic transfer (blotting) of the protein onto a nitrocellulose membrane was done. The electrophoresis chamber filled with transfer buffer (25 mM Tris, 190 mM glycine, 20 % methanol) and the gel holder cassette was placed on ice. After 1 h of blotting at 300 mA the membrane was blocked for 10 min with 5 % skim milk, followed by the incubation of the primary antibody (Table 4) over night at 4 °C. On the next day, the membrane was washed three times for 5 min with PBST

(137 mM NaCl, 2.7 mM KCl, 4.3 mM Na₂HPO₄, 1.47 mM KH₂PO₄, 0.1 % Tween 20) and incubated with the secondary antibody (Table 4) at room temperature for 1 h. After the incubation with the secondary antibody, the membrane was washed three times for 5 min with PBST. The Amersham ECL™ Prime Western Blotting Detection Reagent (GE Healthcare Life Sciences) was used to detect the proteins with the ChemiDoc System (BioRad).

Table 4 Antibodies used for Western Blot

primary antibody	company	reference
rabbit anti-CaVβ3	828 HOM-made	Berggren <i>et al.</i> , 2004; Link <i>et al.</i> , 2009;
rabbit anti-CaVβ2	425 HOM-made	Berggren <i>et al.</i> , 2004; Link <i>et al.</i> , 2009;
mouse anti-myc	Roche (9E10)	
rat anti-YFP/GFP	PL1H6D7 HOM-made	this study
rat anti-TRPC1	9F2E4 HOM-made	this study
rabbit anti-TRPC4	781EB HOM-made	Freichel <i>et al.</i> , 2001
rabbit anti-calnexin	Stressgen (SPA-864)	
mouse anti-βactin	Abcam (ab8227)	
secondary antibody	company	reference
goat secondary anti-rat	GE Healthcare (NA935V)	
sheep secondary anti-mouse	GE Healthcare (NA9310)	
donkey secondary anti-rabbit	GE Healthcare (NA9340)	

The mutated TRPC1 protein expression was normalized to the GFP expression using the software Aida Image Analyzer (Version 450; Elysia-raytest GmbH, Straubenhardt, Germany) and the current was multiplied by this expression factor.

2.5 Protein surface localization (Biotinylation)

Biotinylation of surface proteins:

The biotinylation was used to detect the TRPC1 protein in the plasma membrane. Briefly, HEK-cells (75 cm² culture flask) were transfected with either TRPC1 or TRPC4α-C1_{S5-S6} linker chimera constructs. Per culture flask the following protocol was used and all steps were done on ice:

- 2x washing of cells with 10 ml PBSB (pH 8.0; Table 5)
- Incubation with 10 ml NHS-LC-Biotin (0.5 mg/ml) for 30 min at 4 °C
- 2x washing with 10 ml PBSB + 1 % BSA

- 1x washing with 10 ml PBS (pH 7.4; Table 5)
- Incubation with 10 ml PBS (pH 7.4) + 2 mM EDTA, the culture flask was tapped to remove the cells and cells were transferred into a 10 ml tube
- Centrifugation at 1000xg for 5 min at 4 °C
- Pellet was resuspended in 400 µM lysis buffer + protease inhibitor (Table 5), transferred into 1.5 ml tube and sheared with a 24 G cannula
- Incubation for 15 min at 4 °C on shaker
- Suspension was sheared again and incubated for 15 min at 4 °C on shaker
- Centrifugation for 5 min at 1000xg and 4 °C
- Supernatant was transferred into a new 1.5 ml tube
- Protein determination
- Binding of 2000 µg protein extract on 200 µl Avidin-agarose: Incubation for 2 h at 4 °C on shaker
- Centrifugation for 3 min at 100xg and 4 °C
- 4x washing with 1 ml lysis buffer + 0.25 M NaCl (without protease inhibitor)
- 80 µl 2x Laemmli buffer was added to the sample
- Incubation for 20 min at 60 °C
- SDS-Page/ Western Blot (see chapter 2.4 protein detection by Western Blot)

Table 5 Buffers for Biotinylation. Composition of all buffers used for Biotinylation with the indicated pH.

PBS pH 7.4	PBSB pH 8.0	Lysis buffer pH 7.4
137 mM NaCl	PBS pH 7.4	PBS pH 7.4
2.7 mM KCl	+ 1 mM MgCl ₂	+ 1 % Triton
1.5 mM KH ₂ PO ₄	+ 0.5 mM CaCl ₂	+ 1 mM EDTA
8 mM Na ₂ HPO ₄		+ protease inhibitor

Biotinylation of oocytes:

Two days after RNA injection into the oocytes the surface protein biotinylation was performed. Per group 15 intact oocytes were treated according to the following protocol:

- Washing of the oocytes 3x with ice-cold PBS (pH 7.4 (1x) Phosphate Buffered Saline (-) CaCl₂; (-) MgCl₂; Gibco™; Thermo Fisher Scientific)
- Incubation with 0.5 mg/ml sulfo-NHS-SS-Biotin (EZ-Link™ sulfo-NHS-SS-Biotin; Thermo Fisher Scientific) for 1 h at RT on shaker
- Removing the Biotin and adding 1 ml of 1 M NH₄Cl for 2 min
- Washing 3x with ice-cold PBS

- Oocytes were transferred into a 1.5 ml tube
- Lysis buffer + protease inhibitor (40 µl per oocyte) was added and oocytes were lysed
- Centrifugation for 15 min at 4 °C and 13.2 rpm
- 50 µl of the supernatant was taken, loading dye was added and the sample was heated for 5 min at 65 °C and stored at -20 °C
- 350 µl of the remaining supernatant was taken into a new 1.5 ml tube
- Streptavidin beads (Streptavidin Agarose Resin; Thermo Fisher Scientific) were washed 3x with ice-cold PBS by centrifugation at 2 rpm and 4 °C for 2 min
- 60 µl of beads were added to the supernatant
- Incubation over night at 4 °C shaking

Next day

- Centrifugation for 2 min at 4 °C and 2 rpm, afterwards 50 µl of the supernatant were separated as flow-through, loading dye was added, incubated for 5 min at 65 °C and stored at -20 °C
- the beads were washed 3x with ice-cold PBS
- 30 µl of loading buffer was added, incubated for 5 min at 65 °C and stored at -20 °C or Western Blot was performed as described in section 2.4.

2.6 Dot blot

2.6.1 *in vitro* transcription

The protocol of the TnT® Quick Coupled Transcription/Translation System kit (Promega GmbH, Germany) was used to generate the proteins and to introduce the radioactive labelled methionine (L- [³⁵S] Methionine SRM-01, Hartman Analytic) into the CaVβ3.

reticulocytan lysate	25 µl
cDNA	1.5 µg
³⁵ S-methionine	1 µl
water	ad. to 30 µl

The mixture was incubated for 1 h 30 min in a 30 °C warm water bath.

2.6.2 Gel filtration and radioactivity detection

The sample from section 2.6.1 was filtered according to the protocol of the Nick™ Coulum Sephadex G50 DNA grate Kit (GE Healthcare GmbH, Solingen) with the BPTL

buffer (50 mM Tris, 150 mM NaCl, 0.1 % Triton X, 1 mM CaCl₂, 10 mM EDTA; pH 7.4) into 10 different 1.5 ml reaction tubes. After the filtration 1 µl of each sample was mixed with 400 µl scintillation liquid to measure (exposure time 1 min) the radioactivity by using the BAS 2500 Image Analysis System (FUJIFILM Life Science, Düsseldorf, Germany). Furthermore, the protein expression was controlled by Western Blot (see section 2.4). After the SDS-gel was dried over night at 35 °C it was transferred onto a film (Phosphor-imaging plate Fujifilm BAS-SR 2040) and the radioactive dots were labelled and wrapped into plastic wrap. The membrane with the spotted protein dots was cut and incubated with the BPTL buffer for 2 h at room temperature followed by an incubation of 1 h with 5 % skim milk to block the membrane. The membrane was washed 3 times for 10 min with BPTL buffer before the membrane was incubated with the radioactive sample (diluted in BPTL buffer and protease inhibitor) over night. On the next day the membrane was exposed on a film for 3 h followed by the detection of the signals using the BasReader 3.14 (Fujifilm).

2.7 Electrophysiology

2.7.1 Patch clamp technique

The biophysicist Erwin Neher and the physiologist Bert Sakmann developed the patch clamp technique 1976 in Göttingen for which they received the Nobel Prize in 1991. This technique allows to study the membrane properties of electrically active cells, the mode of operation and pharmacology of ion channels due to certain intracellular as well as extracellular ionic compositions.

The patch clamp technique can be used to measure either single channel currents or whole cell currents. Furthermore, there are two different patch clamp recording methods: voltage-clamp and current-clamp. I used the voltage-clamp mode where the membrane potential of the derived cell is kept under control the patch clamp amplifier at predetermined value and the resulting ion currents are registered. This is used in particular, to analyze the biophysical properties of ion channels regarding the currents. While in the current-clamp mode the derivation of the membrane potential in response to injected current pulses are recorded. With this approach, action potentials and postsynaptic potentials can be measured, as well as the changes of membrane potentials due to the activity of electrogenic transporters. The voltage-clamp mode can be performed in five different configurations. The patch pipette has to be moved to the cell via a micromanipulator until the patch pipette is tightly attached to the plasma membrane. A tight attachment of the patch pipette on the plasma membrane is indicated

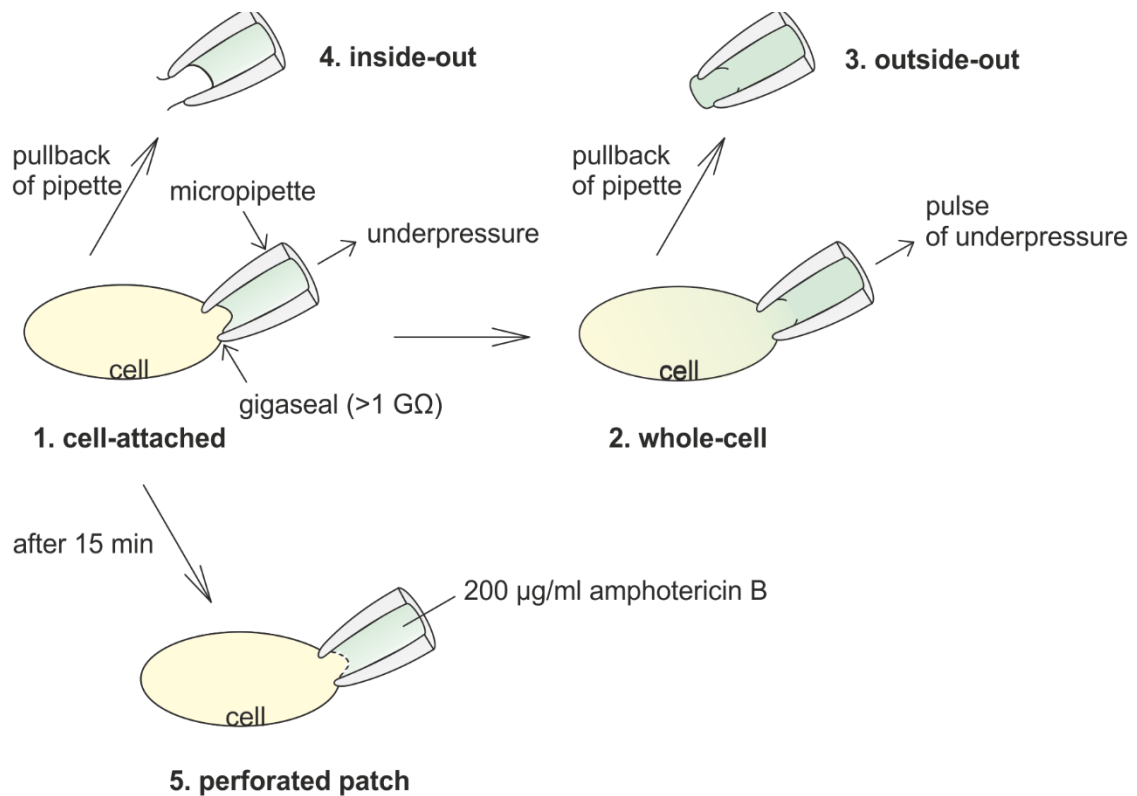


Figure 7 Patch clamp configurations. The cell-attached configuration (1) is the initial configuration, where the patch pipette is tightly attached to the cell membrane (Gigaseal). A pulse of underpressure breaks the cell membrane (2), which leads to an access to the whole cell. The cytosol is exchanged by the intracellular solution by diffusion (2). A pullback of the patch pipette can lead to the outside-out configuration (3), where the former outside of the plasma membrane faces the extracellular solution. While a pullback of the patch pipette from the cell-attached configuration (1) leads to the inside-out configuration (4), where the former intracellular side of the plasma membrane is facing the extracellular solution. The patch pipette can be filled with 200 µg/ml amphotericin B and after 15 minutes in the cell-attached configuration, the plasma membrane will be perforated (5). In the perforated patch, the cytosol is not exchanged by the intracellular solution, so that the cytosolic composition of ions and molecules will be not changed.

by a pipette resistance higher than 1 GΩ (Gigaseal); this mode is called “cell-attached configuration” (Figure 7; 1). This configuration is the initial point for four more configurations: whole-cell, outside-out, inside-out, and the perforated patch (Figure 7). The whole-cell configuration is used to record currents from all ion channels in the plasma membrane. To reach the whole-cell configuration the plasma membrane under the pipette has to be removed by a pulse of underpressure, which leads to an access to the cytosol (Figure 7; 2). This results in an exchange of the cytosol and the internal solution in the patch pipette. To avoid an exchange of the cytosol, the perforated patch is used. Here, an antibiotic usually amphotericin B is placed in the patch pipette, which perforates the plasma membrane forming ion permeable pores. This results in an electrical access to the cell, but the cytosol remains unchanged (Figure 7; 5).

Furthermore, the outside-out and inside-out configurations are used to record currents from single channels. The outside-out configuration results from the whole-cell

configuration after a fast retraction of the patch pipette. A patch of the plasma membrane will be removed which closes in front of the pipette opening and forms a half vesicle. The extracellular side of the plasma membrane (outside) is orientated to the external solution while the intracellular side is orientated to the internal solution (pipette; Figure 7; 3). Analog to the outside-out configuration, an inside-out configuration can be achieved. Here the patch pipette is pulled back from the cell-attached configuration and a patch of the plasma membrane is removed. The former intracellular side of the plasma membrane is now exposed to the external solution while the former extracellular side of the plasma membrane is exposed to the intracellular solution. This configuration is used to investigate the influence of intracellular components such as second messengers on the single-channel conductance (Figure 7; 4).

2.7.1.1 Patch clamp set-up

Patch-clamp experiments had been performed under visual control and the set-up I used was based on an inverted microscope (Axiovert 135 M, Zeiss, Germany) with a video camera (TVCCD 200 Monacor, Bremen, Germany). Furthermore, the microscope was surrounded by a Faraday cage to reduce electrical noise from the surrounding equipment and placed on a vibration-damped table to reduce the vibrations from the building. Coverslips with the cells were placed in the measuring chamber, which was filled with an external solution (Table 6; Table 7). This measuring chamber also contains a chlorinated

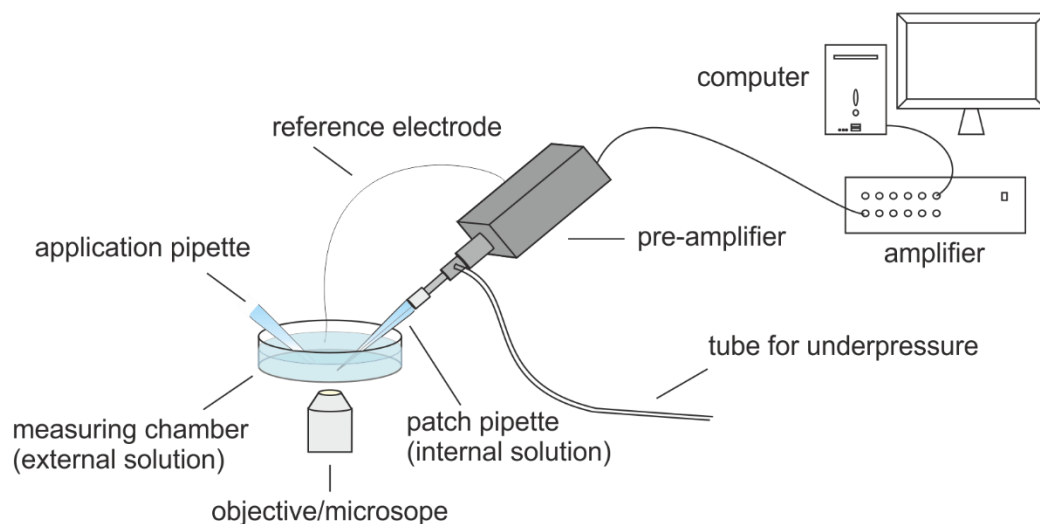


Figure 8 Schematic setting of a patch clamp set-up. The inverted microscope is placed in a Faraday cage (not shown here) to avoid electrical noises during the measurements. The coverslip containing the cells is placed in the measuring chamber which is filled with an external solution. For the measurements a patch pipette is needed. This patch pipette is connected to a pre-amplifier which is connected to an amplifier. The patch pipette is filled with an internal solution and contains a chlorinated silver wire. A reference electrode is connecting the pre-amplifier with the external solution leading to a closed electric circuit. Furthermore, the amplifier is connected to a computer where the measurements are controlled, registered and stored.

silver wire as a reference electrode which is connected to a pre-amplifier. The used patch pipette was filled with an internal solution (Table 5; Table 6), contained a chlorinated silver wire and could be moved relative to the measuring chamber via a micromanipulator (PatchMan, Eppendorf, Hamburg, Germany). This patch pipette was connected via a pre-amplifier to the main amplifier (EPC9, HEKA Elektronik GmbH, Lambrecht/Pfalz, Germany), which was connected to a computer for controlling, registration and storage (patch master, HEKA) of the measurements (Figure 8).

2.7.1.2 Experimental procedure and protocols for patch clamp

The experiments were performed either with HEK-cells, dissociated pituitary cells, mouse embryonic fibroblasts or osteoclasts. The cells were plated on glass cover-slips and fixed with silicone (dow corning 111 valve lubricant and sealant, Dow Corning Corporation) into the measuring chamber, which was filled afterwards with an external solution (Table 6; Table 7). The measuring chamber was placed onto the stage of the microscope and connected via the reference electrode to the pre-amplifier. The liquid junction was calculated as 5 mV for the CaV solutions and 10 mV for the TRP solutions. After a vital cell was found, the patch pipette was filled with an internal solution (Table 6; Table 7) and fixed in the pipette holder, which was connected to the pre-amplifier. Pipettes were pulled from glass capillaries (GB150 T-8P, Science Products GmbH, Hofheim, Germany) using a pipette puller (PC-10, Narishige, Tokio, Japan) and had resistances between 2 and 4 M Ω when filled with internal solution. The patch pipette was moved with a micromanipulator to the cell, underpressure was applied until the patch pipette resistance was higher than 1 G Ω (Gigaseal), and with a further pulse of under pressure the plasma membrane under the pipette tip was removed. By using a second pipette, drugs (Table 8) were applied directly onto the patch clamped cell. All experiments were performed in the whole-cell configuration and for the analysis the current amplitudes were normalized to the cell capacitance.

Table 6 External and internal solutions for TRPC measurements. pH of 7.2 was adjusted by NaOH or CsOH. The Ca^{2+} concentration of the internal solution was chosen according to the TRPC isoform.

internal solution [mM]	external solution [mM]	monovalent-free external solution [mM]	divalent-free external solution [mM]
120 CsGlutamate	140 NaCl	10 CaCl_2	130 NaCl
8 NaCl	1 CaCl_2	150 NMDG	50 (D)-sorbitol
1 MgCl_2	2.8 KCl		10 HEPES
10 HEPES	2 MgCl_2		
10 CsBapta	10 HEPES		
	10 glucose		

Table 7 External and internal solution for CaV measurements. pH of 7.4 was adjusted by NaOH or CsOH.

internal solution [mM]	external solution [mM]
135 CsCl	102 NaCl
3 MgCl_2	10 $\text{CaCl}_2/\text{BaCl}_2$
10 EGTA	5.4 CsCl
5 HEPES	1 MgCl_2
5 MgATP	20 TEA-Cl
	5 HEPES
	10 glucose

Table 8 List of TRP and CaV agonists and antagonists.

substance	agonist/antagonist	supplier
carbachol	agonist of M2R and M3R	Tocris
DAMGO	agonist of μOR	Tocris
Englerin A	agonist of TRPC4 and TRPC5	Roth
OAG	agonist of TRPC2, TRPC3 and TRPC6	Cayman Chemical
SKF 96365	antagonist of TRP channels	Cayman Chemical

substance	agonist/antagonist	supplier
(s)-(-)-Bay K 8644	agonist of L-type CaV	Tocris
ω -agatoxin IVA	antagonist of P/Q-type CaV	Tocris
ω -conotoxin GVIA	antagonist of N-type CaV	alomone labs
isradipine	antagonist of L-type CaV	Cayman Chemical
nifedipine	antagonist of L-type CaV	Tocris
SNX 482	antagonist of R-type CaV	Tocris
verapamil	antagonist of L-type CaV	Cayman Chemical
TTX	antagonist of NaV	Tocris

2.7.1.2.1 Transient receptor potential channel recordings

The patch protocol for TRP channels is similar to the ramp protocol of CaV channels. The current-voltage relationship of TRP channels depends on the isoform of the channel. The holding potential was chosen at 0 mV due to the reversal potential of the TRP currents. Cells were clamped continuously from -100 mV to +100 mV over 400 ms and ramps were repeated every 2 s. The currents at -80 mV and +80 mV were extracted for further analysis of the current over time (Figure 9). Since the activation of TRP channels is not voltage-dependent, drugs had to be used to activate them. Agonists were applied after 2 min from the start of the measurement for a duration of 2 min followed by a washout of 2 min. In some experiments, monovalent-free and divalent-free solutions (Table 6) were applied to measure the reversal potential of the currents under the respective conditions. These reversal potentials were needed to calculate the permeability ratio of Ca²⁺ and Na⁺ ions (P_{Ca}/P_{Na}), using the following equation:

$$\frac{P_{div}}{P_{Na}} = \frac{e^{((RP_{div} - RP_{Na}) R^{-1} T^{-1} F)} [Na]_o (1 + e^{(RP_{div} R^{-1} T^{-1} F)})}{4[div]_o}$$

The extracellular Na⁺ concentration is indicated by [Na]_o and the extracellular Ca²⁺ concentration is indicated by [div]_o. RP_{Na} and RP_{Ca} represent the reversal potential of the Na⁺ and Ca²⁺ currents, respectively. R is the gas constant (8.31 J/(K·mol)), T the absolute temperature (293 K) and F the Faraday constant (96485.3 A*s/mol).

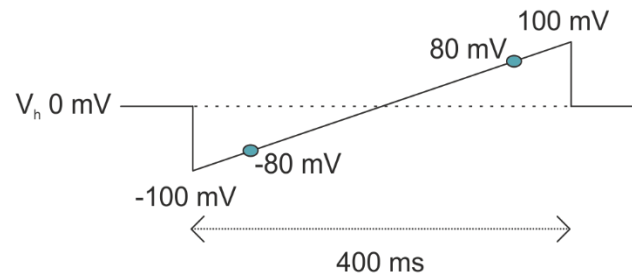


Figure 9 Ramp protocol and application protocol for the TRP current recordings. The holding potential was set to 0 mV and the cell was depolarized from -100 mV to +100 mV within 400 ms. This ramp was repeated every 2 s and for every ramp values of ± 80 mV were extracted for the analysis (indicated by blue dots).

2.7.1.2.2 Voltage-gated calcium channel recordings

In this thesis two different isoforms of voltage-gated calcium channels (CaV) were investigated: L-type CaV1.2 and T-type CaV3.2. The activation of the isoforms depends on different voltages. L-type CaVs are activated at more positive voltages (at -30 mV) as compared to T-type CaVs, which are activated at more negative voltages like -60 mV. Furthermore, the voltages at which both isoforms reveal maximum current are different. L-type CaVs reach their maximum current between 0 mV and +10 mV, whereas T-type CaVs reach their maximum current at -10 mV. Therefore, different protocols had to be used for the respective isoforms. Cells expressing L-type CaVs were measured with two protocols, where the cells were clamped to a holding potential (V_h) of -60 mV. A ramp protocol followed by a step protocol were applied to each cell. In the ramp protocol cells were clamped continuously from -100 mV to +100 mV within 50 ms, with a repetition every 2 s (Figure 10 A). Subsequently a step protocol was applied to the same cell: The cell was clamped in 17 steps from -70 mV up to +90 mV. Each voltage was set for 400 ms and every 2 s the voltage was increased in 10 mV increments. In between of each step, the cell was clamped to -60 mV (Figure 10 B). The ramp protocol was used

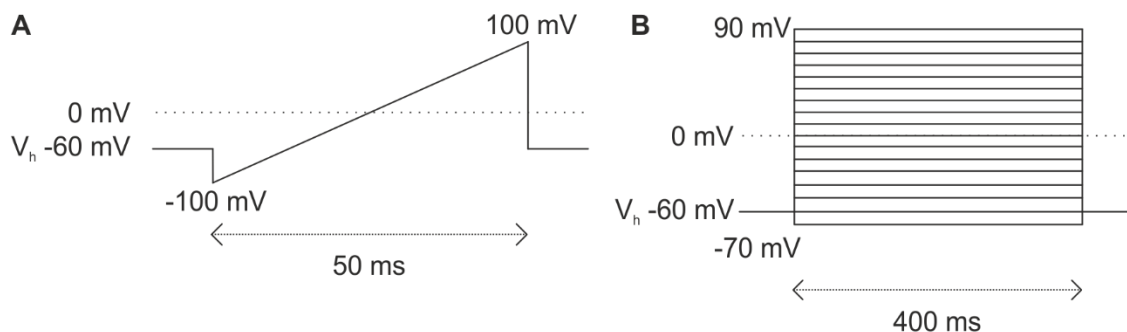


Figure 10 Patch clamp protocols for recording currents from L-type voltage-gated calcium channels. Two different protocols were used to measure the L-type CaVs. The holding potential (V_h) was -60 mV and the cells were depolarized continuously from -100 mV to +100 mV over 50 ms. (A). The same cell was measured afterwards with a step protocol, where the cell was clamped from -70 mV to +90 mV (Δ -10 mV), each for 400 ms in between the voltage steps cells were clamped to -60 mV (B). Ramps were repeated every 2 s and the dotted line indicates the 0 mV.

to analyze the current-voltage relationship, while the step protocol was used to identify the activating voltage and the voltage of the maximum CaV current. For the activation kinetics the rising phase of the current at the potential with the maximal CaV current was fitted with a single exponential equation ($y=y_0 + A\exp [(-(x-x_0))/\tau]$) to calculate the time constant (τ_{act}). For the inactivation kinetics (τ_{fast} and τ_{slow}) the current decrease at the potential with the maximal CaV-current was fitted with a double exponential equation ($y=y_0 + A_1\exp [(-(x-x_0))/\tau_1] + y_0 + A_2\exp [(-(x-x_0))/\tau_2]$) to calculate the time constants of $\tau_{inact,fast}$ and $\tau_{inact,slow}$.

T-type expressing cells were measured with other protocols due to the different channel kinetics. The holding potential (V_h) was set to -80 mV to prevent continuous activation of the channels. For some experiments four different protocols were sequentially applied to each cell. In the ramp protocol the T-type CaV expressing cells were depolarized continuously from -100 mV to +100 mV over 50 ms. The ramps were repeated every 2 s. This protocol was used to analyze the current-voltage relationship and for drug application (Figure 11 A). The ramp protocol was followed by a step protocol, where the cell was clamped in 10 mV steps from -90 mV to +70 mV for 200 ms per step (Figure 11 B). Furthermore, the current during the repolarization, the tail current, was measured

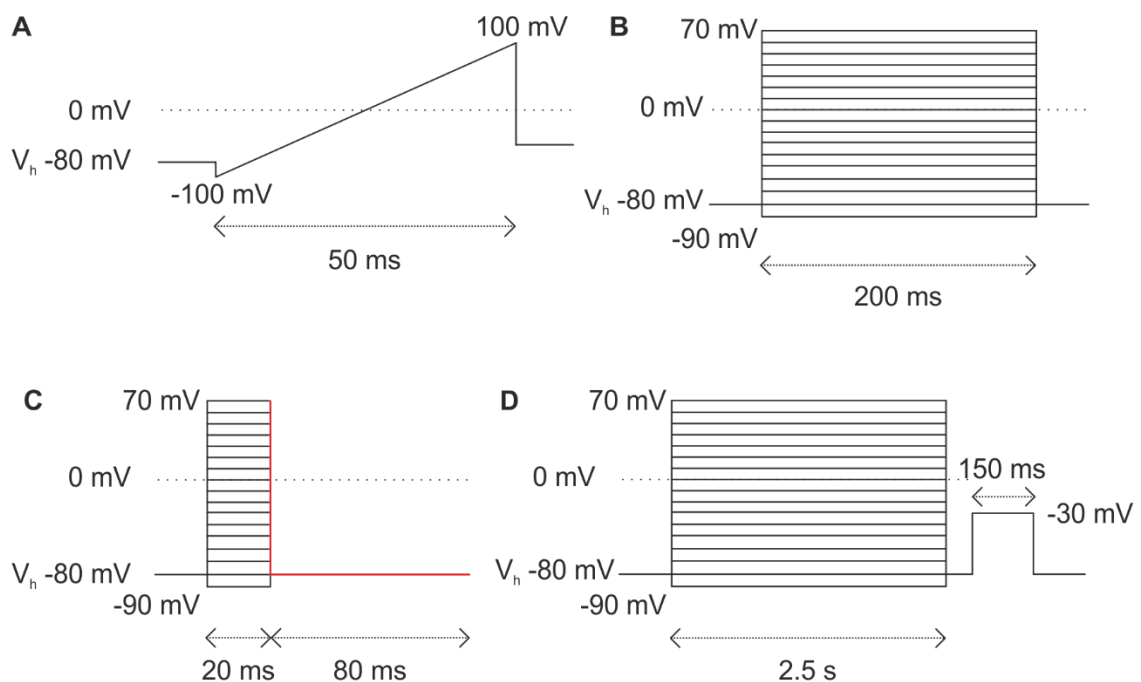


Figure 11 Protocols for current recordings of T-type voltage-gated calcium channels. T-type CaV-expressing cells were investigated with a series of four protocols. The cells were clamped to a holding potential (V_h) of -80 mV. **A** Ramp protocol: the cell was clamped continuously from -100 mV to +100 mV over 50 ms (used to generate the current-voltage relationship). **B** Step protocol: depolarization of the cells in 10 mV steps from -90 mV to +70 mV for 200 ms each step. Between the steps cells were clamped to -80 mV. **C** Tail protocol: a modified step protocol, where the cell was depolarized from -90 mV to +70 mV. Each step lasts 20 ms and is followed by an 80 ms depolarisation to -80 mV (red lines). **D** Inactivation step protocol: a modified step protocol with a duration of 2.5 s each step followed by a step to -30 mV for 150 ms after every step.

with a modified step protocol. The cell was clamped from -90 mV to +70 mV (in 10 mV steps) for 20 ms followed by an 80 ms depolarization to -80 mV after each step (Figure 11 C). The inactivation kinetics of the CaV channel was measured with a depolarization from -90 mV to +70 mV over 2.5 s followed by a step to -30 mV for 150 ms (Figure 11 D). The voltage of -30 mV was chosen because at this voltage the T-type CaV channels reveal their maximum current amplitude.

2.7.2 Two-electrode voltage clamp technique

Using the two-electrode voltage clamp (TEVC) configuration, the membrane potential of a cell is kept constant at a desired value, while the required current for this is measured. To do this, two electrodes are used, from which the name of the technology derived. The membrane potential was measured with the help of a reference electrode and by the current electrode, the current, necessary to maintain the defined potential, was injected (Deitmer and Schild, 2000). The reference electrode as well as the current electrode were connected with the amplifier (TEV-200A voltage clamp, Cornerstone, Dagan Corporation) via a pre-amplifier (Dagan Corporation). The detected signals were digitized via the digitizer Digidata 1320a (Axon Instruments) and recorded on a PC with the software Clampex 9.2 (Axon™ pCLAMP®, Axon Instruments), which also controlled the voltage clamp.

2.7.2.1 TEVC set-up

In parallel, TRPC1 and TRPC4 expression studies were performed in *Xenopus laevis* oocytes. The method is described here; the results are summarized in the Appendix, point 5.2.

The entire experimental set up was in a Faraday cage, which shields the measurements from external electrical noise. In this Faraday cage a binocular microscope and the measuring chamber, which has an inlet and an outlet for the solution perfusion, were located. Moreover, the measuring chamber contained the bath electrode, which closed the circuit between measuring chamber and amplifier and which was used to ground the chamber. Two micromanipulators were used to control the electrodes.

2.7.2.2 Experimental procedure and protocols for TEVC

The reference and the current electrode (Premium Thin Wall Borosilicate with Filament, G100TF-6, Warner Instruments, Holliston, USA) were dipped in the measuring solution

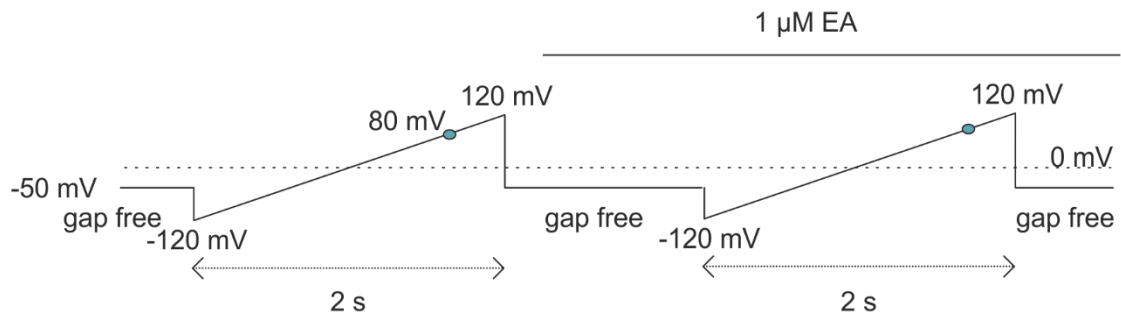


Figure 12 TEVC protocol. The oocytes were clamped to -50 mV (gap free protocol) followed by a ramp protocol where the membrane was continuously clamped from -120 mV to 120 mV within 2 s. Afterwards the gap free protocol was started and 1 μ M EA was applied until the maximal current was reached. To obtain the current-voltage relationship in the presence of EA, the ramp protocol was used. The blue dots indicate the current at +80 mV, which was used for statistical analysis.

and the circuit was set to 0 mV. Afterward both electrodes were stabbed into an oocyte, the cell membrane was clamped to -50 mV and the measurement started. Two protocols were used: a gap free and a ramp protocol. The gap free protocol was used first. Here the oocyte was clamped to -50 mV and the current was continuously recorded. After 30 s the ramp protocol was started to obtain the current in the standard solution (STD; 100 mM NaCl, 2 mM KCl, 0.5 mM MgCl₂, 10 mM HEPES, pH 7.5). The oocyte was continuously clamped during the ramp protocol from -120 mV to 120 mV within 2 s before returning to the gap free protocol. Then 1 μ M Englerin A (EA) was perfused over the oocyte to activate the expressed TRPC channels until the current reached a plateau. At the plateau the ramp protocol was started to register the current-voltage relationship in the presence of EA (Figure 12). The current at +80 mV was extracted for further analysis and plotted versus time.

2.8 Analysis, graphing and statistics

The analysis of the patch clamp experiments was done with IGOR Pro 6.31 (WaveMetrics), Microsoft Excel (Microsoft Corporation, Redmond, USA) and OriginPro 8.6 (Microcal Software Inc., Northampton, USA). TEVC experiments were analyzed with the clampfit 11.0.3 software (Axon Instruments), Microsoft Excel and OriginPro 8.6.

Western Blots of the oocytes were analyzed with the software Image Lab (BioRad).

All graphical representations of the data were prepared with CoreIDRAW X7 (Corel Corporation, Ottawa, Canada).

Statistical analysis of the data was performed with the softwares Microsoft Excel (Microsoft Corporation) and OriginPro 8.6 (Microcal Software Inc.). Depending on the number of groups to be compared, either a Student's t-test or one-way ANOVA followed by the Bonferroni correction were applied. Significances were indicated with asterisks or

pound key (*; # $p \leq 0.05$; **; ## $p \leq 0.01$; ***; ### $p \leq 0.001$), while not significant differences were labeled with non-significant (ns; $p > 0.05$).

Results

3.1 Electrophysiological characterization of canonical Transient Receptor Potential (TRPC) channels

3.1.1 Electrophysiological properties of TRPC1

The function of TRPC1 is still not solved and there is a debate if TRPC1 is a functional ion channel. Therefore, TRPC1, the very long version, was overexpressed in HEK-cells and it has been tried to activate the channel with Englerin A (EA), a potent TRPC4 and TRPC5 agonist. However, no EA-induced current was detectable (Figure 13 A), although the protein was expressed (Figure 13 B). In cells expressing TRPC4 or TRPC5, EA induced robust double rectifying currents with a “s” shaped current-voltage relationship (Figure 13 C, E). In HEK-cells expressing TRPC1 with TRPC4 or TRPC5, an EA-induced current was measured (Figure 13 D, F left), but the presence of TRPC1 together with

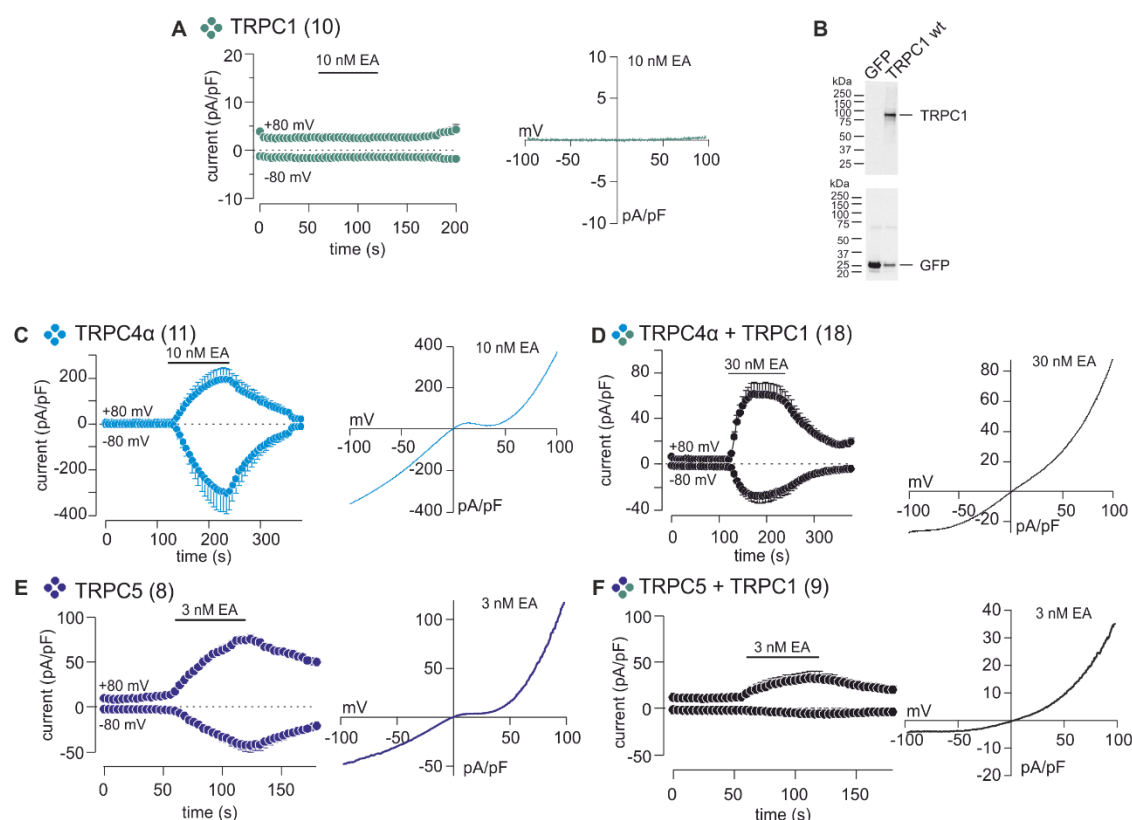


Figure 13 Electrophysiological properties of TRPC1. **A** Current in TRPC1 expressing cells at +80 mV and -80 mV over time. Englerin A (EA) application is indicated by the bar on top of the current (left) and current-voltage relationship (right). **B** Western Blot of HEK-cells transfected with GFP (control) and TRPC1, both detected by the corresponding antibody. **C-F** Current at +80 mV and -80 mV plotted over time (left panels) of TRPC4 α (**C**), TRPC4 α /TRPC1 (**D**), TRPC5 (**E**) and TRPC5/TRPC1 (**F**) expressing HEK-cells with the corresponding current-voltage relationships (right panels) in the presence of EA. Data are represented as means \pm SEM (left panels of A, C-F) and as mean (right panels of A, C-F). Number of experiments are shown in parenthesis.

TRPC4 or TRPC5 changed the current-voltage relationship of the TRPC4 α and TRPC5 channels to a soup ladle like shape (Figure 13 D, F right). These results demonstrate, that TRPC1 by itself does not form homotetrameric channels, which can be activated by EA. However, if present as a subunit in heterotetrameric TRPC4 α /TRPC1 or TRPC5/TRPC1 channels, TRPC1 is essential for the channel function contributing to the ion permeating pathway.

3.1.2 Effect of Englerin A on the heteromeric TRPC4 α /TRPC1 channel

Akbulut and colleagues described the very potent TRPC4 and TRPC5 direct agonist Englerin A (EA) extracted from the tree *Phyllanthus engleri* [Akbulut *et al.*, 2015]. Figure 14 shows the dose-dependent activation of TRPC4 α /TRPC1 channels by EA. The TRPC4 α /TRPC1 current at +80 mV (outward) and -80 mV (inward) was plotted against time. EA induced in- and outward currents in TRPC4 α /TRPC1 expressing cells, in a dose-dependent manner with an EC₅₀ of 20.09 nM (+80 mV) and 23.84 nM (-80 mV; Figure 14 C, D). While 0.1 nM EA had no effect on the TRPC4 α /TRPC1 current (outward 0.69 ± 0.73 pA/pF; inward -0.12 ± 0.2 pA/pF, $n = 6$), 1 μ M EA induced an outward current of 136.45 ± 22.64 pA/pF and an inward current of -73.31 ± 15.82 pA/pF, ($n = 7$). A robust TRPC4 α /TRPC1 current was already induced by 10 nM (outward 47.64 ± 13.47 pA/pF; inward -20.40 ± 8.58 pA/pF; Figure 14 A). The current-voltage relationship of heteromeric

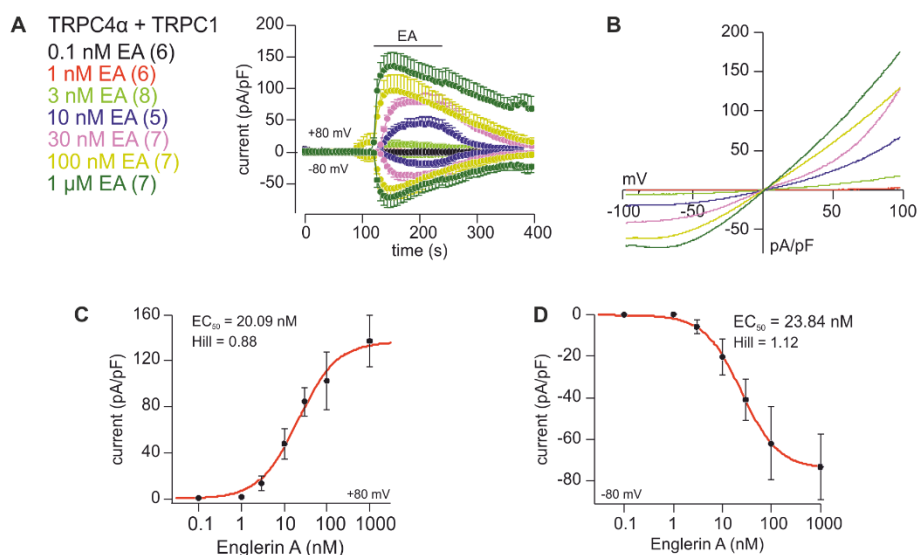


Figure 14 EA-induced currents in TRPC4 α /TRPC1 expressing HEK-cells. **A** In- and outward currents at -80 mV and +80 mV, respectively, extracted from 400 ms voltage ramps spanning from -100 mV to 100 mV ($V_h = 0$ mV) in HEK-cells stably expressing the μ -opioidreceptor (μ OR), TRPC4 α and TRPC1, plotted versus time. The bar indicates application of different Englerin A (EA) concentrations. **B** Current-voltage relationships of maximal currents in A. **C**, **D** Dose-response relationship of outward (C) and inward (D) current amplitude and the applied EA concentration. Data are shown as means \pm SEM (A, C, D) and as mean (B). Numbers in parenthesis represent number of experiments. Current-voltage relationships are shown as netto current with basal current subtracted.

TRPC4 α /TRPC1 currents revealed a soup ladle shape, which was independent of the EA concentration (Figure 14 B). For further experiments, 10 nM or 30 nM were used to activate TRPC4 α /TRPC1 heteromeric channels.

3.1.3 Mutations of the putative lower gate of TRPC1

In TRPC4 α the isoleucine at position 617 (I617; Figure 15 in red) was described as the single-residue gate in S6. A mutation of I617 to asparagin resulted in an increased TRPC4 current. This isoleucine is in the conserved LIAM motif (Figure 15 bold) and is suggested to be important in the channel gating [Zheng *et al.*, 2018]. To study the contribution of TRPC1 to the TRPC4/TRPC1 channel pore, the valine residue 741 (V741) corresponding to I617 in TRPC4 (Figure 15) was replaced by alanine. In addition, residues M743 and L744 of the LIAM motif in TRPC1 (Figure 15 A, Figure 16 A, B) were replaced by alanine. The single mutants were cloned and coexpressed with TRPC4 α . The application of 10 nM EA induced a robust current (Figure 16) with a typical soup ladle like current-voltage relationship of TRPC4 α /TRPC1 channels. However, the coexpression of TRPC4 α with TRPC1 V741A led to a significantly increased outward (wt



Figure 15 Alignment of TRPC channels. Alignment of the S4-S5 linker to the TRP helix of mouse TRPC1, TRPC2, TRPC3, TRPC4, TRPC5, TRPC6 and TRPC7 including S5, pore loop and S6. The mutations in the putative lower gate of TRPC1 are indicated by arrows (F639T; M642Q; V741 A, N, Q, S, T, G; M743A; L744A; E755S). TRPC1 is highlighted in gray.

115.29 ± 30.49 pA/pF, n = 18; V741A 247.82 ± 34.77 pA/pF) and inward current (wt -77.53 ± 24.38 pA/pF; V741A -169.33 ± 22.09 pA/pF; Figure 16 C, D). EA induced, independent of the TRPC1 mutant, an outward (wt 115.29 ± 30.49 pA/pF, n = 18; M743A 126.39 ± 17.49 pA/pF, n = 12; L744A 91.94 ± 20.92 pA/pF, n = 13) and inward current (wt -77.53 ± 24.38 pA/pF; M743A -100.74 ± 16.66 pA/pF; L744A -72.59 ± 18.62 pA/pF; Figure 16 C). However, the coexpression with one of these TRPC1 mutants led to a changed current-voltage relationship of the TRPC4 α /TRPC1 current. The current was not anymore shaped like the typical soup ladle TRPC4 α /TRPC1 current, but had the typical homomeric TRPC4 current-voltage relationship (Figure 16 C). Furthermore, valine 741 was exchanged by the bigger amino acid residue glutamine (Q). The change to glutamine resulted in a reduced EA-induced outward current (V741Q 17.95 ±

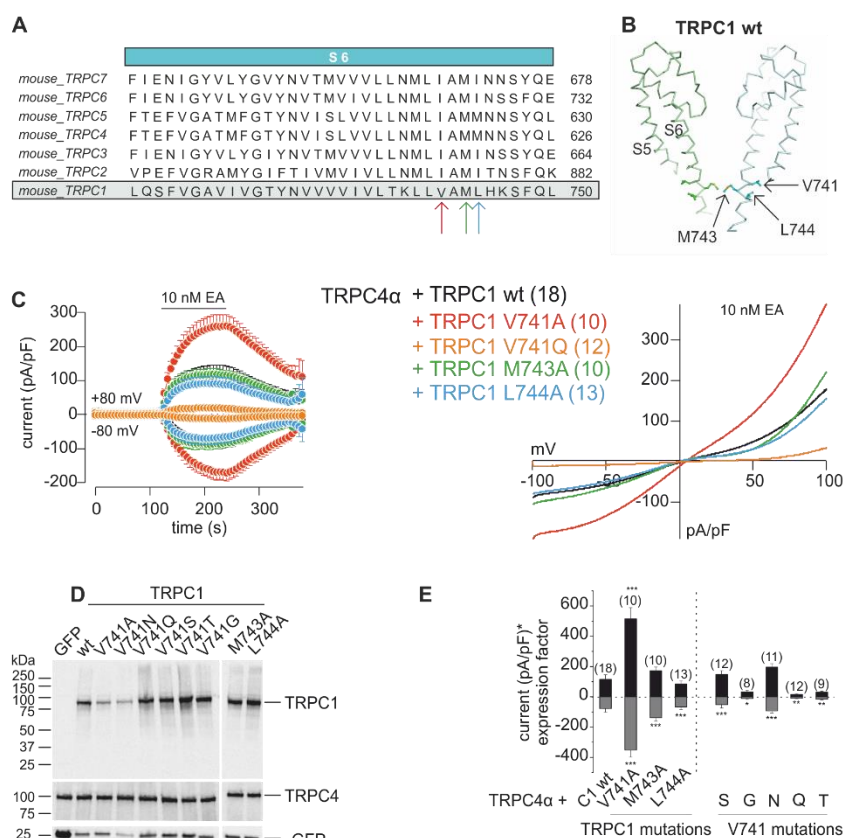


Figure 16 Mutations within the LIAM motif of TRPC1. **A** Alignment of the S6 from TRPC channels with TRPC1 marked in gray. The mutations are indicated by arrows (V741 in red, M743 in green, L744 in blue). **B** Proposed structure of TRPC1 wt based on the cryo-EM structure of human TRPC3 [Tang *et al.*, 2018] and the mutated residues are indicated by arrows. **C** Currents at +80 mV and -80 mV (left panel) in cells coexpressing TRPC4 α with TRPC1 wt (black), TRPC1 V741A (red), TRPC1 V741Q (orange), TRPC1 M743A (green) and TRPC1 L744A (blue) with the corresponding current-voltage relationships (right panel). **D** Western Blot of TRPC1 wt, TRPC1 V741 mutants, TRPC1 M743 and TRPC1 L744 transfected into HEK-cells stably expressing TRPC4 α with GFP as a control. **E** The expression of the mutated TRPC1 proteins was normalized to the GFP expression and the expression factor was used to normalize the current to the protein expression. Data are shown as means ± SEM (C left, E) and as mean (C right). Numbers of experiments are indicated in parenthesis. The current-voltage relationships are shown as net currents (basal current was subtracted).

95 pA/pF, $n = 12$; wt 115.29 ± 30.49 pA/pF, $n = 18$) and inward current (V741Q -11.30 ± 2.48 pA/pF; wt -77.53 ± 24.38 pA/pF) compared to TRPC1 wt. Only the mutation of TRPC1 V741 had an impact on the heterotetrameric TRPC4/TRPC1 current amplitude: V741A increased and V741Q decreased the current amplitude (Figure 16 C).

The proteins of all mutants could be detected by Western Blot (Figure 16 D). The expression of the mutated TRPC1 proteins was normalized to the GFP expression and this expression factor was used to normalize the current to the protein expression. The coexpression of TRPC1 V741S or TRPC1 V741N tend to increase the TRPC4 α /TRPC1 outward current (V741S 164.01 ± 26.48 pA/pF, $n = 12$; V741N 167.66 ± 18.94 pA/pF, $n = 11$). However, the inward current tended to be reduced due to the presence of TRPC1 V741S (-57.33 ± 24.92 pA/pF) or unaffected in the case of TRPC1 V741N (-79.46 ± 11.23 pA/pF). The presence of either TRPC1 V741G or TRPC1 V741T tended to reduce the outward (V741G 46.25 ± 17.36 pA/pF, $n = 8$; V741T 39.39 ± 9.75 pA/pF, $n = 9$) and

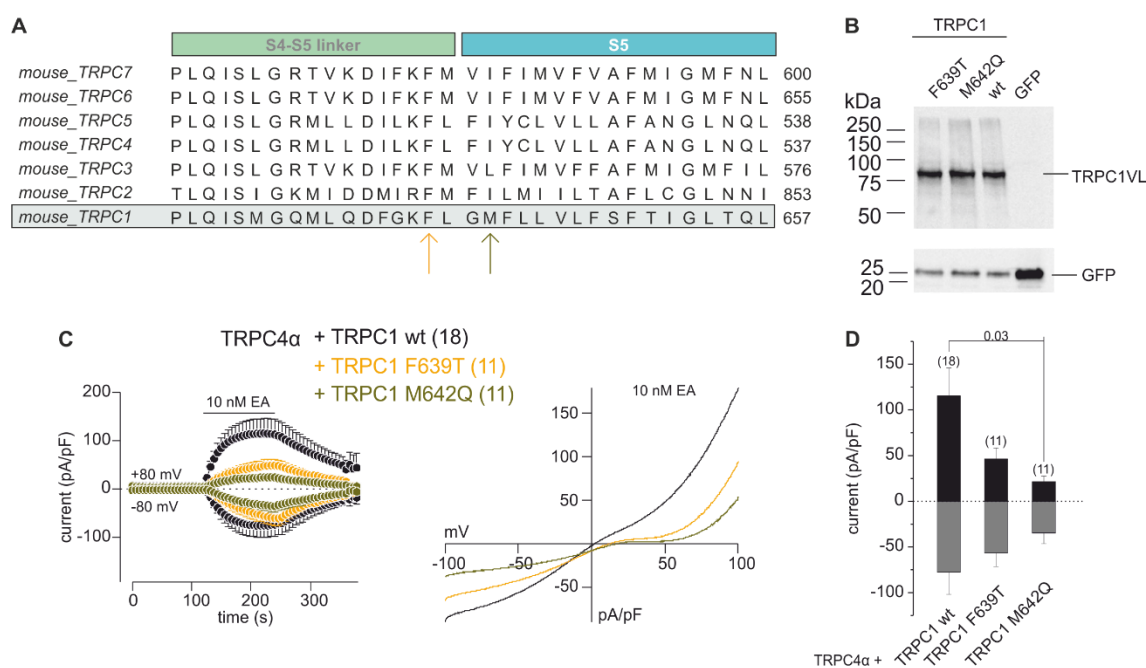


Figure 17 Mutation within the S4-S5 linker and the S5 of TRPC1. **A** Alignment of the S4-S5 linker and S5-transmembrane domain of all TRPC channel members (TRPC1-TRPC7) with TRPC1 highlighted in gray. Mutations of TRPC1 are labeled with arrows: phenylalanine (F) at position 639 was exchanged to threonine (T) in the S4-S5 linker (yellow) and the methionine (M) at position 642 was exchanged to glutamine (Q) in the S5-transmembrane domain (green). **B** Western Blot of TRPC1 wt, TRPC1 F639T and TRPC1 M642Q expression in TRPC4 expressing cells and GFP as a control. **C** EA-induced (10 nM) outward (+80 mV) and inward (-80 mV) currents of TRPC4 α coexpressed with either TRPC1 wt (black), TRPC1 F639T (yellow) or TRPC1 M642Q (green) plotted against the time (left panel) with the current-voltage relationship (right panel). **D** Maximal current amplitudes of TRPC1 wt, TRPC1 F639T and TRPC1 M642Q transfected into stably TRPC4 α expressing cells. All data are shown as mean \pm SEM (C left, D) and as mean (C right). Number of experiments are indicated in parenthesis, the number on top of the bar graph indicates the p-value (one-way ANOVA followed by the Bonferroni correction). Current-voltage relationships are shown as net current with subtracted basal current.

the inward current (V741G -17.48 ± 6.58 pA/pF; V741T -19.52 ± 6.64 pA/pF) of TRPC4 α /TRPC1 (Figure 16 E). The results suggest, that the valine at position 741 contributes to the pore function of heteromeric TRPC4/TRPC1 channels.

Furthermore, mutations within the S4-S5 linker and the S5-transmembrane domain of TRPC1 were analyzed (Figure 15; Figure 17). In the S4-S5 linker the phenylalanine (F) at position 639 was exchanged to threonine (T), while in the S5-transmembrane domain the methionine (M) at position 642 was exchanged to glutamine (Q) (Figure 15; Figure 17 A). Mutations of corresponding amino acid residues in TRPML1 [Dong *et al.*, 2009] and TRPV4 [Rock *et al.*, 2008] yielded constitutive active channels. In addition, the phenylalanine (F) of the S4-S5 linker is conserved among the TRPCs, whereas TRPC1 is the only TRPC family member with a methionine at the position 642 (Figure 15, Figure 17 A). Coexpression of TRPC1 F639T with TRPC4 α tend to reduce the EA-induced TRPC4 α /TRPC1 outward (wt 115.29 ± 30.49 pA/pF, n = 18; F639T 46.19 ± 12.28 pA/pF, n = 11) and inward (wt -77.53 ± 24.38 pA/pF; F639T -56.37 ± 15.04 pA/pF) current of the heteromeric channel (Figure 17 C, D).

Similarly, the coexpression of TRPC1 M642Q significantly reduced the TRPC4 α /TRPC1 outward current (21.46 ± 6.12 pA/pF, n = 11) as well as the inward current (-34.76 ± 1.79 pA/pF; Figure 17 C, D). Moreover, the presence of either TRPC1 F639T or TRPC1 M642Q had an impact on the current-voltage relationship of the heteromeric channels. Both TRPC1 mutants resulted in a typical TRPC4 current-voltage relationship instead of the typical soup ladle like shape of TRPC4/TRPC1 (Figure 17 C right panel). In summary, both mutants appear to prevent, that TRPC1 contributes to channel activity, although both mutant TRPC1 proteins were expressed (Figure 17 B).

The next mutation introduced into the TRPC1 cDNA is located in the TRP helix, where the glutamic acid (E) at position 755 was exchanged to a serine (S) and coexpressed with TRPC4 α (Figure 18 A, B). The EA-induced outward current in TRPC4 α /TRPC1 E755S expressing cells was slightly reduced (83.03 ± 19.58 pA/pF, n = 11) as compared to the outward current of TRPC4 α /TRPC1 wt cells (115.29 ± 30.49 pA/pF, n = 18), while the inward current was not changed (TRPC4 α /TRPC1 E755S -82.82 ± 26.89 pA/pF; TRPC4 α /TRPC1 wt -77.53 ± 24.38 pA/pF; Figure 18 C, D). However, coexpression of TRPC4 α and TRPC1 E755S changed the current-voltage relationship of the heteromeric TRPC4/TRPC1 channel, to a typical TRPC4 shape current and not the soup ladle like TRPC4/TRPC1 current (Figure 18 C right panel). Also, this mutant of TRPC1 appears not to contribute to the channel function.

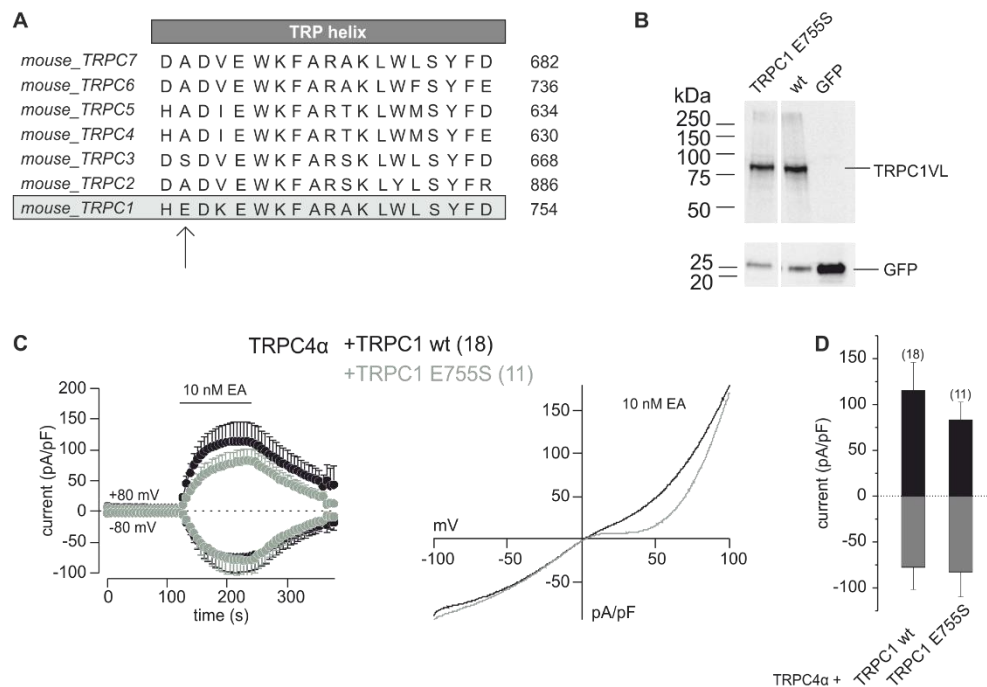


Figure 18 Mutation in the TRPC1 TRP helix. **A** Alignment of the TRP helix of all seven TRPC family members with TRPC1 highlighted in gray. The arrow indicates the glutamic acid (E) at position 755 of the TRPC1, which was exchanged to serine (S). **B** Western Blot of TRPC1 wt, TRPC1 E755S and GFP as a control TRPC4 α expressing. **C** EA-induced outward and inward current of stably TRPC4 α expressing cells transfected with TRPC1 wt (black) or TRPC1 E755S (olive green; left panel) and the current-voltage relationship of TRPC4 α /TRPC1 wt and TRPC4 α /TRPC1 E755S expressing cells (right panel). **D** Maximal outward (black; 80 mV) and inward (gray; -80 mV) current amplitudes of TRPC4 α /TRPC1 wt and TRPC4 α /TRPC1 E755S. In the left panel of C and D the data are shown as mean \pm SEM and in C (right) as mean. Number of experiments are indicated in parenthesis. Current-voltage relationships are subtracted from the basal current.

Summarized, the coexpression of TRPC1 V741A was the only mutation, which had an impact on the TRPC4/TRPC1 current. The outward and the inward current were significantly increased due to the coexpression of TRPC1 V741A without any impact on the shape of the current (Figure 16, Figure 19). However, the other TRPC1 mutants did not have any impact on the maximal current amplitude but TRPC1 F639T, TRPC1 M642Q, TRPC1 M743A, TRPC1 L744A as well as TRPC1 E755S had an impact on the shape of the current. All these mutations resulted in currents with the typical TRPC4 current-voltage relationship indicating that the mutant TRPC1 proteins are not part of the channel.

The only TRPC1 mutation with an impact on the TRPC4 α /TRPC1 current was TRPC1 V741A (Figure 16), therefore this mutation was studied more in detail. TRPC1 V741A was expressed in stably TRPC4 α expressing cells and also alone in μ OR-cells (Figure 20) and 5 μ M DAMGO/100 μ M CCh was used for activation. The μ OR stands for opioid

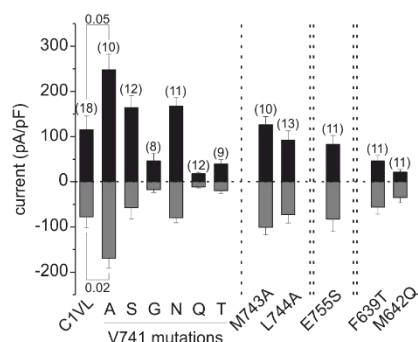


Figure 19 Summary of all TRPC1 mutations and their impact on TRPC4 α /TRPC1 currents. EA-induced outward (black, 80 mV) and inward (gray; -80 mV) currents of all used TRPC1 mutations compared to the TRPC1 wt in stably TRPC4 α expressing cells. Data are shown as means \pm SEM and numbers on top of the bars indicate the p-values (one-way ANOVA followed by Bonferroni correction), while the numbers in parenthesis represent the number of experiments.

receptor type μ , a $G_{i/o}$ -coupled receptor, which is stably expressed in the HEK-cell line and DAMGO specifically stimulates this receptor. Carbachol (CCh) stimulates the muscarinic m3 receptors (M3R), which is coupled to a $G_{q/11}$ -protein and which is endogenously present in HEK-cells. By applying DAMGO and CCh both, the $G_{i/o}$ and the $G_{q/11}$ pathways are activated. Both pathways are required to activate TRPC channels (Figure 4; Figure 20 A). Application of DAMGO/CCh induced robust outward (wt 106.08 ± 38.33 pA/pF, $n = 13$; V741A 194.71 ± 30.78 pA/pF, $n = 8$) and inward (wt -8.23 ± 5.84 pA/pF; V741A -23.17 ± 6.77 pA/pF) currents in TRPC4 α /TRPC1 wt as well as in TRPC4 α /TRPC1 V741A expressing cells (Figure 20 B, C), which tend to be increased in the presence of TRPC1 V741A without an impact on the current-voltage relationship (Figure 20 B right panel). These experiments confirmed the results obtained with EA (Figure 16).

Since coexpression of TRPC1 V741A with TRPC4 α led to increased EA- as well as DAMGO/CCh-induced currents, the current of TRPC1 V741A expressed in μ OR-cells alone was analyzed (Figure 20 D, E). Therefore, μ OR-cells were transfected with either TRPC4 α , TRPC1 wt or TRPC1 V741A and treated with 5 μ M DAMGO/100 μ M CCh. In TRPC4 α expressing cells, DAMGO/CCh induced a typical TRPC4 shaped current (outward 13.02 ± 1.72 pA/pF; inward -1.38 ± 0.4 pA/pF, $n = 6$), while in the TRPC1 wt as well as in TRPC1 V741A expressing cells no currents were detectable (Figure 20 D, E). Apparently, the TRPC1 wild-type and the TRPC1 V741A mutant significantly contribute to the functional pore of heterotetrameric TRPC4/TRPC1 channels, but do not form functional homotetrameric TRPC1 or TRPC1 741A channels. Because of these results we changed strategy as described in the following chapter.

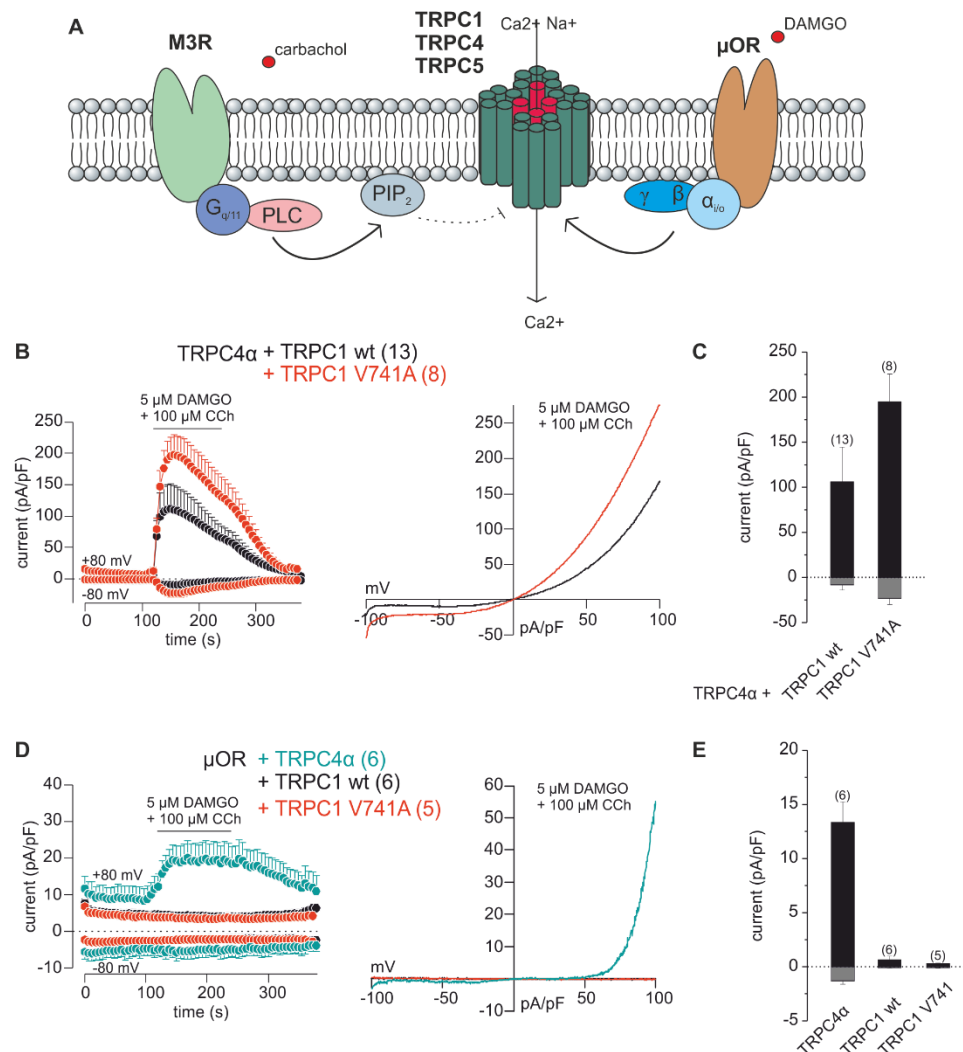


Figure 20 DAMGO/CCh-induced currents in the presence of TRPC1 V741A. **A** Scheme of GPCR stimulation of TRPCs. **B** Outward and inward currents of stably TRPC4 α expressing HEK-cells transfected with either TRPC1 wt (black) or TRPC1 V741A (red) induced by DAMGO/CCh (5 μ M/100 μ M; left panel). Current-voltage relationship of TRPC4 α /TRPC1 wt and TRPC4 α /TRPC1 V741A (right panel). **C** DAMGO/CCh-induced maximal current amplitudes of TRPC4 α /TRPC1 wt and TRPC4 α /TRPC1 V741A at +80 mV and -80 mV. **D** DAMGO/CCh-induced outward and inward currents of μ OR-cells transfected with either TRPC4 α (green), TRPC1 wt (black) or TRPC1 V741A (red; left panel). Current-voltage relationship of TRPC4 α , TRPC1 wt or TRPC1 V741A expressing μ OR-cells treated with 5 μ M DAMGO/100 μ M CCh (right panel). **E** Maximal current amplitudes of TRPC4 α , TRPC1 wt or TRPC1 V741A. Data are shown as mean \pm SEM (B left, C, D left, E) and as mean (right panels of B and D). Number of experiments are shown in parenthesis. Current-voltage relationships are shown as netto currents with basal currents subtracted.

3.1.4 Characterization of TRPC4-TRPC1_{S5-S6 linker} chimera

We cloned a cDNA construct where the pore-forming S5-S6 linker of TRPC4 α was replaced by the S5-S6 linker of TRPC1 (Figure 21 A, B). This TRPC4 α -C1 pore chimera was targeted to the plasma membrane, as shown by surface biotinylation of μ OR-cells transfected with either the TRPC1 or the chimeric TRPC4 α -C1_{S5-S6 linker} cDNAs. The presence of the chimera at the cell surface could be verified, and TRPC1 was also

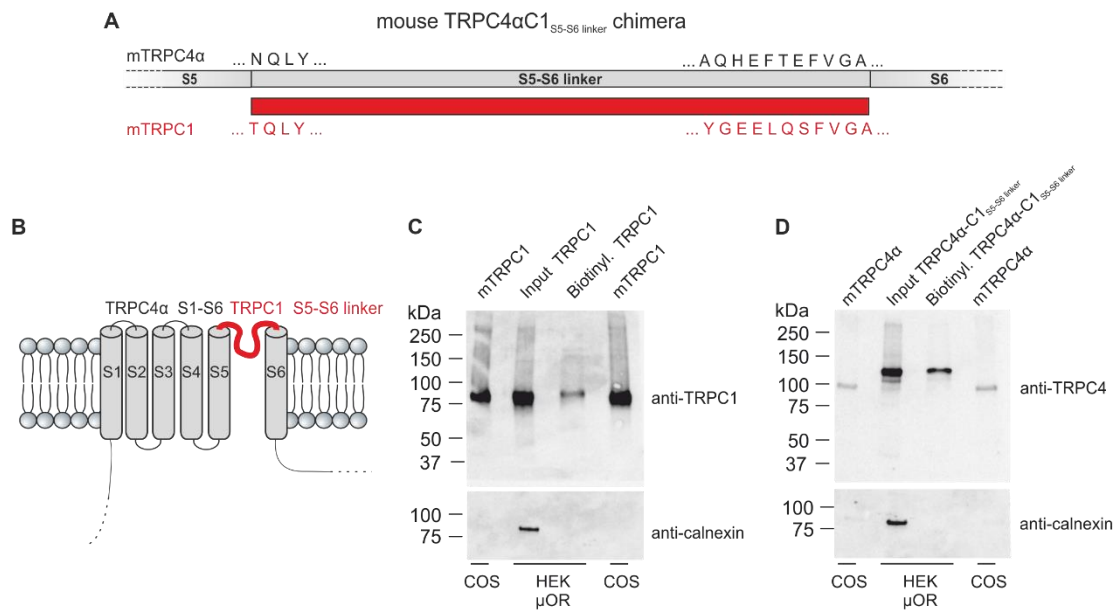


Figure 21 The TRPC4 α -TRPC1_{S5-S6 linker} chimera. **A** Scheme of the TRPC4 α -C1_{S5-S6 linker} chimera, where parts of TRPC4 α were exchanged by the homologues parts of TRPC1 (red). **B** Topology of the TRPC4 α -C1_{S5-S6 linker} chimera with the transmembrane domains S1-S6 from TRPC4 α (gray) and with the TRPC4 S5-S6 linker exchanged by the TRPC1_{S5-S6 linker} (red). **C, D** Cell surface biotinylation of TRPC1 (~80 kDa) and the TRPC4 α -C1_{S5-S6 linker} chimera (about 100 kDa) overexpressed in HEK μ OR-cells and detected with either TRPC1 or TRPC4 antibody. COS cells transfected with either TRPC1 or TRPC4 α -C1_{S5-S6 linker} served as a positive control for the used antibodies. The cytosolic housekeeping protein calnexin served as a control that biotin only bound to membrane-bound proteins.

detected in a lower amount in the plasma membrane (Figure 21 C, D). Since the TRPC4 α -C1_{S5-S6 linker} chimera was translocated to the plasma membrane, this construct was used for further analysis of the TRPC1 pore by patch clamp. μ OR-cells were transfected with TRPC4 α , TRPC1 or the TRPC4 α -C1_{S5-S6 linker} chimera for patch clamp experiments. TRPC4 α was activated by DAMGO/CCh with an outward current of 34.69 ± 6.39 pA/pF ($n = 7$) and an inward current of -2.39 ± 0.75 pA/pF (Figure 22 A, D) with the typical TRPC4 current-voltage relationship (Figure 22 B). In cells expressing the TRPC4 α -C1_{S5-S6 linker} chimera alone, DAMGO/CCh failed to induce a current (Figure 22 A, B, D) but a constitutive DAMGO/CCh-independent current was present from the beginning (Figure 22 A, B inset, C). The basal outward current (21.96 ± 5.28 pA/pF, $n = 6$) was significantly increased as compared to the break-in currents in TRPC4 (6.85 ± 0.88 pA/pF, $n = 7$) or TRPC1 (6.04 ± 0.83 pA/pF, $n = 6$) expressing cells. The basal inward current of TRPC4 (-2.96 ± 0.77 pA/pF, $n = 7$) and TRPC1 (-2.38 ± 0.54 pA/pF, $n = 6$) were significantly smaller compared to cells expressing the TRPC4 α -C1_{S5-S6 linker} chimera as well (-12.95 ± 3.52 pA/pF, $n = 6$; Figure 22 A, B inset, C).

The same experiments were performed using 10 nM EA instead of DAMGO/CCh and TRPC4 α -C1_{S5-S6 linker} chimera, TRPC4 α and TRPC1 were overexpressed in empty μ OR-

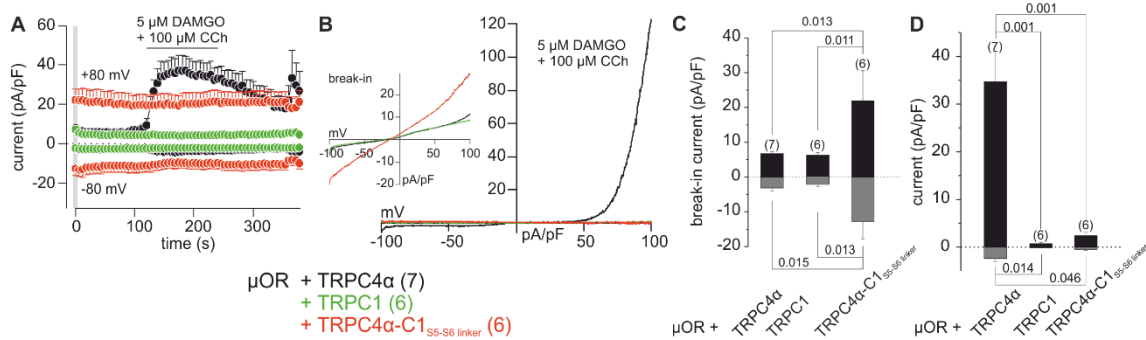


Figure 22 Effect of DAMGO/CCh on the TRPC4 α -C1_{S5-S6} linker currents. μ OR-cells transfected with TRPC4 α , TRPC1 or the TRPC4 α -C1_{S5-S6} linker chimera. **A** DAMGO/CCh-induced outward (at +80 mV) and inward (at -80 mV) currents of TRPC4 α (black), TRPC1 (green) or TRPC4 α -C1_{S5-S6} linker chimera (red) plotted against the time. **B** Current-voltage relationship of the DAMGO/CCh-induced current of TRPC4 α , TRPC1 or the TRPC4 α -C1_{S5-S6} linker chimera. The inset shows the break-in currents of the TRPC4 α -C1_{S5-S6} linker chimera compared to TRPC4 α and TRPC1 expressing cells. **C** Bar graph of the break-in currents. **D** Maximal outward (black) and inward (gray) current amplitude of TRPC4 α , TRPC1 and TRPC4 α -C1_{S5-S6} linker chimera expressing cells. Data are shown as means \pm SEM (A, C, D) and without SEM (B). Numbers in parenthesis indicate the number of experiments, while the numbers on top of the bars indicate the p-values (one-way ANOVA followed by Bonferroni correction). Currents in B are shown as net currents with basal currents subtracted. The gray bar in A indicates the break-in current shown as inset in B.

cells (Figure 23). Like in the experiments shown in Figure 22, the presence of the TRPC4 α -C1_{S5-S6} linker chimera led to an increased break-in outward current (TRPC4 6.75 ± 0.48 pA/pF, $n = 4$; TRPC1 10.24 ± 4.49 pA/pF, $n = 4$; chimera 21.95 ± 8.65 pA/pF, $n = 3$) and inward current (TRPC4 -3.14 ± 0.84 pA/pF; TRPC1 -5.47 ± 2.93 pA/pF; chimera -12.78 ± 4.97 pA/pF) as compared to TRPC4 α and TRPC1 (Figure 23 A, B inset, C). Although the break-in current was increased due to the TRPC4 α -C1_{S5-S6} linker chimera expression, EA failed to enhance this current further. Only in TRPC4 α transfected cells

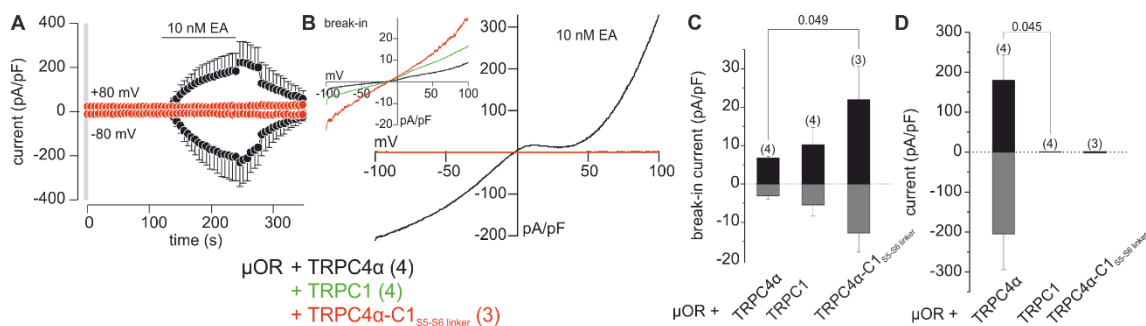


Figure 23 Impact of EA on TRPC4 α -C1_{S5-S6} linker chimera. μ OR-cells transfected with TRPC4 α , TRPC1 or the TRPC4 α -C1_{S5-S6} linker chimera. **A** EA-induced currents over time of TRPC4 α (black), TRPC1 (green) or TRPC4 α -C1_{S5-S6} linker chimera (red). **B** Current-voltage relationship of TRPC4 α , TRPC1 and TRPC4 α -C1_{S5-S6} linker chimera with the break-in currents in the inset. **D** Statistical analysis of the maximal current amplitudes. All data shown as mean \pm SEM (A, C, D) and without SEM (B). For statistical analysis one-way ANOVA followed by the Bonferroni correction was used and the p-values are indicated on top of the bars. Number of experiments are shown in parenthesis. Current-voltage relationships are subtracted by the basal current (B). The gray bar in A indicates the break-in current shown as inset in B.

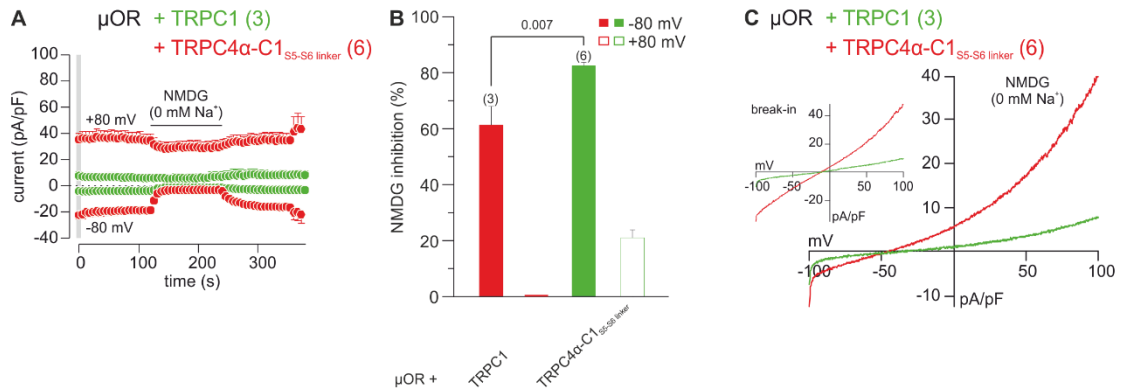


Figure 24 Effect of NMDG on the TRPC4α-C1_{S5-S6 linker} chimera current. **A** Current over time measured in μ OR-cells transfected with either TRPC1 (green) or the TRPC4α-C1_{S5-S6 linker} chimera (red). Application of NMDG saline is indicated by the bar. **B** Percentage of inhibition of the outward (black) and inward currents (gray) of TRPC1 and TRPC4α-C1_{S5-S6 linker} chimera due to NMDG-application. **C** Current-voltage relationship of TRPC1 and TRPC4α-C1_{S5-S6 linker} chimera due to the NMDG application with the break-in currents as inset. Data shown as mean \pm SEM (A, B) and as mean (C). One-way ANOVA followed by the Bonferroni correction was used for statistical analysis and the p-values are shown on top of the bars. Number of experiments are represented in parenthesis. The break-in currents shown as inset in C are indicated by the gray bar in A.

an outward (179.59 ± 64.62 pA/pF) and inward current (204.91 ± 89.5 pA/pF, $n = 4$) was recorded depending on the presence of EA (Figure 23 A, B, D).

In summary, the expression of the TRPC4α-C1_{S5-S6 linker} chimera always led to increased break-in currents independent of the presence of EA or receptor stimulation.

Since the break-in current was always enhanced in the presence of the TRPC4α-C1_{S5-S6 linker} chimera, the question rises if the measured current is just a leak in the plasma membrane. Therefore, sodium was exchanged to N-Methyl-D- Glucamine (NMDG) in the external solution. As seen before, the break-in current was increased in the TRPC4α-C1_{S5-S6 linker} chimera expressing cells (outward 36.28 ± 4.51 pA/pF; inward -21.75 ± 2.28 pA/pF, $n = 6$) as compared to the TRPC1 expressing cells (outward 7.09 ± 2.17 pA/pF; inward -4.15 ± 1.15 pA/pF, $n = 3$; Figure 24 A, C inset). However, the replacement of sodium by NMDG in the external solution led to an inhibition mainly of the inward currents. The effect was more prominent in the TRPC4α-C1_{S5-S6 linker} chimera expressing cells with an inhibitory effect of 82.48 ± 1.21 %, while in the TRPC1 expressing cells 61.24 ± 6.75 % of the current was inhibited. The outward current of TRPC1 expressing cells was not affected by the NMDG-solution, while 20.97 ± 2.82 % of the outward current was inhibited in TRPC4α-C1_{S5-S6 linker} chimera expressing cells (Figure 24 A, B, D). Furthermore, due to the absence of sodium ions in the external solution, the reversal potential was shifted to more negative potentials (TRPC1 Na⁺ -12.84 ± 0.57 mV; NMDG -33.39 ± 1.57 mV, $n = 3$; chimera Na⁺ -12.04 ± 0.34 mV; NMDG -45.01 ± 1.26 mV, $n = 6$; Figure 24 C). Since the replacement of sodium ions by NMDG resulted in an inhibition

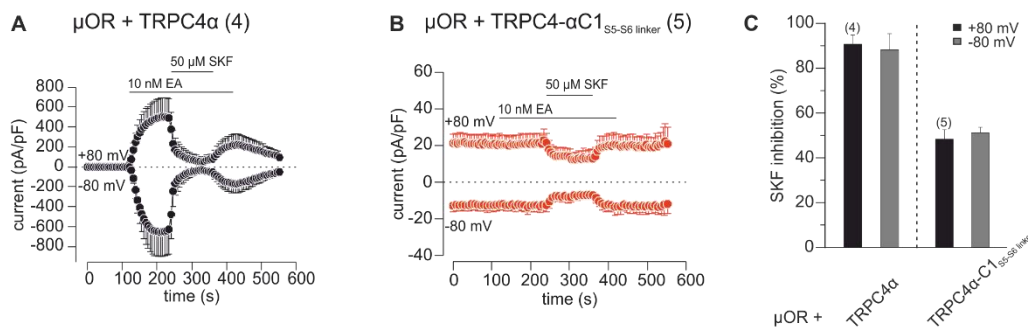


Figure 25 Effect of the non-specific TRP-blocker SKF on homomeric TRPC4 α and homomeric TRPC4 α -C1_{S5-S6 linker} chimera. **A** Current over time in TRPC4 α expressing cells in the presence of 10 nM EA. Application of 10 nM EA and 50 μ M SKF 96365 are indicated by the respective bars. **B** Outward and inward currents of cells expressing the TRPC4 α -C1_{S5-S6 linker} chimera with 10 nM EA and 50 μ M SKF 96365 application indicated by bars. **C** Inhibition of the EA-induced outward (+80 mV; black) and the inward (-80 mV; gray) current in the presence of 50 μ M SKF 96365. All data are shown as mean \pm SEM. Number of experiments are represented in parenthesis.

of the inward current, the increased basal current in TRPC4 α -C1_{S5-S6 linker} chimera expressing cells seemed to be no leak, but a real cation current.

For further proof that the measured basal current is mediated by a cation channel, i.e. TRPC channel, a non-specific TRP channel antagonist (SKF 96365) was used. For this experiments μ OR-cells were transfected with TRPC4 α as a control or with the TRPC4 α -C1_{S5-S6 linker} chimera and after the activation with 10 nM EA, 50 μ M SKF 96365 were applied (Figure 25 A, B). SKF 96365 inhibited the EA-induced TRPC4 α outward current (90.71 ± 4.12 %, $n = 4$) as well as the constitutive outward current in TRPC4 α -C1_{S5-S6 linker} chimera expressing cells (48.34 ± 4.24 %, $n = 5$). The inward currents were inhibited by SKF 96365 as well (TRPC4 88.16 ± 7.23 %; chimera 51.14 ± 2.56 %; Figure 25 C). All in all, the currents in TRPC4 α and in TRPC4 α -C1_{S5-S6 linker} chimera expressing cells were inhibited by SKF 96365, indicating that the TRPC4 α -C1_{S5-S6 linker} chimera like TRPC4 α forms SKF 96365 sensitive homomeric channels.

I also coexpressed the TRPC4 α -C1_{S5-S6 linker} chimera either together with TRPC4 α or with TRPC1. These data are described in the Appendix 5.3.1 and 5.3.3 and shown in Figures A3 (coexpression with TRPC4 α) and A6 (coexpression with TRPC1). In brief, the following results were obtained: Coexpressed with TRPC4 α the TRPC4 α -C1_{S5-S6 linker} chimera induces a constitutive current immediately after break-in. In the presence of DAMGO/CCh TRPC4 α /TRPC4 α -C1_{S5-S6 linker} channels were stimulated but to a smaller extent than homomeric TRPC4 α channels. In the presence of EA, the TRPC4 α /TRPC4 α -C1_{S5-S6 linker} current was increased compared to the homomeric TRPC4 α current (Figure A3). Coexpressed with TRPC1 the TRPC4 α -C1_{S5-S6 linker} chimera induces a constitutive

current immediately after break-in, which cannot be enhanced further by DAMGO/CCh or EA (Figure A6).

For the previous experiments the long version of TRPC4 (TRPC4 α) was used. For the following experiments, two different variants of the S5-S6 linker of TRPC1 were cloned into the short TRPC4 version (TRPC4 β). TRPC4 β has been reported to show much stronger current responses to PLC-coupled receptor activation than TRPC4 α [Schaefer et al., 2002]. We therefore replaced the S5-S6 linker of TRPC4 β by the corresponding linker of TRPC1 (Figure 26 A top) as shown for TRPC4 α in Figure 21 A. This TRPC4 β -C1_{S5-S6 linker} was called chimera 1. In a second chimera, chimera 2, the S5-S6 linker plus transmembrane segment 6 of TRPC4 β was replaced by the corresponding domains of

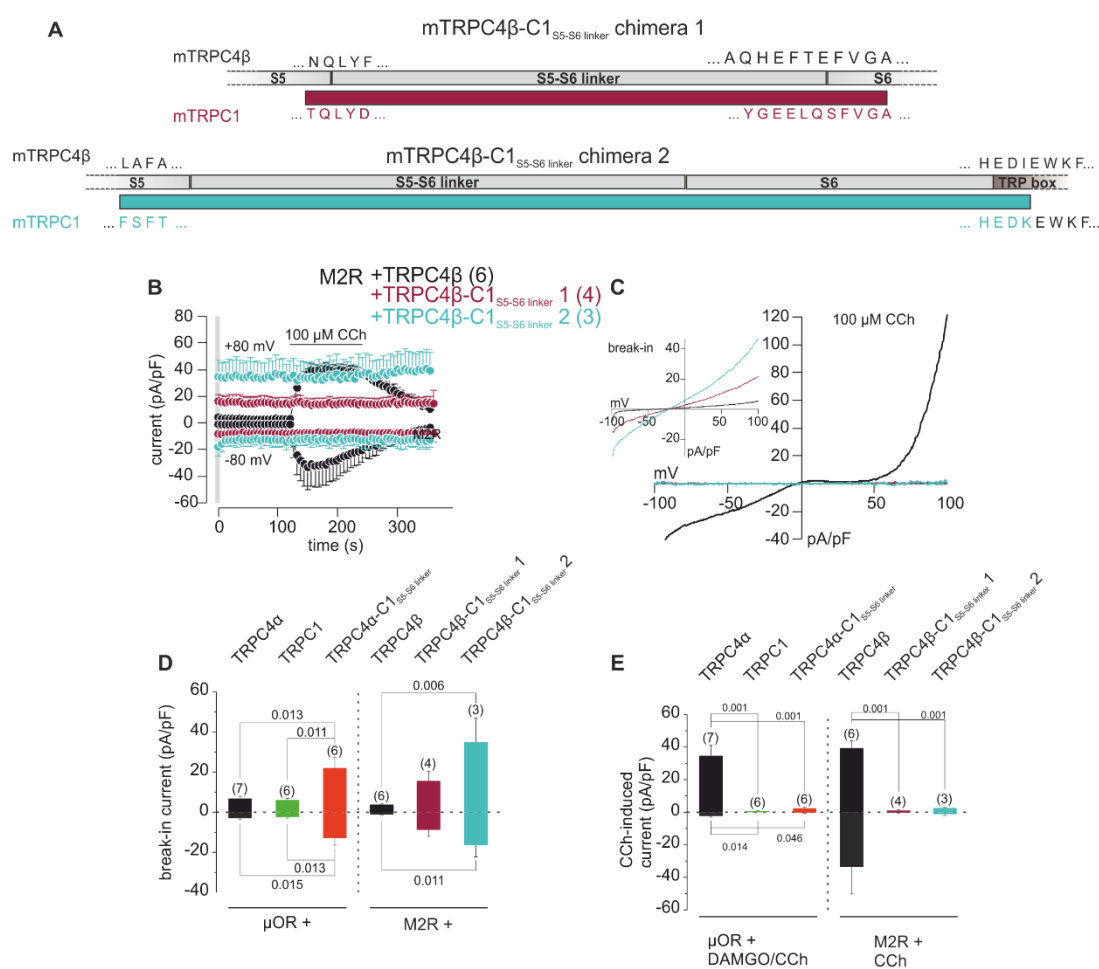


Figure 26 CCh-induced currents through TRPC4 β -C1_{S5-S6 linker} chimera. **A** Scheme of the TRPC4 β -C1_{S5-S6 linker} 1 (purple) and the TRPC4 β -C1_{S5-S6 linker} 2 (blue) chimera, where parts of TRPC4 β were exchanged by the homologous parts of TRPC1. **B** The outward (+80 mV) and inward (-80 mV) current TRPC4 β , TRPC4 β -C1_{S5-S6 linker} 1 and TRPC4 β -C1_{S5-S6 linker} 2 chimera plotted over time. The bar indicates the application of 100 μ M CCh. **C** Current-voltage relationship of TRPC4 β , TRPC4 β -C1_{S5-S6 linker} 1 and TRPC4 β -C1_{S5-S6 linker} 2 chimera currents in the presence of 100 μ M CCh with the break-in currents in the inset. **D** Comparison of the break-in currents. **E** Maximal current amplitudes in the presence of the different chimeras. Data in B, D and E are shown as means \pm SEM and in C as mean. Number of experiments are indicated in parenthesis. The basal current was subtracted for the current-voltage relationship. Break-in currents shown in C as inset are represented in B by the gray bar.

TRPC1 (Figure 26 A bottom). These constructs were transfected into HEK-cells stably expressing muscarinic m2 acetylcholine receptor (M2R) and carbachol was used as an activator. After break-in the currents of TRPC4 β -C1_{S5-S6 linker} 1 chimera (outward 15.62 ± 4.05 pA/pF; inward -8.82 ± 2.81 pA/pF, n = 4) as well as of TRPC4 β -C1_{S5-S6 linker} 2 chimera (outward 34.99 ± 9.79 pA/pF; inward -16.49 ± 4.76 pA/pF, n = 3) expressing cells were increased compared to the break-in current of TRPC4 β expressing cells (outward 3.64 ± 0.45 pA/pF; inward -1.12 ± 0.29 pA/pF (Figure 26 D). This effect was stronger in cells expressing the TRPC4 β -C1_{S5-S6 linker} 1 chimera and the application of 100 μ M CCh could not enhance the current, just in TRPC4 β expressing cells a current was induced by CCh (outward 40.12 ± 3.85 pA/pF; inward -33.97 ± 15.25 pA/pF, n = 6; Figure 26 E).

3.1.5 TRPC1 function *in vivo*

To be able to identify TRPC1 expressing cells *in vivo* my colleague Dr. Ahsan Raza generated a TRPC1-IRES-Cre mouse strain as part of his PhD work. These mice express a bicistronic mRNA, which enables expression of two proteins, TRPC1 and IRES-Cre-recombinase. Mice of this strain were mated with eR26- τ GFP mice provided by Professor Ulrich Boehm of our institute. As shown in Figure 27 A, in the offspring, the Cre recombinase, only expressed in *Trpc1* positive cells, removes a floxed termination signal (stop, Figure 27 A) and as a result the τ GFP is expressed under control of the enhanced constitutive promoter. By this approach TRPC1-expressing cells can be visualized by their green fluorescence, for example in the pituitary (Figure 27 B). The presence of TRPC1 transcripts and protein in the pituitary was confirmed by PCR (Figure 27 C) and by Western Blot (Figure 27 D).

Since the green cells are all TRPC1 positive, the pituitary gland was dissociated to get single cells for patch clamp experiments. Dissociated cells from TRPC1-deficient pituitary gland were used as a control although they were non-green.

For optimal conditions different intracellular Ca²⁺ concentrations (0 μ M, 0.1 μ M, 0.3 μ M) were applied via the patch pipette (Figure 28 A, B, C) and 1 μ M EA was added to activate TRPC5. The EA-induced current slightly, but not significantly increased with the elevation of the intracellular Ca²⁺ concentration in TRPC1- τ GFP as well as in TRPC1-deficient pituitary cells (Figure 28 D). The currents in TRPC1- τ GFP pituitary cells were similar in the presence of 0 μ M (wt outward 48.82 ± 12.46 pA/pF; inward -12.85 ± 3.16 pA/pF, n = 13; KO outward 21.28 ± 7.66 pA/pF; inward -13.50 ± 4.74 pA/pF, n = 9) or 0.1 μ M Ca²⁺ (wt outward 47.19 ± 13.99 pA/pF; inward -16.75 ± 5.01 pA/pF, n = 16; KO outward 19.63

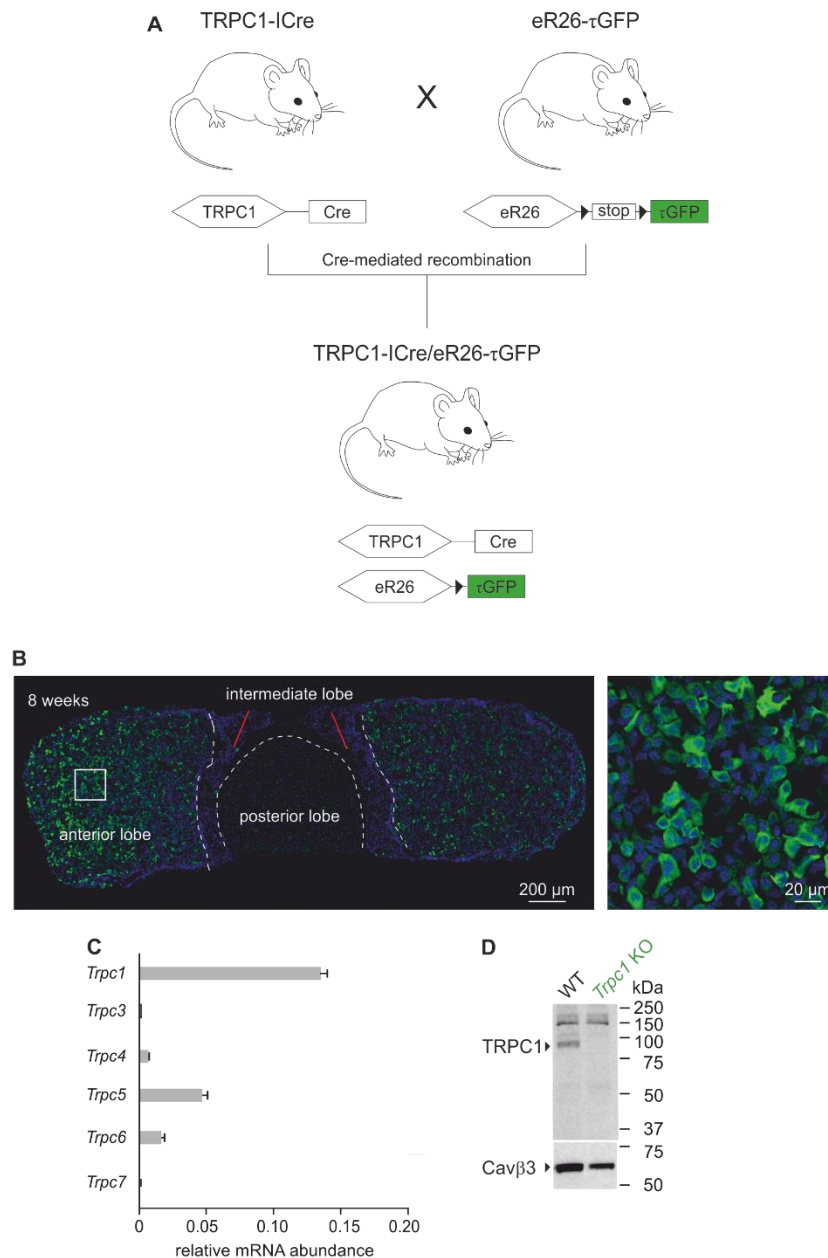


Figure 27 Visualizing TRPC1-expressing cells. **A** The TRPC1-IRES-Cre mouse, generated by Dr. Ahsan Raza in our own laboratory, was mated with the reporter mouse strain eR26-τGFP mouse by Cre-mediated recombination to get TRPC1-IRES/eR26-τGFP (see text). After Cre-recombinase mediated recombination in the offsprings, TRPC1-expressing cells are visualized by their green fluorescence. **B** Sections of TRPC1-IRES/eR26-τGFP pituitary gland with the anterior, posterior and the intermediate lobe of eight weeks old mice. The white box indicates the enlarged area on the right panel. Nuclei are shown in blue (DAPI). **C** Transcript expression of TRPC1, TRPC3, TRPC4, TRPC5, TRPC6 and TRPC7 in the pituitary gland of eight weeks old mice. **D** Western Blot of whole pituitary gland of wt and TRPC1-deficient mice. Cavβ3 was used as a loading control.

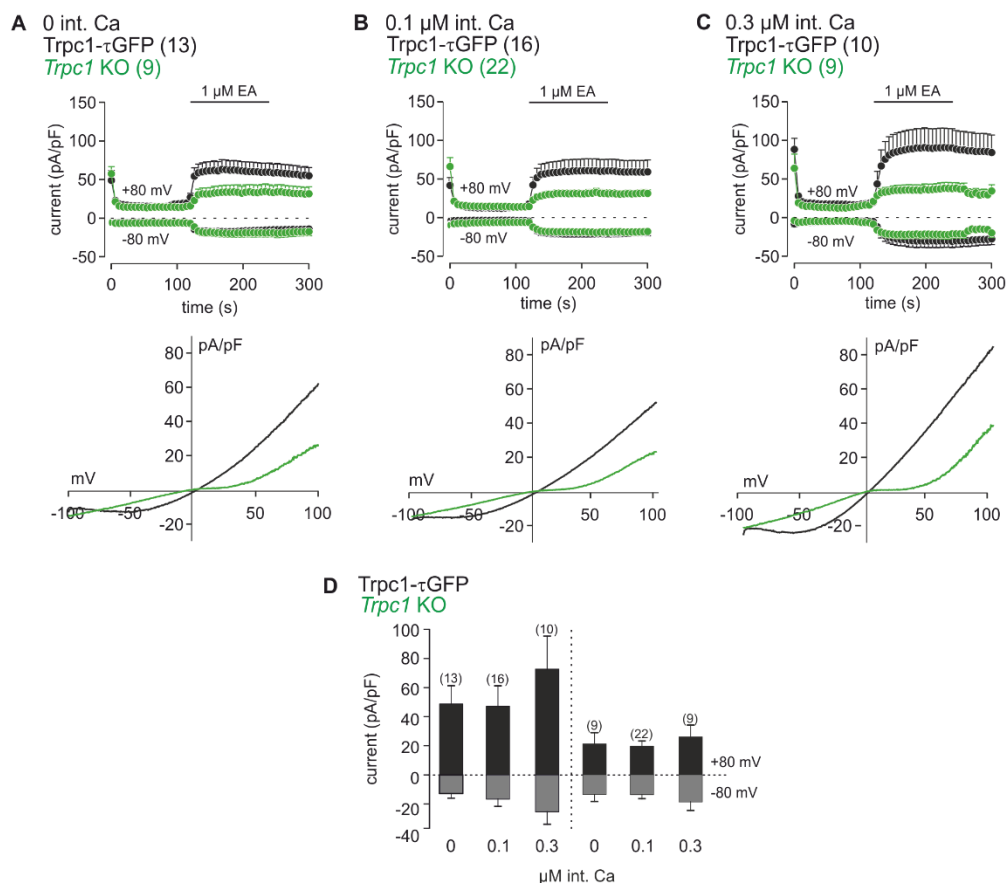


Figure 28 Impact of different intracellular Ca²⁺ concentrations on current in TRPC1-τGFP and TRPC1-deficient pituitary cells. TRPC1-τGFP and TRPC1-deficient pituitary glands were dissociated and used for patch clamp experiments. **A** Current over time (upper panel) and current-voltage relationship (lower panel) of TRPC1-τGFP (black) and TRPC1-deficient (green) pituitary cells in absence of intracellular Ca²⁺ (0 μM). **B** EA-induced current over time (upper panel) and corresponding current-voltage relationship (lower panel) in TRPC1-τGFP (black) and TRPC1-deficient (green) pituitary cells measured with 0.1 μM intracellular Ca²⁺. **C** Outward and inward currents (upper panel) and current-voltage relationship (lower panel) of TRPC1-τGFP (black) and TRPC1-deficient (green) pituitary cells activated by EA in the presence of 0.3 μM intracellular Ca²⁺. **D** Statistical analysis of the maximal outward (+80 mV; black) and inward (-80 mV; gray) currents in TRPC1-τGFP and TRPC1-deficient pituitary cells due to the different (0 μM, 0.1 μM, 0.3 μM) intracellular Ca²⁺ concentrations. Data in A, B, C (upper panel) and D are shown as means ± SEM and in A, B and C (lower panel) as mean. In parenthesis the numbers of experiments are indicated. For the current-voltage relationship the basal current was subtracted.

± 3.63 pA/pF; inward -13.59 ± 2.76 pA/pF, n = 22; Figure 28). However, 0.3 μM intracellular Ca²⁺ enhanced the EA-induced outward (wt 72.76 ± 22.67 pA/pF, n = 10; KO 26.18 ± 8.07 pA/pF, n = 9) and inward currents (wt -25.42 ± 8.52 pA/pF; KO -18.60 ± 5.86 pA/pF; Figure 28 D). The soup ladle current-voltage relationship in TRPC1-τGFP pituitary cells, suggested that a heteromeric TRPC5/TRPC1 channel was activated, because 1) it was EA-sensitive and 2) TRPC5 is the most abundantly expressed TRPC beyond TRPC1 (Figure 27 C). The TRPC1-deficient pituitary cells revealed a typical TRPC5 current-voltage relationship with the inward and outward rectifying currents.

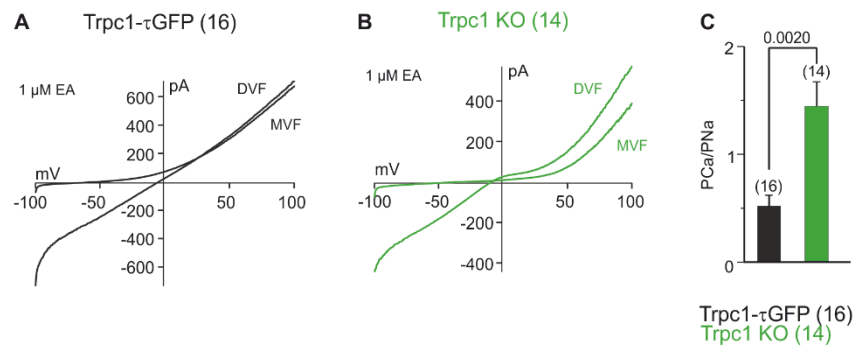


Figure 29 Ion permeability in TRPC1- τ GFP and TRPC1-deficient pituitary cells. A Current-voltage relationship measured in TRPC1- τ GFP pituitary cells during application of a divalent-free solution (DVF) together with 1 μ M EA followed by an application of a monovalent-free solution (MVF) together with 1 μ M EA. **B** Current-voltage relationship in TRPC1-deficient pituitary cells in the presence of 1 μ M EA either in a divalent-free solution (DVF) or a monovalent-free solution (MVF). **C** Ratio of Ca²⁺ over Na⁺ permeability (P_{Ca}/P_{Na}) calculated from the reversal potentials obtained in A and B for TRPC1- τ GFP (black) and TRPC1-deficient (green) pituitary cells. Data shown as mean \pm SEM in C and as mean in A and B. Numbers in parenthesis represent the number of experiments and on the top of the bar the p-value (one-way ANOVA followed by the Bonferroni correction).

Because, the EA-induced current was most prominent in the presence of 0.3 μ M intracellular Ca²⁺, this Ca²⁺ concentration was used for further experiments. To distinguish whether the channel in TRPC1-deficient cells has a different ion permeability than the channels in cells from wild-type animals, I determined the relative permeabilities for Ca²⁺ and Na⁺. To measure the Ca²⁺ over Na⁺ permeability through the heteromeric TRPC5/TRPC1 channels in TRPC1- τ GFP cells (corresponding to wild-type) and the homomeric TRPC5 channels in TRPC1-deficient cells, a monovalent-free (MVF) and a divalent-free (DVF) extracellular solution were applied and the currents were activated by EA. In TRPC1- τ GFP pituitary cells, the reversal potential was shifted to more negative potentials in the absence of monovalent ions (DVF -4.24 ± 0.69 mV; MVF -59.56 ± 3.94 mV, n = 16; Figure 29 A). The reversal potential in TRPC1-deficient pituitary cells was also changed in the same manner (DVF -10.32 ± 1.16 mV; MVF -39.96 ± 5.02 mV, n = 14; Figure 29 B). The current-voltage relationship of DVF + EA showed in TRPC1- τ GFP cells (corresponding to wild-type) more the heteromeric TRPC5/TRPC1 current-voltage relationship, while in TRPC1-deficient cells the current-voltage relationship was that of homomeric TRPC5 (Figure 29 A, B). The reversal potentials were used to calculate the relative Ca²⁺ permeability in TRPC1- τ GFP and TRPC1-deficient pituitary cells. The relative Ca²⁺ permeability ratio (P_{Ca}/P_{Na}) was significantly higher in TRPC1- τ GFP pituitary cells (0.53 ± 0.10 , n = 16) as compared to TRPC1-deficient pituitary cells (1.45 ± 0.22 , n = 14; Figure 29 C).

3.1.6 TRPC channels in murine osteoclasts

In addition to the pituitary, TRPC1 expression was also found in bone absorbing, multinucleate cells, the osteoclasts, induced from bone marrow derived stem cells and cultured by my colleague Dr. Ahsan Raza. The TRPC1- τ GFP osteoclasts do express the full-length 2679 bp TRPC1 transcripts (Figure 30 A) but I could not detect EA-induced currents by patch clamp recordings (Figure 30 B). Since, there are no agonists for homomeric TRPC1 channels, there was no possibility to proof the function of TRPC1 in osteoclasts by patch clamp recordings.

In addition, I applied OAG (100 μ M) to screen the osteoclasts for OAG-sensitive TRPC channels. Again, no currents could be recorded (Figure 30 C).

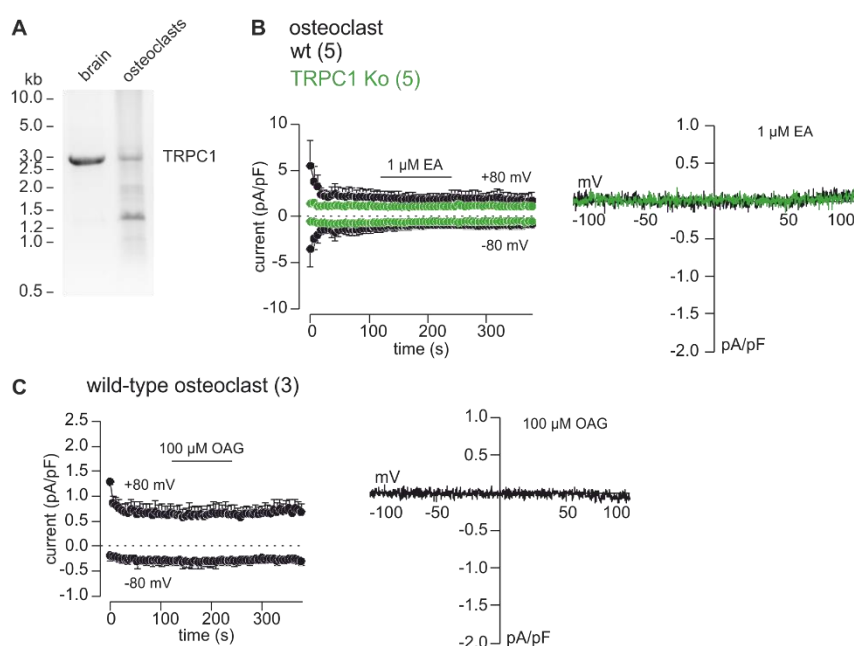


Figure 30 TRPC channels in osteoclasts. **A** PCR of osteoclasts and brain for TRPC1 mRNA. **B** Osteoclasts from TRPC1-ICre/eR26- τ GFP (black) and TRPC1-deficient (green) mice were used for patch clamp experiments. Outward and inward current over time of both genotypes due to the application of 1 μ M EA (left panel). Current-voltage relationship of both genotypes (right panel). **C** Current over time in the presence of 100 μ M OAG (left panel) with the corresponding current-voltage relationship (right panel). In the left panels of B and C data are shown as means \pm SEM and in the right panels of B and C as mean. Number of experiments are shown in parenthesis. Current-voltage relationships are shown as net OAG current (subtraction of the basal current).

3.2 Electrophysiological characterization of voltage-gated calcium channels

3.2.1 Characterization of L-type CaV currents

3.2.1.1 Interaction of CaV1.2 with different CaV β subunits

3.2.1.1.1 Impact of different CaV β 2 splice variants on CaV1.2

The L-type CaV1.2 channels need auxiliary proteins for the correct translocation of the ion conducting pore $\alpha 1$ to the plasma membrane and for its channel function. Four different CaV β -subunits interact with CaV1.2: CaV β 1, CaV β 2, CaV β 3, and CaV β 4 but in most tissues it is mainly CaV β 2 and CaV β 3. All CaV β proteins share the same domain

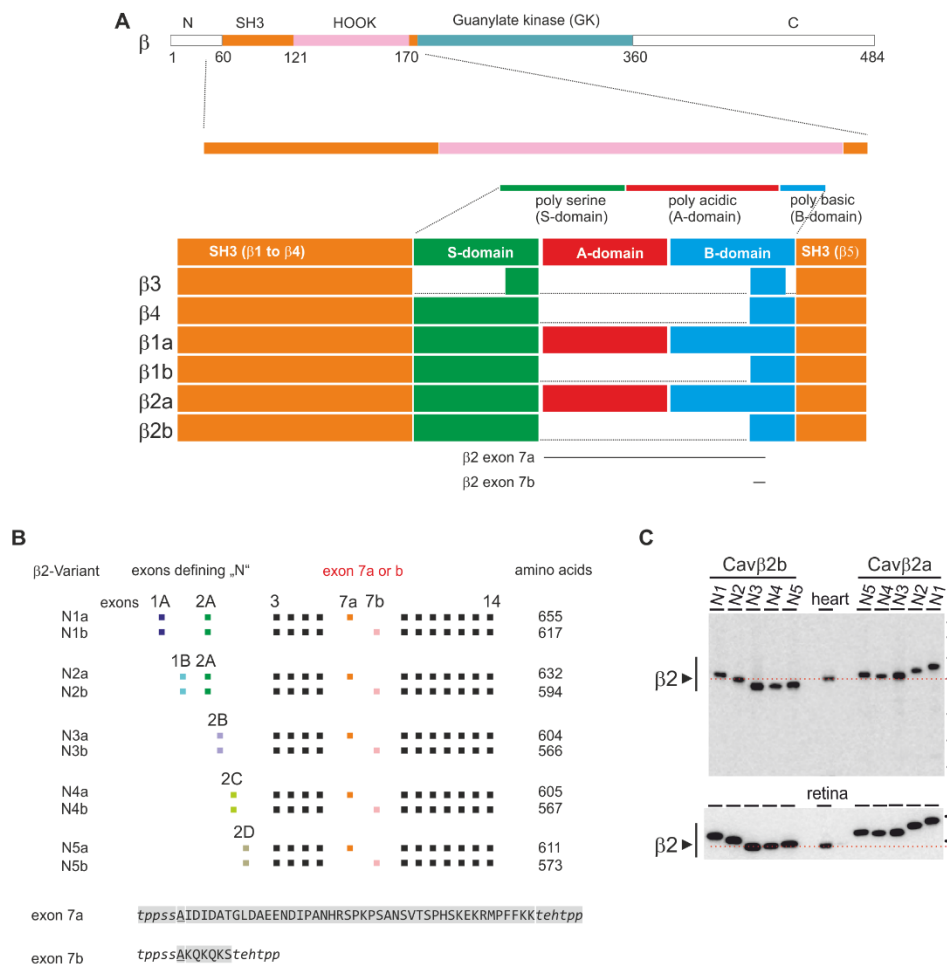


Figure 31 Protein domain and exon structure of CaV β subunits. **A** Structure of the CaV β subunit protein domains. The Src homology 3 (SH3, orange) is linked via the HOOK domain (pink) with the guanylate kinase module (GK, blue). The HOOK domain differs among the CaV β subunits in length of the poly serine (S-domain, green), poly acidic (A-domain, red) and poly basic (B-domain, blue). **B** Exon composition of the different CaV β 2 splice variants with the N defining specific exons encoding 5 different N-termini. Exon 7 exists in two variants, a and b. either variant is combined with each of the 5 N-termini yielding 10 CaV β 2 splice variants. **C** Western Blot of reconstituted CaV β 2 splice variants (altogether 10 according to **B**) and the CaV β 2 present in heart and retina. The reconstituted CaV β 2s were obtained by expressing the 10 variants in COS cells, followed by SDS PAGE and Western Blot. For example, in retina, only CaV β 2b variants, defined by exon 7, are present.

structure with a Src homology 3 module and a guanylate kinase module linked by a HOOK domain (Figure 31 A). They interact with CaV channels via the highly conserved SH3 region, while the HOOK region may be involved in the inactivation of the CaV channels [Richards *et al.*, 2007; Park *et al.*, 2017]. In this study the different CaV β 2 splice variants and their impact on the CaV1.2 were analysed. The CaV β 2 splice variants differ in their amino acid length and exon composition (Figure 31 B). Previously, Sabine Link from our group has shown that only the exon 7a is expressed in mouse heart yielding the CaV β 2a proteins [Link *et al.*, 2009]. Accordingly, CaV β 2N4a seemed to be the CaV β 2 splice variant in the heart, whereas the CaV β 2N3b and CaV β 3N4b are the main CaV β 2 subunits in the retina (Figure 31 C).

For patch clamp experiment HEK-cells stably expressing CaV1.2 were transfected with the different CaV β 2 subunit splice variants, CaV β 2N3a, CaV β 2N3b, CaV β 2N4a, and

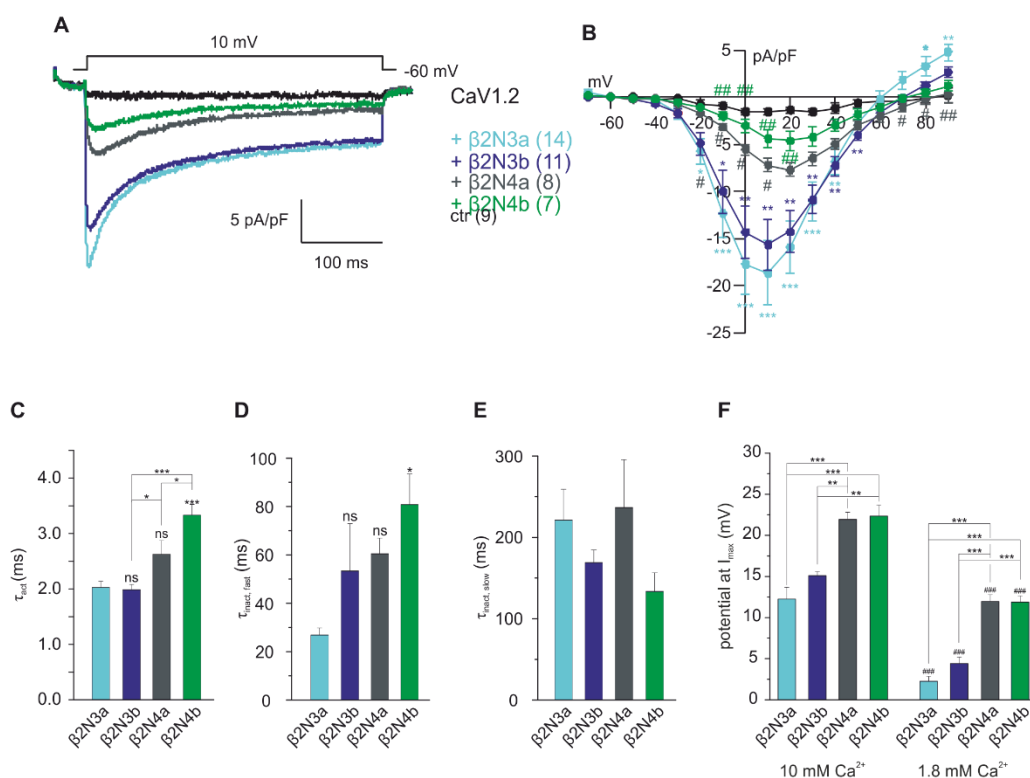


Figure 32 Impact of different CaV β 2 splice variants on CaV1.2. **A** Maximal calcium current at the voltage step to 10 mV of CaV1.2 (black) with CaV β 2N3a (light blue), CaV β 2N3b (dark blue), CaV β 2N4a (dark green) and CaV β 2N4b (light green). **B** Voltage dependent response to depolarization from -70 mV to +90 mV in 10 mV increments from a holding potential of -60 mV in CaV1.2 HEK-cells coexpressing different CaV β 2 splice variants. One-way ANOVA was used followed by Bonferroni correction for statistical analyses. Asterisks (*) indicate statistical differences to the control (ctr) and numbers (#) indicate statistical significance compared to CaV1.2/CaV β 2N3a coexpressing cells. **C** To analyze activation time constant (τ_{act}) of the current at 10 mV was fitted with a single exponential equation. **D** and **E** For inactivation kinetics (τ_{fast} and τ_{slow}) the decay phase of the current at 10 mV was fitted with a double exponential equation. **F** Potential at I_{max} in the presence of 10 mM or 1.8 mM external Ca^{2+} , were extracted from the response of the voltage ramps from -100 mV to 100 mV. Asterisks indicate statistical differences tested with one-way ANOVA followed by Bonferroni correction. HEK-cells coexpressing the same β subunit were tested with a Student's t-test. Statistical differences between 10 mM and 1.8 mM Ca^{2+} are indicated by numbers (#). Data are shown as mean \pm SEM (A, C, D, E, F) and as mean (A) and the number of analyzed cells indicated in parenthesis in A.

CaV β 2N4b (Figure 32) to investigate their impact on the CaV1.2 current. The CaV β 2 cDNAs were expressed as CaV β 2-IRES-GFP constructs in order to identify transfected cells by their green fluorescence. For controls, cells were transfected with IRES-GFP only, the “empty vector”. The CaV1.2 variant expressed here contained the short N-terminus encoded by exon 1b [Hofmann *et al.*, 2014], which is primarily expressed in smooth muscle and brain. Overexpression of all four CaV β 2 subunit splice variants significantly increased the CaV1.2 current compared to CaV1.2 currents obtained by α 1 alone (control; Figure 32 A). However, there were differences between CaV β 2N3 and CaV β 2N4 splice variants. The CaV1.2 current (control -1.59 ± 0.3 pA/pF, $n = 9$) in the presence of CaV β 2N3a (-18.66 ± 3.4 pA/pF, $n = 14$) and CaV β 2N3b (-15.63 ± 2.7 pA/pF, $n = 11$) had larger amplitudes as compared to the CaV1.2 current in the presence of CaV β 2N4a (-7.72 ± 0.73 pA/pF, $n = 8$) or CaV β 2N4b (-4.64 ± 1.04 pA/pF, $n = 7$; Figure 32 A, B).

Since L-type CaV channels belong to the high voltage activated (HVA) CaV channels, they are activated at -30 mV with a maximal current amplitude between 0 mV and 10 mV (Figure 32 A, B). Nevertheless, the time of activation (τ_{act}) was significantly increased in the presence of CaV β 2N4b (3.33 ± 0.19 ms, $n = 7$) as compared to the other CaV β 2 subunit splice variants (CaV β 2N3a: 2.03 ± 0.11 ms, $n = 14$, CaV β 2N3b: 1.98 ± 0.09 ms, $n = 11$, CaV β 2N4a: 2.62 ± 0.25 ms, $n = 8$; Figure 32 C). However, the time constants for the fast ($\tau_{inact fast}$, Figure 32 D) and slow ($\tau_{inact slow}$, Figure 32 D) inactivation of the channel were not changed in the presence of the CaV β 2 subunits (fast: CaV β 2N3a 26.93 ± 2.92 ms, $n = 14$; CaV β 2N3b 53.39 ± 19.52 ms, $n = 11$; CaV β 2N4a 60.45 ± 6.52 ms, $n = 8$; CaV β 2N4b 80.85 ± 12.62 ms, $n = 7$; Figure 32 D; slow: CaV β 2N3a 221.24 ± 37.97 ms, $n = 14$; CaV β 2N3b 169.13 ± 15.29 ms, $n = 11$; CaV β 2N4a 236.66 ± 58.82 ms, $n = 8$; CaV β 2N4b 133.67 ± 22.99 ms, $n = 7$; Figure 32 E). The L-type CaV channels have their maximal current amplitude at 10 mV. However, this potential was slightly different, depending on the expressed CaV β 2 subunits and on the external Ca $^{2+}$ concentration. In the presence of 10 mM external Ca $^{2+}$ CaV β 2N3a (12.25 ± 1.45 mV, $n = 14$) reached its maximum at the lowest potential while CaV β 2N4b (22.35 ± 1.32 mV, $n = 7$) revealed a significant higher potential at which the maximal current appeared (CaV β 2N3b 15.09 ± 0.5 mV, $n = 11$; CaV β 2N4a 21.94 ± 0.87 mV, $n = 8$). These potentials were reduced in the presence of 1.8 mM Ca $^{2+}$ (CaV β 2N3a 2.26 ± 0.59 mV, $n = 14$; CaV β 2N3b 4.41 ± 0.79 mV, $n = 11$; CaV β 2N4a 11.87 ± 0.76 mV, $n = 8$; CaV β 2N4b 11.97 ± 0.81 mV, $n = 7$; Figure 32 F). Altogether, CaV β 2N3 and CaV β 2N4 variants seem to differ in I_{act} and the potential of the maximal activation, and only I_{act} appeared to be different between the β 2N4a and β 2N4b variants.

Ca $^{2+}$ can inhibit the CaV channels, therefore Ba $^{2+}$ is often used for the measurements to

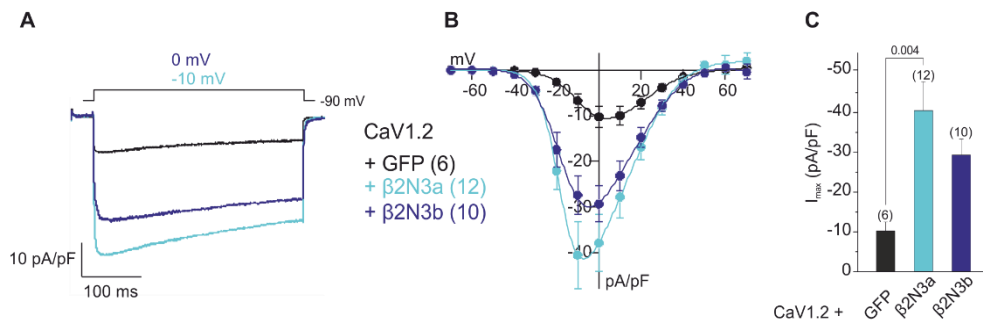


Figure 33 Ba^{2+} currents of CaV1.2 coexpressed with CaVβ2N3a or CaVβ2N3b. **A** Maximal current amplitudes (I_{max}) of CaV1.2 alone (GFP) or with the different CaVβ2-subunits (CaVβ2N3a; CaVβ2N3b). **B** Ba^{2+} -current (voltage steps -70 mV to +90 mV (Δ +10 mV)) over 400 ms from a V_h of -60 mV every 2 s of stably expressing CaV1.2 cells (GFP, black) coexpressed with either CaVβ2N3a (light blue) or CaVβ2N3b (dark blue). **C** Maximal currents at voltage steps of either to -10 mV (CaVβ2N3a) or 0 mV (CaVβ2N3b). Data are shown as mean \pm SEM (B, C) and as mean (A). Numbers of experiments are indicated in parenthesis and the number on top of the bar indicates the p-value (one-way ANOVA followed by Bonferroni correction).

avoid this Ca^{2+} -dependent inhibition. For the next set of experiments, Ca^{2+} in the external solution was substituted by Ba^{2+} (Figure 33). The CaV1.2 current (Ba^{2+} -10.24 ± 2.27 pA/pF; $n = 6$) without any auxiliary protein was increased compared to the former measured Ca^{2+} -driven current (Ca^{2+} -1.59 ± 0.3 pA/pF, $n = 9$; Figure 33 A). However, the presence of the CaVβ2N3a and CaVβ2N3b increased the maximal Ba^{2+} current to -40.51 ± 7.25 pA/pF ($n = 12$) and to -29.33 ± 3.97 pA/pF ($n = 10$), respectively (Figure 33). The CaV1.2 channel was activated independent of the CaVβ2 subunits at a potential of -30 mV but the maximal Ba^{2+} -current amplitude appeared at different potentials (GFP 10 mV; CaVβ2N3a -10 mV; CaVβ2N3b 0 mV; Figure 33 A, B). However, no difference in current amplitudes were obvious after coexpression of the β2N3a or β2N3b variant.

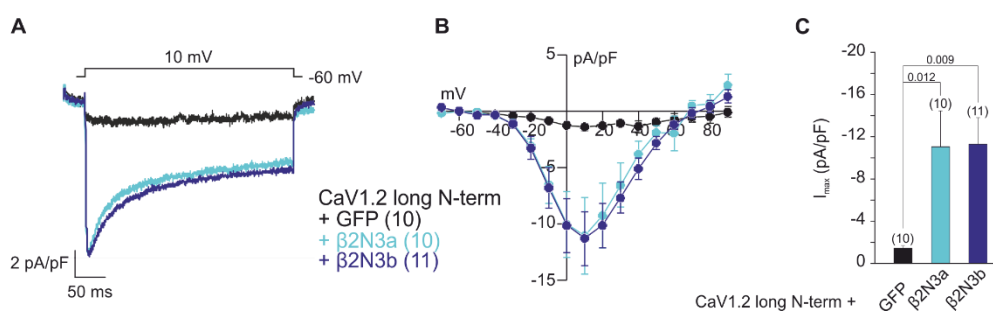


Figure 34 Currents of CaV1.2 with a long N-terminus. **A** Current at steps to 10 mV in the presence and absence of CaVβ2 subunits. **B** Current-voltage relationship of cells stably expressing CaV1.2 with a long N-terminus transfected with either CaVβ2N3a (light blue), CaVβ2N3b (dark blue) or empty GFP-vector (black). **C** Maximal current amplitudes from A. Data are shown as mean \pm SEM (B, C) and as mean (A). Numbers of experiments are indicated in parenthesis and the p-value is indicated on top of the bars (one-way ANOVA followed by Bonferroni correction).

The impact of the CaV β 2N3a and CaV β 2N3b variants on the CaV1.2 splice variant with the long N-terminus, primarily present in smooth muscle, was also analyzed (Figure 34). The long N-terminus is encoded by exon 1a of the *CACNA1C* gene, and this splice variant is mainly expressed in cardiac myocytes. Independent of the presence of the CaV β 2 subunits, the CaV1.2 with the long N-terminus was activated at -30 mV and had the maximal current amplitude at 10 mV (-1.43 ± 0.26 pA/pF, $n = 10$). However, the presence of either CaV β 2N3a (-11.05 ± 3.38 pA/pF, $n = 10$) or CaV β 2N3b (-11.31 ± 2.49 pA/pF, $n = 11$) increased the CaV1.2 current significantly (Figure 34 A, B, C). But the effects of both β 2 variants, β 2N3a and β 2N3b were not different.

3.2.1.1.2 Effect of Englerin A on CaV1.2 currents

Englerin A (EA) is a potent and specific agonist for two members of the TRPC family, TRPC4 and TRPC5 [Akbulut *et al.*, 2015]. To study the effect of EA on the cardiac CaV1.2 α 1 subunit (with the long N-terminus) coexpressed with β 2N3a or β 2N3b EA at

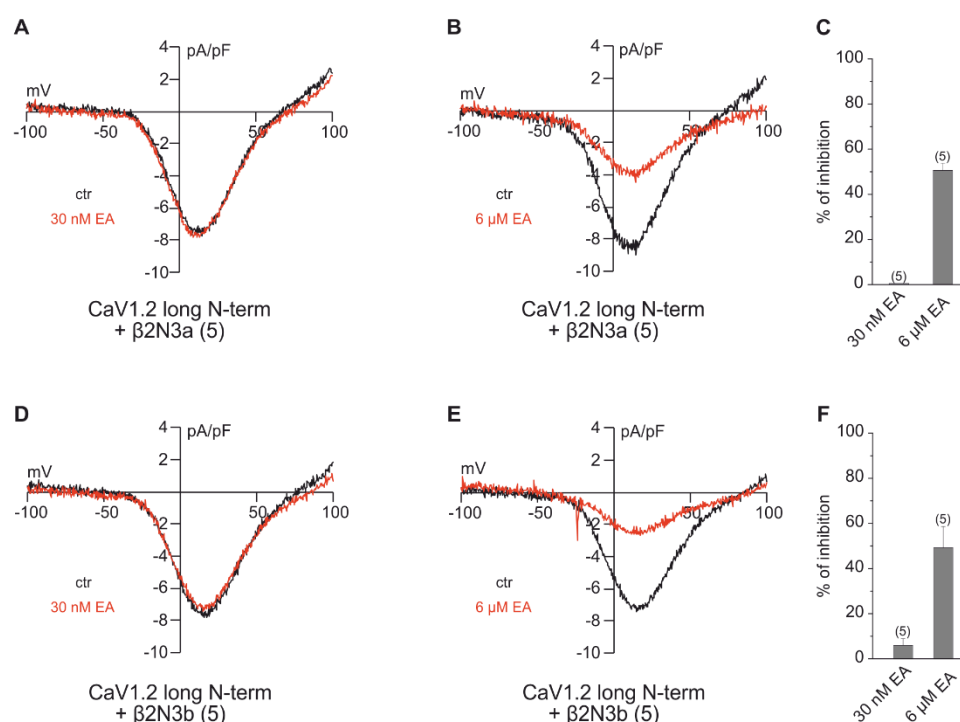


Figure 35 Effect of EA on the current of CaV1.2 with the long N-terminus. **A** Current-voltage relationship of CaV1.2 with the long N-terminus coexpressed with CaV β 2N3a in the absence (ctr, black) and presence (red) of 30 nM EA. **B** Current-voltage relationship of cells coexpressing CaV1.2 with the long N-terminus and CaV β 2N3a before (ctr, black) and during (red) the application of 6 μ M EA. **C** Inhibitory effect of 30 nM and 6 μ M EA on the CaV1.2 current from A and B in percent. **D** Current-voltage relationship of CaV1.2 with the long N-terminus coexpressed with CaV β 2N3b before (ctr, black) and during (red) the 30 nM EA-application. **E** Current-voltage relationship of cells coexpressing CaV1.2 with the long N-terminus together with CaV β 2N3b in the absence (ctr, black) and the presence (red) of 6 μ M EA. **F** Percentage of inhibition due to EA-application at concentrations of either 30 nM or 6 μ M EA. Data shown as means \pm SEM (C, F) and as mean (A, B, D, E). Numbers of experiments are indicated in parenthesis.

30 nM and 6 μ M was applied. The application of 30 nM EA had no effect on CaV1.2/CaV β 2N3a currents (-EA -8.08 ± 2.74 pA/pF; +EA -8.01 ± 3.17 pA/pF, n = 5), while the application of 6 μ M EA inhibited the current by 50% (-EA -9.32 ± 0.97 pA/pF; +EA -4.50 ± 0.30 pA/pF, n = 5; Figure 35 A, B C). Similar results were obtained for CaV1.2/CaV β 2N3b currents: 30 nM EA reduced the currents (-EA -8.01 ± 1.28 pA/pF; +EA -7.52 ± 1.24 pA/pF, n = 5) by 6 % and 6 μ M EA reduced the current by 49 % (-EA -6.25 ± 1.05 pA/pF; +EA -2.94 ± 0.54 pA/pF, n = 5; Figure 35 D, E, F). The results indicate that EA inhibits CaV currents at μ M concentrations.

3.2.1.1.3 Impact of the CaV β 3 subunit on CaV1.2

Next, the impact of the CaV β 3 subunit on CaV1.2 with the short N-terminus currents was investigated. Therefore, the stably CaV1.2 expressing cells were transfected either with GFP (as control), CaV β 3 or CaV β 2N4a. CaV β 3 did not increase the Ca $^{2+}$ current significantly compared to the control (GFP -1.93 ± 0.57 pA/pF, n = 5; CaV β 3 -2.78 ± 0.43 pA/pF, n = 5; CaV β 2N4a -3.94 ± 0.42 pA/pF, n = 9) at 10 mV (Figure 36 A, B, C).

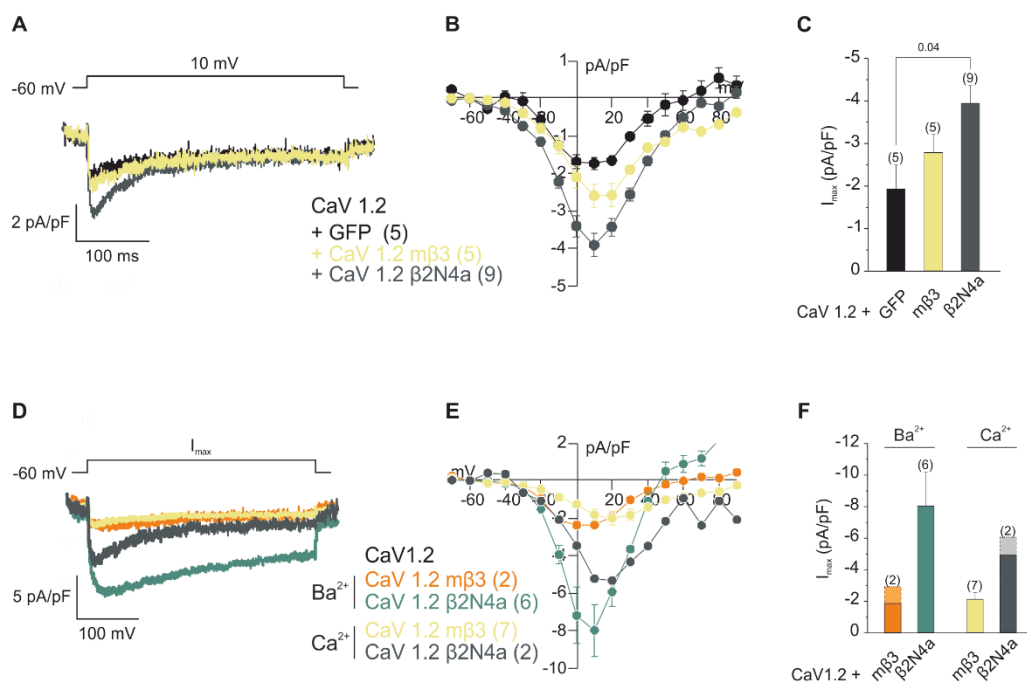


Figure 36 Ba $^{2+}$ and Ca $^{2+}$ currents via CaV1.2 channels coexpressed with CaV β 3 or CaV β 2N4a. **A** Maximal current at a step to 10 mV of CaV1.2 without (GFP, black) or coexpressed with mouse CaV β 3 (m β 3, yellow) or CaV β 2N4a (dark green). **B** Current-voltage relationship of CaV1.2 without (GFP, black) or coexpressed with mouse CaV β 3 (m β 3, yellow) or CaV β 2N4a (dark green). **C** Maximal current amplitudes of CaV1.2 currents in presence and absence of CaV β subunits. **D** Maximal current of each condition at a step to 20 mV (Ca $^{2+}$ solution) or 10 mV (Ba $^{2+}$ solution). **E** Current-voltage relationship of CaV1.2 in the presence of either m β 3 (Ca $^{2+}$: yellow; Ba $^{2+}$: orange) or CaV β 2N4a (Ca $^{2+}$: dark green; Ba $^{2+}$: green) in 10 mM Ca $^{2+}$ or 10 mM Ba $^{2+}$ containing external solution. **F** Comparison of the maximal Ba $^{2+}$ and Ca $^{2+}$ current amplitude. Data are shown as mean \pm SEM (B, C, E, F) and as mean (A, D). Numbers of experiments are indicated in parenthesis. The p-values are indicated by the numbers on top of the bars (one-way ANOVA followed by Bonferroni correction).

The currents were activated at -30 mV (Figure 36 B). However, the presence of CaV β 2N4a increased both Ba $^{2+}$ (-8.04 ± 2.15 pA/pF, $n = 6$) and Ca $^{2+}$ (-6.07 and -4.89 pA/pF, $n = 2$) currents in contrast to expression of CaV β 3 (Ba $^{2+}$ -2.94 and -1.85 pA/pF, $n = 2$; Ca $^{2+}$ -2.13 ± 0.43 pA/pF, $n = 7$; Figure 36 E, F).

Summarized, the presence of CaV β 2N3 enhanced the CaV1.2 currents more as compared to CaV β 2N4. Ba $^{2+}$ as a charge carrier shifted the voltage-dependents of CaV1.2 to more positive potentials independent of the coexpressed CaV β 2, and EA, a TRPC4 and TRPC5 agonist, at μ M concentrations had an inhibitory effect on CaV1.2/CaV β 2N3 currents.

3.2.2 Characterization of the CaV current in rat Ins-1 cells

In the previous experiments, characterization of L-type CaV channels had been performed in HEK-cells overexpressing the channels. CaV channels are endogenously expressed in skeletal and cardiac muscle or the endocrine pancreas [Yang and Berggren, 2006]. Ins-1 cells are an immortal insulinoma cell line derived from insulin secreting β -cells of the rat pancreas. They express endogenous voltage-gated calcium channels including the CaV β 3 subunit. We wanted to know, whether the CaV β 3 subunit has a major impact on CaV currents in Ins-1 cells, and Stephan Philipp and Alexander Becker knocked out the CaV β 3 gene in these cells by CRISPR-Cas9 approach. In the following I compared wild-type Ins-1 cells and CaV β 3 $^{-/-}$ Ins-1 cells. It was checked whether CaV β subunits are also expressed in the Ins-1 cells. In Ins-1 CaV β 3 was expressed, while in CaV β 3 $^{-/-}$ Ins-1 cells it was missing (Figure 37 A). Ins-1 wt and CaV β 3 $^{-/-}$ cells were used for patch clamp experiments to determine the impact of CaV β 3 on the L-type CaV channels in these cells. Therefore, Ins-1 wt cells were transfected with either an empty GFP-vector as a control and CaV β 3 $^{-/-}$ Ins-1 cells were transfected with

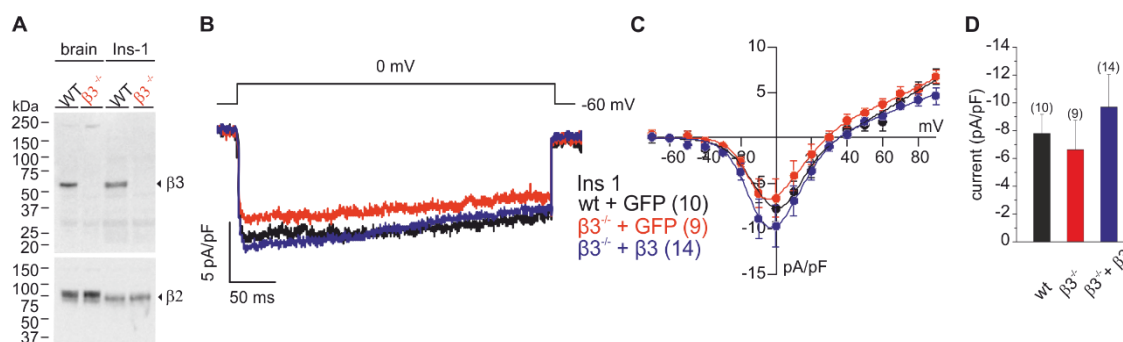


Figure 37 CaV currents in Ins-1 wt and Ins1 CaV β 3 $^{-/-}$ cells. **A** Western Blot of wt and CaV β 3 $^{-/-}$ Ins-1 cells using anti- β 3 (upper blot) and anti- β 2 (lower blot) antibodies. **B** Maximal current of wt and CaV β 3 $^{-/-}$ Ins-1 cells at a potential of 0 mV. **C** Current-voltage relationship of Ins-1 wt (black), Ins-1 CaV β 3 $^{-/-}$ (red) or CaV β 3 $^{-/-}$ transfected with CaV β 3 (blue) cells. Ins-1 wt and Ins1 CaV β 3 $^{-/-}$ cells were transfected with an empty GFP-vector for a better comparison. **D** Maximal current amplitude of each cell type shown as mean \pm SEM (C, D) and as mean (B). Number of experiments are indicated in parenthesis.

GFP or with CaV β 3 (for rescue). The current-voltage relationship of the Ins-1 wt, CaV β 3^{-/-} and CaV β 3^{-/-} transfected with CaV β 3 cells were similar to each other as well as the maximal current at 0 mV (wt -7.79 ± 1.38 pA/pF, n = 10; CaV β 3^{-/-} -6.63 ± 2.11 pA/pF, n = 9; CaV β 3^{-/-} + CaV β 3 -9.69 ± 2.34 pA/pF, n = 14; Figure 37). The results show, that Ins-1 cells do express CaV channels and their activation and currents are independent from the presence of CaV β 3.

To characterize the pharmacology of CaV channels present a cocktail of different CaV blockers, containing nifedipine (10 μ M; L-type), ω -aga-toxine (500 nM; P/Q-type), ω -cono-toxine (1 μ M; N-type), NiCl₂ (50 μ M, non-specific blocker at high concentrations, at low concentrations T-type blocker) and TTX (10 μ M; NaV blocker) was used. This cocktail reduced the CaV current amplitude in Ins-1 wt cells to about 74 % (ctr $-12. \pm 2.85$ pA/pF, cocktail -8.37 ± 1.32 pA/pF, n = 7; Figure 38 A, E). However, the application of all these compounds alone did not inhibit the CaV current. During the application of 10 μ M nifedipine 98 % of the current in the Ins-1 wt and and 88 % Ins-1 CaV β 3^{-/-} cells was still detectable. Same applies for the application of ω -aga-toxin (wt 102.78 %; CaV β 3^{-/-} 95.22 %), ω -cono-toxin (wt 102.16 %; CaV β 3^{-/-} 101.12 %), NiCl₂ (wt 85.89 %; CaV β 3^{-/-} 80.29 %) or TTX (wt 106.21 %; CaV β 3^{-/-} 91.48 %; Figure 38 E). The inhibitory effect of 10 μ M verapamil, another L-type blocker, on the CaV current in Ins-1 wt as well as CaV β 3^{-/-} cells was about 60 % (ctr -11.72 ± 1.3 pA/pF; verapamil -4.39 ± 0.16 pA/pF, n = 6; Figure 38 B, E). To find out if the remaining current is due to the expression of R-type CaV channels, the R-type inhibitor SNX482 (300 nM) was used (Figure 38 C, E). With a remaining current of 94 % for the Ins-1 wt cells and 100 % for the Ins-1 CaV β 3^{-/-} cells, SNX482 had no effect on the CaV currents (ctr -13.46 ± 1.94 pA/pF; SNX -12.31 ± 1.82 pA/pF, n = 9; Figure 38 C, E).

Isradipine, another L-type CaV channel blocker, reduced the current in these cells about 12% at a concentration of 2 μ M, while the application of 100 μ M isradipine reduced the current about 41 % (Figure 38 D, E). The treatment of Ins-1 CaV β 3^{-/-} cells with either 2 μ M or 100 μ M isradipine resulted in an inhibition of around 17 % and 22 %, respectively (Figure 38 E).

In summary, the main fraction of CaV channels in rat Ins-1 cells are L-type channels. Current amplitude did not differ between wild-type and CaV β 3^{-/-} cells indicating that CaV β 3 has very little or no effect on CaV currents in these cells.

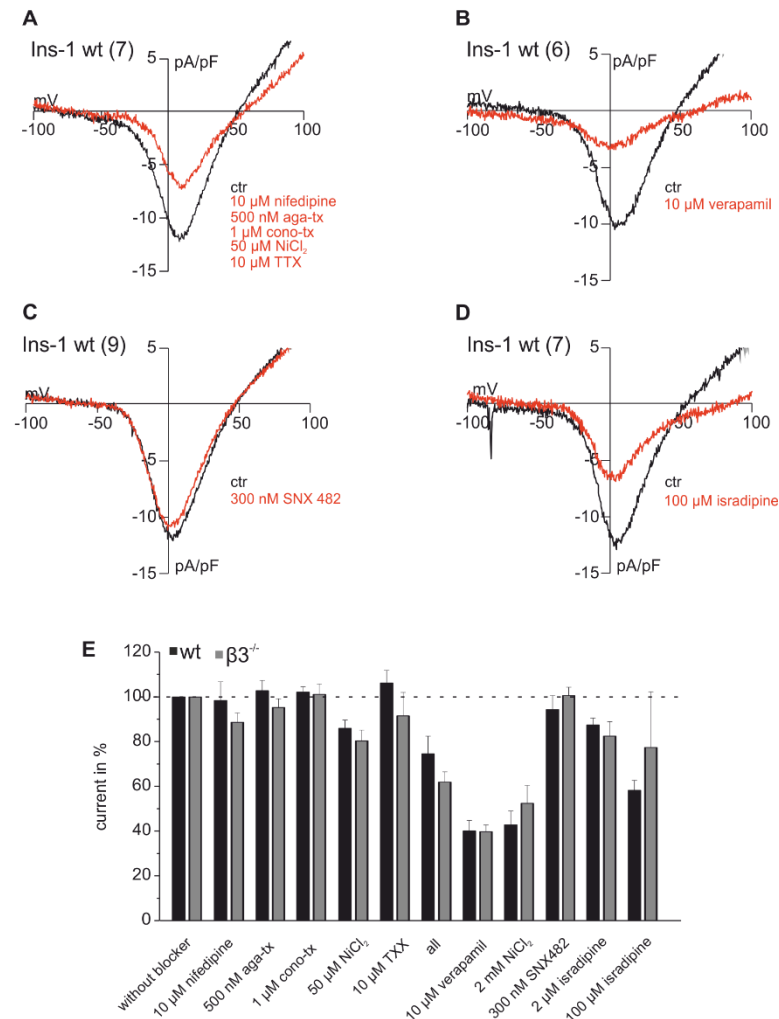


Figure 38 Pharmacological characterization of the CaV current in Ins-1 cells. **A** Current-voltage relationship of Ins-1 wt cells before (ctr; black) and during (red) the application of a blocker cocktail containing the L-type blocker nifedipine (10 μM), the P/Q-type blocker aga-toxin (500 nM), the N-type blocker cono-toxin (1 μM), NiCl₂ (50 μM) as a non-specific blocker and the NaV blocker TTX (10 μM). **B** Current-voltage relationship of CaV channels in the presence (red) and absence (ctr; black) of the L-type CaV blocker verapamil (10 μM). **C** Current-voltage relationship of Ins-1 wt cells untreated (ctr; black) or treated (red) with the R-type CaV blocker SNX482 (300 nM). **D** Current-voltage relationship of CaV channels in Ins-1 wt cells before (ctr; black) and during (red) the application of 100 μM isradipine. **E** The remaining current in percent during the application of different CaV blockers in Ins-1 wt (black) and Ins-1 CaVβ^{3-/-} cells (gray). The current without any application was set to 100 % and the remaining current was calculated. Data in E are shown as mean ±SEM (number of experiments from 4 to 9), while data in A, B, C and D are shown as mean. Number of experiments are indicated in parenthesis.

3.2.3 CaV channels in murine embryonic fibroblasts

The murine embryonic fibroblast (MEF) is another cell type where CaV channels and CaVβ subunits are expressed [Belkacemi *et al.*, 2018]. MEFs were prepared from wt and CaVβ^{3-/-} embryos at embryonic day 14.5 and cultured by Dr. Anouar Belkacemi as described in Belkacemi *et al.*, 2018. CaVβ³ was found in MEF wt cells, while the protein was absent in CaVβ^{3-/-} cells (Figure 39 A). MEF wt and CaVβ^{3-/-} cells

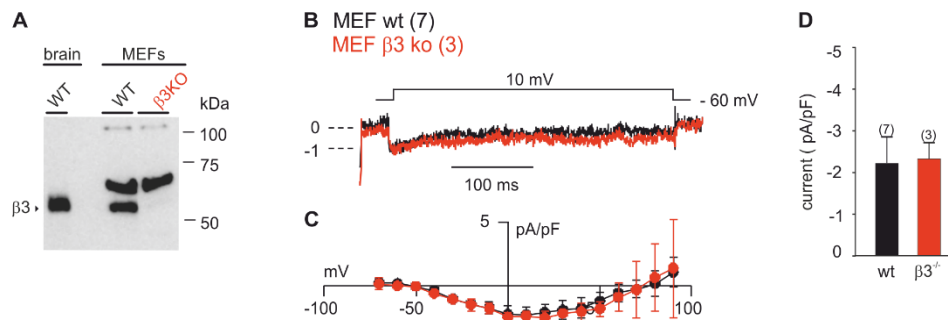


Figure 39 CaV currents in wt and CaV β 3^{-/-} murine embryonic fibroblast. **A** Western Blot of wt and CaV β 3^{-/-}MEF cells. **B** Normalized maximal current amplitude of a voltage step to 10 mV in wt (black) and CaV β 3^{-/-} (red) MEF cells. **C** Current-voltage relationship recorded in wt (black) and CaV β 3^{-/-} (red) MEF cells by using a step protocol from -70 mV to 90 mV ($V_h = -60$ mV). **D** Maximal CaV current amplitude at a voltage step to 10 mV of wt (black) and CaV β 3^{-/-} (red) MEF cells. Data are shown as mean \pm SEM (C, D) and in B as mean. Numbers of experiments are indicated in parenthesis.

were used for electrophysiological characterization of potential CaV currents in the presence and absence of CaV β 3. In both genotypes a very small CaV current could be measured. In the MEF wt as well as in CaV β 3^{-/-} cells the CaV channels maximal current appeared at a potential of 10 mV (wt -2.23 ± 0.63 pA/pF; $n = 7$; CaV β 3^{-/-} -2.33 ± 0.34 pA/pF, $n = 3$; Figure 39 B, C, D). The kinetics were not changed due to the presence (wt) or absence (CaV β 3^{-/-}) of CaV β 3 in these cells and the channels seem to have the same activation and inactivation kinetics (Figure 39 B).

In addition to CaV β 3, the CaV β 2 subunit was expressed in the MEF cells, while in CaV β 2^{-/-} MEF cells [Katiyar *et al.*, 2015] the protein was absent (Figure 40 A). Since the absence of CaV β 3 had no impact on the tiny CaV current in these cells, the CaV β 2^{-/-} were electrophysiological analyzed to see if the CaV β 2 compensate the loss of CaV β 3. However, the CaV current was not changed due to the absence of CaV β 2 (wt 1.05 ± 0.27 pA/pF, $n = 3$; CaV β 2^{-/-} 1.46 ± 0.35 pA/pF, $n = 4$) in MEF cells and the maximal current was at a potential of 10 mV and revealed the same kinetics (Figure 40 B, C, D).

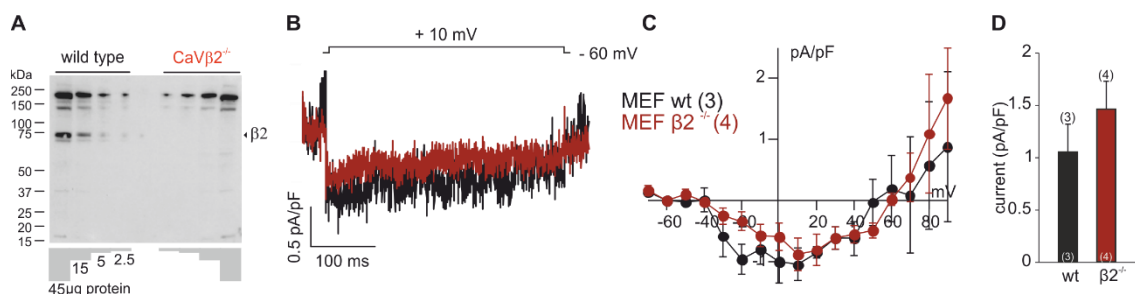


Figure 40 CaV currents in wt and CaV β 2^{-/-} murine embryonic fibroblast. **A** Western Blot of wt and CaV β 2^{-/-} MEF cells. Different protein amounts were loaded on the gel (from 2.5 μ g to 45 μ g). **B** Maximal current of a voltage step to 10 mV in the presence (wt; black) or absence (CaV β 2^{-/-}; red) of CaV β 2. **C** Current-voltage relationship in wt (black) and CaV β 2^{-/-} (red) MEF cells measured with a step protocol from -70 mV to 90 mV ($V_h = -60$ mV). **D** Maximal CaV current amplitudes of a voltage step to 10 mV in wt (black) and CaV β 2^{-/-} (red) cells. Student's t-test was used for statistical analysis and data are shown as mean \pm SEM (C, D) and as mean (B). Numbers of experiments are indicated in parenthesis.

3.2.4 CaV channels in osteoclasts

CaV β 3 is also present in osteoclasts differentiated from bone marrow derived cells (Figure 41 A). But it is not known yet, whether CaV channels are functional in osteoclasts. Osteoclasts are bone cells, which are involved in the degradation of bone tissue. Here, the functional role of CaV channels was investigated in bone marrow precursor cells and yet not differentiated cells (pre-osteoclasts) and fully differentiated osteoclasts from wild-type mice and CaV β 3 gene deficient mice.

The bone marrow precursor cells (day 0 pre-osteoclasts) were used on the day of preparation (day 0), one (day 1), two (day 2) and three (day 3) days after preparation to see if there are changes in the current during differentiation of the cells (Figure 41 B). But at all four time points there was no CaV current detectable (Figure 41 C). Even in the presence of 10 μ M BayK 8644, an enhancer of CaV currents, no current was detectable in pre-osteoclasts (Figure 41 D).

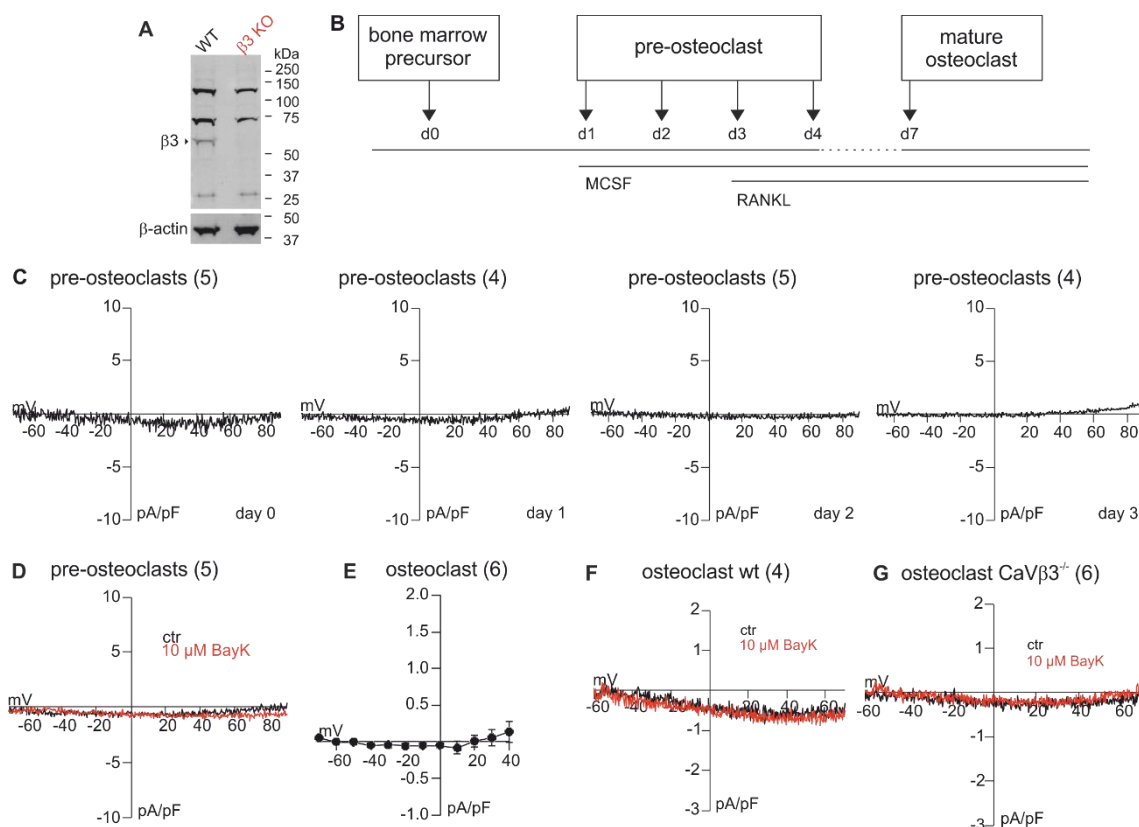


Figure 41 CaV currents in pre-osteoclast and multinucleated osteoclast. **A** Western Blot of wt and CaV β 3^{-/-} osteoclasts with β -actin a house keeping gene as loading control. **B** Scheme of osteoclast differentiation from bone marrow precursor cells (day 0) to mature osteoclast (day 7). MCSF from day 1 and RANKL from day 3 are needed for maturation. **C** Current-voltage relationship of pre-osteoclasts from the day of preparation (day 0), one (day 1), two (day 2) and three (day 3) after preparation. **D** Current-voltage relationship in the presence of 10 μ M BayK 8644 (red) in pre-osteoclasts. **E** Current-voltage relationship of fully differentiated multinucleated osteoclast using a step protocol (-70 mV to +90 mV; V_h = -60 mV). **F** Current-voltage relationship in the multinucleated osteoclasts due to 10 μ M BayK8644 (red) application. **G** Current-voltage relationship registered from CaV β 3^{-/-} osteoclasts. Data in E are shown as mean \pm SEM, while all other data are shown as mean. Numbers of experiments are indicated in parenthesis.

There was also no current detectable in the multinucleated fully differentiated osteoclasts (Figure 41 E, F, G). Again, 10 μM BayK 8644 did not result in a measurable CaV current, neither in wt nor CaV $\beta 3^{-/-}$ osteoclasts (Figure 41 F, G).

All in all, there was no detectable CaV current neither in the pre-osteoclasts nor in the fully differentiated multinucleated osteoclasts.

3.2.5 Characterization of hCaV3.2 wt and hCaV3.2 G1064R

Mutations in the CaV3.2 channel can cause a variety of diseases [Broicher *et al.*, 2008; Cain *et al.*, 2011; Tsakiridou *et al.*, 1995]. One of these diseases is characterized by the excessive production and secretion of the hormone aldosterone from the zona glomerulosa cells of the adrenal cortex. Physiologically, aldosterone synthesis and release are regulated by angiotensin II receptors of type 1 (AT1 receptors; Figure 42 A). Angiotensin II stimulates the AT1 receptor, a G-protein-coupled receptor which inhibits potassium channels. Inhibition of potassium channels depolarizes the cell and voltage-gated Ca $^{2+}$ channels open. In parallel the AT1 receptor leads to IP $_3$ and DAG formation.

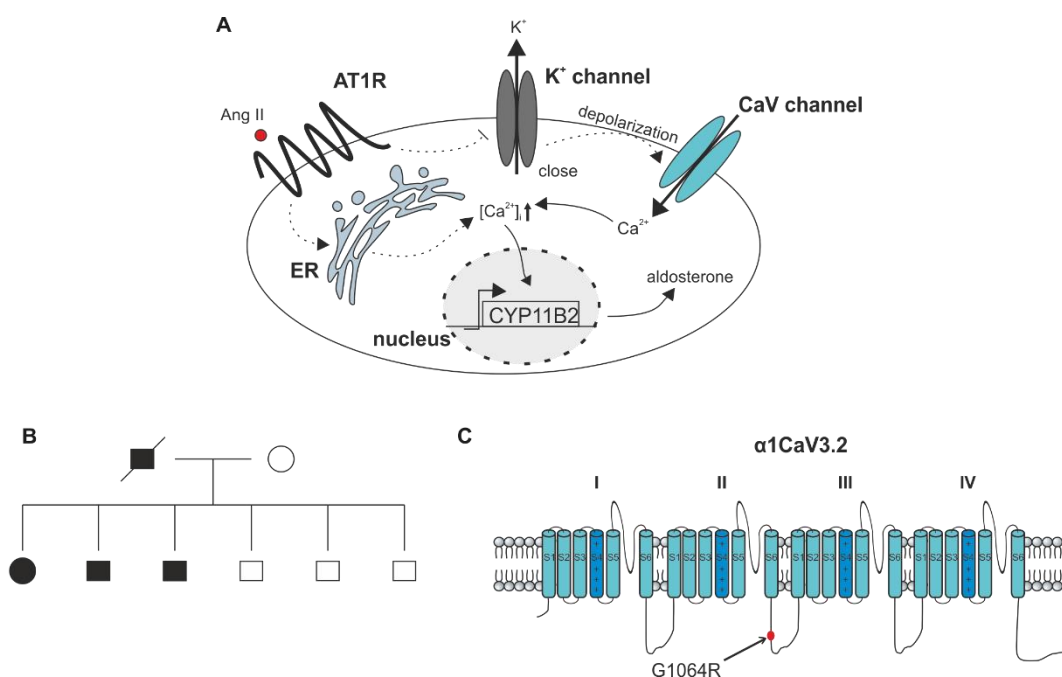


Figure 42 Pedigree of the Spanish family carrying the CaV3.2 G1064R mutation. **A** Scheme of aldosterone production. Stimulation by angiotensin II receptors type 1 (AT1R) inhibits K $^{+}$ channels leading to a membrane depolarization and activation of CaV channels. At the same time, AT1R activation leads to Ca $^{2+}$ release from ER via the IP $_3$ pathway. The increased intracellular Ca $^{2+}$ concentration stimulates the transcription of aldosterone synthase (CYP11B2) gene leading to increased aldosterone production and release. **B** Pedigree of the family suffering from primary aldosteronism indicating the family members with the CaV3.2 mutation (black) and the CaV3.2 wt (white). Boxes are indicating the male family members, while the circles indicate the female family members. Crossed box represents the death of the father. **C** Topology of the Cav3.2 with the point mutation at position 1064 (indicated by the arrow) in the cytosolic linker between domain II and domain III.

IP₃ activates the IP₃ receptor and Ca²⁺ is released from the ER. The Ca²⁺ entering the cytoplasm via voltage-gated Ca²⁺ channels and via the IP₃ receptor stimulates the transcription of aldosterone synthase (CYP11B2) and thus increases the production of aldosterone, which diffuses freely across the plasma membrane (Figure 42 A).

Several members of a Spanish family suffering from high aldosterone levels in blood and high blood pressure (Figure 42 B), carry a mutation in the CACNA1H gene which encodes the ion-conducting pore of CaV3.2. The mutation causes replacement of the glycine residue (G) at position 1064 by an arginine residue (R; Figure 42 C). In order to find out whether this mutation alters CaV3.2 channel function we cloned the cDNA of human wild-type CaV3.2 and the cDNA of the mutant CaV3.2 G1064R. Both cDNAs were subcloned into the pcDNA5/FRT vector. Using these expression plasmids two cell lines were generated which stably express the wild-type and the mutant cDNA in a tetracycline-inducible way. Expression of the cDNAs in these cells were induced in the presence of tetracycline. Figure 43 A shows Western Blots of the wild-type CaV3.2 (left) and of the CaV3.2 G1064R mutant (right), present only after tetracycline induction. Thus, both proteins are synthesized from the cells. Because no valid anti-CaV3.2 antibodies are available we had fused the CaV3.2 cDNAs to the cDNAs encoding a FLAG-tag and

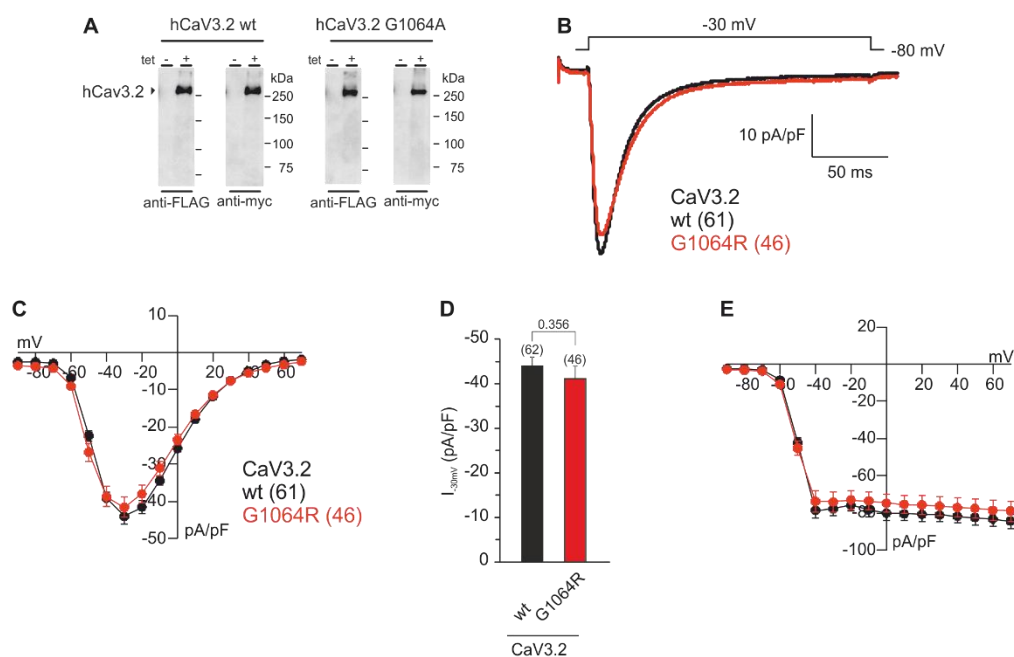


Figure 43 Comparison of hCaV3.2 and hCaV3.2 G1064R currents. **A** Western Blot of Flp-In HEK-cell lines stably expressing CaV3.2 wt and CaV3.2 G1064R under control of tetracycline induction (+ with tet, - without tet) with antibodies directed to the myc and FLAG tags fused to CaV3.2. **B** Maximal inward current of hCaV3.2 and hCaV3.2 G1064R at depolarization to -30 mV. **C** Current-voltage relationship obtained by voltage steps from -90 mV to +70 mV (Δ +10 mV) (V_h = -80 mV). **D** Mean maximal current amplitude (± SEM) at -30 mV. **E** Repolarization currents of hCaV3.2 and hCaV3.2 G1064R after depolarization from -90 mV to +70 mV (Δ +10 mV) for 20 ms followed by a voltage step to -80 mV for 80 ms. Data represent mean with ± SEM (C, D, E) or as mean (B). Numbers of experiments are indicated in parenthesis. Numbers on top of the bars in D indicates p-value (student's t-test).

a myc-tag. Against both tags good antibodies are available and they were used in Figure 43 A. By Western Blot, proteins of the correct size of about 260 kDa were recognized by the anti-FLAC antibody and the anti-myc antibody (Figure 43 A).

Next, I recorded CaV3.2 currents from these cells. The currents, measured with a step protocol, did not differ between hCaV3.2 wt and hCaV3.2 G1064R (Figure 43 B, C). hCaV3.2 and hCaV3.2 G1064R channels were activated at -70 mV or -60 mV, respectively, and both had their maximal current at -30 mV (wt 44.20 ± 1.84 pA/pF, $n = 62$; G1064R 41.19 ± 2.80 pA/pF, $n = 46$; Figure 43 D). At the end of each set of experiments the repolarization currents of hCaV3.2 and hCaV3.2 G1064R were measured by using a 2 ms step protocol followed by a depolarization of the cell for 80 ms to -80 mV. However, the mutation had no effect on the repolarization currents of CaV3.2 (Figure 43 E).

In 2001, Chemin and colleagues [Chemin *et al.*, 2001] studied the properties of splice variants of hCaV3.2, not mutants. They observed that the deletion of exon 26 significantly changed the electrophysiological characteristics of CaV3.2. Therefore, new CACNA1H cDNA constructs were cloned in which the exon 26 encoding DNA was removed from the CaV3.2 wild-type and mutant cDNA. Again, we generated Flp-In cell lines and recorded CaV currents from these cells.

The maximal current amplitudes as well as the current-voltage relationship were not significantly different in Δ Ex26 CaV3.2 wt and Δ Ex26 CaV3.2 G1064R expressing cells (wt Δ Ex26 -36.67 ± 6.15 pA/pF, $n = 13$; G1064R Δ Ex26 -46.34 ± 2.89 pA/pF, $n = 11$; Figure 44 A, B). However, the hCaV3.2 G1064R Δ Ex26 containing channels tend to reveal an increased current compared to the hCaV3.2 wt Δ Ex26 channels (Figure 44 B).

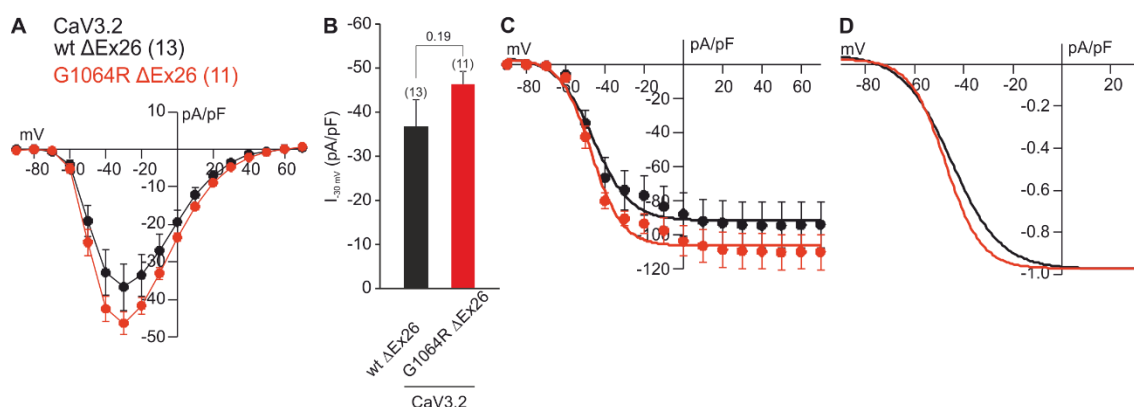


Figure 44 Impact of exon 26 deletion on CaV3.2 wt and CaV3.2 G1064R currents. **A** Current-voltage relationship of the CaV3.2 wt Δ Ex26 (black) and the CaV3.2 G1064R Δ Ex26 (red) were generated using steps from -90 mV to +70 mV ($V_h = -80$ mV) with 10 mV increments. **B** Mean maximal current amplitude (\pm SEM) with indicated p-value (student's t-test). **C** Repolarization currents of hCaV3.2 Δ Ex26 and hCaV3.2 G1064R Δ Ex26 after depolarization from -90 mV to +70 mV ($\Delta +10$ mV) for 20 ms followed by a voltage step to -80 mV for 80 ms. Data were fitted with an exponential equation. **D** Normalized repolarization currents from C. Data are shown as mean (D) or as mean with \pm SEM (A, B, C). Numbers of experiments are indicated in parenthesis.

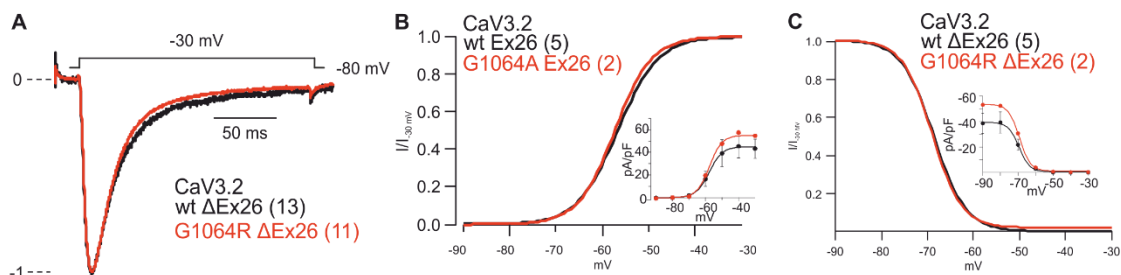


Figure 45 Steady-state activation and inactivation of hCaV3.2 Δ Ex26 and hCaV3.2 G1064R Δ Ex26 currents. **A** Normalized maximal inward current of hCaV3.2 Δ Ex26 (black) and hCaV3.2 G1064R Δ Ex26 (red) during a depolarization step to -30 mV. **B** Normalized steady-state activation ($I/I_{-30 \text{ mV}}$) of hCaV3.2 Δ Ex26 and hCaV3.2 G1064R Δ Ex26 during voltage steps from -90 mV to -30 mV ($\Delta+10 \text{ mV}$), fitted by an exponential equation. Maximal current shown in inset. **C** Normalized exponentially fitted steady-state inactivation ($I/I_{-30 \text{ mV}}$) of hCaV3.2 Δ Ex26 and hCaV3.2 G1064R Δ Ex26. The maximal current is shown in the inset. Tetracycline induction was done 24 to 48 h before measurements. Numbers of experiments are indicated in parenthesis.

The repolarization current seemed to be increased in hCaV3.2 G1064R Δ Ex26 expressing cells in contrast to the hCaV3.2 wt Δ Ex26 (Figure 44 C). After normalization to the maximal current, a shift of the repolarization current to more negative voltages were observed but however, there is no significant difference (Figure 44 D). When the maximal currents at -30 mV of hCaV3.2 wt Δ Ex26 and hCaV3.2 G1064R Δ Ex26 were normalized and the steady-state activation and inactivation were calculated. There was no difference between wild-type and mutant (Figure 45 A, B, C).

3.2.6 Effect of Englerin A on CaV3.2 currents

An effect of EA on CaV3.2 has not been shown so far, but I already showed in 3.2.1.1.2, that at least CaV1.2 is inhibited at high ($> \mu\text{M}$) EA concentrations (Figure 35). In order to reveal differences between CaV3.2 and CaV3.2 G10364R currents I investigated the effect of EA on the CaV3.2 wt and CaV3.2 G1064R channels. HEK-cells stably expressing the CaV3.2 wt were treated with different EA concentrations (0.1, 1, 3, 10, 30, 100, 1000, 6000 nM; Figure 46 C, D). The inhibitory effect of EA on the CaV3.2 wt current was much more prominent with a higher EA concentration, like the current was significantly reduced in the presence of 6 μM EA from $-49.78 \pm 8.34 \text{ pA/pF}$ to $-3.46 \pm 0.54 \text{ pA/pF}$ ($n = 6$), i.e. by $92.38 \pm 1.34 \%$ (Figure 46 A).

Similar effects of EA were observed with the current in CaV3.2 G1064R expressing cells. The CaV3.2 G1064R current ($-33.61 \pm 4.22 \text{ pA/pF}$) was reduced by $15.95 \pm 2.97 \%$ ($n = 4$) by 1 nM EA (Figure 46 C). However, with a higher EA concentration (1 μM) the inhibitory effect was more prominent and the CaV3.2G1064R current (ctr $-22.46 \pm$

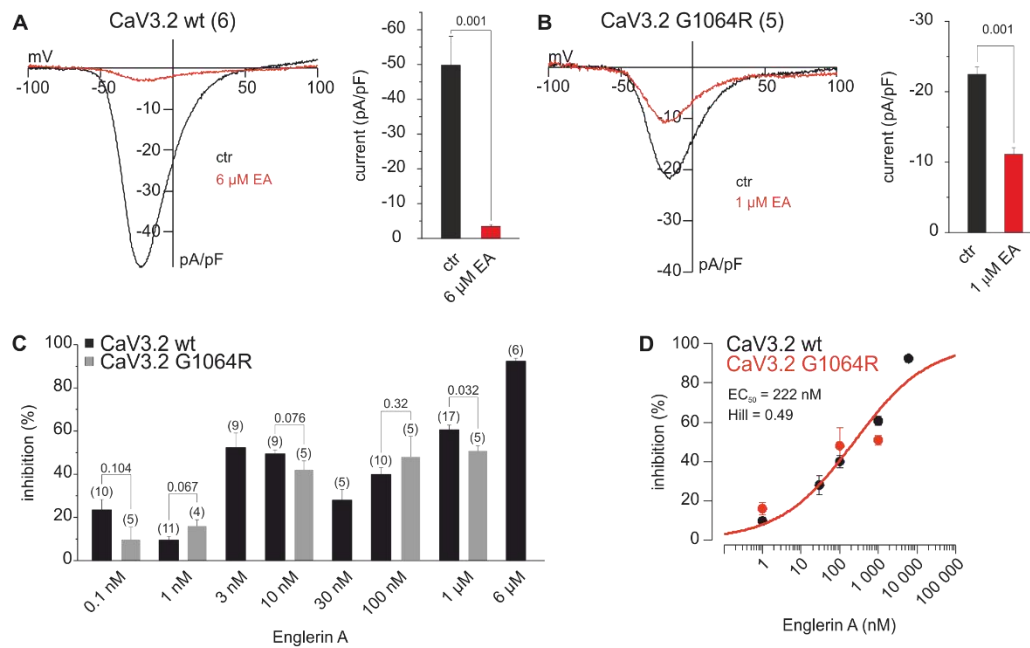


Figure 46 Inhibitory effect of EA on the CaV3.2 wt and CaV3.2 G1064R currents. **A** Current of CaV3.2 wt before (black) and during (red) application of 6 μM EA (left panel) with the maximal current amplitude (right panel). **B** Current-voltage relationship of CaV3.2 G1064R current in the absence (ctr, black) and presence (red) of 1 μM EA (red) with the maximal current amplitude in the right panel. **C** Inhibition of different EA concentrations (0.1, 1, 3, 10, 30, 100, 1000, 6000 nM) of the CaV3.2 wt (black) and CaV3.3 G1064R (gray) current. **D** Dose-response curve for all used EA concentrations with an EC_{50} of 222 nM and a Hill coefficient of 0.49 for CaV3.2 wt (black) and for CaV3.2 G1064R (red). Data shown as mean \pm SEM in the right panels of A and B, and in C and D, while in the left panels of A and B data are shown as mean. Numbers of experiments are indicated in parenthesis and the numbers on the top of the bars are the p-values calculated with the student's t-test.

1.03 pA/pF, 1 μM -11.11 ± 0.94 pA/pF, $n = 5$) was reduced by 50.77 ± 2.44 % (Figure 46 B, C).

In summary, EA had an inhibitory effect in a concentration dependent manner on CaV3.2 wt as well as on CaV3.2 G1064R currents (Figure 46 C, D). Already the lowest EA concentration of 0.1 nM inhibited the current of CaV3.2 wt and CaV3.2 G1064R by 23.54 ± 4.76 % and 9.77 ± 5.67 %, respectively. The inhibition of the CaV3.2 wt current was stronger than the inhibition of the CaV3.2 G1064R current. An exception here were the EA concentrations of 1 nM (wt 9.58 ± 1.61 %; G1064R 15.95 ± 2.97 %) and 100 nM (wt 39.97 ± 3.12 %; G1064R 47.93 ± 9.36 %; Figure 46 C). Nevertheless, the half maximal effective concentration (EC_{50}) was 222 nM for both CaV3.2 and CaV3.2 G1064R currents (Figure 46 D).

3.2.7 Impact of different CaV β subunits on the CaV3.2 current

It is generally assumed that the T-type CaV channels do not require auxiliary proteins for their proper translocation to the plasma membrane or function [Dolphin *et al.*, 1999;

Perez-Reyes, 2006]. To study the impact of the presence CaV β subunits on CaV3.2 currents, we coexpressed the cDNAs of CaV β subunits in the cells stably expressing the CaV3.2 cDNA under control of tetracycline. To identify cells which express CaV β cDNA, the CaV β cDNAs were subcloned in an expression vector in front of an internal ribosomal entry site followed by the GFP cDNA. Transfected cells can be identified by their green fluorescence and do express both CaV β and GFP, in addition to CaV3.2.

First, currents were analysed after coexpression of the skeletal muscle variant CaV β 1a [Ruth *et al.*, 1989] and the neuronal variant CaV β 1b (Figure 47). Currents were activated at -70 mV, but the presence of CaV β 1a and CaV β 1b had no effect on the CaV3.2 currents and its current-voltage relationship. The current at a potential of -30 mV tended to be reduced as compared to the GFP-control (GFP -61.97 and -72.65 pA/pF, n = 2; CaV β 1a -53.25 \pm 6.78 pA/pF, n = 11; CaV β 1b -49.11 \pm 8.02 pA/pF, n = 9). However, the effect was not significant (Figure 47 C).

Next, I coexpressed the splice variants, CaV β 2N3a or CaV β 2N3b and GFP as control. The coexpression of both CaV β 2N3 variants with the CaV3.2 channel had no significant impact on the Ca²⁺-current amplitude (Figure 48). The channel was activated at -70 mV with a maximal current (GFP -61.97 and -72.65 pA/pF, n = 2; CaV β 2N3a -64.03 \pm 6.49 pA/pF, n = 12; CaV β 2N3b -46.81 \pm 7.40 pA/pF, n = 11) at -30 mV (Figure 48 A, B, C). However, both CaV β 2N3a as well as CaV β 2N3b proteins were bound by a CaV3.2 peptide corresponding to the amino acid sequence responsible for CaV β binding in CaV1 and CaV2 channels. To study binding, peptides were synthesized containing the CaV β binding side of CaV1.2 and the corresponding peptide from CaV3.2. The peptides were synthesized as dots on a derivatized cellulose membrane. The CaV β 2 proteins were *in vitro* transcribed in the presence of ³⁵S and incubated with the membrane containing the spotted peptides. After washing, the membranes were exposed to a phosphoimager screen. Figure 48 D shows that both CaV β 2s are bound by the CaV1.2 and the CaV3.2

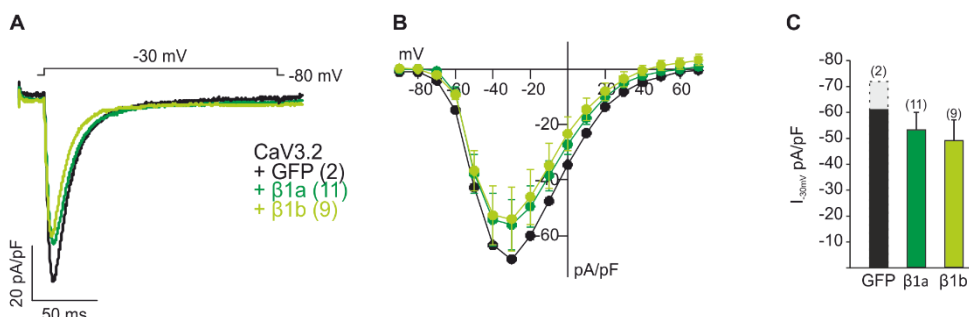


Figure 47 Impact of CaV β 1 splice variants on the CaV3.2 current. **A** Maximal current at the voltage step to -30 mV in cells stably expressing CaV3.2 transfected either with GFP (black), CaV β 1a (dark green) or CaV β 1b (light green). **B** Current-voltage relationship measured by a step protocol (-90 mV to 70 mV, $V_h = -80$ mV). **C** Corresponding statistical analysis of the maximal currents at the voltage step of -30 mV. Data represent means (A) or mean \pm SEM (B, C). Numbers of experiments are indicated in parenthesis.

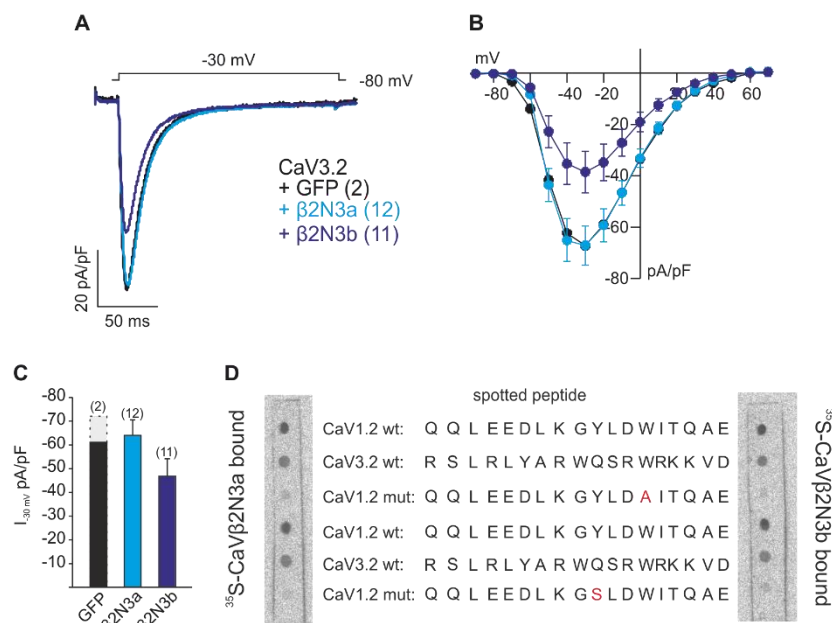


Figure 48 CaVβ2-subunit splice variants and their impact on the CaV3.2 current. **A** Maximal current at the voltage step to -30 mV in the absence and presence of the CaVβ2-subunits. **B** Current-voltage relationship of CaV3.2 in the presence of CaVβ2N3a (light blue) or CaVβ2N3b (dark blue) compared to the GFP-control (black) measured with a step protocol (-90 mV to +70 mV, $V_h = -80$ mV). **C** Maximal amplitude at the voltage step to -30 mV of CaV3.2 currents in the presence of CaVβ2N3a and CaVβ2N3b compared to the GFP-control. **D** Dot blot binding assay of CaV3.2 and CaV1.2 with CaVβ2N3a (left blot) and CaVβ2N3b (right blot). The spotted peptides are aligned in between the blots. CaV1.2 mutants lack the binding side of CaVβ, changed amino acids are indicated in red. The dark dots indicate the binding of the CaVβs to the spotted peptide. Data are shown as means (A) or as mean \pm SEM (B, C) and the number of experiments is indicated in parenthesis.

peptide but not to peptides were tryptophan (W) or tyrosine (Y) of the CaV1.2 peptide were replaced by alanine (A), respectively. The W and Y residues are critical determinants of CaVβ binding in CaV1.2 and their replacement by alanine residues abolished CaVβ binding. The W residue is conserved in CaV3.2.

After CaVβ1 and CaVβ2N3, I investigated the effect of CaVβ2N4b and CaVβ3 on the CaV3.2 current. The presence of both CaVβ2N4b and CaVβ3 subunits significantly reduced the CaV3.2-mediated Ca^{2+} -current (Figure 49 A, B). The CaV3.2 current was significantly decreased from -88.57 ± 5.65 pA/pF ($n = 18$) to -50.10 ± 9.58 pA/pF ($n = 13$) in CaVβ2N4b expressing cells and to -68.29 ± 6.41 pA/pF ($n = 13$) in CaVβ3 expressing cells without any effect of the maximal current amplitude or the current-voltage relationship (Figure 49 A, B). Normalization of the current traces at the -30 mV step in the absence and presence of CaVβ2N4b or CaVβ3 (Figure 49 C) showed no difference indicating that the two CaVβs did not alter current kinetics. However, also here a Western Blot and a dot blot binding assay were performed (Figure 49 D, E). Therefore, the CaVβ3 protein was *in vitro* transcribed in the presence of 35 S and incubated with the membrane

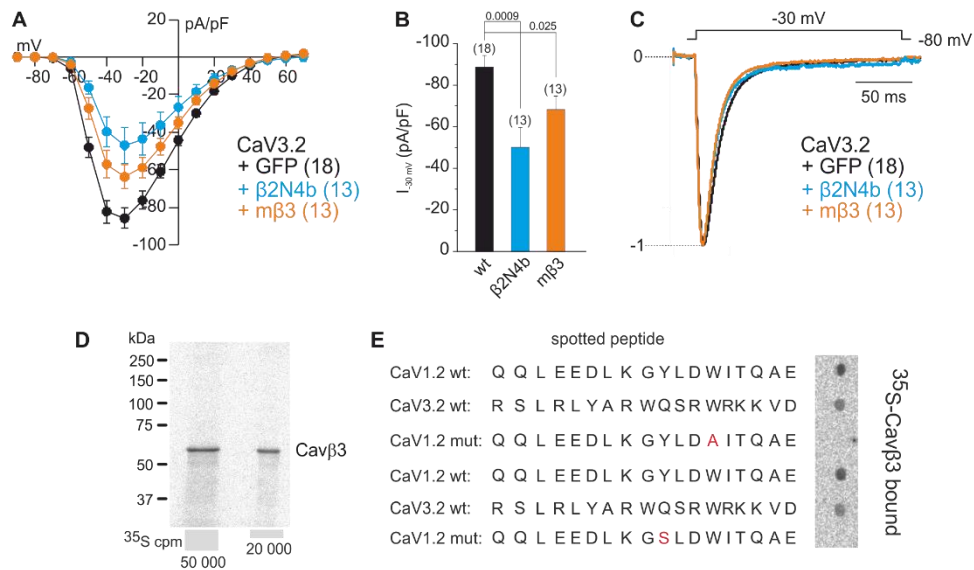


Figure 49 CaV3.2 coexpression with CaVβ2N4b or CaVβ3. **A** Current-voltage relationship measured with a step protocol from -90 mV to +70 mV in +10 mV steps ($V_h = -80$ mV) in CaV3.2 cells (black) transfected with CaVβ2N4b (blue) or CaVβ3 (orange). **B** Maximal current amplitude of CaV3.2 (black) or after coexpression with CaVβ2N4b (blue) or CaVβ3 (orange). **C** Normalized maximal current at the voltage step to -30 mV. **D** Western Blot of the radioactive CaVβ3 protein with different counts per minute (cpm). **E** Dot blot binding assay of CaV3.2 and CaV1.2 with CaVβ3. The spotted peptides are aligned in between the blots. The CaV1.2 mutants lack the binding side of CaVβ, changed amino acids are indicated in red. The dark dots indicate the binding of the CaVβ3 to the spotted peptide. Data represent means with \pm SEM (A, B) or as mean (C). Number of experiments is indicated in parenthesis, while the numbers on top of the bars in B indicate p-values (one-way ANOVA followed by Bonferroni correction).

containing the same spotted peptides like in Figure 48 D. The CaVβ3 was binding to CaV1.2 and to CaV3.2 peptides but also here the CaVβ3 did not bound to the CaV1.2 mutant.

Discussion

4.1 Electrophysiological characterization of TRP channels

4.1.1 Does TRPC1 function as an ion channel?

TRPC1 was the first cloned mammalian TRP protein and it is expressed in many tissues but until now the function remains unclear [Riccio *et al.*, 2002; Wes *et al.*, 1995; Zitt *et al.*, 1996]. Most of the studies on TRPC1 were not able to detect a current, neither in heterologous overexpression, nor in cultured or acutely isolated cells endogenously expressing TRPC1. If a TRPC1 current was measured it was a current with a linear current-voltage relationship and very small amplitudes [Alfonso *et al.*, 2008; Hofmann *et al.*, 2002]. Strübing *et al.* characterized overexpressed TRPC1 function in HEK-M1 cells (HEK-cells stably expressing the muscarinic M1 receptor). They showed that TRPC1 cDNA expressed alone did not yield a functional channel, but expressed together with TRPC5 gives rise of a heteromeric TRPC5/TRPC1 channel with different current-voltage relationship compared to homomeric TRPC5 channels. [Strübing *et al.*, 2001]. Other studies predict that TRPC1 has a role in cancer cells migration and invasion [Asghar and Törnquist, 2020; Elzamzamy *et al.*, 2020].

One of the reasons of the lack of functional studies could be the fact, that TRPC1 is not well translocated to the plasma membrane. However, this can be avoided if TRPC1 is expressed together with TRPC4 or TRPC5, since these proteins form functional heterotetrameric channels [Alfonso *et al.*, 2008; Hofmann *et al.*, 2002]. In 2018, a single-residue gate in TRPC4 was found: The current of TRPC4 was increased when isoleucine was exchanged at position 617 (I617) to asparagine (N) [Zheng *et al.*, 2018]. Furthermore, these currents showed similarities to the TRPC4 gain-of-function mutation G503S [Beck *et al.*, 2013]. However, the expression of the double mutant G503S/I617N resulted in a decreased TRPC4 current [Zheng *et al.*, 2018]. Other mutations of I617 did not have any effect. This isoleucine is located in the conserved LIAM motif (Figure 15). It was suggested to play an important role in the channel gating [Zheng *et al.*, 2018]. Supported by the TRPC4 cryo-EM structure [Duan *et al.*, 2018] we introduced corresponding mutations in the putative lower gate of TRPC1 and coexpressed the TRPC1 mutants with TRPC4. The TRPC1 mutants F639T and M642Q reduced the current and changed the TRPC4/TRPC1 current-voltage relationship to the homomeric TRPC4 current shape when coexpressed with TRPC4. Same was observed when TRPC4 was coexpressed with the TRPC1 mutants M743A, L744A or E755S, where the current-voltage relationship looked like the pure TRPC4 current-voltage relationship. In addition, these TRPC1 mutants did not have any effect on the maximal current

amplitude. Either these TRPC1 mutants change the pore of the heteromeric channels resulting in a changed current-voltage relationship or the TRPC1 mutants lacked the ability to form heteromeric channels with TRPC4 and therefore, only the homomeric TRPC4 currents were measured. However, the interaction of the TRPC1 mutants F639T, M642Q, M743A, L744A and E755S with TRPC4 have to be further analyzed to explain the lack of changes of the current-voltage relationships.

Corresponding to the published TRPC4 mutants in the LIAM motif [Zheng *et al.*, 2018], the TRPC1 was mutated at the same position. The valine at position 741 (V741) in the TRPC1 was exchanged to either alanine (A), serine (S), glycine (G), asparagine (N), glutamine (Q) or threonine (T). The only amino acid replacement with a significant effect on the current amplitude, was the exchange of valine to alanine. This change had a huge impact on the current amplitude without any effect on the current-voltage relationship. Although the TRPC1 V741A had such an impact on the TRPC4/TRPC1 current, the expression of this mutant without TRPC4 did not lead to a measurable current. However, the effect of the coexpression of TRPC1 V741A with TRPC4 suggest a role of TRPC1 in the formation of the pore in heteromeric channels. Since the current-voltage relationship of heteromeric TRPC4/TRPC1 channels differs from the homomeric current-voltage relationship of TRPC4 channels, TRPC1 is contributing to the pore formation. The increased current of the TRPC4/TRPC1 V741A channels confirms the role of TRPC1 as a subunit contributing to the channel pore. It confirms that the valine at position 741 in the TRPC1 is involved in channel gating.

Furthermore, in 2018, Duan *et al.* showed by using the cryo-EM technique, that the residues I617, N621 and Q625 at the putative lower gate of TRPC4 are forming the narrowest point of the conduction pathway with around 3.6 Å [Duan *et al.*, 2018]. The corresponding residue in TRPC1 of the N622 in TRPC4 is the lysine (K) at position 747. This K747 in TRPC1 is a positive charged residue and could be another target for a mutation to a smaller and neutral amino acid. This could widen the opening of the TRPC1 pore, which could result in a measurable current.

Since the TRPC1 mutants were expressed but not functional without the presence of TRPC4, TRPC4-TRPC1 chimeras were generated. The TRPC4 α was used as a backbone and its pore was exchanged by the TRPC1 pore. This approach was used to translocate the TRPC1 pore to the plasma membrane and to study the function of the TRPC1 pore without the interference of the TRPC4 pore (Figure 21). The protein surface biotinylation confirmed the translocation of the chimera to the plasma membrane and the coexpression with TRPC4 resulted in a decreased DAMGO/CCh-induced current with a typical TRPC4 current-voltage relationship (Appendix Figure A3). However, if the TRPC4 α -C1_{S5-S6 linker} chimera was expressed without TRPC4 α , an increased basal

current was observed. This current was not enhanced by the TRPC4 agonist EA (Figure 23) or by hormones (Figure 22), but the substitution of Na⁺ by NMDG in the external solution led to a decreased current (Figure 24). Furthermore, the application of the non-specific TRP blocker SKF 96365 inhibited the inward current nearly completely (Figure 25). These results suggest that the measured current is a real cation current, most probably a Na⁺ current, and not just a leak in the membrane. It seems that TRPC1 could be a constitutive active Na⁺ channel, which can be inhibited by the non-specific TRP blocker SKF 96365.

The increased basal current was also observed in the TRPC4 β -C1_{S5-S6 linker} 1 and TRPC4 β -C1_{S5-S6 linker} 2 chimeras (Figure 26). These currents were also not enhanced by application of EA or CCh. These results confirm the results with the TRPC4 α -C1_{S5-S6 linker} chimera and give a further hint for the hypothesis of a constitutive active TRPC1 channel.

4.1.2 TRPC1 function in osteoclasts and in pituitary cells

In our laboratory a new TRPC1-ICre mouse was generated by Dr. Ahsan Raza. This mouse can be mated with the eR26- τ GFP reporter mouse to visualize TRPC1 expressing cells. Due to this, TRPC1 expressing cells were identified by their green fluorescence in the pituitary gland and the bone. Although the TRPC1 mRNA was expressed in the osteoclasts, I could not detect any current in these cells. A new splice variant of TRPC1 found in early pre-osteoclasts [Ong *et al.*, 2013] was suggested previously to be involved in the regulation of osteoclastogenesis. It was concluded, that interaction of TRPC1 and the inhibitor of MyoD (I-mfa) regulates the osteoclastogenesis via the store-operated Ca²⁺ entry [Ong *et al.*, 2013]. For this regulation TRPC1 has to interact with STIM1 and Orai1, whereas I-mfa suppresses the store-operated currents and acts like a break for the Ca²⁺ entry [Ong *et al.*, 2013]. In addition to TRPC1, other TRP mRNAs are expressed in osteoclasts, such as TRPV1, TRPV2, TRPV4 and TRPV5 [Lieben and Carmeliet, 2012].

In contrast to the osteoclasts, in isolated pituitary cells a TRPC current was detected. For this study only male mice at the age of 8 weeks were used, since the hormonal status of female mice is changing due to their estrogen cycle, which may interfere with TRPC expression patterns [Beck *et al.*, 2017; Qiao *et al.*, 2016]. In TRPC1- τ GFP as well as in TRPC1-deficient pituitary cells, a current with different amplitudes and current-voltage relationships were detected. The current in TRPC1- τ GFP cells had the typical soup ladle like shape of heteromeric TRPC5/TRPC1 channels, while the current in TRPC1-deficient cells had the typical TRPC5 current-voltage relationship. These results suggested the presence of heteromeric TRPC5/TRPC1 channels. However, these TRPC5/TRPC1 current was not detectable in all TRPC1- τ GFP cells. TRPC5 is expressed in the

gonadotrope cells, which are stimulated by gonadotropin-releasing hormone (GnRH) and which release the gonadotropins follicle-stimulating hormone (FSH) and luteinizing hormone (LH) [Beck *et al.*, 2017], TRPC1 seemed to be expressed in different cell types of the pituitary gland. The current in TRPC1- τ GFP pituitary cells was always larger compared to the current measured in TRPC1-deficient pituitary cells. This result was surprising, since in the HEK-cell experiments the current of homomeric TRPC5 channels is bigger compared to heteromeric TRPC5/TRPC1 currents [Beck *et al.*, 2017]. Moreover, the deletion of TRPC1 in hippocampal CA1 neurons increases the TRPC current in these cells [Kepura *et al.*, 2020] whereas Lepannetier *et al.* showed a reduction of TRPC1-dependent Ca^{2+} transients in cultured hippocampal neurons [Lepannetier *et al.*, 2018]. This means the wild-type CA1 neurons express the heteromeric TRPC/TRPC1 channels with a smaller current than detected in the TRPC1-deficient CA1 neurons [Kepura *et al.*, 2020] but a larger Ca^{2+} influx [Lepannetier *et al.*, 2018]. Other studies also showed that the presence of TRPC1 is decreasing the inward current and increasing the outward current compared to TRPC4 or TRPC5 expressed alone. TRPC1 seems to have an inhibitory effect on TRPC4 and TRPC5 channels. But this was not the case in the pituitary cells, where the opposite was observed. An explanation for this observation could be, that the Ca^{2+} permeability in TRPC1-deficient pituitary cells was increased compared to the Ca^{2+} permeability in wild-type pituitary cells (Figure 29). This means TRPC1 is reducing the Ca^{2+} permeability of the channel, whereas homomeric TRPC5 channels in the TRPC1-deficient cells yield smaller currents but with a higher Ca^{2+} permeability. This conclusion is supported by the results of quantitative polymerase chain reactions, which show, that the amount of *Trpc5* transcripts are identical in wild-type cells, containing TRPC1, and in the corresponding TRPC1-deficient cell [Wang *et al.*, to be published].

The TRPC5/TRPC1 current could prevent the cells from Ca^{2+} overload and cell death. Storch *et al.* could also show the reduced Ca^{2+} permeability of TRPC5/TRPC1 and TRPC4/TRPC1 in cell culture systems [Storch *et al.*, 2012]. Their findings and my results lead to the suggestion of TRPC1 as a regulator for the Ca^{2+} permeability of the TRPC channels and an important role of TRPC1 in the Ca^{2+} homeostasis. This is especially important in the pituitary gland where the intracellular Ca^{2+} concentration triggers the release of LH and FSH from the gonadotropes. Activation of TRPC5/TRPC1 in the gonadotropes increases the intracellular Ca^{2+} concentration, causes a depolarization of the plasma membrane, resulting in the activation of L-type Ca_V channels, leading to a further increase of the intracellular Ca^{2+} concentration [Beck *et al.*, 2017]. Therefore, the tight control of the Ca^{2+} influx into the cells is important and an adaptive reduction of TRPC5 activity could be an explanation of the reduced TRPC5 inward current amplitude

in the TRPC1-deficient pituitary cells. In 2008, a study of coexpressed TRPC1 and TRPC5 in CHO cells also showed a reduced current of TRPC5 channels compared to TRPC5/TRPC1 currents like in the pituitary cells. This experiments were done with transfected cells, not native cells [Alfonso *et al.*, 2008]. It seems that the role of TRPC1 as part of heteromeric channels depends on the expression system, the cell type, the used agonist and the TRPC partner, TRPC5 or TRPC4.

In summary, I can show that TRPC1 has an inhibitory effect on the current of heteromeric TRPC channels and on the Ca^{2+} permeability both in cell culture systems and *in vivo*, in acutely isolated cells. This inhibitory effect of TRPC1 plays a major role in the control of the intracellular Ca^{2+} concentration and the related signaling pathways, especially in the endocrine cells of the anterior pituitary.

4.2 Electrophysiological characterization of voltage-gated calcium channels

4.2.1 Impact of $\text{CaV}\beta$ subunits on L-type and T-type CaV channels

Voltage-gated calcium channels (CaV) are associated with auxiliary $\text{CaV}\beta$ proteins. Several studies showed the necessity of $\text{CaV}\beta$ subunits for the translocation to the plasma membrane and the function of high voltage activated (HVA) CaV s. There are four different $\text{CaV}\beta$ subunits ($\text{CaV}\beta 1$ – $\text{CaV}\beta 4$) and all bind to the linker of domain I and domain II of the $\text{CaV}\alpha 1$ subunit, the so called $\alpha 1$ -interaction domain (AID) [Marquart and Flockerzi, 1997; Pragnell *et al.*, 1994].

The effect of $\text{CaV}\beta$ subunits on the L-type CaV channel depends on which $\text{CaV}\beta$ subunit is coexpressed [Link *et al.*, 2009]. The L-type $\text{CaV}1.2$ interacts mainly with $\text{CaV}\beta 2$, but there are hints for an interaction with $\text{CaV}\beta 3$ as well [Hofmann *et al.*, 2014]. In this work the effect of different $\text{CaV}\beta 2$ splice variants on the $\text{CaV}1.2$ was analysed. All $\text{CaV}\beta 2$ splice variants increased the current through $\text{CaV}1.2$ independent of the extracellular Ca^{2+} concentration (1.8 mM or 10 mM; Figure 32). The results of the dot blot binding assay also confirmed a binding of $\text{CaV}\beta 2$ subunits to the $\text{CaV}1.2$ wild-type but not to a $\text{CaV}1.2$ mutant lacking the $\text{CaV}\beta$ binding side (AID; Figure 48; Figure 49). Link *et al.* could show the impact of $\text{CaV}\beta 2$ subunits in the murine heart with similar results as obtained in this thesis. They could show an enhancement of the $\text{CaV}1.2$ current coexpressed with the $\text{CaV}\beta 2$ subunits and also an endogenous coexpression of both proteins in the murine cardiomyocytes [Link *et al.*, 2009].

Since the $\text{CaV}\beta 2\text{N}3\text{a}$ and $\text{CaV}\beta 2\text{N}3\text{b}$ splice variants had the largest effect on the $\text{CaV}1.2$, these two splice variants were further investigated together with another splice variant of $\text{CaV}1.2$ containing a long N-terminus. The long N-terminus is encoded by exon

1a of the *CACNA1C* gene, and this splice variant is mainly expressed in cardiac myocytes. The coexpression of these CaV β 2 subunits also increased the current through CaV1.2 with the long N-terminus. So, the N-terminus of CaV1.2 does not play an important role in the interaction of the CaV β 2 subunits, since the AID side is in the linker of domain I and domain II of the CaV1.2.

The coexpression of CaV β 3 had no impact on the CaV1.2 current, although it tended to increase the current a little bit. There are studies, which show the coexpression of L-type CaV channels and CaV β 3 in some tissues. A reduced L-type current was observed in sympathetic CaV β 3^{-/-} neurons compared to the wild-type sympathetic neurons, giving a hint that these two proteins interact in these cells: CaV1.2 and CaV β 3 are coexpressed and do interact [Ludwig *et al.*, 1997; Namkung *et al.*, 1998]. With a dot blot binding assay, we could show an interaction, but somehow the coexpression of CaV β 3 and CaV1.2 had no impact on current amplitude compared to the current amplitude obtained after CaV1.2 expression alone (Figure 36). We have previously shown that HEK-cells endogenously express CaV β 3 [Belkacemi *et al.*, 2018], which might be sufficient to regulate the CaV1.2 pore after CaV1.2 cDNA expression.

Moreover, for more physiological conditions I used rat Ins-1 cells, since these cells express endogenous CaV channels and their auxiliary subunits [Yang and Berggren, 2006]. Using the CRISPR-Cas9 method, Stephan Philipp and Alexander Becker from our laboratory knocked down the CaV β 3 in Ins-1 cells. However, comparing Ins-1 wild-type cells with Ins-1 CaV β 3^{-/-} cells, the measured CaV current was unchanged (Figure 37). The CaV current in the Ins-1 cells was further analyzed by using specific blockers for different CaV channels. The strongest inhibition was found after application of verapamil, a L-type CaV channel blocker. These results lead to the conclusion, that the main part of the measured CaV current in rat Ins-1 cells was through L-type CaV channels, since other CaV blockers also had an inhibitory effect although not as prominent as verapamil. This is consistent with the mRNA expression in Ins-1 cells, where the CaV1.2 mRNA level is two-fold higher than the CaV1.3 and CaV2.3 mRNA levels. Moreover, CaV1.2 is involved in insulin secretion in Ins-1 cells, since the knock down of CaV1.2 results in a reduced insulin secretion [Nitert *et al.*, 2008]. It could be also shown, that in human β -cells, CaV1.2 plays a role in the insulin secretion as point mutations of the channel increase the channel activity and cause excessive insulin secretion [Yang and Berggren, 2006].

In contrast to the L-type CaV channels, there is until now a debate about the interaction of T-type CaV channels with auxiliary CaV β proteins. Some studies claim that the CaV β subunits have no significant effect on the T-type CaV channel [Arias *et al.*, 2005], while

other studies could show an interaction of some CaV β subunits with CaV3.1 and CaV3.3 resulting in an increased functional expression and current density [Bae *et al.*, 2010; Dolphin *et al.*, 1999; Dubel *et al.*, 2004]. In our hands the coexpression of CaV3.2 with CaV β 1 subunits did not show any impact on the CaV3.2 current, although Dolphin *et al.* and Dubel *et al.*, claimed an interaction of CaV3.1 and CaV3.3 with CaV β 1, respectively. Coexpression of CaV β 2 subunits did not have any effect on the CaV3.2 current either. It was shown that CaV β 2 increased the functional expression of CaV3.1 and interacts with CaV3.3 [Bae *et al.*, 2010; Dolphin *et al.*, 1999]. Although there was no impact on the current, an interaction between CaV3.2 and the CaV β 2 subunits was detectable with a dot blot binding assay (Figure 48 D). In contrast, the coexpression of CaV β 2N4b and CaV β 3 with CaV3.2 had an inhibitory effect on the CaV3.2 current in my experiments (Figure 49). According to the scheme in Figure 31 A, the CaV β 3 and CaV β 2b variants share a similar structure of the HOOK domain, which might be responsible for a CaV β protein configuration favouring interaction with CaV3.2.

4.2.2 The CaV channel independent function of CaV β 3

CaV β 3 is one of the four auxiliary proteins of CaV channels. However, this protein has also a CaV channel independent function [Belkacemi *et al.*, 2018; Berggren *et al.*, 2004; Berggren *et al.*, 2018]. This could also apply to CaV β 3 in the rat Ins-1 cells, since the absence of CaV β 3 protein had no effect on the measured CaV current (Figure 37). These results are consistent with the observations by Berggren *et al.* in mice [Berggren *et al.*, 2004], since they also found no difference in the Ca²⁺ current through the L-type CaV channel using wild-type and CaV β 3^{-/-} pancreatic β -cells demonstrating a CaV channel independent function of CaV β 3. Furthermore, the CaV β 3^{-/-} mice have increased glucose-induced insulin secretion, which is a result from increased Ca²⁺ release from intracellular stores resulting in increased intracellular Ca²⁺ oscillations. On the other hand CaV β 3^{-/-} mice had no obvious phenotype and a normal morphology of the pancreatic islets [Berggren *et al.*, 2004].

Another cell type, expressing CaV β 3 are murine embryonic fibroblast (MEF) cells. In this cell type a very small CaV current could be detected in wild-type and in CaV β 3^{-/-} cells. The deletion of CaV β 3 in these cells had no effect on the measured currents. Belkacemi *et al.* could demonstrate the CaV β 3 modulation of the IP₃ sensitivity of fibroblast cells independent of the CaV β 3 function as a CaV channel subunit [Belkacemi *et al.*, 2018]. The CaV β 3 protein reduced the binding of IP₃ to the IP₃ receptor, which leads to a desensitization of the cell to low IP₃ levels. Deletion of CaV β 3 increases IP₃ binding and

the Ca^{2+} release from the intracellular stores compared to wild-type cells and affects fibroblast migration *in vitro* and wound healing *in vivo* [Belkacemi *et al.*, 2018].

The same $\text{CaV}\beta 3$ function could, maybe, play a role in osteoclast cells, since $\text{CaV}\beta 3$ is expressed in osteoclasts but no functional CaV channel currents have been detectable in this cell type. I used cells of different developmental stages for current recordings, but in none a CaV current was detectable (Figure 41). BayK 8644, a L-type CaV channel agonist, did not unmask any CaV current, although in 1990, Miyauchi *et al.* claimed an increased Ca^{2+} signal in chicken osteoclasts, which was inhibited by nifedipine, a dihydropyridine Ca^{2+} channel blocker [Miyauchi *et al.*, 1990]. In the same year, Datta *et al.* showed that the intracellular Ca^{2+} concentration in rat osteoclasts is voltage-independent and insensitive to BayK 8644 as well as to nifedipine [Datta *et al.*, 1990]. The osteoclasts could also be a cell type where the $\text{CaV}\beta 3$ protein has a CaV independent function, however, this needs further analysis besides patch clamp measurements.

4.2.3 hCaV3.2 G1064R mutation and hypertension in a Spanish family

Primary aldosteronism is the excessive production and secretion of the hormone aldosterone from zona glomerulosa cells of the adrenal cortex, which causes low levels of renin and hypertension. Angiotensin II stimulates the angiotensin II receptors of type 1 (AT1 receptors), a G-protein-coupled receptor of zona glomerulosa cells regulating the aldosterone synthesis and release. The activation of AT1 receptors inhibits potassium channels leading to a depolarization of the cell and the opening of voltage-gated Ca^{2+} channels. At the same time, the AT1 receptor activation leads to IP_3 and DAG formation followed by the activation of IP_3 receptors and the release of Ca^{2+} from the ER (Figure 42 A). The Ca^{2+} entering the cytoplasm via voltage-gated Ca^{2+} channels and via the IP_3 receptors stimulates the transcription of aldosterone synthase (CYP11B2) and thus increases the production of aldosterone, which diffuses freely across the plasma membrane [Scholl *et al.*, 2015; Spät and Hunyady, 2004]. Around 5 % to 10 % of patients with high blood pressure suffer from hyper-aldosteronism, however, the familial form of this disease is very rare and only a few genes could be correlated with it so far [Morimoto *et al.*, 2018]. Mutations close to the selectivity filter of K^+ channels (encoded by *KCNJ5*) result in Na^+ permeability, which leads to a depolarization of the adrenal glomerulosa cells and finally to the activation of CaV channels causing primary aldosteronism. Accordingly these patients are treated with Ca^{2+} channel blockers, which reduce the plasma aldosterone levels as well as the blood pressure [Felizola *et al.*, 2014; Sasaki *et al.*, 2009]. Felizola and colleagues could show that $\text{CaV}3.2$ is expressed in adrenocortical

aldosterone-producing adenomas as well as in cortisol-producing adenomas and that the CaV3.2 mRNA level correlates with the plasma aldosterone level [Felizola *et al.*, 2014].

Several mutated genes were identified in aldosterone-producing adenoma cells, like the *ATP1A1*, *ATP2B3* and *CACNA1D* [Choi *et al.*, 2011; Daniil *et al.*, 2018; Scholl *et al.*, 2015]. In addition, several germline mutations of CaV3.2 (*CACNA1H*) are associated with primary aldosteronism and high blood pressure. Patients suffering from primary aldosteronism were screened and several point mutations in the *CACNA1H* gene (*CACNA1H* M1549V, M1549I, S196L, P2083L, V1951E) were identified. All these mutations lead to a gain-of-function of CaV3.2 with an increased aldosterone production. The mutation M1549I changed the channel activation and inactivation properties to more negative potentials, while the mutations S196L and P2083L showed slower activation and inactivation, changed steady-state inactivation and an increased voltage dependent facilitation. The latter was also increased with the V1951E mutation (Daniil *et al.*, 2018). In a Spanish family with late-onset primary aldosteronism, another mutation of the *CACNA1H* gene was found. All family members suffering from this disease had a point mutation at position 1064 localized in the linker between domain II and domain III (unpublished data from Professor Dr. Jochen Schneider, Luxembourg). However, my functional characterization of the CaV3.2 G1064R mutation, which were performed in the present study showed no difference in kinetics and in the activity of mutant and wild-type CaV3.2. The current remained unchanged, indicating that CaV3.2 current gain-of-function is not the case here, what is in contrast to published CaV3.2 mutations linked to hypertension [Daniil *et al.*, 2018; Scholl *et al.*, 2015; Seidel *et al.*, 2019].

The CaV3.2 M1549V mutation leads to a 7-fold higher aldosterone level in transfected HAC15 cells compared to HAC15 cells transfected only with the vector [Reimer *et al.*, 2016]. However, by using Mibefradil, a non-specific T-type CaV blocker, the effect on the coexpressed aldosterone synthase (CYP11B2) was abrogated. This leads to the conclusion of a direct link between CaV3.2 and the CYP11B2 [Reimer *et al.*, 2016; Scholl *et al.*, 2015, Seidel *et al.*, 2019]. In perspective, maybe HEK-cells are not the right expression system, therefore, HAC15 (ATCC® CRL-3301™) cells are going to be used for my further experiments of CaV3.2 G1064R. This cell line is a clonal cell line isolated from NCI-H295R (ATCC® CRL-2128™), which is from human adrenal tissue and is widely used for studies of adrenal cell function. Moreover, these cells are supposed to express CaV3.2 endogenously. If this is the case, they do not have to be transfected, what could exclude artefacts. After reliably showing CaV3.2 expression in these cells, the mutation will be introduced by using the CRISPR-Cas9 method. This set of experiments are still ongoing. They could be more physiological than the HEK-cell

system. Since CaV channels are involved in primary aldosteronism and because the CaV3.2 G1064R mutation was linked to hypertension in the Spanish family, the CaV3.2 G1064R mutation could still play a role in this disease.

4.3 Effect of Englerin A on TRPC channels and CaVs

In 2015, a new compound extracted from the tree *Phyllanthus engleri* named Englerin A (EA) was introduced to the TRP community by Akbulut [Akbulut *et al.*, 2015]. This compound is a specific agonist of TRPC4 and TRPC5, while it has no effect on other TRP channels. EA is a very potent agonist, since the channels are activated by nM concentrations with an EC₅₀ of 11.2 nM for TRPC4 and of 7.6 nM for TRPC5 [Akbulut *et al.*, 2015]. EA also activates the heteromeric TRPC4/TRPC1 and TRPC5/TRPC1 channels, however, the EC₅₀ for the heteromeric channels is increased to 20-24 nM for the TRPC4/TRPC1 heteromeric channel (Figure 14), which is slightly higher than the 9.5 nM published by Akbulut [Akbulut *et al.*, 2015].

The EA-induced inward current of the TRPC4 current was always higher than after stimulation of the current by G_{q/11} and G_{i/o} coupled GPCRs by DAMGO/CCh or CCh (Figure A8-A11). EA activates TRPC4 and TRPC5 channels from the extracellular side, since it failed to activate them from the intracellular side [Akbulut *et al.*, 2015]. As a potent agonist it may activate the channels for a longer time period, so it may change the open probability or the number of activated channels at the same time as compared to the activation with hormones. In 2019, Jeong *et al.* identified three amino acid residues (K554, H594, E598) that may be involved in the binding and thus in the activation of TRPC5 by EA. These residues are located in the lower gate of TRPC5 and they are conserved among the TRPC family with TRPC1 being an exception [Jeong *et al.*, 2019]. However, current amplitudes of the mutants are considerably smaller than those of wild-type channels, making the interpretation of the data difficult.

I can show that EA is not only an agonist for TRPC4 and TRPC5 channels, but it also modulates L-type CaV currents. The Ca²⁺ influx is significantly reduced in the presence of 6 μM EA [Rodrigues *et al.*, 2016]. In contrast to the stimulatory effect on TRPC4 and TRPC5, EA seems to be an antagonist for the L-type CaV channels. The same results were obtained in current recordings of HEK-cells expressing CaV1.2 together with CaVβ2 subunits (Figure 35). EA had an inhibitory effect on L-type CaV channels but only at high concentrations (6 μM). Furthermore, EA was tested on CaV3.2 and CaV3.2 G1064R expressing cells. Also, here EA had an inhibitory effect at high concentrations and an EC₅₀ of 222 nM for both channels CaV3.2 wild-type and CaV3.2 mutant was calculated.

Since EA is inhibiting L-type and T-type CaV channels it is not a specific blocker for CaV channel subtypes. Moreover, it cannot be used as a non-specific CaV blocker for *in vivo* studies because of the required concentrations. EA would cause a Ca²⁺ influx into cells expressing TRPC4 or TRPC5 followed by cell death, as shown for cells overexpressing the gain-of-function mutations TRPC4 G503S and TRPC5 G504S (Beck *et al.*, 2013). Furthermore, Akbulut and colleagues showed that cell viability depends on the EA concentration (0.1 nM to 1 μM; IC₅₀ 28.1 nM) used to treat the cells. EA was further suggested as a drug to treat renal cell carcinoma due to its ability to increase activation of TRPC4 and TRPC5, resulting in an increased Ca²⁺ influx and cell death [Akbulut *et al.*, 2015]. In A498 cells, a human renal cell carcinoma model, EA-induced apoptosis, autophagy and necrosis with a LC₅₀ (lethal concentration) of 79 nM [Williams *et al.*, 2013]. According to the EC₅₀ for EA-induced inhibition of CaV3.2 (222 nM; Figure 46) the inhibition of CaV3.2 could contribute to these results. Moreover, the activation of TRPC4 or TRPC5 in cancer cells inhibits their proliferation and therefore the tumor cell growth. *In vivo* experiments with rodents show that EA is not stable in the blood serum and that concentrations (intravenous 1 mg/kg) needed to activate TRPC4 and TRPC5 are lethal [Carson *et al.*, 2015]. These concentrations are sufficient to block CaV currents.

References

- Akbulut, Y.**, Gaunt, H.J., Muraki, K., Ludlow, M.J., Amer, M.S., Bruns, A., Vasudev, N.S., Radtke, L., Willot, M., Hahn, S., *et al.* (2015). (-)-Englerin A is a potent and selective activator of TRPC4 and TRPC5 calcium channels. *Angew Chem Int Ed Engl* 54, 3787-3791.
- Alfonso, S.**; Benito, O.; Alicia, S.; Angelica, Z.; Patricia, G.; Diana, K.; Vaca, L. (2008) Regulation of the cellular localization and function of human transient receptor potential channel 1 by other members of the TRPC family. *Cell Calcium*, 43, 375–387.
- Antzelevitch, C.**, Pollevick, G. D., Cordeiro, J. M., Casis, O., Sanguinetti, M. C., Aizawa, Y., Guerchicoff, A., *et al.* (2007) L Loss-of-Function Mutations in the Cardiac Calcium Channel Underlie a New Clinical Entity Characterized by ST-Segment Elevation, Short QT Intervals, and Sudden Cardiac Death. *Circulation*. 115:442–449
- Arias, J. M.**, Murbartiána, J., Vitkoa, I., Leea, J-H. and Perez-Reyes, E. (2005) Transfer of β subunit regulation from high to low voltage-gated Ca^{2+} channels. *FEBS Letters* 579, 3907–3912.
- Asghar, M. Y.** and Törnquist, K. (2020) Transient Receptor Potential Canonical (TRPC) Channels as Modulators of Migration and Invasion. *Int J Mol Sci.*;21(5):1739.
- Autzen, H. E.**, Myasnikov, A. G., Campbell, M. G., Asarnow, D., Julius, D., and Cheng, Y. (2018) Structure of the human TRPM4 ion channel in a lipid nanodisc. *Science* 359, 228–232
- Azumaya, C. M.**, Sierra-Valdez, F., Cordero-Morales, J. F. and Nakagawa, T. (2018) Cryo-EM structure of the cytoplasmic domain of murine transient receptor potential cation channel subfamily C member 6 (TRPC6). *J. Biol. Chem.* 293(26) 10381–10391.
- Bae, J.**, Suh E. J. and Lee, C. (2010) Interaction of T-Type Calcium Channel $\text{Ca}_v3.3$ with the β -Subunit. *Mol. Cells* 30, 185-191.
- Baig, S. M.**, Koschak, A., Lieb, A., Gebhart, M., Dafinger, C., Nürnberg, G., Ali, A., *et al.* (2011) Loss of $\text{Cav}1.3$ (CACNA1D) function in a human channelopathy with bradycardia and congenital deafness. *Nature Neuroscience* volume 14, pages77–84.
- Beck, A.**, Götz, V., Qiao, S., Weissgerber, P., Flockerzi, V., Freichel, M. and Boehm, U. (2017) Functional Characterization of Transient Receptor Potential (TRP) Channel C5 in Female Murine Gonadotropes. *Endocrinology*, 158(4):887–902.
- Beck, A.**, Speicher, T., Stoerger, C., Sell, T., Dettmer, V., Jusoh, S.A., Abdulmughni, A., Cavalie, A., Philipp, S.E., Zhu, M.X., *et al.* (2013). Conserved gating elements in TRPC4 and TRPC5 channels. *J Biol Chem* 288, 19471-19483.
- Belkacemi, A.**, Hui, X., Wardas, B., Laschke, M. W., Wissenbach, U., Menger, M. D., Lipp, P., Beck, A. and Flockerzi V. (2018) IP_3 Receptor-Dependent Cytoplasmic Ca^{2+} Signals Are Tightly Controlled by $\text{Cav}\beta 3$. *Cell Reports* 22, 1339–1349
- Belkacemi, T.**, Niermann, A., Hofmann, L., Wissenbach, U., Birnbaumer, L., Leidinger, P., Backes, C., Meese, E., Keller, A., Bai, X., Scheller, A., Kirchhoff, F., Philipp, S. E., Weissgerber, P., Flockerzi, V. and Beck A. (2017) TRPC1- and

TRPC3-dependent Ca²⁺ signaling in mouse cortical astrocytes affects injury-evoked astrogliosis in vivo. *Glia*.;65(9):1535-1549.

Berger, S. M. and Bartsch, D. (2014) The role of L-type voltage-gated calcium channels Cav1.2 and Cav1.3 in normal and pathological brain function. *Cell Tissue Res.*;357(2):463-76.

Berggren, P.O., Yang, S.N., Murakami, M., Efanov, A.M., Uhles, S., Köhler, M., Moede, T., Fernström, A., Appelskog, I.B., Aspinwall, C.A., et al. (2004). Removal of Ca²⁺ channel β 3 subunit enhances Ca²⁺ oscillation frequency and insulin exocytosis. *Cell* 119, 273–284.

Besprozvannaya, M., Dickson, E., Li, H., Ginburg, K. S., Bers, D. M., Auwerx, J. and Nunnari, J. (2018) GRAM domain proteins specialize functionally distinct ER-PM contact sites in human cells. *eLife* 2018;7:e31019.

Blair, N. T., Kaczmarek, J. S. and Clapham, D. E. (2009) Intracellular calcium strongly potentiates agonist-activated TRPC5 channels. *J. Gen. Physiol.* Vol. 133 No. 5 525–546.

Breton, H. M., Harland, M. L., Auld, A. M. and Barritt, G. J. (2000) Evidence that the TRP-1 protein is unlikely to account for store-operated Ca²⁺ inflow in *Xenopus laevis* oocytes. *Mol Cell Biochem.*;214(1-2):63-74.

Broicher, T., Kanyshkova, T., Meuth, P., Pape, H-C. and Buddeet, T. (2008) Correlation of T-channel coding gene expression, I_T, and the low threshold Ca²⁺ spike in the thalamus of a rat model of absence epilepsy. *Molecular and Cellular Neuroscience* 39, 384–399.

Burgess, D. L., Jones, J. M., Meisler, M. H. and Noebels, J. L. (1997) Mutation of the Ca²⁺ Channel β Subunit Gene *Cchb4* Is Associated with Ataxia and Seizures in the Lethargic (lh) Mouse. *Cell*, Vol. 88, 385–392.

Cain, S. M. and Snutch, T. P. (2011) Voltage-gated calcium channels and disease. *Biofactors*, 37 (3), 197-205.

Cannon, S. C. (2010) Voltage-sensor mutations in channelopathies of skeletal muscle. *J Physiol* 588.11, pp 1887–1895.

Cao, E., Liao, M., Cheng, Y. and Julius, D. (2013) TRPV1 structures indistinct conformations reveal activation mechanisms. *Nature*, 504 (7478), 113-8.

Carbone, E. and Lux, H. D. (1984) A low voltage-activated calcium conductance in embryonic chick sensory neurons. *Biophys J* 46(3):413–418.

Carbone, E., Calorio, C. and Vandael, D. H. F. (2014) T-type channel-mediated neurotransmitter release. *Pflugers Arch - Eur J Physiol*, 466:677–687.

Carson, C., Raman, P., Tullai, J., Xu, L., Henault, M., Thomas, E., et al. (2015) Englerin A Agonizes the TRPC4/C5 Cation Channels to Inhibit Tumor Cell Line Proliferation. *PLoS ONE* 10(6): e0127498. doi:10.1371/journal.pone.0127498

Catterall, W. A. (2000) Structure and Regulation of Voltage-Gated Ca²⁺ Channels. *Annu Rev Cell Dev Biol*, 16, 521-55.

Catterall, W.A. (2011) Voltage-Gated Calcium Channels. *Cold Spring Harb Perspect Biol*;3: a003947.

- Chaudhari, N.** (1992) A single nucleotide deletion in the skeletal muscle-specific calcium channel transcript of muscular dysgenesis (mdg) mice. *J Biol Chem.*;267(36):25636-25639.
- Chemin, J.,** Monteil, A., Bourinet, E., Nargeot, J. and Lory, P. (2001) Alternatively Spliced α_{1G} (CaV3.1) Intracellular Loops Promote Specific T-Type Ca^{2+} Channel Gating Properties. *Biophysical Journal* 80(3) 1238–1250.
- Choi, M.,** Scholl, U. I., Yue, P., Björklund, P., Zhao, B., Nelson-Williams, C., Ji, W., Cho, Y., et al. (2011) K^+ Channel Mutations in Adrenal Aldosterone-Producing Adenomas and Hereditary Hypertension. *Science*, 331 (6018), 768-72.
- Clapham, D. E.,** Runnels, L. W. and Strübing, C. (2001) The TRP ion channel family. *Nat Rev Neurosci.*;2(6):387-96.
- Clapham, D. E.** (2007) Calcium Signaling. *Cell*, 131 (6), 1047-58.
- Cordeiro, J. M.,** Marieb, M., Pfeiffer, R., Calloe, K., Burashnikov, E., and Antzelevitch, C. (2009) Accelerated Inactivation of the L-type Calcium Current Due to a Mutation in CACNB2b Underlies Brugada Syndrome. *J Mol Cell Cardiol*; 46(5): 695–703.
- Cosens, D. J.** and Manning, A. (1969) Abnormal Electroretinogram from a *Drosophila* Mutant. *Nature* volume 224, pages285–287(1969).
- Courjaret, R.,** Hubrack, S., Daalis, A., Dib, M. and Machaca, K. (2013) The *Xenopus* TRPV6 homolog encodes a $\text{Mg}(2+)$ -permeant channel that is inhibited by interaction with TRPC1. *J Cell Physiol.*;228(12):2386-2398.
- Daniil, G.,** Fernandes-Rosa, F. L., Chemin, J., Blesneac, I., Beltrand, J., Polak, M., Jeunemaitre, X., Boulkroun, S., Amar, L., Strom, T. M., Lory, P. and Zennaro, M. C. (2016) CACNA1H Mutations Are Associated With Different Forms of Primary Aldosteronism. *EBioMedicine.*;13:225-236.
- Datta, H. K.,** MacIntyre, I. and Zaidi, M. (1990) Intracellular calcium in the control of osteoclast function. I. Voltage-insensitivity and lack of effects of nifedipine, BAYK8644 and diltiazem. *Biochem Biophys Res Commun*;167(1):183-8.
- Deitmer, J. W.** and Schild D. (2000) Ca^{2+} und pH: Ionenmessungen in Zellen und Geweben. Spektrum Akademischer Verlag; 1 edition.
- Dietrich, A.,** Kalwa, H., Storch, U., Mederos y Schnitzler, M., Salanova, B., & Pinkenburg, O., Dubrovskaja, G., Essin, K., Gollasch, M., Birnbaumer, L., and Gudermann, T. (2007) Pressure-induced and store-operated cation influx in vascular smooth muscle cells is independent of TRPC1. *Pflugers Arch - Eur J Physiol*, 455:465–477.
- Dietrich, A.,** Fahlbusch, M. and Gudermann, T. (2014) Classical Transient Receptor Potential 1 (TRPC1): Channel or Channel Regulator?. *Cells*, 3, 939-962.
- Dolphin, A. C.,** Wyatt, C. N., Richards, J., Beattie, R. E., Craig, P., Lee, J. H., Cribbs, L. L., Volsen, S. G. and Perez-Reyes, E. (1999) The effect of $\alpha 2\text{-}\delta$ and other accessory subunits on expression and properties of the calcium channel $\alpha 1G$. *J Physiol.*; 519(Pt 1): 35–45.
- Dong, X.P.,** Wang, X., Shen, D., Chen, S., Liu, M., Wang, Y., Mills, E., Cheng, X., Delling, M. and Xu, H. (2009) Affiliations expand Activating mutations of the TRPML1

channel revealed by proline-scanning mutagenesis. *J Biol Chem.*;284(46):32040-32052.

Duan, J., Lib, Z., Lie, J., Hulsea, R. E., Santa-Cruza, A., Valinskyc, W. C., Abiriaa, S. A., Krapivinskya, G., Zhanga, J. and Claphama, D. E. (2018) Structure of the mammalian TRPM7, a magnesium channel required during embryonic development. *Proc Natl Acad Sci U S A*, 115 (35), E8201-E8210.

Duan, J., Li, J., Zeng, B., Chen, G-L., Peng, X., Zhang, Y., Wang, J., Clapham, D. E., Li, Z. and Zhang, J. (2018) Structure of the mouse TRPC4 ion channel. *Nat Commun*, 9 (1), 3102.

Duan, J., Li, J., Chen, G-L., Ge, Y., Liu, J., Xie, K., Peng, X., Zhou, W., Zhong, J., Zhang, Y., Xu, J., Xue, C., Liang, B., Zhu, L., Liu, W., Zhang, C., Tian, X-L., Wang, J., Clapham, D. E., Zeng, B., Li, Z. and Zhang, J. (2019) Cryo-EM structure of TRPC5 at 2.8-Å resolution reveals unique and conserved structural elements essential for channel function. *Sci Adv*, 5 (7), eaaw7935.

Dubel, S. J., Altier, C., Chaumont, S., Lory, P., Bourinet, E., and Nargeot, J. (2004) Plasma Membrane Expression of T-type Calcium Channel $\alpha 1$ Subunits Is Modulated by High Voltage-activated Auxiliary Subunits. *J Biol Chem*, 279 (28), 29263-9.

Elzamzamy, O. M., Penner, R. and Hazlehurst, L. A. (2020) The Role of TRPC1 in Modulating Cancer Progression. *Cells.*;9(2):388.

Escayg, A., De Waard, M., Lee, D. D., Bichet, D., Wolf, P., Mayer, T., Johnston, J., Baloh, R., Sander, T. and Meisler, M. H. (2000) Coding and Noncoding Variation of the Human Calcium-Channel β_4 -Subunit Gene CACNB4 in Patients with Idiopathic Generalized Epilepsy and Episodic Ataxia. *Am J Hum Genet.*; 66(5): 1531–1539.

Fedulova, S. A., Kostyuk, P. G. and Veselovsky, N. S. (1985) Two Types of Calcium Channels in the Somatic Membrane of New-Born Rat Dorsal Root Ganglion Neurones. *J Physiol*, 359, 431-46.

Felizola, S. J. A., Maekawa, T., Nakamura, Y., Satoh, F., Ono, Y., Kikuchi, K., Aritomi, S., Ikeda, K., Yoshimura, M., Tojo, K. and Sasano, H. (2014) Voltage-gated calcium channels in the human adrenal and primary aldosteronism. *J Steroid Biochem Mol Biol*, 144 Pt B, 410-6.

Feng, S. (2017) TRPC Channel Structure and Properties. In: Wang Y, editor. *Transient Receptor Potential Canonical Channels and Brain Diseases*. Dordrecht: Springer Netherlands. p 9–23.

Flockerzi, V., Wardas, B., (in print) *Encyclopedia of Molecular Pharmacology*, Chapter: TRP channels, Springer-Verlag Berlin Heidelberg.

Freichel, M., Suh, S. H., Pfeifer, A., Schweig, U., Trost, C., Weissgerber, P., Biel, M., Philipp, S., Freise, D., Droogmans, G., Hofmann, F., Flockerzi, V. and Nilius, B. (2001) Lack of an endothelial store-operated Ca^{2+} current impairs agonist-dependent vasorelaxation in TRP4 $^{-/-}$ mice. *Nat Cell Biol.*;3(2):121-127.

Fukunaga, K., Izumi, H., Yabuki, Y., Shinoda, Y., Shioda, N. and Han, F. (2019) Alzheimer's disease therapeutic candidate SAK3 is an enhancer of T-type calcium channels. *J Pharmacol Sci*, 139 (2), 51-58.

Gregg, R. G., Messing, A., Strube, C., Beug, M., Moss, R., Behan, M., Sukhareva, M., Haynes, S., Powell, J. A., Coronado, R. and Powers, P. A. (1996) Absence of the

β subunit (cchb1) of the skeletal muscle dihydropyridine receptor alters expression of the α 1 subunit and eliminates excitation-contraction coupling. *Proc Natl Acad Sci U S A*, 93 (24), 13961-6.

Griffin, C. S., Bradley, E., Dudem, S., Hollywood, M. A., McHale, N. G, Thornbury, K. D. and Sergeant, G. P. (2016) Muscarinic Receptor Induced Contractions of the Detrusor are Mediated by Activation of TRPC4 Channels. *J Urol.*;196(6):1796-1808.

Grunewald, T. G. P. and Butt, E. (2008) The LIM and SH3 domain protein family: structural proteins or signal transducers or both?. *Mol Cancer*, 7, 31.

Hess, P., Lansman, J. B. and Tsien, R. W. (1984) Different modes of Ca channel gating behaviour favoured by dihydropyridine Ca agonists and antagonists. *Nature*, 311 (5986), 538-44.

Hirschi, M., Herzik Jr, M. A., Wie, J., Suo, Y., Borschel, W. F., Ren, D., Lander, G. C. and Lee, S-Y. (2017) Cryo-electron microscopy structure of the lysosomal calcium-permeable channel TRPML3. *Nature*, 550 (7676), 411-414.

Hofmann, F., Biel, M. and Flockerzi, V. (1994) Molecular Basis for Ca²⁺ Channel Diversity. *Annu Rev Neurosci*, 17, 399-418.

Hofmann, F., Flockerzi, V., Kahl, S. and Wegener, J. W. (2014) L-type CaV1.2 Calcium Channels: From in Vitro Findings to in Vivo Function. *Physiol Rev*, 94 (1), 303-26.

Hofmann, L., Wang, H., Zheng, W., Philipp, S. E., Hidalgo P., Cavalié, A., Chen, X-Z., Beck, A. and Flockerzi, V. (2017) The S4–S5 linker – gearbox of TRP channel gating. *Cell Calcium*, 67, 156-165.

Hofmann, T., Obukhov, A. G., Schaefer, M., Harteneck, C., Gudermann, T. and Schultz, G. (1999) Direct activation of human TRPC6 and TRPC3 channels by diacylglycerol. *Nature.*;397(6716):259-263.

Hofmann, T., Schaefer, M., Schultz, G. and Gudermann, T. (2002) Subunit composition of mammalian transient receptor potential channels in living cells. *Proc Natl Acad Sci U S A.*; 99(11): 7461–7466.

Hope, C. I., Sharp, D. M., Hemara-Wahanui, A., Sissingh, J.I., Lundon, P., Mitchell, E. A., Maw, M. A. and Clover, G. M. (2005) Clinical Manifestations of a Unique X-linked Retinal Disorder in a Large New Zealand Family With a Novel Mutation in CACNA1F, the Gene Responsible for CSNB2. *Clin Exp Ophthalmol*, 33 (2), 129-36.

Hughes, T. E. T., Lodowski, D. T., Huynh, K. W., Yazici, A., Del Rosario, J., et al. (2018) Structural basis of TRPV5 channel inhibition by econazole revealed by cryo-EM. *Nat Struct Mol Biol*, 25 (1), 53-60.

Jalkanen, R., Mäntyjärvi, M., Tobias, R., Isosomppi, J., Sankila, E-M., Alitalo, T. and Bech-Hansen, N. T. (2006) X linked cone-rod dystrophy, CORDX3, is caused by a mutation in the CACNA1F gene. *J Med Genet.*; 43(8): 699–704.

Jang, H. S. and Greenwood, J. A. (2009) Glycine-rich region regulates cysteine-rich protein 1 binding to actin cytoskeleton. *Biochem Biophys Res Commun*, 380 (3), 484-8.

Jeong, S. J., Ko, J., Kim, M., Park, K. C., Park, E. Y. J., Kim, J., Baik, Y., Wie, J., Cho, A. E., Jeon, J-H. and So, I. (2019) Englerin A-sensing charged residues for

- transient receptor potential canonical 5 channel activation. *Korean J Physiol Pharmacol.*;23(3):191-201.
- Katiyar, R.**, Weissgerber, P., Roth, E., Dörr, J., Sothilingam, V., Garrido, M. G., Beck, S. C., Seeliger M. W., Beck A., Schmitz F. and Flockerzi, V. (2015) Influence of the β 2-Subunit of L-Type Voltage-Gated Cav Channels on the Structural and Functional Development of Photoreceptor Ribbon Synapses. *Invest Ophthalmol Vis Sci.*;56(4):2312-24.
- Kepura, F.**, Braun, E., Dietrich, A. and Plant, T. D. (2020) TRPC1 Regulates the Activity of a Voltage-Dependent Nonselective Cation Current in Hippocampal CA1 Neurons. *Cells.*; 9(2): 459.
- Kim, J.**, Ko, J., Myeong, J., Kwak, M., Hong, C. and So, I. (2019) TRPC1 as a negative regulator for TRPC4 and TRPC5 channels. *Pflugers Arch*, 471 (8), 1045-1053.
- Lee, J-H.**, Gomora, J. C., Cribbs, L. L., and Perez-Reyes E. (1999) Nickel Block of Three Cloned T-Type Calcium Channels: Low Concentrations Selectively Block α 1H. *Biophys J*, 77 (6), 3034-42.
- Lee, K.**, Kim, J., Köhler, M., Yu, J., Shi, Y., Yang, S. N., Ryu, S. H. and Berggren, P. O. (2018) Blocking Ca^{2+} Channel β 3 Subunit Reverses Diabetes. *Cell Rep.*;24(4):922-934.
- Lemonnier, L.**, Trebak, M., and Putney Jr, J. W. (2009) Complex Regulation of the TRPC3,6,7 Channel Subfamily by Diacylglycerol and Phosphatidylinositol 4,5-bisphosphate. *Cell Calcium*. 43(5): 506–514.
- Lepannetier, S.**, Gualdani, R., Tempesta, S., Schakman, O., Seghers, F., Kreis, A., Yerna, X., Slimi, A., de Clippele, M., Tajeddine, N., Voets, T., Bon, R. S., Beech, D. J., Tissir, F. and Gailly, P. (2018) Activation of TRPC1 Channel by Metabotropic Glutamate Receptor mGluR5 Modulates Synaptic Plasticity and Spatial Working Memory. *Front Cell Neurosci.*;12:318.
- Li, H.** (2017) TRP Channel Classification. In: Wang Y, editor. *Transient Receptor Potential Canonical Channels and Brain Diseases*. Dordrecht: Springer Netherlands. p 1–8.
- Lieben, L.** and Carmeliet, G. (2012) The Involvement of TRP Channels in Bone Homeostasis. *Front Endocrinol (Lausanne)*;3:99.
- Link, S.**, Meissner, M., Held, B., Beck, A., Weissgerber, P., Freichel, M. and Flockerzi, V. (2009) Diversity and Developmental Expression of L-type Calcium Channel β 2 Proteins and Their Influence on Calcium Current in Murine Heart. *J Biol Chem*, 284 (44), 30129-37.
- Lintschinger, B.**, Balzer-Geldsetzer, M., Baskaran, T., Graier, W. F., Romanin, C., Zhu, M.X. and Groschner, K. (2000) Coassembly of Trp1 and Trp3 Proteins Generates Diacylglycerol- And Ca^{2+} -sensitive Cation Channels. *J Biol Chem*, 275 (36), 27799-805.
- Liu, X.**, Cheng, K. T., Bandyopadhyay, B. C., Pani, B., Dietrich, A., Paria, B. C., Swaim, W. D., et al. (2007) Attenuation of store-operated Ca^{2+} current impairs salivary gland fluid secretion in TRPC1(-/-) mice. *Proc Natl Acad Sci U S A*, 104 (44), 17542-7.

- Ludwig, A.**, Flockerzi, V. and Hofmann, F. (1997) Regional Expression and Cellular Localization of the $\alpha 1$ and β Subunit of High Voltage-Activated Calcium Channels in Rat Brain. *J Neurosci*, 17 (4), 1339-49.
- Ma, X.**, Chengc, K-T., Wonga, C-O., O'Neild, R. G. and Birnbaumere, L. (2011) Heteromeric TRPV4-C1 channels contribute to store-operated Ca^{2+} entry in vascular endothelial cells. *Cell Calcium*, 50 (6), 502-9.
- McEnergy, M. W.**, Vance, C. L., Begg, C. M. Lee, W-L., Choi, Y. and Dubel, S. J. (1998) Differential Expression and Association of Calcium Channel Subunits in Development and Disease. *J Bioenerg Biomembr*, 30 (4), 409-18.
- Miyauchi, A.**, Hruska, K. A., Greenfield, E. M., Duncan, R., Alvarez, J., Barattolo, R., Colucci, S., Zambonin-Zallone, A., Teitelbaum, S. L. and Teti, A. (1990) Osteoclast cytosolic calcium, regulated by voltage-gated calcium channels and extracellular calcium, controls podosome assembly and bone resorption. *J Cell Biol.*;111(6 Pt 1):2543-52.
- Monnier, N.**, Procaccio, V., Stieglitz, P. and Lunardi, J. (1997) Malignant-Hyperthermia Susceptibility Is Associated with a Mutation of the $\alpha 1$ -Subunit of the Human Dihydropyridine-Sensitive L-Type Voltage-Dependent Calcium-Channel Receptor in Skeletal Muscle. *Am J Hum Genet*, 60 (6), 1316-25.
- Monteil, A.**, Chemin, J., Bourinet, E., Mennessier, G., Lory, P. and Nargeot, J. (2000) Molecular and Functional Properties of the Human $\alpha 1G$ Subunit That Forms T-type Calcium Channels. *J Biol Chem*, 275 (9), 6090-100.
- Monteil, A.**, Chausson, P., Boutourlinsky, K., Mezghrani, A., Huc-Brandt, S., Blesneac, I., Bidaud, I., Lemmers, C., Leresche, N., Lambert, R. C. and Lory, P. (2015) Inhibition of Cav3.2 T-type Calcium Channels by Its Intracellular I-II Loop. *J Biol Chem.*;290(26):16168-76.
- Montell, C.** and Rubin, G. M. (1989) Molecular Characterization of the Drosophila Trp Locus: A Putative Integral Membrane Protein Required for Phototransduction. *Neuron*, 2 (4), 1313-23.
- Montell, C.**, Birnbaumer, L. and Flockerzi, V. (2002) The TRP Channels, a Remarkably Functional Family. *Cell*, 108 (5), 595-8
- Morimoto, R.**, Omata, K., Ito, S. and Satoh, F. (2018) Progress in the Management of Primary Aldosteronism. *Am J Hypertens*. 31(5): 522–531.
- Mu, F. T.**, Callaghan, J. M., Steele-Mortimer, O., Stenmark, H., Parton R. G., Campbell, P. L., McCluskey, J., Yeo, J. P., Tock, E. P. and Toh, B. H. (1995) EEA1, an Early Endosome-Associated Protein. *J Biol Chem*, 270 (22), 13503-11.
- Murakami, M.**, Yamamura, H., Suzuki, T., Kang, M-G., Ohya, S., Murakami, A., et al. (2003) Modified Cardiovascular L-type Channels in Mice Lacking the Voltage-dependent Ca^{2+} Channel $\beta 3$ Subunit. *J Biol Chem*, 278 (44), 43261-7.
- Murakami, M.**, Nakagawasaib, O., Yanaic, K., Nunokid, K., Tan-Nob, K., Tadanob, T. and Iijimaa, T. (2007) Modified behavioral characteristics following ablation of the voltage-dependent calcium channel $\beta 3$ subunit. *Brain Res*, 1160, 102-12.
- Namkung, Y.**, Smith, S. M., Lee, S. B., Skrypnik, N. V., Kim, H. L., Chin, H., Scheller, R. H., Tsien, R. W. and Shin, H. S. (1998) Targeted Disruption of the Ca^{2+} Channel $\beta 3$ Subunit Reduces N- And L-type Ca^{2+} Channel Activity and Alters the Voltage-

- Dependent Activation of P/Q-type Ca²⁺ Channels in Neurons. *Proc Natl Acad Sci U S A*, 95 (20), 12010-5.
- Nilius, B.** and Owsianik, G. (2011) The transient receptor potential family of ion channels. *Genome Biol*, 12 (3), 218.
- Nitert, M. D.**, Nagorny, C. L., Wendt, A., Eliasson, L. and Mulder, H. (2008) CaV1.2 rather than CaV1.3 is coupled to glucose-stimulated insulin secretion in INS-1 832/13 cells. *J Mol Endocrinol*;41(1):1-11.
- Ohmori, I.**, Ouchida, M., Miki, T., Mimaki, N., Kiyonaka, S., Nishiki, T., Tomizawa, K., Mori, Y. and Matsui, H. et al. (2008) A CACNB4 mutation shows that altered Ca_v2.1 function may be a genetic modifier of severe myoclonic epilepsy in infancy. *Neurobiol Dis*, 32 (3), 349-54.
- Ong, E. C.**, Nesin, V., Long, C. L., Bai, C-X., Guz, J. L., Ivanov, I. P., Abramowitz, J., Birnbaumer, L., Humphrey, M. B., and Tsiokas, L. (2013) A TRPC1 Protein-dependent Pathway Regulates Osteoclast Formation and Function. *J Biol Chem*, 288 (31), 22219-32.
- Otsuguro, K-i.**, Tang, J., Tang, Y., Xiao, R., Freichel, M., Tsvilovskyy, V., Ito, S., Flockerzi, V., Zhu, M. X. and Zholos, A. V. (2008) Isoform-specific inhibition of TRPC4 channel by phosphatidylinositol 4,5-bisphosphate. *J Biol Chem*;283(15):10026-36.
- Parekh, A. B.** and Penner, R. (1997) Store depletion and calcium influx. *Physiol Rev*, 77 (4), 901-30.
- Park, C. G.**, Park, Y. and Suh, B. C. (2017) The HOOK region of voltage-gated Ca²⁺ channel β subunits senses and transmits PIP₂ signals to the gate. *J Gen Physiol*;149(2):261-276.
- Paulsen, C. E.**, Armache, J-P., Gao, Y., Cheng, Y. and Julius, D. (2015) Structure of the TRPA1 ion channel suggests regulatory mechanisms. *Nature*, 520 (7548), 511-7.
- Perez-Reyes, E.** (2003) Molecular Physiology of Low-Voltage-Activated T-type Calcium Channels. *Physiol Rev*;83(1):117-61.
- Perez-Reyes, E.** (2006) Molecular characterization of T-type calcium channels. *Cell Calcium*, 40 (2), 89-96.
- Perez-Reyes, E.** (2010) G Protein-Mediated Inhibition of Cav3.2 T-Type Channels Revisited. *Mol Pharmacol*;77(2):136-8.
- Philipp, S.**, Cavalié, A., Freichel, M., Wissenbach, U., Zimmer, S., Trost, C., Marquart, A., Murakami, M. and Flockerzi V. (1996) A mammalian capacitative calcium entry channel homologous to *Drosophila* TRP and TRPL. *EMBO J*;15(22):6166-71.
- Philipp, S.**, Hambrecht, J., Braslavski, L., Schroth, G., Freichel, M., Murakami, M., Cavalié, A. and Flockerzi, V. (1998) A novel capacitative calcium entry channel expressed in excitable cells. *EMBO J*;17(15):4274-4282.
- Plant, T. D.** and Schaefer M. (2003) TRPC4 and TRPC5: receptor-operated Ca²⁺-permeable nonselective cation channels. *Cell Calcium*;33(5-6):441-50.

- Pragnell, M.**, De Waard, M., Mori, Y., Tanabe, T., Snutch, T. P. and Campbell, K. P. (1994) Calcium Channel Beta-Subunit Binds to a Conserved Motif in the I-II Cytoplasmic Linker of the Alpha 1-subunit. *Nature*, 368 (6466), 67-70.
- Qiao, S.**, Nordström, K., Muijs, L., Gasparoni, G., Tierling, S., Krause, E., Walter, J. and Boehm, U. (2016) Molecular Plasticity of Male and Female Murine Gonadotropes Revealed by mRNA Sequencing. *Endocrinology*;157(3):1082-93.
- Reimer, E. N.**, Walenda, G., Seidel, E. and Scholl, U. I. (2016) CACNA1H^{M1549V} Mutant Calcium Channel Causes Autonomous Aldosterone Production in HAC15 Cells and Is Inhibited by Mibefradil. *Endocrinology*, 157 (8), 3016-22.
- Reuter, H.** (1967) The dependence of slow inward current in Purkinje fibres on the extracellular calcium-concentration. *Physiol*;192(2):479-92.
- Riccio, A.**, Medhurst, A. D., Mattei C., Kelsell R. E., Calver A. R., Randall A. D., Benham C. D. and Pangalosa, M. N. (2002) mRNA distribution analysis of human TRPC family in CNS and peripheral tissues. *Brain Res Mol Brain Res*, 109 (1-2), 95-104.
- Rice, R. A.**, Berchtold, N. C., Cotman, C. W. and Green, K. N. (2014) Age-related downregulation of the CaV_{3.1} T-type calcium channel as a mediator of amyloid beta production. *Neurobiol Aging*, 35 (5), 1002-11.
- Richards, M. W.**, Leroy, J., Pratt, W. S. and Dolphin, A. C. (2007) The HOOK-domain between the SH3 and the GK domains of Cavbeta subunits contains key determinants controlling calcium channel inactivation. *Channels (Austin)*;1(2):92-101.
- Rock, M. J.**, Prenen, J., Funari, V. A., *et al.* (2008) Gain-of-function mutations in TRPV4 cause autosomal dominant brachyolmia. *Nat Genet*;40(8):999-1003.
- Rodrigues, T.**, Sieglitz, F., Somovilla, V. J., Cal, P. M. S. D., Galione, A., Corzana, F. and Bernardes, G. J. L. (2016) Unveiling (-)-Englerin A as a Modulator of L-Type Calcium Channels. *Angew Chem Int Ed Engl*, 55 (37), 11077-81.
- Ruth, P.**, Röhrkasten, A., Biel, M., Bosse, E., Regulla, S., Meyer, H. E., Flockerzi, V. and Hofmann, F. (1989) Primary structure of the beta subunit of the DHP-sensitive calcium channel from skeletal muscle. *Science*;245(4922):1115-1118.
- Sasaki, H.**, Saiki, A., Endo, K., Ban, N., Yamaguchi, T., Kawana, H., *et al.* (2009) Protective Effects of Efonidipine, a T- And L-type Calcium Channel Blocker, on Renal Function and Arterial Stiffness in Type 2 Diabetic Patients with Hypertension and Nephropathy. *J Atheroscler Thromb*, 16 (5), 568-75.
- Schaefer, M.**, Plant, T. D., Obukhov, A. G., Hofmann, T., Gudermann, T. and Schultz G. (2000) Receptor-mediated regulation of the nonselective cation channels TRPC4 and TRPC5. *J Biol Chem*;275(23):17517-26.
- Schaefer, M.**, Plant, T. D., Stresow, N., Albrecht, N. and Schultz, G. (2002) Functional differences between TRPC4 splice variants. *J Biol Chem*;277(5):3752-3759.
- Schindl, R.**, Fritsch, R., Jardin, I., Frischauf; I., Kahr, H., Muik, M., Riedl, M. C., Groschner, K. and Romanin, C. (2012) Canonical Transient Receptor Potential (TRPC) 1 Acts as a Negative Regulator for Vanilloid TRPV6-mediated Ca²⁺ Influx. *J Biol Chem*, 287 (42), 35612-20.

- Scholl, U. I.**, Stölting, G., Nelson-Williams, C., Vichot, A. A., Choi, M., et al. (2015) Recurrent gain of function mutation in calcium channel CACNA1H causes early-onset hypertension with primary aldosteronism. *Elife*, 4, e06315.
- Scholz, N.**, Gehring, J., Guan, C., Ljaschenko, D., Fischer, R., Lakshmanan, V., Kittel, R. J. and Langenhan, T. (2015) The Adhesion GPCR Latrophilin/CIRL Shapes Mechanosensation. *Cell Rep.*;11(6):866-874.
- Seisenberger, C.**, Specht, V., Welling, A., Platzner, J., Pfeifer, A., Kühbandner, S., Striessnig, J., Klugbauer, N., Feil, R. and Hofmann, F. (2000) Functional embryonic cardiomyocytes after disruption of the L-type alpha1C (Cav1.2) calcium channel gene in the mouse. *J Biol Chem.*;275(50):39193-39199.
- Selvaraj, S.**, Sun, Y., Watt, J. A., Wang, S., Lei, S., Birnbaumer, L. and Singh, B. B. (2012) Neurotoxin-induced ER stress in mouse dopaminergic neurons involves downregulation of TRPC1 and inhibition of AKT/mTOR signaling. *J Clin Invest*, 122 (4), 1354-67.
- Senatore, A.** and Spafford J. D. (2015) Physiology and Pathology of Voltage-Gated T-Type Calcium Channels. In: Schaffer SW, Li M, editors. *T-Type Calcium Channels in Basic and Clinical Science*. Vienna: Springer Vienna. p 3–17.
- Shen, P. S.**, Yang, X., DeCaen, P. G., Liu, X., Bulkley, D., Clapham, D. E. and Cao, E. (2016) The Structure of the Polycystic Kidney Disease Channel PKD2 in Lipid Nanodiscs. *Cell*, 167 (3), 763-773.e11.
- Shigematsu, H.**, Sokabe, T., Danev, R., Tominaga, M. and Nagayama; K. (2010) A 3.5-nm Structure of Rat TRPV4 Cation Channel Revealed by Zernike Phase-contrast Cryoelectron Microscopy. *J Biol Chem*, 285 (15), 11210-8.
- Silva, J-P.** and Ushkaryov, Y. A. (2010) The latrophilins, “split-personality” receptors. *Adv Exp Med Biol.*; 706: 59–75.
- Silva, J-P.**, Lelianovaa, V. G., Ermolyukb, Y. S., Vysokova, N., Hitchenc, P. G., Berninghausena, O. et al. (2011) Latrophilin 1 and its endogenous ligand Lasso/teneurin-2 form a high-affinity transsynaptic receptor pair with signaling capabilities. *Proc Natl Acad Sci U S A*, 108 (29), 12113-8.
- Singer, D.**, Biel, M., Lotan, I., Flockerzi, V., Hofmann, F. and Dascal, N. (1991) The roles of the subunits in the function of the calcium channel. *Science.*;253(5027):1553-7.
- Singh, A. K.**, Saotome, K., McGoldrick, L. L. and Sobolevsky, A. I. (2018) Structural bases of TRP channel TRPV6 allosteric modulation by 2-APB. *Nat Commun*, 9 (1), 2465.
- Singh, A. K.**, McGoldrick, L. L. and Sobolevsky, A. I. (2018) Structure and gating mechanism of the transient receptor potential channel TRPV3. *Nat Struct Mol Biol*, 25 (9), 805-813.
- Spät, A.** and Hunyady, L. (2004) Control of Aldosterone Secretion: A Model for Convergence in Cellular Signaling Pathways. *Physiol Rev*, 84 (2), 489-539.
- Spławski, I.**, Yoo, D. S., Stotz, S. C., Cherry, A., Clapham, D. E. and Keating, M. T. (2006) CACNA1H Mutations in Autism Spectrum Disorders. *J Biol Chem*, 281 (31), 22085-91.

- StAAF, S.**, Maxvall, I., Lind, U., Husmark, J., Mattsson, J. P., Ernfors, P. and Pierroua, S. (2009) Down regulation of TRPC1 by shRNA reduces mechanosensitivity in mouse dorsal root ganglion neurons in vitro. *Neurosci Lett*, 457 (1), 3-7.
- Stiber, J. A.**, Zhang, Z-S., Burch, J., Eu, J. P., Zhang, S. (2008) Mice Lacking Homer 1 Exhibit a Skeletal Myopathy Characterized by Abnormal Transient Receptor Potential Channel Activity. *Mol Cell Biol*, 28 (8), 2637-47.
- Storch, U.**, Forst, A-L., Philipp, M., Gudermann, T. and Mederos y Schnitzler, M. (2012) Transient Receptor Potential Channel 1 (TRPC1) Reduces Calcium Permeability in Heteromeric Channel Complexes. *J Biol Chem*, 287 (5), 3530-40.
- Storch, U.**, Forst, A-L., Pardatscher, F., Erdogmus, S., Philipp, M., Gregoritzka, M., Mederos y Schnitzler, M. and Gudermann, T. (2017) Affiliations expand Dynamic NHERF interaction with TRPC4/5 proteins is required for channel gating by diacylglycerol. *Proc Natl Acad Sci U S A.*;114(1):E37-E46.
- Strom, S. P.**, Stone, J. L., ten Bosch, J. R., Merriman, B., Cantor, R. M., Geschwind, D. H. and Nelson, S. F. (2010) High Density SNP Association Study of the 17q21 Chromosomal Region Linked to Autism Identifies CACNA1G as a Novel Candidate Gene. *Mol Psychiatry*, 15 (10), 996-1005.
- Strübing, C.**, Krapivinsky, G., Krapivinsky, L. and Clapham D. E. (2001) TRPC1 and TRPC5 Form a Novel Cation Channel in Mammalian Brain. *Neuron.*;29(3):645-55.
- Su, Q.**, Hu, F., Liu, Y., Ge, X., Mei, C., Yu, S., Shen, A. et al. (2018) Cryo-EM structure of the polycystic kidney disease-like channel PKD2L1. *Nat Commun*, 9 (1), 1192.
- Takahashi, M.**, Seagar, M. J., Jones, J. F., Reber, B. F. and Catterall, W. A. (1987) Subunit structure of dihydropyridine-sensitive calcium channels from skeletal muscle. *Proc Natl Acad Sci* 84(15):5478–5482.
- Talavera, K.** and Nilius, B. (2006) Biophysics and structure–function relationship of T-type Ca^{2+} channels. *Cell Calcium*, 40 (2), 97-114.
- Tang, Q.**, Guo, W., Zheng, L., Wu, J-X., Liu, M., Zhou, X., Zhang, X. and Chen, L. (2018) Structure of the receptor-activated human TRPC6 and TRPC3 ion channels. *Cell Res*, 28 (7), 746-755.
- Thakur, D. P.**, Tian, J-b., Jeon, J., Xiong, J., Huang, Y., Flockerzi, V. and Zhu, M. X. (2016) Critical roles of Gi/o proteins and phospholipase C- δ 1 in the activation of receptor-operated TRPC4 channels. *Proc Natl Acad Sci U S A.*;113(4):1092-7.
- Trost, C.**, Marquart, A., Zimmer, S., Philipp, S., Cavalié, A. and Flockerzi V. (1999) Ca^{2+} -dependent interaction of the trpl cation channel and calmodulin. *FEBS Lett.*;451(3):257-63.
- Trost, C.**, Bergs, C., Himmerkus, N. and Flockerzi, V. (2001) The transient receptor potential, TRP4, cation channel is a novel member of the family of calmodulin binding proteins. *Biochem J.*;355(Pt 3):663-70.
- Tsakiridou, E.**, Bertollini, L., de Curtis, M., Avanzini, G. and Pape, H-C. (1995) Selective Increase in T-Type Calcium Conductance of Reticular Thalamic Neurons in a Rat Model of Absence Epilepsy. *J Neurosci*, 15 (4), 3110-7.

- Tsiokas, L.**, Arnould, T., Zhu, C., Kim, E., Walz, G. and Sukhatme, V. P. (1999) Specific Association of the Gene Product of PKD2 with the TRPC1 Channel. *Proc Natl Acad Sci U S A*, 96 (7), 3934-9.
- Tsvilovskyy, V. V.**, Zholos, A. V., Aberle, T., Philipp, S. E., Dietrich, A., Zhu, M. X., Birnbaumer, L., Freichel, M. and Flockerzi, V. (2009) Deletion of TRPC4 and TRPC6 in mice impairs smooth muscle contraction and intestinal motility in vivo. *Gastroenterology*.;137(4):1415-24.
- Van Petegem, F.**, Clark, K. A., Chatelain, F. C., Minor, D. L. Jr. (2004) Structure of a complex between a voltage-gated calcium channel beta-subunit and an alpha-subunit domain. *Nature*.;429(6992):671-5.
- Van Petegem, F.**, Chatelain, F. C., Minor, D. L. Jr. (2005) Insights into voltage-gated calcium channel regulation from the structure of the CaV1.2 IQ domain-Ca²⁺/calmodulin complex. *Nat Struct Mol Biol*.;12(12):1108-15.
- Varga-Szabo, D.**, Authi, K. S., Braun, A., Bender, M., Ambily, A., Hassock, S. R., Gudermann, T. Dietrich, A. and Nieswandt, B. (2008) Store-operated Ca²⁺ entry in platelets occurs independently of transient receptor potential (TRP) C1. *Pflugers Arch*, 457 (2), 377-87.
- Vijayaraghavan, B.**, Jafferli, M. H., Figueroa, R. A. and Hallberg, E. (2016) Samp1, a RanGTP binding transmembrane protein in the inner nuclear membrane. *Nucleus*, 7 (4), 415-23.
- Wang, L.**, Fu, T-M., Zhou, Y., Xia, S., Greka, A. and Wu, H. (2018) Structures and gating mechanism of human TRPM2. *Science*, 362 (6421).
- Weissgerber, P.**, Held, B., Bloch, W., Kaestner, L., Chien, K. R., Fleischmann, B. K., Lipp, P., Flockerzi, V. and Freichel, M. (2006) Reduced Cardiac L-Type Ca²⁺ Current in Cavβ2 -/- Embryos Impairs Cardiac Development and Contraction with Secondary Defects in Vascular Maturation. *Circ Res*, 99 (7), 749-57.
- Wes, P. D.**, Chevesich, J., Jeromin, A., Rosenberg, C., Stetten, G. and Montell, C. (1995) TRPC1, a Human Homolog of a Drosophila Store-Operated Channel. *Proc Natl Acad Sci U S A*, 92 (21), 9652-6.
- Westheimer, F. H.** (1987) Why nature chose phosphates. *Science*, 235 (4793), 1173-8.
- Wieland, T.**, Hippe, H-J., Ludwig, K., Zhou, X-B. Korth, M. and Klumpp, S. (2010) Reversible Histidine Phosphorylation in Mammalian Cells: A Teeter-Totter Formed by Nucleoside Diphosphate Kinase and Protein Histidine Phosphatase 1. *Methods Enzymol*, 471, 379-402.
- Williams, R. T.**, Yu, A. L., Diccianni, M. B., Theodorakis, E. A. and Batova, A. (2013) Renal cancer-selective Englerin A induces multiple mechanisms of cell death and autophagy. *J Exp Clin Cancer Res*.;32(1):57.
- Wong King Yuen, S. M.**, Campiglioc, M., Tunga, C-C., Flucherc, B. E. and Van Petegema, P. (2017) Structural insights into binding of STAC proteins to voltage-gated calcium channels. *Proc Natl Acad Sci U S A*, 114 (45), E9520-E9528.
- Wu, J.**, Yan, Z., Li, Z., Yan, C., Lu, S., Dong, M. and Yan, N. (2015) Structure of the voltage-gated calcium channel Cav1.1 complex. *Science*.;350(6267):aad2395.

- Wu, Q.** and Krainer, A. R. (1999) AT-AC Pre-mRNA Splicing Mechanisms and Conservation of Minor Introns in Voltage-Gated Ion Channel Genes. *Mol Cell Biol*, 19 (5), 3225-36.
- Yang, S-N.** and Berggren, P-O. (2006) The Role of Voltage-Gated Calcium Channels in Pancreatic β -Cell Physiology and Pathophysiology. *Endocr Rev*, 27 (6), 621-76.
- Yin, Y.**, Wu, M., Zubcevic, L., Borschel, W. F., Lander, G. C. and Lee, S-Y. (2018) Structure of the Cold- And Menthol-Sensing Ion Channel TRPM8. *Science*, 359 (6372), 237-241.
- Yuan, J. P.**, Kiselyov, K., Shin, D. M., Chen, J., Shcheynikov, N., Kang, S.H. et al. (2003) Homer Binds TRPC Family Channels and Is Required for Gating of TRPC1 by IP₃ Receptors. *Cell*, 114 (6), 777-89.
- Zanou, N.**, Shapovalov, G., Louis, M., Tajeddine, N. Gallo, C., Van Schoor, M. et al. (2010) Role of TRPC1 channel in skeletal muscle function. *Am J Physiol Cell Physiol*, 298 (1), C149-62.
- Zanou, N.**, Schakman, O., Louis, P., Ruegg, U. T., Dietrich, A., Birnbaumer, L., and Gailly, P. (2012) Trpc1 Ion Channel Modulates Phosphatidylinositol 3-Kinase/Akt Pathway during Myoblast Differentiation and Muscle Regeneration. *J Biol Chem*, 287 (18), 14524-34.
- Zhang, P.**, Luo, Y., Chasan, B., González-Perrett, S., Montalbetti, N., Timpanaro, G. A. et al. (2009) The multimeric structure of polycystin-2 (TRPP2): structural-functional correlates of homo- and hetero-multimers with TRPC1. *Hum Mol Genet*, 18 (7), 1238-51.
- Zhang, S.**, Li, N., Zeng, W., Gao, N. and Yang, M. (2017) Cryo-EM structures of the mammalian endo-lysosomal TRPML1 channel elucidate the combined regulation mechanism. *Protein Cell*, 8 (11), 834-847.
- Zhao, Y.**, Huang, G., Wu, Q., Wu, K., Li, R., Lei, J., Pan, X. and Yan, N. (2019) Cryo-EM structures of apo and antagonist-bound human Ca_v3.1. *Nature*.;576(7787):492-497.
- Zheng, W.**, Cai, R., Hofmann, L., Nesin, V., Hu, Q., Long, W., Fatehi, M., Liu, X., Hussein, S., Kong, T., Li, J., Light, P. E., Tang, J., Flockerzi, V., Tsiokas, L. and Chen, X. Z. (2018) Direct Binding between Pre-S1 and TRP-like Domains in TRPP Channels Mediates Gating and Functional Regulation by PIP₂. *Cell Rep.*;22(6):1560-1573.
- Zheng, W.**, Hu, R., Cai, R., Hofmann, L., Hu, Q., Fatehi, M., Long, W. et al. (2018) Identification and characterization of hydrophobic gate residues in TRP channels. *FASEB J*, 32 (2), 639-653.
- Zheng, W.**, Yang, X., Hu, R., Cai, R., Hofmann, L., Wang, Z., Hu, Q., Liu, X., Bulkley, D., Yu, Y., Tang, J., Flockerzi, V., Cao, Y., Cao, E. and Chen, X. Z. (2018) Hydrophobic pore gates regulate ion permeation in polycystic kidney disease 2 and 2L1 channels. *Nat Commun.*;9(1):2302.
- Zhu X.**, Chu, P. B., Peyton, M. and Birnbaumer, L. (1995) Molecular cloning of a widely expressed human homologue for the *Drosophila* trp gene. *FEBS Lett.*;373(3):193-8.

Zhu, M. X. (2005) Multiple roles of calmodulin and other Ca²⁺-binding proteins in the functional regulation of TRP channels. *Pflugers Arch*, 451 (1), 105-15.

Zitt, C., Zobel, A., Obukhov, A. G., Harteneck, C., Kalkbrenner, F., Lückhoff, A. and Schultz, G. (1996) Cloning and Functional Expression of a Human Ca²⁺-permeable Cation Channel Activated by Calcium Store Depletion. *Neuron*, 16 (6), 1189-96.

Zubcevic, L., Herzik Jr, M. A., Chung, B. C., Liu, Z., Lander, G. C. and Lee, S-Y. (2016) Cryo-electron microscopy structure of the TRPV2 ion channel. *Nat Struct Mol Biol*, 23 (2), 180-186.

Zufall, F. (2005) The TRPC2 ion channel and pheromone sensing in the accessory olfactory system. *Naunyn Schmiedebergs Arch Pharmacol.*;371(4):245-250.

Appendix

- 5.1 Cell lines and plasmids
- 5.2 TRPC4/TRPC1 cRNA expression in *Xenopus laevis* oocytes
 - 5.2.1 Mutations of the lower gate of TRPC1
 - 5.2.2 Characterization of the TRPC4 β -C1_{S5-S6 linker} chimera in *Xenopus laevis* oocytes
- 5.3 Additional characterization of the TRPC4 α -C1_{S5-S6 linker} chimeras in HEK-cells
 - 5.3.1 Coexpression of TRPC4 α -C1_{S5-S6 linker} with TRPC4 α and stimulation with hormones (CCh plus DAMGO) and with Englerin A (EA)
 - 5.3.2 Coexpression of TRPC4 β -C1_{S5-S6 linker} chimera 1 or 2 with TRPC4 β and stimulation with hormone (CCh)
 - 5.3.3 Coexpression of TRPC4 α -C1_{S5-S6 linker} with TRPC1 and stimulation with hormones (CCh plus DAMGO) and with Englerin A (EA)
- 5.4 Functional interaction of TRPC4 with non-TRPC proteins
 - 5.4.1 Summary: Functional interaction of TRPC4 with non-TRPC proteins

5.1 Cell lines and plasmids

Table A1 Immortal cell lines. Cells stable expressing plasmids of indicated channels used for measurements. Each cell line was cultured in indicated culture medium containing FBS and antibiotics at 37 °C and 5 % CO₂. The HEK293, FLP TRex293, HEK μ OR and HEKM2R are from human embryonic kidney. The Ins-1 cells are from pancreas tissue. The abbreviation h. i. stands for heat inactivated.

Cell line	Plasmids	Culture medium	Source
HEK293	-----	MEM 31095-029; 10 % FBS	ATCC CRL 1573
FLP TRex 293	hCaV3.2 pcDNA 5 FRT/TO	DMEM 41965-039; 10 % FBS, 100 μ g/ml Hygromycin B, 2 mM Glutamax	this study
FLP TRex 293	hCaV3.2 G3190A Myc- Flag pcDNA 5 FRT/TO	DMEM 41965-039; 10 % FBS, 100 μ g/ml Hygromycin B, 2 mM Glutamax	this study
FLP TRex 293	pSB177.13 α 1C long N- term pcDNA 5 FRT/TO	DMEM 41965-039; 10 % FBS, 100 μ g/ml Hygromycin B, 2 mM Glutamax	Link <i>et al.</i> , 2009
Ins-1	-----	RPMI 1640; 10 % FBS, 50 μ M β - Mercaptoethanol, 1 mM Na-Pyruvat, 10 mM HEPES, Penicillin/Streptomycin	gift from Prof. Dr. P.-O. Berggren, Karolinska-Institut, Stockholm
HEK μ OR	pSB225_17 koz mTRPC4- Myc-stop koz mTRPC1 VLd-Myc stop/clone D2	DMEM 41966-029; 10 % FBS, 100 μ g/ml Hygromycin B, 500 μ g/ml G 418	gift from Prof. Dr. M. X. Zhu, Houston
HEK μ OR	TRPC4 α	DMEM 41966-029; 10 % h. i. FBS 100 μ g/ml Hygromycin B 500 μ g/ml G 418	gift from Prof. Dr. M. X. Zhu, Houston
HEK μ OR	-----	DMEM 41966-029; 10 % h. i. FBS 100 μ g/ml Hygromycin B	gift from Prof. Dr. M. X. Zhu, Houston
HEK μ OR	TRPC1 VL	DMEM 41966-029; 10 % h. i. FBS 100 μ g/ml Hygromycin B	this study

Cell line	Plasmids	Culture medium	Source
HEKM2R		DMEM 41966-029; 10 % h. i. FBS 100 µg/ml Hygromycin B	gift from Prof. Dr. M. X. Zhu, Houston
HEKM2R	TRPC5	DMEM 41966-029; 10 % h. i. FBS 100 µg/ml Hygromycin B 500 µg/ml G 418	gift from Prof. Dr. M. X. Zhu, Houston

Table A2 List of transfected plasmids. Different cell lines were transfected with indicated plasmids using the transfection reagents indicated.

Cell line	Plasmid	cDNA	Vector	Transfection reagent
FLP TRex 293	pSB94_17	CaV β 1a	pcAGGS IRES GFP	Biotool
FLP TRex 293	pSB98_13	CaV β 1b	pcAGGS IRES GFP	Biotool
HEK293	pSB395_9	m β 3	pcAGGS IRES GFP	Biotool or FuGene HD
HEK293	pSB14_23	β 2N3a	pcAGGS IRES GFP	Biotool or FuGene HD
HEK293	pSB15_28	β 2N3b	pcAGGS IRES GFP	Biotool or FuGene HD
HEK293	pSB18_5	β 2N4a	pcAGGS IRES GFP	Biotool or FuGene HD
HEK293	pSB156b_1 6	α 1C	pcAGGS IRES RFP	Biotool
HEK293	pSB176_6	α 1C long N-term	pcAGGS IRES RFP	Biotool
HEK293	pSB205_12	hCaV3.2 Δ ex26	Myc_Flag pcAGGS IRES GFP	FuGene HD
HEK293	pSB238_34	hCaV3.2 G3190A Δ ex26	Myc_Flag pcAGGS IRES Tag RFP-T	FuGene HD
HEK μ OR pSB225_17/ HEK293 TRPC4 α	pSB285	hEEA1	pEGFP_C1_Tag RFP-T	Lipofectamine 3000

Cell line	Plasmid	cDNA	Vector	Transfection reagent
HEK μ OR pSB225_17/ HEK293 TRPC4 α		TMEM 201	pcAGGS IRES GFP	Lipofectamine 3000
HEK293 TRPC4 α		STAC1	pcDNA3 GFP	Lipofectamine 3000
HEK μ OR pSB225_17/ HEK μ OR TRPC4 α		Latrophilin2	pcAGGS IRES GFP	Lipofectamine 3000
HEK μ OR TRPC4 α / HEKM2R TRPC5	pSB478_2	mNDPK-B	pcAGGS IRESTag RFP-T	Lipofectamine 3000
HEK μ OR TRPC4 α / HEKM2R TRPC5	pSB479_18	mNDPK-B H118N	pcAGGS IRESTag RFP-T	Lipofectamine 3000
HEK μ OR	pSB518_24	mTRPC4 α	IGFP pMax	Lipofectamine 3000
HEK μ OR TRPC4 α	pSB480c_3	mGramd1a GFP	IGFP pMax	Lipofectamine 3000
HEK μ OR TRPC4 α	pSB484_6	mGramd3 GFP	IGFP pMax	Lipofectamine 3000
HEK μ OR TRPC4 α / HEK μ OR	pSB355_7	mTRPC1VL	IGFP pMax	Lipofectamine 3000
HEK μ OR TRPC4 α / HEK μ OR	pSB356_8	mTRPC1VL V741Q	IGFP pMax	Lipofectamine 3000
HEK μ OR TRPC4 α	pSB357_19	mTRPC1VL V741S	IGFP pMax	Lipofectamine 3000
HEK μ OR TRPC4 α	pSB358_22	mTRPC1VL V741T	IGFP pMax	Lipofectamine 3000
HEK μ OR TRPC4 α	pSB359_26	mTRPC1VL V741G	IGFP pMax	Lipofectamine 3000
HEK μ OR TRPC4 α	pSB360_34	mTRPC1VL M642Q	IGFP pMax	Lipofectamine 3000
HEK μ OR TRPC4 α	pSB361_38	mTRPC1VL F639T	IGFP pMax	Lipofectamine 3000
HEK μ OR TRPC4 α	pSB367_17	mTRPC1VL V741N	IGFP pMax	Lipofectamine 3000
HEK μ OR TRPC4 α	pSB372_22	mTRPC1VL E755S	IGFP pMax	Lipofectamine 3000
HEK μ OR TRPC4 α / HEK μ OR	pSB432_25	mTRPC1VL V741A	IGFP pMax	Lipofectamine 3000

Cell line	Plasmid	cDNA	Vector	Transfection reagent
HEK μ OR TRPC4 α	pSB 567	TRPC1 short V611A	IRFP pMax	Lipofectamine 3000
HEK μ OR TRPC4 α	pSB460_1	mTRPC1VL M743A	IGFP pMax	Lipofectamine 3000
HEK μ OR TRPC4 α	pSB461_22	mTRPC1VL L744A	IGFP pMax	Lipofectamine 3000
HEK μ OR TRPC4 α	LH/UW	eGFP-TRPC4- C1 Pore	IGFP pMax	Lipofectamine 3000
HEK μ OR TRPC4 α	pSB293_1	GFP	IRES GFP pMax	Lipofectamine 3000
HEK293	pSB	GFP	pcAGGS IRES GFP	Biotool or FuGene HD
HEK μ OR pSB225_17	LH	GFP	pcAGGS IRES GFP	Lipofectamine 3000
HEK293		GFP	pcDNA3 GFP II	Biotool or FuGene HD
HEK μ OR pSB225_17	pSB230_6	RFP	Tag RFP-T pMax	Lipofectamine 3000
HEK M2R	pSB 570	TRPC4 β -C1 Pore1	IRFP pMax	Lipofectamine 3000
HEK M2R	pSB 571	TRPC4 β -C1 Pore2	IRFP pMax	Lipofectamine 3000
HEK M2R		TRPC4 short	IGFP pCAGGS	Lipofectamine 3000
HEK M2R	pSB 537	TRPC1short	IRFP pMax	Lipofectamine 3000

Table A3 List of plasmids used for cRNA synthesis. The plasmids were used for the *in vitro* transcription to cRNA for injection into the *Xenopus laevis* oocytes.

Plasmid	cDNA	Vector
pSB 587	TRPC1 short MALK-GFRT	pMXT MCS
pSB 589	TRPC1 short MALK-GFRT V611A	pMXT MCS
mTRPC4 β -pSGEM Klon L13-12.1	TRPC4 β	pSGEM
pSB 592	TRPC4 β -C1 Pore1	pMXT MCS
pSB 593	TRPC4 β -C1 Pore2	pMXT MCS

5.2 TRPC4 β /TRPC1 cRNA expression in *Xenopus laevis* oocytes

Although *Xenopus laevis* oocytes do endogenously express TRPC1 [Brereton *et al.*, 2000] they have been demonstrated to be a valid expression system to study structure-function relationships of TRP channel [Zhen *et al.*, 2018a; Zhen *et al.*, 2018b; Zhen *et al.*, 2018c]. To validate the results obtained in the HEK-cell system, we subcloned the cDNA of TRPC4 β , TRPC1 and their mutants in the vectors pSGEM or pMXT, respectively, for cRNA synthesis. *In vitro* transcription was performed as described in Material and Methods (2.3.5).

5.2.1 Mutations of the lower gate of TRPC1

First, we subcloned a truncated version of mouse TRPC1 (TRPC1ss: Δ 1-47; Δ 800-809; ensemble genome TRPC1 transcript 204) corresponding to the truncated TRPC4 construct used for the cryo-EM structure by Duan *et al.*, 2018. Figure A1 A shows a schematic comparison of mouse TRPC1 VL and TRPC1ss. In addition, the corresponding TRPC1 VL V741A mutation was introduced to the TRPC1ss construct (TRPC1ss V611A). The cRNA of TRPC1ss or TRPC1ss V611A constructs were injected into oocytes either alone or together with the TRPC4 β cRNA and after two days TEVC experiments were performed.

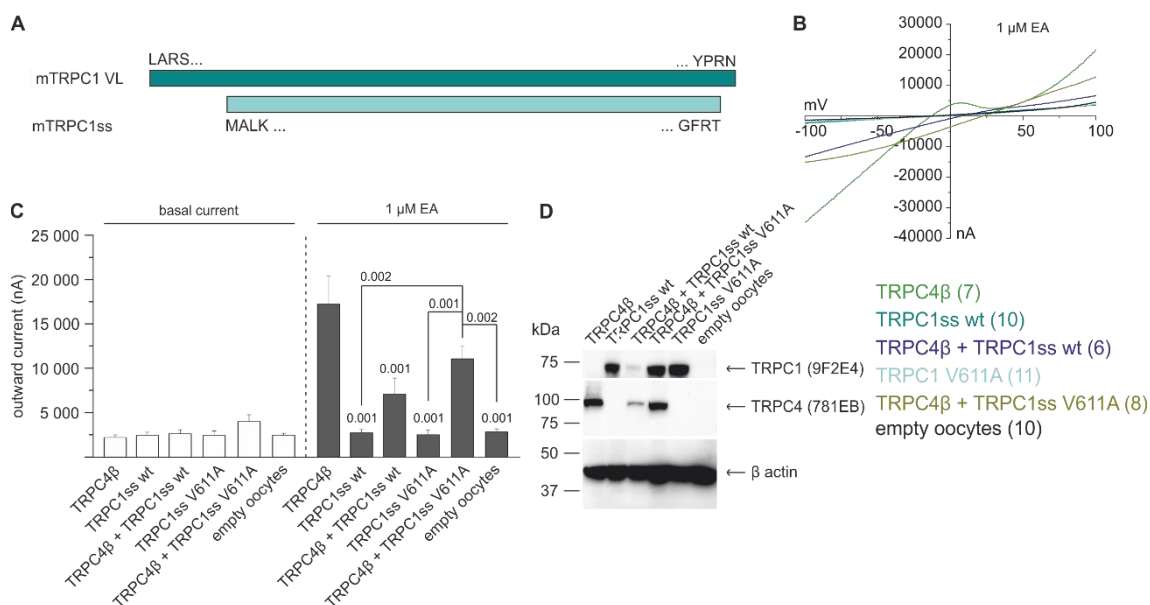


Figure A1 TRPC1ss V611A heterologous protein expression in *Xenopus laevis* oocytes. **A** Comparison of TRPC1 VL (892 aa; top) and TRPC1ss (742 aa; bottom) amino acid sequence. **B** Current-voltage relationship of TRPC4 β (green), TRPC1ss wt (petrol), TRPC4 β /TRPC1ss wt (purple), TRPC1ss V611A (light blue), TRPC4 β /TRPC1ss V611A (olive) and empty (black) oocytes in the presence of 1 μ M EA. **C** Current amplitudes at +80 mV in absence (white boxes) and presence (black boxes) of EA. **D** Western blot of the oocytes from B for TRPC1 (9F2E4) and TRPC4 (781EB). Actin was used as a control. Data in B are shown as mean and in C as mean \pm SEM. The numbers on top of the bars are the p-values compared to TRPC4 β and the number of experiments are shown in parenthesis.

EA induced in oocytes the same double rectifying TRPC4 current (basal 2203.28 ± 290.02 nA; EA 17276.43 ± 3112.4 nA) as in HEK-cells, while TRPC1ss expressed alone could not be detected (basal 2448.8 ± 345.8 nA; EA: 2746 ± 365.82 nA; Figure A1 B). However, the coexpression of TRPC4 β and TRPC1ss lead to a soup ladle like current (basal 2636.66 ± 437.15 nA; EA 7111.66 ± 1783.28 nA), the same applied for the coexpression of TRPC4 β and TRPC1ss V611A (basal 4012.37 ± 756.85 nA; EA 11067.12 ± 1408.81 nA). While the expression of TRPC1ss V611A alone did not result in an EA-inducible current (basal 2439.27 ± 498.83 nA; EA 2521.73 ± 509.9 nA). Both TRPC1ss and TRPC1ss V611A had the same basal current, which was not different to the basal current of non-injected oocytes (basal 2457.3 ± 225.56 nA; EA 2839.4 ± 334.75 nA; Figure A1 B, C). After each current recording the oocytes were collected for Western Blot to control the protein expression. It made no difference whether the cRNAs of the respective constructs were injected alone or together, all proteins were detected with their specific antibody (Figure A1 D).

Compared to the experiments with the corresponding constructs in HEK-cells, the TRPC1ss V611A did not significantly increased the TRPC4/TRPC1 current in oocytes.

5.2.2 Characterization of the TRPC4 β -C1_{S5-S6 linker} chimera in *Xenopus laevis* oocytes

Next, we cloned the two TRPC4 β -C1_{S5-S6 linker} chimera 1 and 2 (Figure 26 A) into the pMXT-MSC vector, transcribed the cRNA *in vitro* and injected the cRNAs into oocytes for protein surface biotinylation, TEVC and Western Blot. Both chimeras were expressed in the oocytes (Figure A2 A left blot) and both chimeras were also detected in the protein surface biotinylation, but, the TRPC4 β -C1_{S5-S6 linker} chimera 2 was translocated better to the plasma membrane than TRPC4 β -C1_{S5-S6 linker} chimera 1 (Figure A2 A middle blot). Since the proteins were translocated to the plasma membrane, the constructs were used for TEVC experiments expressed either alone or with TRPC4 β (Figure A2 B). EA did not induce any current in oocytes expressing the TRPC4 β -C1_{S5-S6 linker} chimera 1 (basal 2045.91 ± 264.31 nA; EA 2023.55 ± 291.59 nA) and TRPC4 β -C1_{S5-S6 linker} chimera 2 (basal 2157.22 ± 327.04 nA; Figure A2 B, C). Neither TRPC4 β -C1_{S5-S6 linker} chimera 1 nor TRPC4 β -C1_{S5-S6 linker} chimera 2 had an impact on the basal current in oocytes. In HEK-cells the presence of both chimeras had increased break-in currents (Figure 26). Coexpressed with TRPC4 β a TRPC4 shaped current was detected, however, the presence of TRPC4 β -C1_{S5-S6 linker} chimera 1 (basal 3558.3 ± 494.58 nA; EA 6412.5 ± 629.3 nA) decreased the current, while the presence of TRPC4 β -C1_{S5-S6 linker} chimera 2 (basal 2852.2 ± 295.93 nA; EA 18598.1 ± 4001.46 nA) had no impact on the current

amplitude compared to the TRPC4 β current (basal 3048 ± 431.85 nA; EA 18936.1 ± 3060.12 nA; Figure A2 C). Although no current was detectable in the presence of one of the chimeras without TRPC4 β expressed, the proteins were expressed (Figure A2 D). The different results obtained in the oocyte and the HEK-cell expression system require additional experiments in the future.

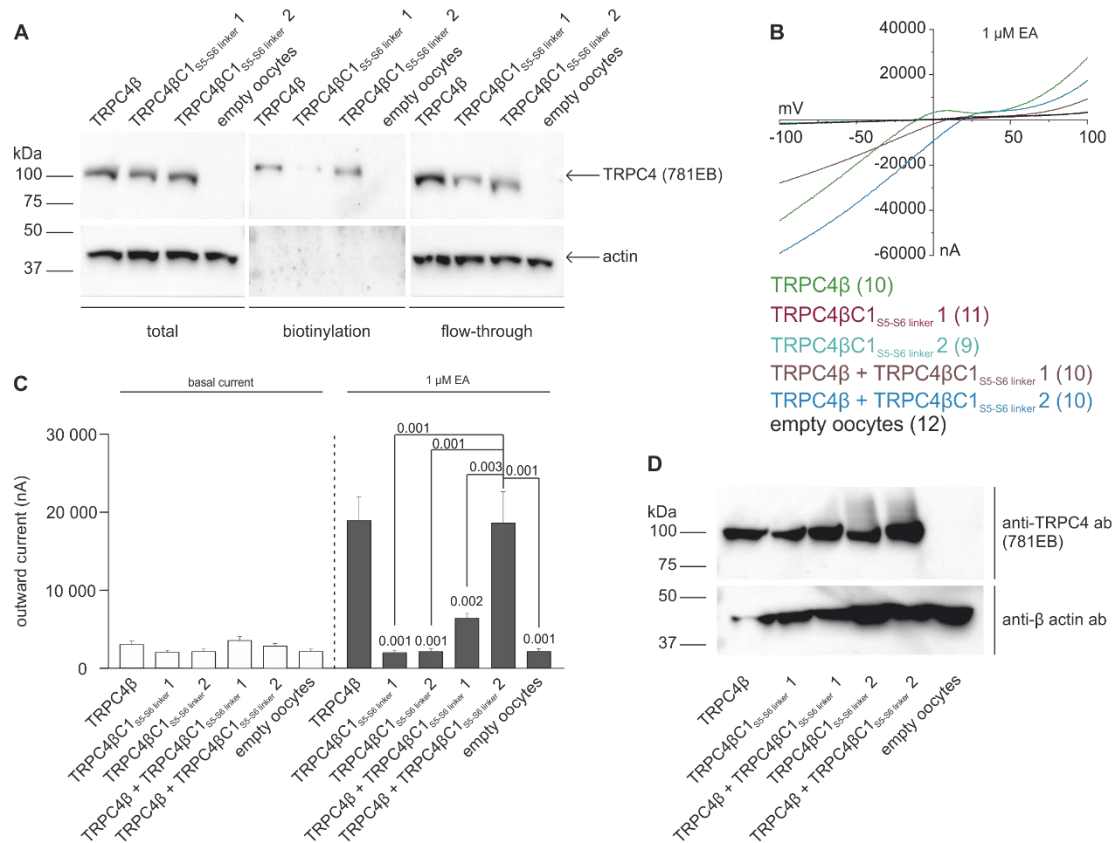


Figure A2 TRPC4 β -C1^{S5-S6 linker} chimera currents in *Xenopus laevis* oocytes. **A** Protein surface biotinylation of TRPC4 β , TRPC4 β -C1^{S5-S6 linker} chimera 1 and TRPC4 β -C1^{S5-S6 linker} chimera 2 in oocytes with the total protein before biotinylation (left blot), the biotinylation (middle blot) and the flow-through (right blot). The flow-through shows the proteins, which did not bound to the Streptavidin beads. **B** Current-voltage relationship in the presence of 1 μ M EA of the TRPC4 β -C1^{S5-S6 linker} chimera alone or expressed with TRPC4 β . **C** Current amplitudes in the absence (white boxes) and presence (black boxes) of 1 μ M EA. **D** Western Blot of oocytes used in B with actin as loading control. In B the data are shown as mean and in C as mean \pm SEM. The numbers on top of the bars are the p-values compared to TRPC4 β . Number of experiments are shown in parenthesis.

5.3 Additional characterization of the TRPC4 α -C1_{S5-S6 linker} chimeras in HEK-cells

5.3.1 Coexpression of TRPC4 α -C1_{S5-S6 linker} with TRPC4 α and stimulation with hormones (CCh plus DAMGO) and with Engerlin A (EA)

The TRPC4 α -C1_{S5-S6 linker} chimera (Figure 26 A) was transfected in μ OR cells stably expressing TRPC4 α .

In TRPC4 α stably expressing cells, the presence of the TRPC4 α -C1_{S5-S6 linker} chimera significantly decreased the current with the typical TRPC4 current-voltage relationship, when coexpressed with TRPC4 α (Figure A3 A-D). In stably TRPC4 α expressing cells the coexpression of the TRPC4 α -C1_{S5-S6 linker} chimera, significantly reduced the

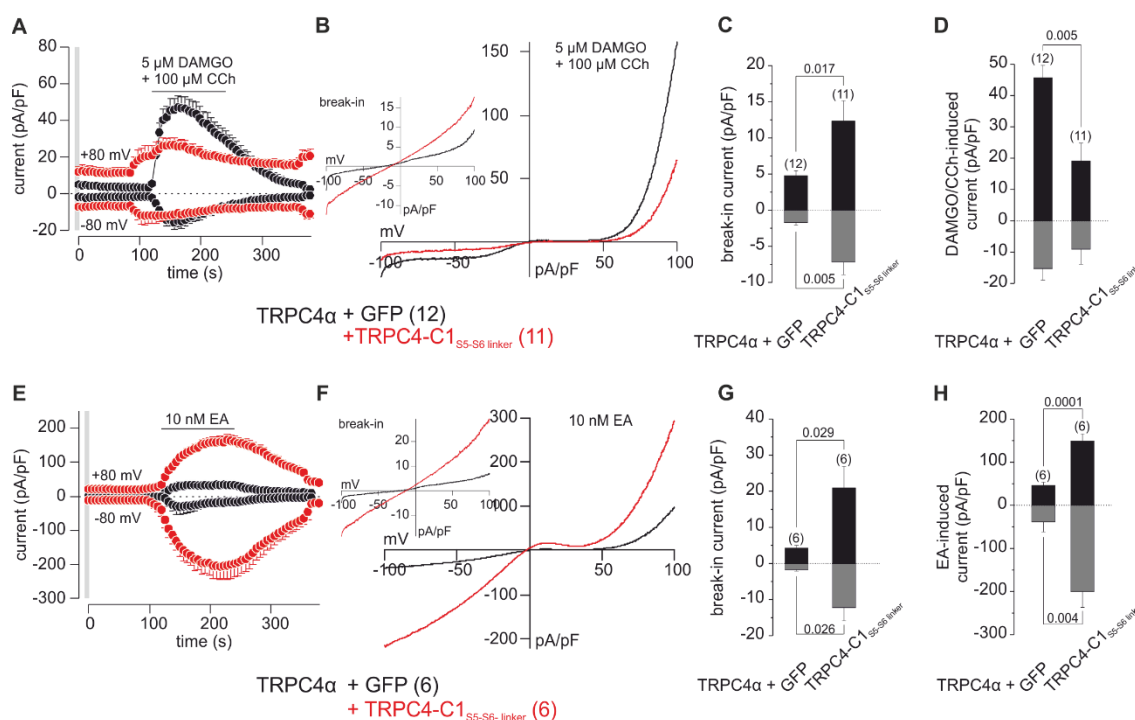


Figure A3 TRPC4 α -C1_{S5-S6 linker} chimera in stable expressing TRPC4 α cells. A Current over time of DAMGO/CCh (5 μ M/100 μ M)-induced current in presence (red) and absence (black) of the TRPC4 α -C1_{S5-S6 linker} chimera. **B** Current-voltage relationship of maximal DAMGO/CCh-induced current of TRPC4 α and TRPC4 α -C1_{S5-S6 linker} chimera coexpressing cells with the break-in currents shown in the inset. **C** Break-in current from A as bar graph. **D** Comparison of the maximal current amplitude between TRPC4 α /GFP and TRPC4 α /TRPC4 α -C1_{S5-S6 linker} chimera. **E** EA-induced outward and inward currents plotted over time for TRPC4 α cells coexpressing with GFP control (black) or the TRPC4 α -C1_{S5-S6 linker} chimera (red). **F** Current-voltage relationship in the presence and absence of the TRPC4 α -C1_{S5-S6 linker} chimera with the break-in currents in the inset. **G** Amplitudes of break-in currents of GFP control versus TRPC4 α -C1_{S5-S6 linker} chimera. **H** Maximal current amplitudes of TRPC4 alone or coexpressed with the TRPC4 α -C1_{S5-S6 linker} chimera. All data are shown as mean \pm SEM (A, C, D, E, G, H) and mean (B, F). For statistical analysis one-way ANOVA followed by the Bonferroni correction was used and the p-values are indicated on top of the bars. Number of experiments are shown in parenthesis. For the current-voltage relationships the basal current was subtracted (B, F). The gray bar in A and E shows the break-in currents shown in the inset of B and F.

DAMGO/CCh-induced outward currents (GFP 45.69 ± 6.37 pA/pF, $n = 12$; chimera 19.07 ± 5.75 pA/pF, $n = 11$), while the inward currents (GFP -15.24 ± 3.65 pA/pF; chimera -9.06 ± 4.84 pA/pF) were unchanged (Figure A3 A, D). Although the current was reduced due to the coexpressing of the TRPC4 α -C1_{S5-S6 linker} chimera, the current shape was unchanged and looked like a TRPC4 current (Figure A3 B). However, the presence of TRPC4 α -C1_{S5-S6 linker} chimera significantly increased the basal outward current (GFP 4.73 ± 0.67 pA/pF; chimera 12.33 ± 2.82 pA/pF) and the basal inward current (GFP -1.70 ± 0.35 pA/pF; chimera -7.20 ± 1.73 pA/pF) detected right after the break-in compared to the control (Figure A3 C).

The same experiments were done with EA instead of DAMGO/CCh. EA significantly increased the outward (GFP 41.63 ± 11.92 pA/pF, $n = 6$; chimera 149.01 ± 16.77 pA/pF, $n = 6$) and the inward currents (GFP -38.29 ± 23.69 pA/pF; chimera -199.93 ± 36.74 pA/pF) in the presence TRPC4 α -C1_{S5-S6 linker} chimera (Figure A3 E, H). Although the current was increased in the presence of the TRPC4 α -C1_{S5-S6 linker} chimera, the shape of the current was unchanged (Figure A3 F). Moreover, the break-in current was

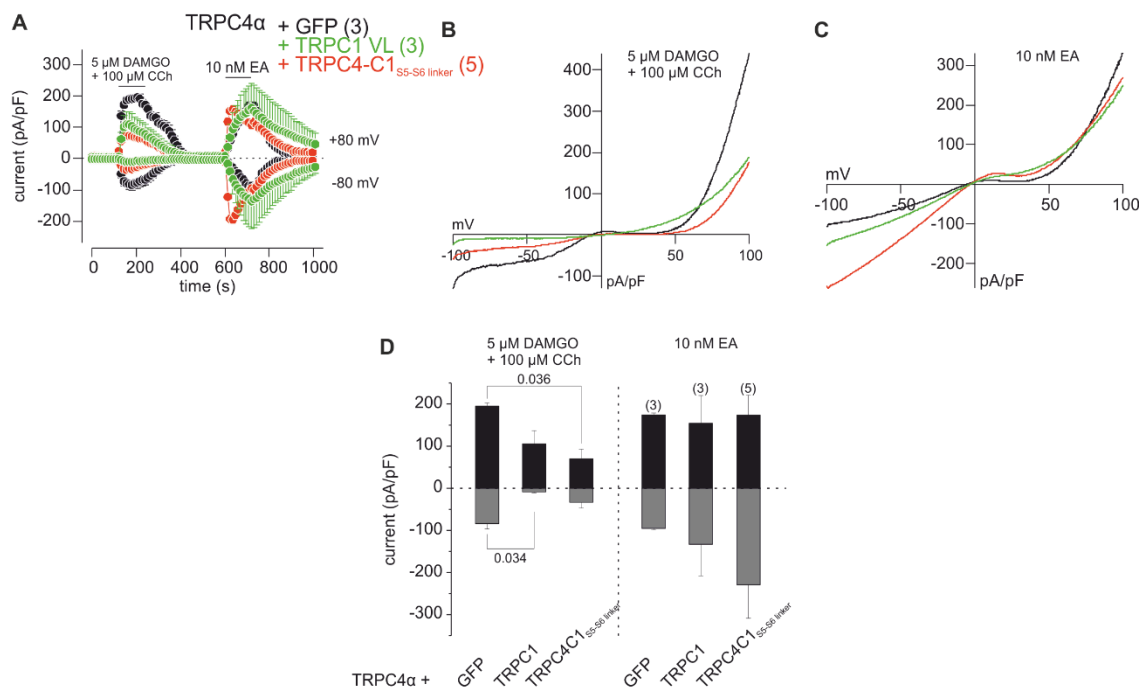


Figure A4 Impact of DAMGO/CCh pre-application on EA-induced current of TRPC4 α coexpressed with TRPC1 VL or TRPC4 α -C1_{S5-S6 linker} chimera. **A** Outward (+80 mV) and inward (-80 mV) currents of stably TRPC4 α expressing cells transfected with empty GFP vector (black), TRPC1 (green) or TRPC4 α -C1_{S5-S6 linker} chimera (red) due to the application of 5 μ M DAMGO + 100 μ M CCh followed by an application of 10 nM EA. **B** Current-voltage relationship of TRPC4 α cells coexpressing empty GFP vector, TRPC1 or the TRPC4 α -C1_{S5-S6 linker} chimera during DAMGO/CCh-application. **C** Current-voltage relationship of stably TRPC4 α expressing cells transfected with empty GFP vector, TRPC1 or the TRPC4 α -C1_{S5-S6 linker} chimera in the presence of EA. **D** Statistical analysis of maximal current amplitudes in the presence of DAMGO/CCh and EA. Data are shown as mean \pm SEM (A, D) and mean (B, C). One-way ANOVA followed by the Bonferroni correction was used for statistical analysis and the p-values are indicated on top of the bars. In parenthesis the numbers of experiments are indicated. The basal current was subtracted to show the net current-voltage relationships (B, C).

significantly increased in cells transfected with the TRPC4 α -C1_{S5-S6 linker} chimera as compared to cell transfected with GFP (outward GFP 4.28 ± 0.71 pA/pF; chimera 20.91 ± 5.95 pA/pF; inward GFP -1.74 ± 0.41 pA/pF; chimera -12.22 ± 3.66 pA/pF; Figure A3 F, G). These results require additional experiments to compare cation permeability of TRPC4 α versus TRPC4 α / TRPC4 α -C1_{S5-S6 linker} chimera channels.

Next, the impact of a preactivation of TRPC4 α with DAMGO/CCh on the EA-induced current was analyzed. The preactivation of TRPC4 α coexpressed with TRPC1 or the TRPC4 α -C1_{S5-S6 linker} chimera by DAMGO/CCh followed by an application of EA showed, that TRPC4 α , TRPC4 α /TRPC1 and TRPC4 α /TRPC4 α -C1_{S5-S6 linker} chimera could be activated with EA after a preactivation with DAMGO/CCh (Figure A4). Again, the EA-induced current amplitude, especially of the inward current, of TRPC4 α /TRPC4 α -C1_{S5-S6 linker} chimera channels appeared to be larger than of homomeric TRPC4 α channels.

5.3.2 Coexpression of TRPC4 β -C1_{S5-S6 linker} chimera 1 or 2 with TRPC4 β and stimulation with hormone (CCh)

The TRPC4 β -C1_{S5-S6 linker} chimeras shown in Figure 26 A were transfected into TRPC4 β stably expressing cells, which also expressed the G_{i/o}-coupled muscarinic receptor M2. The application of CCh (100 μ M) induced double rectifying currents in the absence and presence of the TRPC4 β -C1_{S5-S6 linker} 1 chimera as well as of the TRPC4 β -C1_{S5-S6 linker} 2 chimera (Figure A5). However, the presence of both chimeras reduced the outward currents (RFP 28.04 ± 6.19 pA/pF, $n = 8$; chimera 1 16.28 ± 2.42 pA/pF, $n = 6$; chimera 2 11.50 ± 2.72 pA/pF, $n = 7$), while the inward currents (RFP -19.66 ± 3.61 pA/pF; chimera 1 -7.29 ± 1.36 pA/pF; chimera 2 -8.61 ± 1.73 pA/pF) were significantly reduced compared to the TRPC4 β current (Figure A5 B). However, the break-in currents were not changed in the presence of either the TRPC4 β -C1_{S5-S6 linker} 1 chimera (outward 4.35 ± 0.71 pA/pF, inward -3.33 ± 0.62 pA/pF, $n = 6$) and the TRPC4 β -C1_{S5-S6 linker} 2 chimera (outward 4.60 ± 1.22 pA/pF, inward -3.97 ± 0.86 pA/pF, $n = 7$) as compared to homomeric TRPC4 β (outward 2.51 ± 0.35 pA/pF, inward -2.01 ± 0.38 pA/pF, $n = 8$; Figure A4 A inset in the right panel). Although the current tends to be reduced due to the coexpression of the TRPC4 β -C1_{S5-S6 linker} 1 chimera and the TRPC4 β -C1_{S5-S6 linker} 2 chimera, the shape of the currents was unchanged and revealed the typical TRPC4 characteristics (Figure A5 A right panel).

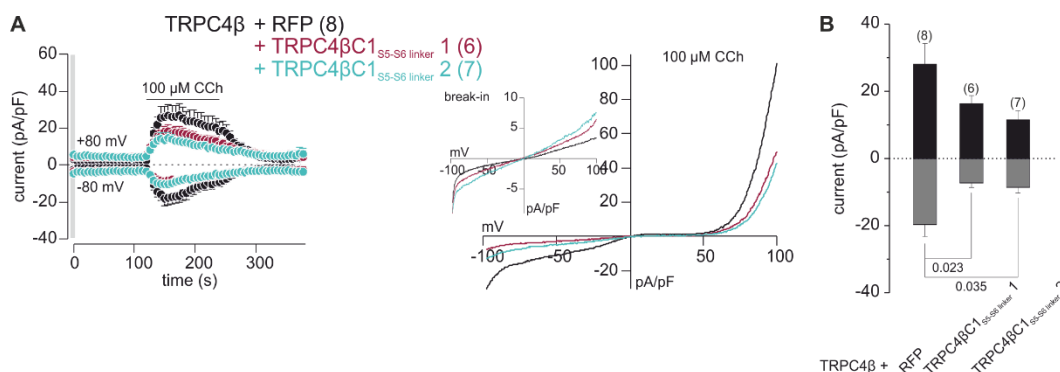


Figure A5 Currents through TRPC4 β -C1^{S5-S6 linker} chimera in TRPC4 β expressing M2R cells. **A** Current over time of stably TRPC4 β expressing M2R-cells together with RFP (control), TRPC4 β -C1^{S5-S6 linker} 1 (purple) or TRPC4 β -C1^{S5-S6 linker} 2 (blue). Application of 100 μ M CCh is represented as a bar (left panel). Current-voltage relationship of homomeric TRPC4 β , heteromeric TRPC4 β /TRPC4 β -C1^{S5-S6 linker} 1 and heteromeric TRPC4 β /TRPC4 β -C1^{S5-S6 linker} 2 with the break-in as inset (right panel). **B** Maximal outward (black) and inward (gray) currents in the absence and presence of one of the chimeras Data represented as means \pm SEM (A left panel, B) and without SEM (A right panel). Number of experiments is shown in parenthesis and numbers under the bars indicate the p-values (one-way ANOVA followed by the Bonferroni correction). Current-voltage relationships are shown as net current, where the basal current was subtracted. Gray bar in A shows the break-in currents shown in the inset of B.

5.3.3 Coexpression of TRPC4 α -C1^{S5-S6 linker} with TRPC1 and stimulation with hormones (CCh plus DAMGO) and with Engerlin A (EA)

The TRPC4 α -C1^{S5-S6 linker} chimera (Figure 26 A) was transfected in μ OR-cells stably expressing the very long version of TRPC1 (TRPC1 VL). DAMGO/CCh only induced a current in stably TRPC1 expressing cells transfected with TRPC4 α (outward 46.85 ± 5.56 pA/pF; inward -1.91 ± 0.46 pA/pF, $n = 3$), while no current was induced in the presence of TRPC1 alone (GFP control) or the coexpression of the TRPC4 α -C1^{S5-S6 linker} chimera (Figure A6 A, D). Moreover, the coexpression of TRPC1 with TRPC4 α in these cells leads to a more heteromeric soup ladle like shape of the current (Figure A6 B). However, the coexpression of the TRPC4 α -C1^{S5-S6 linker} chimera with TRPC1 led to an increased outward break-in current (TRPC4 8.24 ± 0.54 pA/pF; TRPC1 4.68 ± 0.91 pA/pF; chimera 34.23 ± 2.09 pA/pF) and inward break-in current (TRPC4 -3.10 ± 0.31 pA/pF; TRPC1 -1.76 ± 0.69 pA/pF; chimera -19.66 ± 1.39 pA/pF; Figure A6 C). Similar results were obtained using EA as stimulus. The application of 10 nM EA only induced a current in TRPC1 cells transfected with TRPC4 α (outward 185.41 ± 32.92 pA/pF; inward -167.82 ± 37.61 pA/pF, $n = 9$), while the GFP control and the presence of the TRPC4 α -C1^{S5-S6 linker} chimera did not show any measurable currents (Figure A6 E, H). The overexpression of TRPC4 α in stably TRPC1 expressing cells led to a more TRPC4 like shaped current and not like usual to the typical soup ladle like

current of heteromeric TRPC4/TRPC1 currents (Figure A6 F). The presence of the TRPC4 α -C1_{S5-S6 linker} chimera also significantly increased the break-in outward (TRPC4 9.28 \pm 2.19 pA/pF; GFP 6.5 \pm 2.75 pA/pF, n = 6; chimera 29.16 \pm 4.34 pA/pF, n = 7) and inward currents (TRPC4 -3.53 \pm 1.45 pA/pF, GFP -3.56 \pm 1.96 pA/pF; chimera -17.03 \pm 2.64 pA/pF; Figure A6 G).

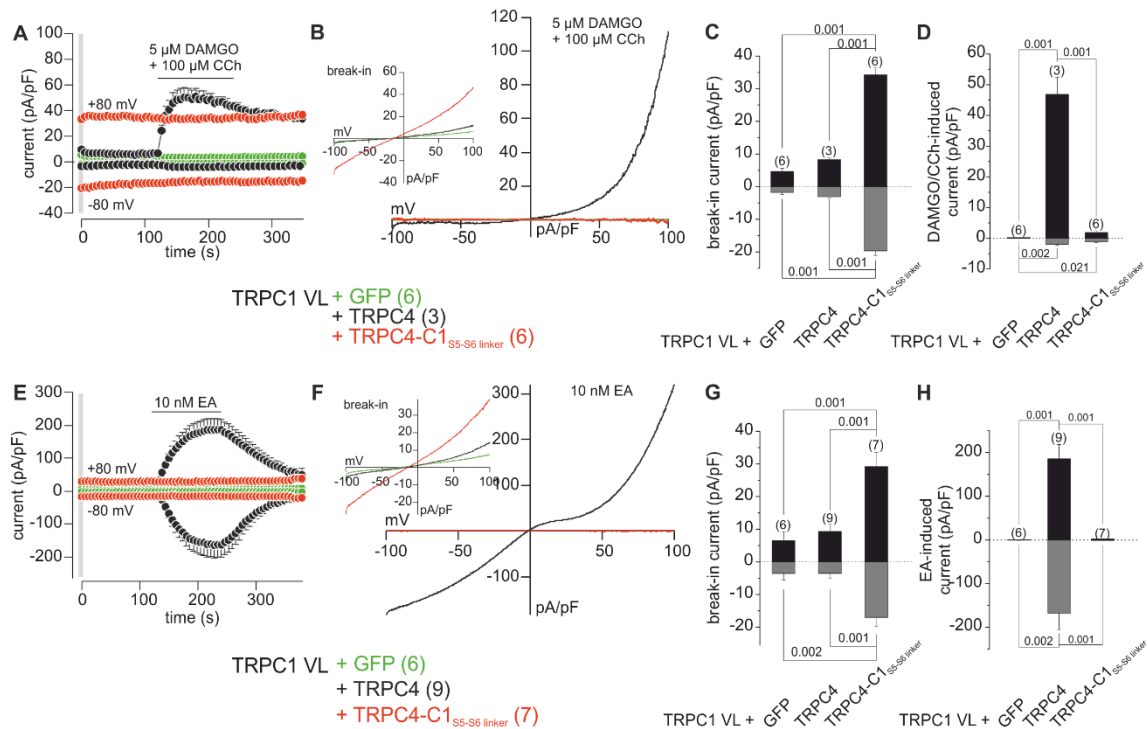


Figure A6 TRPC4 α -C1_{S5-S6 linker} chimera in stable expressing TRPC1 cells. **A** Outward and inward currents of TRPC1 coexpressed with either TRPC4 α (black), TRPC4 α -C1_{S5-S6 linker} chimera (red) or GFP (green) induced by DAMGO/CCh. **B** Current-voltage relationship of TRPC1/GFP, TRPC1/TRPC4 α and TRPC1/TRPC4 α -C1_{S5-S6 linker} chimera with the break-in currents in the inset. **C** Statistical analysis of the break-in currents. **D** Comparison of the maximal current amplitude. **E** EA-induced outward and inward currents over time in TRPC1 cells coexpressing GFP (green), TRPC4 α (black) or the TRPC4 α -C1_{S5-S6 linker} chimera (red). **F** Current-voltage relationship during EA-application of GFP; TRPC4 α or the TRPC4 α -C1_{S5-S6 linker} chimera with the break-in currents shown in inset. **D** Maximal outward (black) and inward (gray) currents of stably TRPC1 expressing cells overexpressing GFP, TRPC4 or the TRPC4 α -C1_{S5-S6 linker} chimera. All data shown as mean \pm SEM (A, C, D, E, G, H) and mean (B, F). For statistical analysis one-way ANOVA followed by the Bonferroni correction was used and the p-values are indicated on top of the bars. Number of experiments are shown in parenthesis. For the current-voltage relationships the basal current was subtracted (B, F). In B and F the green traces are masked by the red traces.

5.4 Functional interaction of TRPC4 non-TRPC proteins

In an ongoing project using several antibodies for TRPC1, TRPC4 and TRPC5 generated in our laboratory, antibody-based enrichment of TRPC target protein containing protein complexes were achieved, which were investigated by mass spectrometry. The cDNAs of identified proteins enriched with the TRPC target proteins were cloned and coexpressed with TRPC4 or TRPC4/TRPC1 cDNAs. The following proteins were identified as possible TRPC4 or TRPC4/TRPC1 interactors in brain protein lysates by mass spectrometry (Table A4): GRAM domain-containing protein (Gramd1a and Gramd3), SH3 and cysteine-rich domain-containing protein 2 (Stac2), early endosome antigen 1 (hEEA1), Latrophilin 2, Transmembrane protein 201 (TMEM 201), Nucleoside-Diphosphate Kinases-B (NDPK-B), cysteine and glycine-rich protein 1 (Csrp1) and LIM and SH3 domain protein 1 (Lasp1). These proteins were coexpressed with TRPC4 or TRPC4/TRPC1 and EA- and DAMGO/CCh-induced currents were recorded and current-voltage relationships for each coexpression are shown in Figure A7 to Figure A16.

Table A4 Summary of the effects of different proteins on TRPC4 and TRPC4/TRPC1 currents. Nine different interactors were coexpressed with TRPC4 or TRPC4/TRPC1 and EA- or DAMGO/CCh-induced currents were registered.

potential TRPC4/TRPC1 interactor	agonist	effect on TRPC4 current	effect on TRPC4/TRPC1 current
Gramd1a	EA	no effect (Figure A7)	-----
Gramd3	EA	no effect (Figure A7)	-----
Stac2	DAMGO/CCh	no effect (Figure A8)	no effect (Figure A8)
	EA	-----	no effect (Figure A8)
hEEA1	DAMGO/CCh	no effect (Figure A9)	no effect (Figure A9)
	EA	-----	no effect (Figure A9)
Latrophilin 2	DAMGO/CCh	significantly reduced (Figure A10)	reduced (Figure A11)
	EA	reduced (Figure A10)	significantly reduced (Figure A11)

potential TRPC4/TRPC1 interactor	agonist	effect on TRPC4 current	effect on TRPC4/TRPC1 current
TMEM 201	DAMGO/CCh	-----	no effect (Figure A12)
	EA	-----	no effect (Figure A12)
Csrp1	GTP γ S	no effect (Figure A13)	-----
	EA	no effect (Figure A13)	-----
Lasp1	GTP γ S	no effect (Figure A13)	-----
	EA	no effect (Figure A13)	-----
NDPK-B	DAMGO/CCh	increased (Figure A14)	-----
	EA	no effect (Figure A14)	-----

The GRAM domain-containing proteins (Gramd1a and Gramd3) are a cholesterol transporter in the plasma membrane, which mediates the cholesterol transport to the endoplasmic reticulum (ER) [Besprozvannaya *et al.*, 2018]. Patch clamp recordings were performed with stably TRPC4 expressing cells transfected with one of those proteins coexpressed. Englerin A (EA; 10 nM) induced a current in TRPC4 alone (outward 71.37 ± 14.79 pA/pF; inward -41.54 ± 11.02 pA/pF, $n = 12$) as well as in TRPC4 coexpressed with Gramd1a (outward 59.38 ± 9.26 pA/pF; inward -29.84 ± 5.63 pA/pF, $n = 9$), which did not differ (Figure A7 A). Same applies for the coexpression of Gramd3, where the application of 10 nM EA induced the same TRPC4 current in absence (outward 25.10 ± 3.96 pA/pF; inward -13.43 ± 2.36 pA/pF, $n = 14$) and presence (outward 26.02 ± 6.49 pA/pF; inward -13.47 ± 3.95 pA/pF, $n = 10$) of Gramd3 (Figure A7 B). The current-voltage relationship of TRPC4 currents remained unchanged in the presence of Gramd1a and Gramd3. Thus, coexpression of either Gramd1a or Gramd3 had no influence on the TRPC4 current amplitude in the presence of EA.

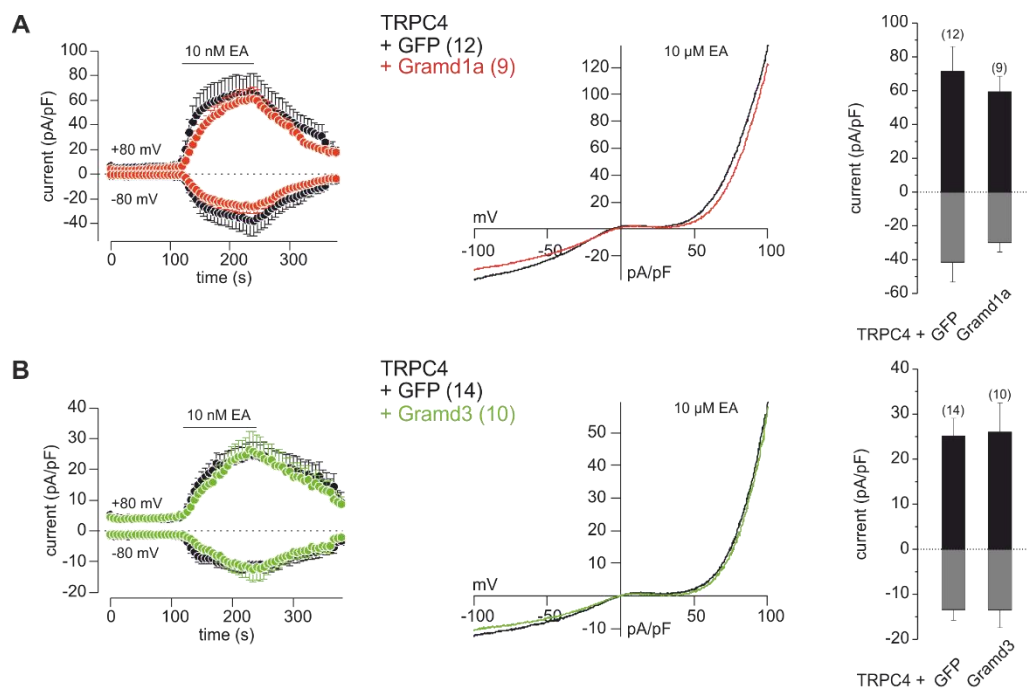


Figure A7 Coexpression of Gramd1a and Gramd3 and TRPC4. **A, B** HEK-cells coexpressing TRPC4 and Gramd1a (red) or Gramd3 (green) were clamped from -100 mV to 100 mV over 400 ms ($V_h = 0$ mV). The bar indicates the application of 10 nM Englerin A (EA). **A** EA-induced (10 nM) current over time in TRPC4/GFP as well as in TRPC4/Gramd1a expressing cells (left panel) and the corresponding current-voltage relationship (middle panel). **B** EA-induced current plotted versus time of TRPC4/GFP and TRPC4/Gramd3 expressing cells (left panel) with the corresponding current-voltage relationship (middle panel). Data are represented as means and means \pm SEM. In parenthesis the numbers of experiments are indicated. Basal current was subtracted from the current-voltage relationships.

The SH3 and cysteine-rich domain-containing protein 2 (Stac2) interacts with voltage-gated calcium channels. It is shown, that CaV2.1 translocation to the plasma membrane and channel activation are increased in the presence of Stac2. However, it interacts also with CaV1.2 in terms of slowing down the inactivation of this channel [Wong King Yuen *et al.*, 2017]. Stac2 was overexpressed in stably TRPC4 expressing μ OR-cells, therefore the μ OR ($G_{i/o}$ -coupled receptor) agonist DAMGO and the muscarinic acetylcholine receptor ($G_{q/11}$ -coupled receptor) agonist carbachol (CCh) were used to activate TRPC4. The outward current tended to be increased in the presence of Stac2 (GFP 68.99 ± 8.88 pA/pF; Stac2 76.36 ± 8.53 pA/pF, $n = 10$), while the inward current tended to be reduced as compared to the control (GFP -41.12 ± 7.67 pA/pF; Stac2 -31.19 ± 6.01 pA/pF; 12.97 pA/pF, $n = 12$). The shape of the TRPC4 current was not changed due to the presence of Stac2 (Figure A8 A).

In addition, stably TRPC4/TRPC1 expressing cells were transfected with Stac2 and the DAMGO/CCh-induced current was recorded. The TRPC4/TRPC1 outward current tended to be increased in presence of Stac2 (GFP 23.75 ± 3.41 pA/pF, $n = 11$; Stac2 34.34 ± 5.7 pA/pF, $n = 12$) as well as the inward current (GFP -3.75 ± 0.57 pA/pF; Stac2 -6.14 ± 1.15 pA/pF; 12.97 pA/pF, $n = 12$; Figure A8 B). The current-voltage relationship

was not changed in the presence of Stac2 and had the typical soup ladle shape as shown for heteromeric TRPC4/TRPC1 currents (Figure A8 B). The DAMGO/CCh-induced TRPC currents are always smaller compared to the EA-induced currents, therefore the experiments were repeated by applying 30 nM EA. In the presence of EA, inward and outward TRPC4/TRPC1 currents were larger (Figure A8 C). The coexpression of Stac2 tended to increase the outward EA-induced TRPC4/TRPC1 currents (GFP $50.71 \pm$

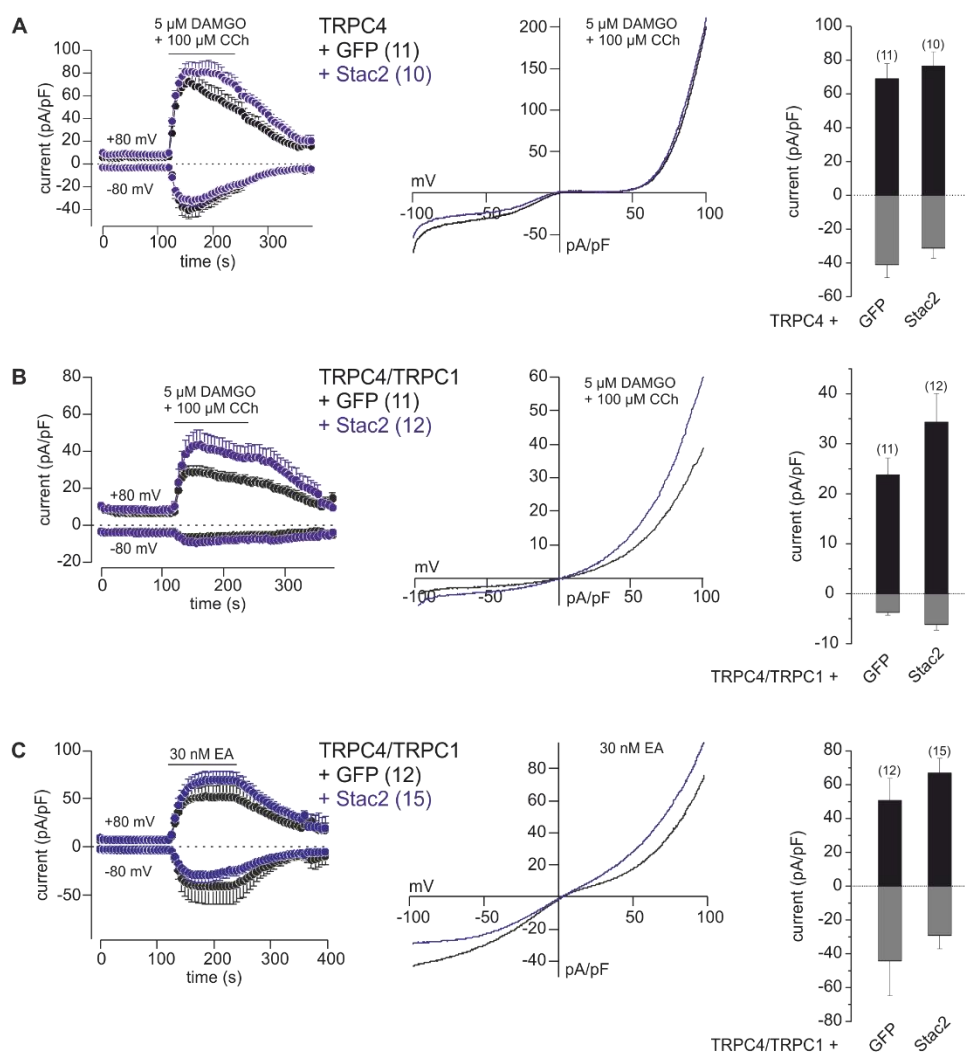


Figure A8 Impact of Stac2 and homomeric TRPC4 and heteromeric TRPC4/TRPC1 currents. **A, B, C** μ OR HEK cells stably expressing either TRPC4 or TRPC4/TRPC1 were transfected with Stac2 or GFP cDNA. The cells were clamped from a holding potential of 0 mV continuously from -100 mV to 100 mV over 400 ms. **A** TRPC4 current over time in presence (blue) and absence (black) of Stac2 induced by 5 μ M DAMGO and 100 μ M CCh (left panel). Current-voltage relationship of TRPC4 coexpressed with Stac2 (blue) or an empty GFP-vector (black; middle panel). The maximal current amplitude at +80 mV and -80 mV (right panel). **B** DAMGO/CCh induced TRPC4/TRPC1 current in the absence and presence of Stac2 (left panel) with the current-voltage relationship (middle panel). The maximal current at +80 mV and -80 mV in the presence and absence of Stac2 (right panel). **C** EA-induced current over time of stably TRPC4/TRPC1 expressing cells in presence (blue) and absence (black) of Stac2 (left panel) with the corresponding current-voltage relationship (middle panel). Maximal TRPC4/TRPC1 current amplitude induced by 30 nM EA (right panel). Data are shown as means \pm SEM (left and right panels) and without SEM (middle panels). Numbers of experiments are represented in parenthesis. Current-voltage relationships are subtracted from the basal current.

12.97 pA/pF, n = 12; Stac2 66.84 ± 8.85 pA/pF, n = 15) and the inward current tended to be reduced by Stac2 coexpression (GFP -44.29 ± 20.52 pA/pF; Stac2 -29.11 ± 7.94 pA/pF; 12.97 pA/pF, n = 12; Figure A8 C). The shape of the current in the presence of Stac2 was the typical TRPC4/TRPC1 current-voltage relationship (Figure A8 B), whereas in this experiment, currents in the absence of Stac2 seemed to be a mixture of typical TRPC4 and TRPC4/TRPC1 currents (Figure A8 C).

The coexpression of Stac2 tended to increase TRPC4 as well as TRPC4/TRPC1 currents independent of the activation mechanisms of the channel, but the changes were not significant.

The early endosome antigen 1 (hEEA1) is supposed to play a role for endosomal trafficking and the connection of vesical and SNARE-proteins [Mu *et al.*, 1995]. It could influence the trafficking of TRPC4 to the plasma membrane. The application of 5 μ M DAMGO and 100 μ M CCh induced a current in TRPC4/RFP and in TRPC4/hEEA1 expressing cells (Figure A9 A), and the outward current tended to be increased in the presence of hEEA1 (RFP 62.34 ± 6.36 pA/pF, n = 6; hEEA1 -31.72 ± 6.06 pA/pF; Figure A9 A) without changing the current-voltage relationship of TRPC4 (Figure A9 A). Coexpression with TRPC4/TRPC1, the presence of hEEA1 did not change TRPC4/TRPC1 outward (RFP 46.39 ± 9.24 pA/pF, n = 11; hEEA1 49.29 ± 6.82 pA/pF, n = 11) or inward currents (RFP -5.79 ± 2.96 pA/pF; hEEA1 -4.24 ± 1.39 pA/pF; Figure A9 B). Under both conditions a typical heteromeric TRPC4/TRPC1 shaped current was detected (Figure A9 B).

However, 30 nM EA tended to induce a smaller inward (RFP -36.24 ± 7.87 pA/pF, n = 11; hEEA1 -32.74 ± 11.45 pA/pF, n = 9) and outward (TRPC4/C1 81.65 ± 13.94 pA/pF; hEEA1 69.46 ± 20.84 pA/pF) current in the presence of hEEA1 (Figure A9 C). The shape of the TRPC4/TRPC1 current was not changed (Figure A9 C).

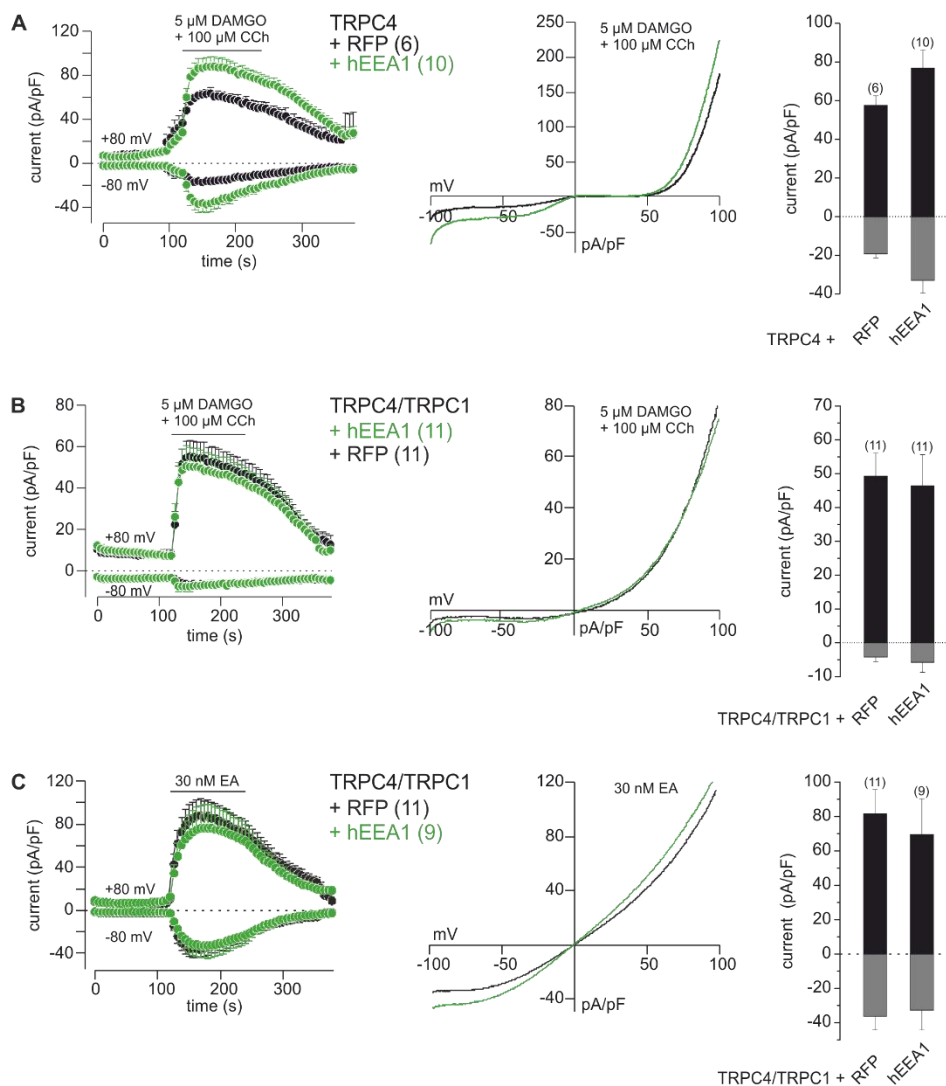


Figure A9 Coexpression of hEEA1 and homomeric TRPC4 and heteromeric TRPC4/TRPC1 currents. **A, B, C** μ OR HEK-cells stably expressing homomeric TRPC4 or heteromeric TRPC4/TRPC1 channels were transfected with hEEA1 or RFP cDNA. Cells were clamped from -100 mV to 100 mV over 400 ms ($V_h = 0$ mV). **A** Current over time of TRPC4 in absence (black) and presence (green) of hEEA1 (left panel) with the corresponding current-voltage relationship (middle panel) induced by 5 μ M DAMGO + 100 μ M CCh. Maximal TRPC4 current amplitudes at +80 mV and -80 mV (right panel). **B** DAMGO/CCh-induced current plotted over time of TRPC4/TRPC1 with hEEA1 (green) or RFP (black; left panel) with a soup ladle like current-voltage relationship (middle panel) and the maximal current at +80 mV and -80 mV (right panel). **C** EA-induced current over time in the presence (green) and absence (black) of hEEA1 (left panel), the current-voltage relationship (middle panel) and maximal current amplitudes (right panel). Data are shown as means with (left and right panels) and without (middle panels) SEM. Numbers in parenthesis are the number of experiments. The current before application was subtracted to show the netto current-voltage relationships.

Latrophilin 2 is a membrane protein and belongs to the adhesion G-protein-coupled receptor family, which binds α -latrotoxin, a spider toxin [Silva *et al.*, 2011].

Coexpression of the Latrophilin 2 cDNA in stably TRPC4 expression cells DAMGO/CCh induced TRPC4 currents (Figure A10 A): The outward current (GFP 24.88 ± 2.82 pA/pF, $n = 25$; Latrophilin 2 16.30 ± 2.09 pA/pF, $n = 13$) was significantly reduced but not the inward current (GFP -8.77 ± 1.57 pA/pF; Latrophilin 2 -8.34 ± 4.21 pA/pF; Figure A10 A). The coexpression of Latrophilin 2 tended to reduce the EA-induced inward (GFP -311.51 ± 91.34 pA/pF, $n = 11$; Latrophilin 2 -146.64 ± 46.24 pA/pF, $n = 13$) and the outward (GFP 198.84 ± 48.91 pA/pF; Latrophilin 2 109.62 ± 28.5 pA/pF) TRPC4 current (Figure A10 B). The current-voltage relationship was also unchanged (Figure A10 B).

Coexpression of Latrophilin 2 and TRPC4/TRPC1 tended to reduce the DAMGO/CCh-induced outward TRPC4/TRPC1 current (GFP 21.43 ± 4.11 pA/pF, $n = 11$; Latrophilin 2 13.11 ± 2.98 pA/pF, $n = 10$) without an impact on the inward current (GFP -0.32 ± 0.11 pA/pF; Latrophilin 2 -0.41 ± 0.12 pA/pF; Figure A11 A). The DAMGO/CCh-induced TRPC4/TRPC1 current had a soup ladle like current-voltage relationship independent of the presence of Latrophilin 2. Similar results were obtained using 30 nM EA to activate

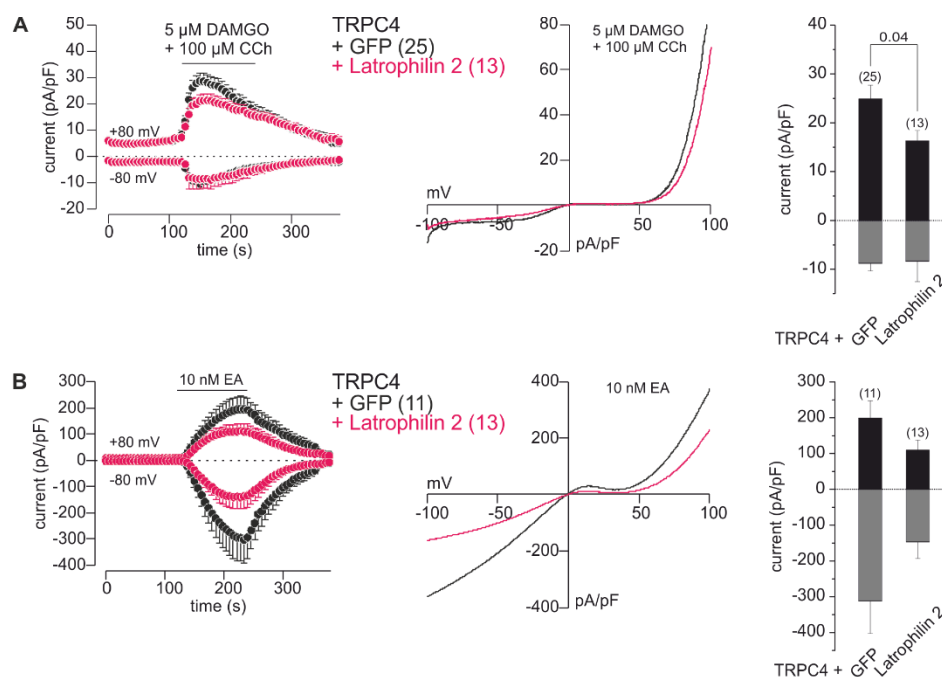


Figure A10 Coexpression of Latrophilin 2 and homomeric TRPC4 channels. **A, B** Stably TRPC4 expressing μ OR HEK-cells were transfected with Latrophilin 2 (pink) or GFP (black). Cells were measured with a ramp protocol from -100 mV to 100 mV from a holding potential of 0 mV over 400 ms. The application of 5 μ M DAMGO + 100 μ M CCh or Englerin A (EA; 10 nM) is indicated by a bar. **A** DAMGO/CCh-induced TRPC4 current in presence (pink) and absence (black) of Latrophilin 2 over time (left panel) with the corresponding current-voltage relationship (middle panel) and the maximal current amplitudes (right panel). **B** Maximal EA-induced TRPC4 current in cells coexpressing Latrophilin 2 (pink) or GFP (black; right panel), the current over time (left panel) and the corresponding current-voltage relationship (middle panel). Data are represented as means \pm SEM (left and right panels) and means (middle panels). Number of experiments is shown in parenthesis. Basal current was subtracted from the current-voltage relationships.

the TRPC4/TRPC1 channels, robust outward (GFP 61.32 ± 10.42 pA/pF, $n = 18$; Latrophilin 2 32.66 ± 7.27 pA/pF) and inward currents (GFP -28.43 ± 6.48 pA/pF; Latrophilin 2 -13.72 ± 6.42 pA/pF; Figure A11 B) were registered, and the current amplitude in the presence of Latrophilin 2 was significantly reduced. Although the current was reduced in the presence of Latrophilin 2, the shape of the current-voltage relationship, which had the soup ladle like shape of heteromeric TRPC4/TRPC1 currents (Figure A11 B), remain unchanged. The data show that the coexpression of Latrophilin 2 had an inhibitory effect on homomeric TRPC4 as well as on heteromeric TRPC4/TRPC1 channels.

The transmembrane protein 201 (TMEM 201) may play a role during migration and is associated with transmembrane actin-associated nuclear induced (TAN) lines [Vijayaraghavan *et al.*, 2016]. Coexpression of the TMEM 201 cDNA and TRPC4/TRPC1 yielded DAMGO/CCh-induced TRPC4/TRPC1 outward currents, which tended to be increased (GFP 44.75 ± 7.36 pA/pF, $n = 10$; TMEM 201 54.36 ± 9.76 pA/pF, $n = 11$) with

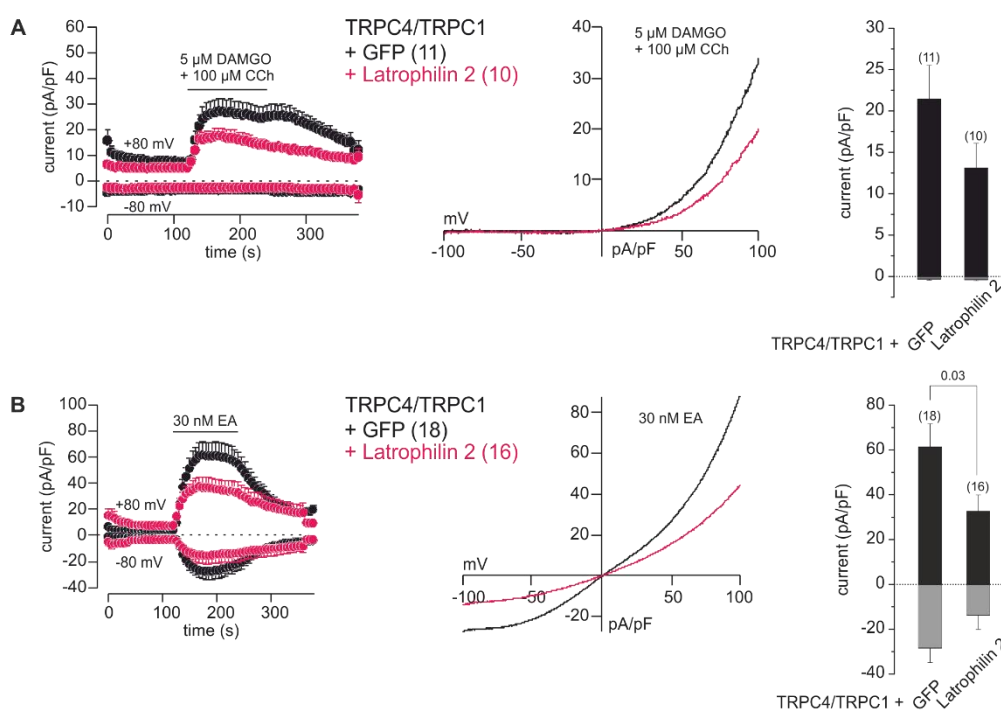


Figure A11 Coexpression of Latrophilin 2 and heteromeric TRPC4/TRPC1 channels. A, B μ OR HEK cells stably TRPC4/TRPC1 expressing were transfected with Latrophilin 2 (pink traces) or GFP (black). Cells were clamped from -100 mV to 100 mV from a holding potential of 0 mV over 400 ms. The bar is indicating the application of 5 μ M DAMGO + 100 μ M CCh or Englerin A (EA; 30 nM). **A** Current over time in TRPC4/TRPC1 and Latrophilin 2 coexpressing cells induced by DAMGO/CCh (left panel) with a soup ladle like current-voltage relationship (middle panel) and the maximal current amplitudes at +80 mV and -80 mV (right panel). **B** EA-induced current in TRPC4/TRPC1 and Latrophilin 2 (pink) coexpressing cells over time (left panel) with the maximal current amplitudes (right panel) and the current-voltage relationship (middle panel). In the left and right panels of A and B are the data shown as means \pm SEM and in the middle panels as mean. Number of experiments is shown in parenthesis. Current-voltage relationships are subtracted from the basal current.

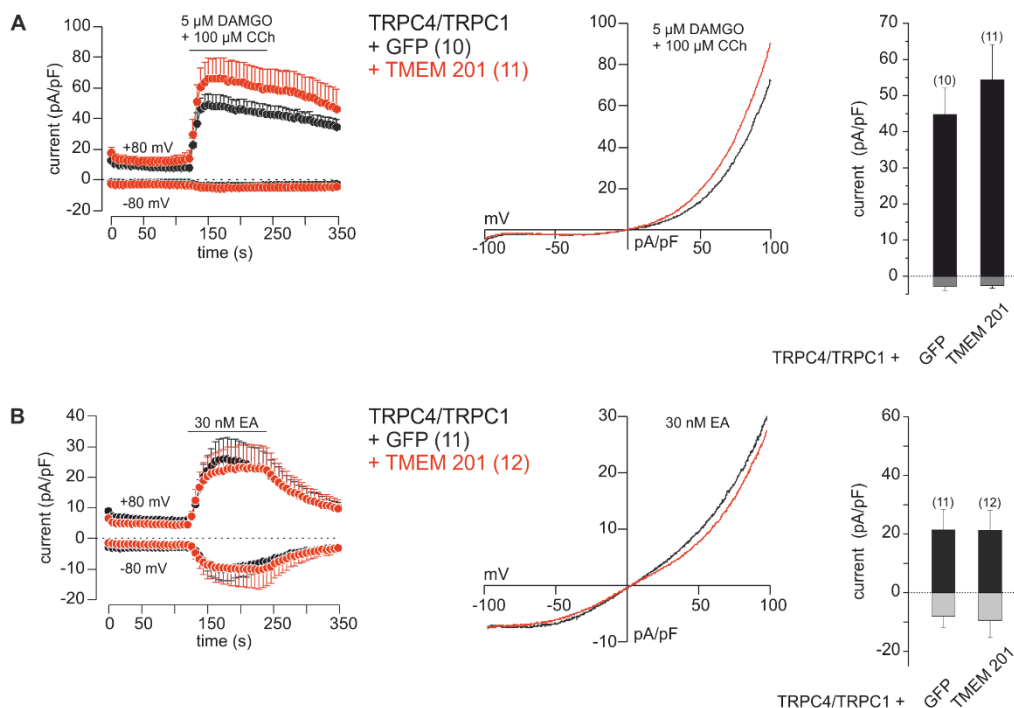


Figure A12 Coexpression of TMEM 201 and heteromeric TRPC4/TRPC1 channel. μ OR HEK-cells stably expressing heteromeric TRPC4/TRPC1 channels were transfected with TMEM 201 (red) or GFP (black), clamped from -100 mV to 100 mV over 400 ms ($V_h = 0$ mV) and activated by 30 nM Englerin A (EA) or 5 μ M DAMGO + 100 μ M CCh. **A** DAMGO/CCh-induced current over time in absence (black) and presence (red) of TMEM 201 (left panel) with the typical soup ladle like current-voltage relationship of heteromeric TRPC4/TRPC1 channels (middle panel). Comparison of the maximal current amplitudes due to the presence and absence of TMEM 201 (right panel). **B** EA-induced current over time (left panel), current-voltage relationship (middle panel) and maximal current amplitudes (right panel) of TRPC4/TRPC1 in absence (black) and presence (red) of TMEM 201. Data are shown as mean \pm SEM in left and right panels of A and B or without SEM in the middle panels. Parenthesis show the numbers of experiments. Current before application was subtracted from the current-voltage relationships.

no impact on the inward current (GFP -2.78 ± 1.27 pA/pF; TMEM 201 -2.58 ± 0.71 pA/pF; Figure A12 A). The current-voltage relationship was typical for TRPC4/TRPC1 currents (Figure A12 A). The application of 30 nM EA induced under both conditions outward (GFP 21.38 ± 6.91 pA/pF, $n = 11$; TMEM 201 21.21 ± 6.87 pA/pF, $n = 12$) and inward (GFP -8.05 ± 3.81 pA/pF; TMEM 201 -9.45 ± 5.84 pA/pF) current amplitudes with the same typical soup ladle current-voltage relationship of heteromeric channels (Figure A12 B).

The cysteine and glycine-rich protein 1 (Csrp1) and the LIM and SH3 domain protein 1 (Lasp1) were coexpressed with TRPC4 or TRPC4/TRPC1. Cysteine and glycine-rich protein 1 (Csrp1) could play a role in regulatory processes important for development and cellular differentiation the actin cytoskeleton of cells [Jang and Greenwood, 2009]. LIM and SH3 domain protein 1 (Lasp1) is ubiquitously expressed and may play an

important role in the regulation of dynamic actin-based and cytoskeletal activities [Grunewald and Butt, 2008]. Stably *Csrp1* or *Lasp1* cDNAs expressing HEK-cells were generated and transfected with TRPC4 for patch clamp recordings. Guanosine 5'-O-[gamma-thio] triphosphate (GTP γ S) a G-protein-activating analog of guanosine triphosphate (GTP), which is not hydrolyzed in the cells and which activates G-proteins directly, was included in the patch pipette solution and used for activation of the channel.

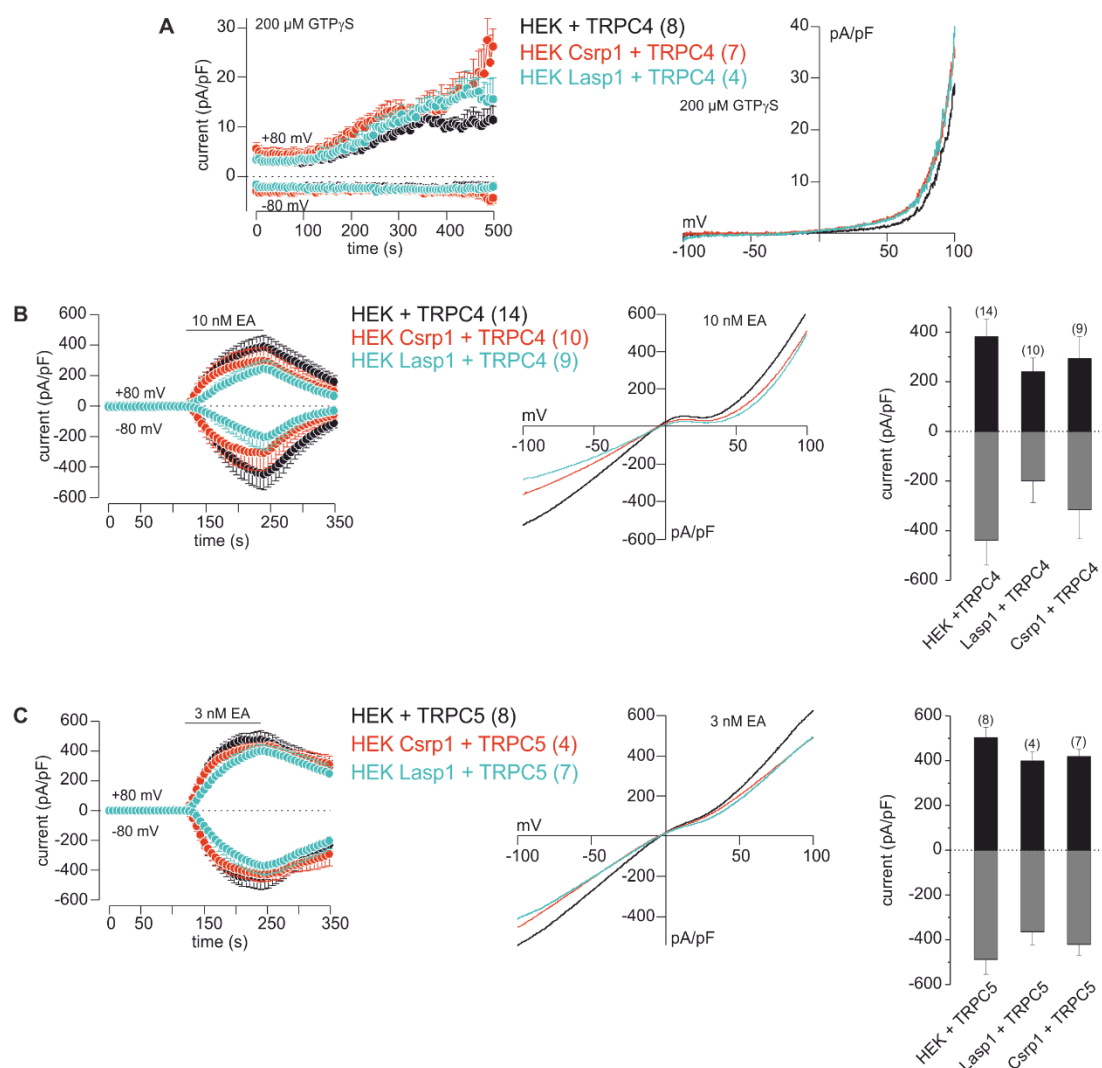


Figure A13 Coexpression of *Csrp1* and *Lasp1* and TRPC4 and TRPC5. **A, B, C** Stably *Csrp1*- or *Lasp1* expressing HEK-cell were transfected with TRPC4 or TRPC5. The cells were clamped over 400 ms from -100 mV to +100 mV ($V_h = 0$ mV). **A** The patch pipette contained 200 μ M GTP γ S for stimulation of TRPC4 and the currents at +80 mV and -80 mV were plotted over time (left panel). Current-voltage relationship of TRPC4 in *Csrp1*-cells (red), *Lasp1*-cells (turquoise) or in HEK-cells (black trace; right panel). **B** EA-induced TRPC4 current over time (left panel) in *Lasp1*-cells (turquoise), *Csrp1*-cells (red) or HEK-cells (black) with the corresponding current-voltage relationship (middle panel) and the maximal current amplitudes (right panel). **C** EA-induced TRPC5 current in *Csrp1*-cells (red), *Lasp1*-cells (turquoise) or HEK-cells (black) plotted over time (left panel), current-voltage relationship (middle panel) and the maximal current at +80 mV and -80 mV (right panel). Data are shown as means with SEM in the left and right panels of A, B and C and without SEM in the middle panels of A, B and C. Numbers of experiments are indicated in parenthesis. Current before application was subtracted from the current-voltage relationship.

The presence of 200 μM GTP γ S induced only an outward current in TRPC4 expressing cells, independent of the presence of Csrp1 or Lasp1. The coexpression of Csrp1 or Lasp1 did not have any influence on the current amplitude and did not lead to a change of the current-voltage relationship of TRPC4 (Figure A13 A). Since the recorded currents were small, 10 nM EA was used for TRPC4 activation. Under all three conditions an outward and an inward current could be recorded in the presence of EA. The TRPC4 outward current seemed to be reduced in the presence of Csrp1 or Lasp1 (TRPC4 381.77 ± 71.09 pA/pF, $n = 14$; Csrp1 240.72 ± 56.07 pA/pF, $n = 10$; Lasp1 293.42 ± 89.06 pA/pF, $n = 9$) as well as the inward current (TRPC4 -437.96 ± 100.72 pA/pF; Csrp1 -199.93 ± 86.69 pA/pF; Lasp1 -315.59 ± 16.95 pA/pF) but without changing the TRPC4 current-voltage relationship (Figure A13 B).

Similar experiments were performed with TRPC5 cells transfected into HEK-cells or Csrp1 or Lasp1 stably expressing cells (Figure A13 C). Here, 3 nM EA was applied to activate TRPC5 either in the absence or presence of Csrp1 or Lasp1. The EA-induced currents were all similar to each other. The current-voltage relationship and the maximal current amplitudes by the coexpression of Csrp1 or Lasp1. However, the presence of Csrp1 or Lasp1 tended to reduce the outward (TRPC5 502.66 ± 47.12 pA/pF, $n = 8$; Csrp1 398.80 ± 40.79 pA/pF, $n = 4$; Lasp1 418.74 ± 32.31 pA/pF, $n = 7$) as well as the inward (TRPC5 -487.99 ± 66.71 pA/pF; Csrp1 -364.16 ± 9.51 pA/pF; Lasp1 to -420.61 ± 48.13 pA/pF) currents of TRPC5 (Figure A13 C). Coexpression of Csrp1 or Lasp1 tended to reduce the TRPC4 as well as the TRPC5 currents without changing the current-voltage relationship.

The Nucleoside-Diphosphate Kinases-B (NDPK-B) is ubiquitously expressed and is one of four isoforms of this kinase, which phosphorylates histidine residues [Wieland *et al.*, 2010]. EA was used to activate the TRPC4 current in the absence or presence of NDPK-B. Under both conditions robust outward (RFP 33.59 ± 3.55 pA/pF, $n = 6$; NDPK-B 44.09 ± 9.75 pA/pF, $n = 9$) and inward (RFP -15.73 ± 2.76 pA/pF; NDPK-B -29.66 ± 8.82 pA/pF) currents were detected. The coexpression of NDPK-B tended to increase both the outward and the inward TRPC4 currents without changing the current-voltage relationship (Figure A14 A). The experiments were performed additionally with DAMGO/CCh. A typical TRPC4 shaped current was registered in absence and presence of NDPK-B (Figure A14 B). The outward currents in the presence of NDPK-B were significantly increased (RFP 40.63 ± 11.36 pA/pF, $n = 7$; NDPK-B 75.20 ± 8.09 pA/pF, $n = 7$) as were the inward currents (RFP -13.39 ± 5.01 pA/pF; NDPK-B -31.11 ± 3.73 pA/pF; Figure A14 B).

Furthermore, a NDPK-B mutant where the histidine (H) at position 118 was exchanged to asparagine (N) was cloned. This mutation is known to result in a non-functional kinase. In contrast to the functional NDPK-B, the coexpression of NDPK-B H118N had no impact on the DAMGO/CCh-induced TRPC4 current (outward: RFP 49.20 ± 4.62 pA/pF, $n = 12$; H118N 55.78 ± 7.01 pA/pF, $n = 12$; inward: RFP -21.35 ± 3.57 pA/pF; H118N -22.88 ± 3.50 pA/pF; Figure A14 C). The current-voltage relationship was identical under both

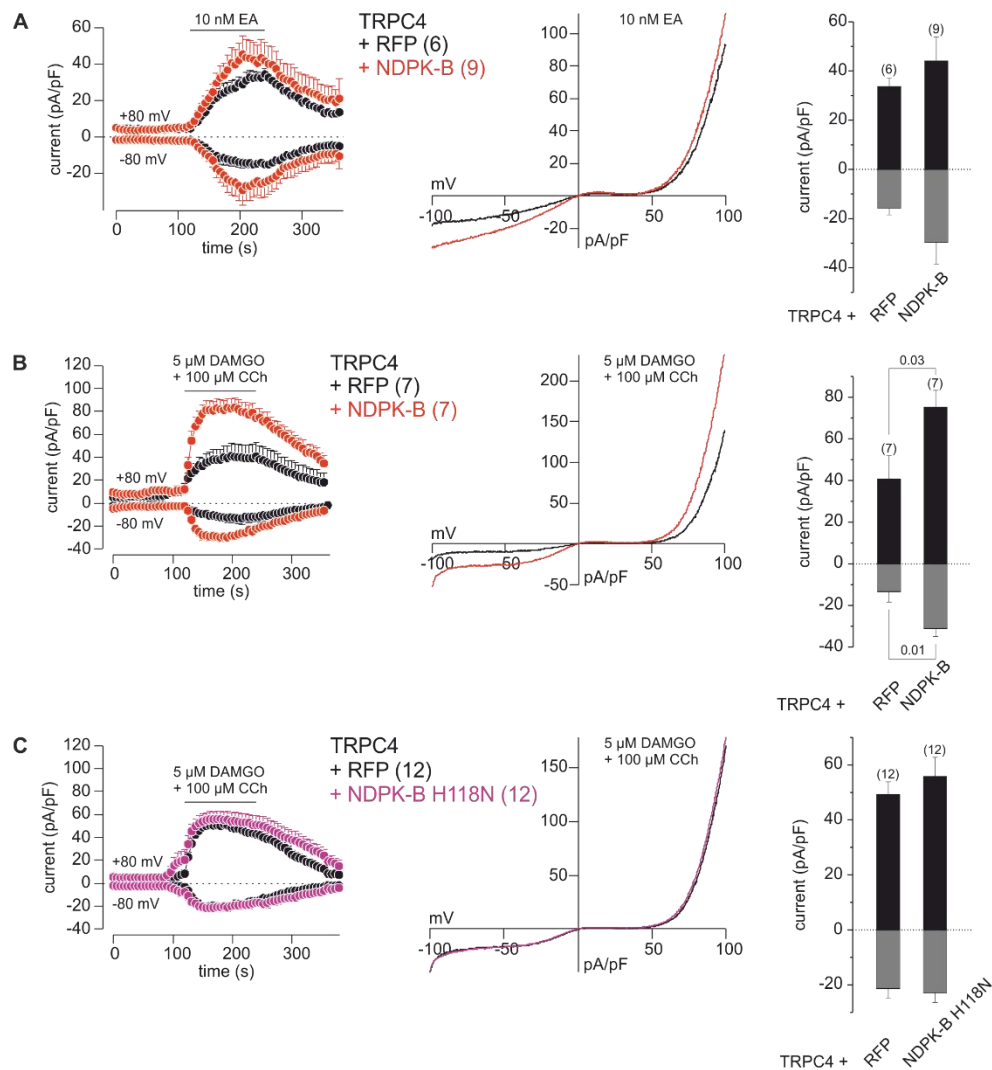


Figure A14 Coexpression of NDPK-B wt and NDPK-B H118N with TRPC4. **A, B, C** μ OR HEK-cells stably expressing TRPC4 were transfected with NDPK-B or RFP. Cells were clamped from a holding potential of 0 mV from -100 mV to 100 mV over 400 ms. The application of 10 nM Engerlin A (EA) or 5 μ M DAMGO + 100 μ M CCh is indicated by a bar. **A** EA-induced TRPC4 current over time in absence (black) or presence (red) of NDPK-B (left panel), current-voltage relationship (middle panel) and the comparison of the maximal current amplitudes at +80 mV and -80 mV (right panel). **B** TRPC4 current induced by DAMGO/CCh in the presence (red) and absence (black; left and right panel) of NDPK-B with the corresponding current-voltage relationship (middle panel). **C** Current over time (left panel) and maximal current amplitude (right panel) of cells stably expressing TRPC4 transfected with the NDPK-B H118N mutant (purple) and current-voltage relationship (middle panel). Data are shown as means \pm SEM (left and right panels of A, B and C) or as mean (middle panels of A, B and C). Number of experiments is indicated in parenthesis. Current-voltage relationships are shown as net current, where the current before application was subtracted.

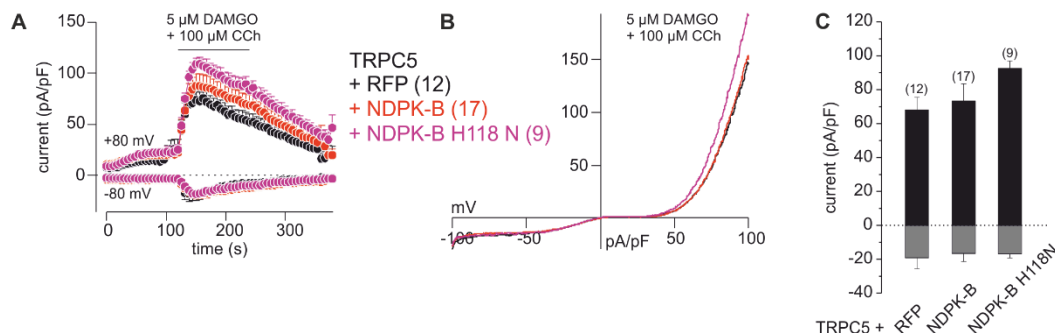


Figure A15 Coexpression of NDPK-B or NDPK-B H118N with TRPC5. Stably expressing TRPC5 HEK-cells were transfected with empty RFP vector (black), NDPK-B (red) or NDPK-B H118N (purple) and TRPC5 was activated by 5 μ M DAMGO/100 μ M CCh. **A** Current at +80 mV and -80 mV was plotted against the time. **B** Current-voltage relationship of RFP, NDPK-B and NDPK-B H118N in stably expressing TRPC5 cells. **C** Statistical analysis of the maximal outward (black; +80 mV) and inward (gray; -80 mV) currents. In A and C, the data are shown as means \pm SEM and in B as means. The number of experiments is represented in parenthesis. Basal current was subtracted from current-voltage relationships.

conditions (Figure A14 C). The results suggest, that NDPK-B coexpression increases TRPC4 currents most probably due to the kinase-activity of NDPK-B.

Since TRPC4 and TRPC5 are very close homologues sharing similar pharmacological properties, the influence of NDPK-B on TRPC5 was also examined. Therefore, stably TRPC5 expressing HEK-cells were transfected with either NDPK-B wt or NDPK-B H118N and DAMGO/CCh (5 μ M/100 μ M) was used for activation. The coexpression of NDPK-B as well as of NDPK-B H118N had no impact on the inward (RFP -19.22 ± 6.37 pA/pF, $n = 12$; NDPK-B -17.71 ± 4.91 pA/pF, $n = 17$; H118N -16.96 ± 2.32 pA/pF, $n = 9$) nor on the outward (RFP 68.07 ± 7.4 pA/pF; NDPK-B 77.82 ± 9.75 pA/pF; H118N 92.56 ± 4.49 pA/pF) currents of TRPC5 (Figure A15 A, C). Furthermore, the current-voltage relationship was not changed due to the coexpression of either NDPK-B wt or NDPK-B H118N (Figure A15 B). Altogether, the coexpression of NDPK-B did not influence the TRPC5 currents.

5.4.1 Summary: Functional interaction of TRPC4 non-TRPC proteins

The Coexpression of GRAM domain-containing proteins, SH3 and cysteine-rich domain-containing protein 2 (Stac2), early endosome antigen 1 (hEEA1), Latrophilin 2, Transmembrane protein 201 (TMEM 201), Nucleoside-Diphosphate Kinases-B (NDPK-B), cysteine and glycine-rich protein 1 (Csrp1) and LIM and SH3 domain protein 1 (Lasp1) had no or little effects on either TRPC4 nor TRPC4/TRPC1 current amplitudes. Latrophilin 2 was an exception among these proteins, since the coexpression of Latrophilin 2 significantly reduced TRPC4 as well as TRPC4/TRPC1 current amplitudes.

It seems that this protein could be a modulating interaction partner of TRPC4 with an inhibitory effect on the channel. Latrophilin is an adhesion G protein-coupled receptor (aGPCR) expressed either in neurons (Latrophilin 1 and 3) or ubiquitous (Latrophilin 2). Activation of Latrophilin with α -latrotoxin (spider venom toxin) stimulates the $G_{q/11}$ modulated PLC- β cascade, where PIP₂ is hydrolyzed to DAG and IP₃ [Silva and Ushkaryov, 2010]. This cascade is part of the activation pathway of TRPC4 and TRPC5 channels (Figure 4 and Figure 20 A). But in the present study, the presence of Latrophilin 2 had an inhibitory effect on TRPC4. However, Latrophilin 2 was not activated by its agonist, so the effect of activated Latrophilin 2 on TRPC4 was not considered.

In *Drosophila melanogaster*, TRP channels are expressed in mechanosensory neurons, where they genetically interact with the homolog of Latrophilin (*dCirl*) and modulate the sensitivity of neuronal mechanosensation [Scholz *et al.*, 2015]. Therefore, Latrophilin 2 could also be a modulator for TRPC4 and the interaction has to be studied further. Colocalization experiments with fluorescent labeling and protein surface biotinylation could be used to show if both proteins are present in the plasma membrane and if they are close enough for an interaction.

Another protein with an effect on the TRPC4 current was NDPK-B, since its presence significantly increased the current in stably TRPC4 expressing cells, which was not observed in the presence of the inactive NDPK-B H118N. Besides Latrophilin 2 and NDPK-B the coexpression of all other proteins had no functional effect on the TRPC4 current.

Curriculum vitae

BARBARA WARDAS

Aus datenschutzrechtlichen Gründen wird der Lebenslauf in der elektronischen Fassung der Dissertation nicht veröffentlicht.

Publications

1. Belkacemi A, Hui X, Wardas B, Laschke M W, Wissenbach U, Menger M D, Lipp P, Beck A, Flockerzi V. IP3 Receptor-Dependent Cytoplasmic Ca²⁺ Signals Are Tightly Controlled by Cavβ3. *Cell Rep*. 2018 Jan 30;22(5):1339-1349.
2. Flockerzi V., Wardas B. *Encyclopedia of Molecular Pharmacology*, Chapter: TRP channels, Springer-Verlag Berlin Heidelberg (in print).

Published abstracts

1. Kaiser N, Wardas B, Flockerzi V, Belkacemi A. Role of calcium channel subunits in endothelial cell function. Abstracts of the 86th Annual Meeting of the German Society for Experimental and Clinical Pharmacology and Toxicology (DGPT) with contribution of the Arbeitsgemeinschaft für Angewandte Humanpharmakologie e.V. (AGAH). *Naunyn-Schmiedeberg's Arch Pharmacol* 393, 1–97 (2020). 2–5 March 2020, Leipzig, Germany.
2. Wardas B, Wang H, Mannebach-Goetz S, Wissenbach U, Beck A, Flockerzi V. TRPC1-mediated currents in heterologous expression and isolated pituitary cells. Abstracts of the 85th Annual Meeting of the German Society for Experimental and Clinical Pharmacology and Toxicology (DGPT) and the 21th Annual Meeting of the Association of the Clinical Pharmacology Germany (VKliPha) With contribution of the Arbeitsgemeinschaft für Angewandte Humanpharmakologie e. V. (AGAH). *Naunyn-Schmiedeberg's Arch Pharmacol* 392, 1–88 (2019). 25–28 February 2019, Stuttgart, Germany.
3. Roomp K, Grzyb K, Wolf C, Rhayem Y, Oliver N, Wardas B, Beck A, Pico A, Beuschlein F, Skupin A, May P, Schneider J G. New germline mutation in CACNA1H calcium channel causing primary aldosteronism. *Endocrine Abstracts* 41 GP7 18th European Congress of Endocrinology 28–31 May 2016, Munich, Germany.
4. Jamali S; Klier M; Wardas B; McKenna R, Deitmer J W, Becker H M. Hypoxia-induced carbonic anhydrase IX enhances lactate transport in human breast cancer cells by a non-catalytic mechanism. Abstracts of the 93rd Annual Meeting of the German Physiological Society. *Acta Physiol (Oxf)*;210 Suppl 695:4-228. 13-15 March 2014, Mainz, Germany.

In preparation

1. Wang H, Raza A, Wardas B, Belkacemi A, Mannebach-Goetz S, Qiao S, Philipp S E, Dietrich A, Boehm U, Beck A, Flockerzi V. TRPC1 tightly controls pituitary growth hormone release by mitigating TRPC5 function.

2. Wardas B, Beck A, Schneider J G, Flockerzi V. Englerin A dose-dependently inhibits CaV3.2 channels.
3. Belkacemi A*, Wardas B*, Jung M, Beck A, Flockerzi V. CaV β binding site in CaV3.2 and inhibition of CaV3.2 currents.
(* equally contributed)
4. Wardas B*, Becker A*, Salah H, Philipp S E, Flockerzi V, Belkacemi A. CaV β function in insulin release in rat Ins-1 cells.
(* equally contributed)